Internal Wave Generation and Near-Resonant Interactions: Theory and Applications

by

Timothy Rees

A thesis
presented to the University of Waterloo
in fulfillment of the
thesis requirement for the degree of
Doctor of Philosophy
in
Applied Mathematics

Waterloo, Ontario, Canada, 2011

I hereby declare that I am the sole author of this thesis. This is a true copy of the thesis, including any required final revisions, as accepted by my examiners.

I understand that my thesis may be made electronically available to the public.

Abstract

Near-resonant triad interactions and wave generation theory are investigated for continuously stratified fluids. Interaction equations are derived for spatially-varying wave trains under the inviscid Boussinesq approximation. Rotational effects are included, and properties of the underlying eigenvalue problem are explored. To facilitate a numerical study of the near-resonant interactions, numerical methods are developed and an analysis of wave generation on a periodic domain is performed.

Numerical experiments using laboratory and ocean-scale parameters are conducted, and the simulations confirm the validity of the wave forcing theory. Interaction experiments demonstrate a strong tendency for waves to exhibit nonlinear behaviour. While resonant interactions are observed in the laboratory scale simulations, nonlinear steepening effects and the formation of solitary-like waves dominate the ocean-scale experiments. The results suggest that the weakly-nonlinear interaction theory is only appropriate in a limited parameter regime.

The problem of analyzing forced wave equations on an infinite domain is also considered. Motivated by the results obtained on a periodic domain, asymptotic analysis is applied to three important wave equations. The method of steepest descents is used to determine the large-time behaviour for the linearized Korteweg-de Vries, Benjamin-Bona-Mahony, and internal gravity wave equations. The asymptotic results are compared with numerical experiments and found to agree to high precision.

Acknowledgements

I would like to thank all of the people who have helped make my research and the writing of this thesis possible. I am grateful to my supervisors, Francis Poulin and Kevin Lamb, for all of the guidance they have given me. Their insight and interest has helped me greatly. Marek Stastna has also been very helpful, and his enthusiasm more than compensates for his questionable taste in music. I would also like to thank Mike Waite, Fue-Sang Lien, and Karl Helfrich for serving on my committee.

I have had many interesting discussions with my lab-mates, and sometimes the topics were even related to research. I would like to thank Anton Baglaenko, Michael Dunphy, Vladimir Gerasik, Wentao Liu, Kris Rowe, Nancy Soontiens, Derek Steinmoeller, and Chris Subich for helping make the graduate student experience enjoyable. I wish them all success in the future and hope our paths will cross again.

I have been fortunate to receive funding through Ontario Graduate Scholarships, and these scholarships have allowed me to pursue my research interests. I am also grateful to Sport Canada and Judo Canada for the additional tuition support and funding I have received.

Finally, I would like to thank my family, especially my wife and two sons. Balancing family time, research, and pursuits in competitive sports is not easy, and without the patience and understanding of my three favourite people it could not happen.

Dedication

This thesis is dedicated to my wife Aya and my sons Walter and William.

Table of Contents

List of Tables

List of Figures

Chapter 1

Introduction

This chapter introduces the main problems to be addressed in this thesis and motivates their study. First, the concept of internal waves is discussed and their importance is explained. Then, an overview of internal wave instabilities and generating mechanisms is given. This is followed by a statement of the problems that are to be investigated and a description of the organization of the remainder of this dissertation.

1.1 Motivation

Wave-watching at the beach is a captivating experience. From fast-moving ripples to crashing surf, waves instill a sense of awe and wonder in their audience. There is a strange sensation that each wave is somehow different but familiar, and simple yet complex. Trying to understand the intriguing properties of these marvelous creations is a rewarding pursuit with significant scientific value.

Surface water waves are probably the most well-known wave phenomenon to the general public. This is largely due to the abundance of water on earth, combined with the differences in the optical properties of air and water that make the waves visible. Waves are also commonly observed on other fluid surfaces, such as the interface between air and oil or alcohol and water, and are accepted as the same phenomenon. Contrary to popular belief, however, waves are not limited to the free surface of a liquid.

The physical mechanism responsible for surface water waves is the restoring force of gravity. Under typical conditions, air has a density of roughly 1 kg/m^3, and, depending on its mineral content and temperature, water has a density of roughly 1000 kg/m^3, resulting in an abrupt jump in density at the water surface. The density difference entices the force of gravity to adjust an uneven water surface, but the inertia of the moving water causes

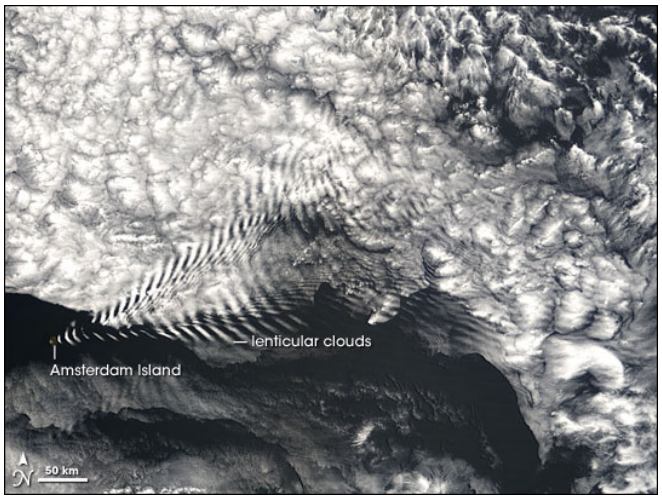

Figure 1.1: Clouds near Amsterdam Island. The island is located in the bottom left (southwest) corner of the image. Airflow to the northeast generates oscillations forming a pattern similar to a ship's wake. Source: NASA earth observatory [55].

the surface to overshoot the equilibrium position, leading to oscillations. Naturally this mechanism could also generate waves in a fluid with density transitions that are not as abrupt as the air-water interface. These waves, known as internal gravity waves, or simply internal waves, exist within the body of a fluid instead of at its free surface.

The possibility of internal wave motion seems reasonable, but it is a fair question to ask where the necessary density variations exist to support such a phenomenon. As it happens, the earth's atmosphere, oceans, and many lakes possess gradual density variations. This gives rise to a wealth of interesting wave behaviour.

1.1.1 Observing Internal Waves

In nature, internal gravity waves are harder to observe than their surface-dwelling cousins. Their presence is relatively unknown to the general public, but internal waves are abundant in a diverse range of environments. Internal waves are no strangers to exotic locations, and have even been detected in Titan's atmosphere, among other places (see Hinson and Tyler [33]). The discussion presented here is limited to their observation in the earth's oceans and atmosphere.

In earth's atmosphere, density variations in clear air are not easily visible, but waves can sometimes be viewed in cloud layers. This is demonstrated in Figure 1.1. The picture

shows a wave pattern in the clouds near Amsterdam Island in the Indian Ocean. The island is located in the bottom left, southwest corner of the image. Warm, moist air is driven upwards as it blows past the island's volcanic cone. As the warm air rises to its peak, it cools and moisture condenses, forming clouds. The cool air then falls, the clouds evaporate, and oscillations ensue. The "V" shape wave pattern is reminiscent of a ship's wake.

Water is relatively opaque to electromagnetic radiation, so events taking place below the surface generally cannot be observed with optical instruments. This makes measurements of internal gravity waves in the oceans particularly challenging. To counter this problem, oceanographers use a combination of *in situ* and remote sensing measurements to detect internal waves.

Internal waves leave a signature on the sea surface that is detectable by radar imaging. In Figure 1.2 a radar image of the Gulf of Mexico sea surface northeast of the Yucatan Peninsula is shown. A striped pattern is visible near the center of the image, indicating alternating patches of surface roughness and smoothness. This pattern indicates the presence of internal gravity waves below. An explanation for this internal wave footprint is given by Alpers [4]. Short surface waves largely determine the sea surface roughness, and in turn, the surface reflectivity. The bright and dark streaks in the radar image indicate regions of increased and decreased reflectivity. Surface films, carried by currents induced by internal waves, accumulate in convergence zones and damp the short surface waves. In addition, surface currents induced by internal waves directly modify the short surface waves through interactions. Damping of the short waves by these two mechanisms causes a reduction in reflectivity.

In situ measurements are another method used by scientists to detect internal waves in the deep ocean. In a recent study, van Haren and Gostiaux [70] observed internal waves breaking off the Great Meteor Seamount at depths exceeding 500 m. Using nearly one hundred high-precision temperature sensors, they were able to infer the passage of internal waves with amplitudes of 5-10 meters. Wave-overturning was also detected through temperature intrusions and attributed to Kelvin-Helmholtz instability.

As an alternative to studying internal waves in nature, laboratory experiments and numerical simulations are often used. These can be a cost-effective choice, requiring less man-power and equipment. In addition, targeted studies of wave processes can be conducted in isolation from uncontrollable external factors. Numerical simulations are used throughout this thesis to study and visualize internal waves.

The inherent difficulties faced by scientists in their attempts to observe internal waves does not detract from the importance of the phenomenon. As discussed below, researchers from a diverse range of disciplines are actively involved in studies of internal waves and their properties.

Figure 1.2: A satellite radar image of the Gulf of Mexico's surface northeast of the Yucatan Peninsula. The bands of well-spaced parallel lines indicate the presence of internal waves below the surface. Source: NASA earth observatory [54].

1.1.2 Why Are Internal Waves Important?

The oceans and atmosphere are teeming with internal waves, and they play a significant role in processes that range in scale from microscopic mixing to climate dynamics. As a result, internal waves are an active area of research in many fields of science. To illustrate this point, consider the following (non-comprehensive) list of research areas with examples of how internal waves are important.

- **Applied Mathematics**. Internal waves pose interesting modelling challenges that lead to complicated differential equations. This has driven the development of a rich mathematical theory and a vast body of literature. In a recent review, Helfrich and Melville [32] discuss the important weakly-nonlinear dispersive equations used to model long internal waves. Other mathematical descriptions are given by Lighthill [45, Chapter 4], Kundu and Cohen [37, Chapter 14], and LeBlond and Mysak [43], among many others.
- **Atmospheric Science.** Internal waves in the atmosphere play an important role in many different processes at various altitudes. In a review by Solomon [62], mixing

and transport of CFCs due to atmospheric internal waves is discussed as a factor in the depletion of the stratospheric ozone layer.

- **Biology.** The mixing and transport of nutrient-rich water by internal waves in lakes and the oceans influences the concentrations of species throughout the water body. For example, Leichter et al. [44] have studied how the zooplankton populations at various depths on a coral reef are related to the presence of cool, chlorophyll-rich water transported by breaking internal waves.

- **Computer Science and Numerical Analysis.** Simulating internal waves numerically is a complicated task requiring advanced algorithms, parallel processing, and novel data analysis techniques. A topic that is currently en vogue is the application of spectrally-accurate methods to simulate internal wave processes. Recent software packages developed by Subich [64] and Winters et al. [73] are examples of this.

- **Physical Oceanography.** As described in the recent review by Garrett and Kunze [27], barotropic tidal flow past topography generates internal tides. Depending on the flow geometry, these waves can have non-tidal frequencies and propagate great distances from their generation sites. The internal tides are believed to be responsible for roughly 30% of all tidal energy dissipated. Another problem of fundamental importance to oceanographers is understanding the nature and cause of mixing in the deep ocean. Polzin et al. [59] found enhanced mixing rates near rough topography in the Brazil Basin, likely due to internal wave motion.

It is primarily in the areas of Applied Mathematics, Numerical Analysis, and Oceanography that this thesis is concerned. In particular, resonant triad interactions and wave generation theory are the focus of this investigation. These topics are introduced in the next section.

1.2 Background and Related Work

A significant body of literature has been developed on many different aspects of internal waves. This is not surprising considering the ubiquity of the phenomenon. In this section, a simple model of the density stratification of the ocean is described, and basic terminology is introduced. After that, some of the important contributions related to instability mechanisms and internal wave generation theory are discussed.

1.2.1 Density Stratification and the Buoyancy Frequency

It is important to understand the character of the density profiles that arise in the environment. The ocean is of primary interest in this investigation, so a basic ocean density model is now presented. This discussion follows Kundu and Cohen [37, Chapter 14] closely, and the interested reader is referred there for a description of atmospheric density profiles.

In the oceans, the density stratification is largely due to temperature variations with depth, but salinity is also a factor. The depth-varying temperature is primarily caused by increased solar absorption near the surface and large-scale circulation patterns. In many places, the oceanic water column can be divided into three regions. Near the surface lies a well-mixed layer. Turbulence from a combination of currents, waves, and convective overturning maintain the mixed state. Below the surface layer lies the pycnocline (or thermocline), a region of relatively strong stratification. Due to its stronger stratification, the pycnocline is where much of the internal wave activity takes place. Finally, below the pycnocline lies a weakly stratified mass of cold water.

A useful quantity known as the Brunt-Väisälä frequency helps to quantify the strength of a stratification. Commonly referred to as the buoyancy frequency and denoted by $N(z)$, it has units s^{-1}. Throughout this thesis, the Boussinesq approximation is used (see Chapter 2), and under this assumption the buoyancy frequency takes the form:

$$N^2(z) = -\frac{g}{\rho_0}\frac{d\bar{\rho}}{dz}. \tag{1.1}$$

Here ρ_0 defines the mean background density, $\bar{\rho}(z)$ is the small vertically-varying component, and g is the gravitational constant. Physically, the buoyancy frequency specifies the oscillation frequency that an infinitesimally vertically-displaced fluid parcel at depth z would experience under gravity.

Based on the discussion above, Figure 1.3 presents a sample oceanic density profile and the corresponding buoyancy frequency profile. Near the surface ($z = 0$) the density is almost constant. Below that, the pycnocline is approximately located in the interval $-450 \leq z \leq -150$ meters. Across the pycnocline the density increases by about 5 kg/m^3. Below the pycnocline the density grows very slowly with depth. These features are clearly evident in the plot of the buoyancy frequency. The pycnocline is identifiable as the region where $N(z)$ is relatively large. The weak stratification below the pycnocline is also apparent because the buoyancy frequency is noticeably positive.

Under the Boussinesq approximation, a fluid is said to be stably stratified if $N^2(z) \geq 0$. A fluid is continuously stratified if $N(z)$ is continuous. A uniformly stratified fluid is one for which $N(z)$ is constant, indicating that $\bar{\rho}(z)$ varies linearly with depth. Internal waves in uniformly stratified fluids have particularly useful analytical properties (see Chapter

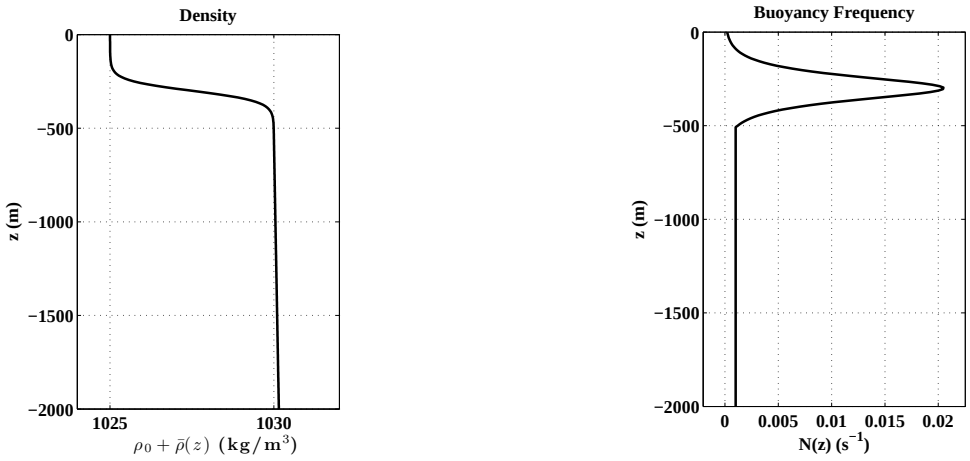

Figure 1.3: A sample density profile (left subplot) and the corresponding buoyancy frequency profile (right subplot) for an ocean of depth 2 km.

2). Many authors have used uniform stratifications as models of oceanic and atmospheric density profiles, and much of the theory of internal waves is built upon this assumption. Studying the effects of nonuniform stratification is a central theme of this thesis.

1.2.2 Internal Wave Instabilities and Resonant Interactions

The splendor of a massive surface breaking wave is rivaled by few events in nature. The wave-breaking process is visually stimulating and vastly complex. Within the frothy foam-pile air is entrained and turbulent mixing occurs. Strong currents are also induced by the wave, and in coastal regions significant volumes of sand and rocks are scraped from the sea-floor and relocated. Breaking waves play an important role in coastal geomorphology where they erode beaches and sculpt cliff faces. In the open ocean the wave-breaking process helps keep the upper water column in a well-mixed state.

Not to be outdone, internal gravity waves can also break. Their sub-surface location makes them an important factor in the mixing and vertical flux of nutrients, heat, and momentum within the ocean body. In the vicinity of the sea-floor, breaking internal waves are also involved in the uptake of sediments.

Technically speaking, wave-breaking is defined as the production of turbulence and irreversible mixing. Internal wave breaking has been studied through numerical simulations and laboratory experiments. This includes work on uniform stratifications by Lombard and Riley [47, 48], who found the breaking process to be dominated by a combination of convective and shear instabilities. Fringer and Street [26] numerically forced progressive internal waves on a thin density interface to the point of breaking, they also observed shear

instabilities. In related laboratory studies, Troy and Koseff [68, 69] studied the breaking of long internal waves in a two-layer miscible fluid. They also observed Kelvin-Helmholtz instabilities in wave crests and troughs.

Thorpe [66] has shown that a necessary, but not sufficient, condition for wave-breaking is the overturning of isopycnals (lines of constant density). For this to occur, breaking is typically preceded by a steepening phase. In their excellent review, Staquet and Sommeria [63] identify three important internal wave steepening mechanisms: wave-focussing by wall reflections, wave-mean flow interactions, and resonant wave interactions. Each mechanism is fascinating, but it is resonant interactions that are the focus of this study.

Resonant wave interactions have a broad importance in many different settings. In an entertaining review by a pioneer in the field, Phillips [58] describes the origins of the idea and how it was developed for phenomenon such as surface gravity waves, plasmas, electronics, and capillary waves. Craik [14] also provides a description of the many applications of the theory. Resonant wave interactions are not limited to continuous media, however, and Drazin and Reid use the example of a double-pendulum to introduce the topic in their text [21, Chapter 7]. In the present setting, it is interactions involving three waves, known as a triad, that are of interest. Higher-order interactions are possible but they are typically weaker. A common theme for all resonant triad interactions is that a set of resonance conditions must hold. For horizontally-propagating waves, these take the form:

$$\begin{aligned} k_1 + k_2 + k_3 &= 0 \\ \omega_1 + \omega_2 + \omega_3 &= 0, \end{aligned} \tag{1.2}$$

where k_n and ω_n denote the wavenumber and frequency of the n^{th} wave, and negative values are permitted. An explanation for these conditions is given by Phillips [58], Craik [14], and Drazin and Reid [21], and is also presented in Chapter 2 of this thesis. If three waves only meet these conditions to within a small error tolerance, they are said to be near-resonant. As will be seen, internal waves meeting these resonant (or near-resonant) constraints obey interesting evolution equations.

Conditions (1.2) limit the possible candidates for wave interactions in a given system. This is because the frequency of a wave depends on the wavenumber through the dispersion relation. For surface gravity waves on deep water, the dispersion relation takes the form $\omega = \sqrt{gk}$, so it is impossible to find three non-trivial waves satisfying (1.2). Phillips' original derivation of resonant interactions for surface gravity waves involved a quartet of waves for which the equivalent resonant condition can be satisfied [57].

An important early contribution to resonant triad interaction theory was made by Davis and Acrivos [17]. In that study, the authors considered a non-rotating, inviscid fluid under the Boussinesq approximation with a stable continuous density stratification. They derived interaction equations for spatially invariant wave trains. Their work demonstrates

the possibility for interactions in practically all stratified fluids of interest, provided the resonance condition can be met for the given stratification. Whether or not the resonance condition can be satisfied for a particular stratification must be determined numerically due to the complicated nature of the dispersion relation.

Several laboratory experiments have been carried out to directly observe resonant triad interactions for internal waves. Martin et al. [49] conducted successful experiments on resonant triad excitation in a uniformly stratified fluid. In addition to their analytical work, Davis and Acrivos [17] were able to demonstrate resonant triad interactions experimentally in a fluid with a thin density interface.

A number of numerical studies have also identified resonant interactions. For example, the evolution of a standing internal wave in a uniformly stratified fluid in two dimensions has been explored numerically by Bouruet-Aubertot et al. [9]. The authors found that the primary wave destabilized by means of a parametric subharmonic instability. Disturbances of half the primary wave frequency were found to grow at the vorticity extremes. It was also found that breaking occurred regardless of the initial wave amplitude. The excitation of lower frequency secondary waves growing on a primary wave can be interpreted as a resonant triad interaction.

Staquet and Sommeria [63] point out that there is no clear evidence showing the presence of resonant triad interactions in measurements of oceanic internal waves. However, in numerical experiments Lamb [41] recently observed the excitation of certain internal waves via near-resonant triad interactions. Generating an internal wave field through tide-topography interactions, Lamb detected a structure dominated by waves nearly coupled to the tidal wave by the aforementioned resonance condition. Even without exact resonance, the strength of the triad was significant. In a related thesis, Hu [34] also explored the interactions of resonant triads in a fluid with constant buoyancy frequency. These works appear to be the first to identify near-resonant triads in tide-topography interactions.

Resonant triad interactions for internal gravity waves have been studied from many perspectives. The majority of research, however, has focussed on fluids with uniform density stratifications. The analysis given by Davis and Acrivos, [17] is a notable exception, but their work has not been extended to include near-resonance, spatially varying wave trains, or the effects of rotation. There is also a dearth of literature on simulations of resonant triad interactions in fluids with nonuniform stratifications. As a consequence of this, many of the tools necessary for such simulations have not been developed.

1.2.3 Internal Wave Generation Mechanisms

Internal waves in nature are excited by a variety of sources. Some of these generating mechanisms are now discussed for oceanic, atmospheric, laboratory, and numerical internal

waves. The more theoretical topic of forcing responses for partial differential equations is also considered.

In many instances, the interaction of stratified flow with topography is an important source of internal gravity waves. This is true in the atmosphere, where wind blowing over topography such as mountains is the dominant source of internal waves (see Wuertele et al. [74]). This is the mechanism responsible for the wave pattern shown in Figure 1.1, and the interested reader is directed to the NASA earth observatory homepage for other impressive images [55].

In the oceans, barotropic tidal flow past topography is a strong source of internal waves. The generated waves are not necessarily of tidal frequency, but are determined by the geometry of the topography and tidal excursion length. The physical theory behind this form of wave generation is reviewed by Garrett and Kunze [27]. In another review, Helfrich and Melville [32] discuss the importance of topography in the production of long, large-amplitude internal waves. Recent numerical and laboratory experiments quantifying the process for a uniform stratification are given by Echeverri et al. [24].

An extension of the tide-topography model for wave generation has been explored by Akylas et al. [3]. In their model, internal wave beams originating at steep topography sites reflect off the thermocline. The wave beam may travel large distances before reflecting, and the reflection generates finite-amplitude solitary waves on the thermocline. Their work provides a possible explanation for the production of internal solitary waves in the deep ocean.

The resonant wave interactions considered in the previous subsection are another mechanism that can generate internal waves. Waves coupled by the resonance condition (1.2) transfer energy amongst themselves. If two of the waves in a triad are present, the interaction will produce the third wave. The growing parasitic wave disturbances observed in numerical experiments by Bouruet-Aubertot et al. [9], and Koudella and Staquet [36] are examples of wave generation through resonant interactions.

Like surface waves, internal waves can be generated in a wave tank with a paddle or other oscillatory sources. The vertically-varying structure of the waves can make it difficult to generate higher modes. As a result most experiments, even for uniform stratifications, are limited to studying just the first few vertical modes. Martin et al. [49] used a vertically oscillating single and triple-paddle assembly to generate mode one and three waves in a uniformly stratified fluid. Echeverri et al. [24] generated internal waves in a uniform stratification with a horizontally oscillating foam topography. Troy and Koseff [68, 69] used lateral channel contractions to force progressive internal waves on a thin density interface. In other recent experiments, Mathur and Peacock [50] studied the propagation of higher-mode internal wave beams in a variety of nonuniform stratifications using a generator consisting of twelve oscillating plates.

The more abstract study of wave generation through the analysis of forced model partial differential equations (PDEs) is also important. Numerical simulations of wave phenomena, internal or otherwise, typically require the solution of underlying PDEs. An analysis of forcing responses naturally facilitates the design of numerical experiments. This is particularly true in wave interaction experiments where it is necessary to generate multiple waves with relatively little transient noise. Lighthill [45, Chapter 4], [46], has laid the foundation for the mathematical study of this problem in a uniformly stratified fluid on an unbounded domain. The problem is also studied in detail by Voisin [71], who presents exact and asymptotic solutions using the Green's function. Voisin's analysis of the impulsively forced problem for Boussinesq fluids is particularly relevant to this study. Similar analysis for internal gravity waves in a region confined by horizontal plane boundaries does not appear to have been considered in the literature. Related problems for internal waves in nonuniform stratifications have also received little attention thus far. In fact, a systematic framework for analyzing the forcing response of dispersive wave equations would be useful to a wide audience.

1.3 Problem Statement

In this thesis three major problems are addressed. These problems are closely related, and each helps to answer questions that have not been fully resolved in the existing body of literature. The problems under investigation are as follows.

Problem 1: Theory of Near-Resonant Triad Interactions. This problem involves performing a weakly-nonlinear analysis to determine how internal wave trains are modified through near-resonant triad interactions. The investigation concerns Boussinesq fluids in bounded domains with rigid lids, rotation, and variable density stratifications. The governing interaction equations must be derived, and their properties characterized. In addition, the properties of the underlying linear problem will be explored in detail.

Problem 2: Near-Resonant Triad Simulations. Given the resolution of Problem 1, fully nonlinear resonant triad interactions will be simulated in laboratory and ocean-scale numerical experiments. This requires the development of useful data analysis methods and numerical wave generation techniques for fluids with variable density stratifications. A major goal of this investigation is to determine the applicability of the weakly-nonlinear theory.

Problem 3: Dispersive Wave Forcing Theory. A necessary ingredient for the resolution of Problem 2 is the ability to accurately force waves numerically in a stratified fluid. This generalizes naturally to the problem of devising methods for generating a desired wave for a linear dispersive equation using an oscillatory source. Asymptotic analysis will be

used to determine the phase, frequency, and amplitude of forced waves. The mathematical results will then be compared with numerical experiments.

The problems under consideration are quite technical in nature and their resolution requires a diverse repertoire of mathematical methods. The close connection between the problems is also apparent, and there is a significant overlap in the methods used to solve them. This thesis is organized in an attempt to treat these problems sequentially, as described in the next section.

1.4 Thesis Layout

The remainder of this thesis is divided into five chapters and four appendices. Chapters 2 – 4 primarily deal with problems of resonant wave interactions and their simulation. Chapter 5 presents a study of impulsively forced wave equations. The appendices provide some of the more laborious calculations.

The basic theory of resonant triad interactions for internal gravity waves is presented in Chapter 2. This includes a derivation of the interaction equations, a survey of some of their properties, and a technical discussion of the underlying linear eigenvalue problem. The study of the eigenvalue problem provides a foundation for much of the mathematics in the chapters that follow.

Before attempting to study resonant interactions through simulations, the necessary numerical methods are presented in Chapter 3. A description of the techniques used to find triads a priori is given, then two numerical models used for simulations are described. The approach used in energy decompositions of simulation data is then presented, and interesting properties of the energy spectrum are explored. The chapter ends with a discussion of the method used to accurately generate internal gravity waves numerically.

Numerical simulations are presented in Chapter 4. Basic experiments are displayed, as well as interaction experiments for laboratory and ocean-scale waves. Two different oceanic stratifications are investigated, with experiments focussing on waves of tidal frequency. The chapter closes with a general discussion to explain some of the interesting simulation results.

In Chapter 5 the focus shifts to the asymptotic analysis of impulsively forced wave equations. Motivated by the numerical forcing problem addressed in Chapter 3, problems on an infinite domain are studied. After an introduction to solution techniques and a review of the forced long-wave equation, asymptotic analysis is applied to the linearized Korteweg-de Vries (KdV) equation, Benjamin-Bona-Mahony (BBM) equation, and internal gravity wave (IGW) equation. The approximate results are compared against numerical solutions for each equation.

Finally, conclusions are drawn in Chapter 6. The important contributions are summarized for each of the three major problems under consideration. Suggestions for interesting future projects are also given. After Chapter 6 the appendices and references are given.

Chapter 2

Near-Resonant Triad Interaction Theory

This chapter presents the theory underlying near-resonant triad interactions for internal waves in continuously stratified fluids. The interaction equations are derived in Section 2.1. Some interesting properties of the interaction equations are described in Section 2.2. In Section 2.3 important properties of the fundamental linear eigenvalue problem for internal gravity waves are discussed in detail.

2.1 Deriving the Interaction Equations

Resonant triads interactions occur in many fields within the physical sciences. The interest here is in how they arise and behave for inviscid, incompressible fluids with continuous density stratifications. The natural approach starting with wave solutions to the equations of motion is pursued here. The notation and methods used here are similar to those of Lamb [40], and Hu [34].

2.1.1 The Boussinesq Equations

Consider an inviscid fluid governed by the Boussinesq equations in a rotating reference frame. Suppose the fluid has depth H, and is confined between rigid, impermeable boundaries at $z = 0, H$. Using the f-plane model (constant Coriolis parameter f), and aligning the x-axis along the direction of propagation so that all variables are independent of y, the basic equations are

$$u_t + uu_x + wu_z - fv = -\frac{p_x}{\rho_0} \tag{2.1a}$$

$$v_t + uv_x + wv_z + fu = 0 \tag{2.1b}$$

$$w_t + uw_x + ww_z = -\frac{p_z}{\rho_0} - \frac{\rho}{\rho_0} g \tag{2.1c}$$

$$\rho_t + u\rho_x + w\rho_z = 0 \tag{2.1d}$$

$$u_x + w_z = 0 \tag{2.1e}$$

$$-\infty < x, y < \infty,\ 0 \le z \le H.$$

Subscripts are used to indicate partial derivatives. The vector field $\vec{u} = (u, v, w)$ defines the velocity, p is the pressure, and g is the gravitational constant. The density ρ used throughout this thesis generally takes the form

$$\rho = \rho_0 + \bar{\rho}(z) + \rho'(x, z, t), \tag{2.2}$$

where ρ_0 is the reference value, $\bar{\rho}(z)$ is the variable background state, and $\rho'(x, z, t)$ is the density perturbation. Typically, density profiles of the form $\bar{\rho}(z) = -\frac{\Delta\rho}{2} \tanh\left(\frac{z - z_0}{D}\right)$ are used to model a fluid consisting of a light fluid overlying a heavy fluid with a smooth transition in density. This scenario is common in the oceans, for instance, where fresher water lies over dense, salty water.

Boundary conditions must be imposed on w and ρ' at the rigid, impermeable boundaries at $z = 0, H$. The natural condition is that no normal flow to the boundaries can occur, and this fixes w and ρ' to be zero at $z = 0, H$. Since the fluid is inviscid, the horizontal velocity components are not constrained at the vertical boundaries.

The main difference between the Boussinesq equations and the Euler equations is that the full expression for density only appears when multiplied with g. The validity of this approximation is discussed at length in Kundu [37, Chapter 4]. In general this set of equations is appropriate for ocean-like flows which have relatively small density variations, finite depth, and low Mach numbers. This approximation is also used for atmospheric flows in certain cases but more care is required because of the large vertical length scales and correspondingly large density variations.

Equations (2.1) specify the evolution of dimensional quantities. For use in both the perturbation analysis that follows and later numerical simulations, a non-dimensionalization process is useful. For the moment, let variables with hats be dimensionless quantities, and capitalized variables be dimensional. Define dimensionless length variables $(\hat{x}, \hat{y}, \hat{z}) = (x, y, z)/H$, where H is the height of the domain. Define a velocity scale U so that $(u, v, w) = U(\hat{u}, \hat{v}, \hat{w})$ and the time scale $T = H/U$. The pressure is scaled like $p = P\hat{p}$ where $P = \rho_0 U^2$, and the density is scaled by $\rho = R\hat{\rho}$, and the dimensionless Coriolis parameter is defined by $\hat{f} = fT$.

The appropriate velocity scale is defined by $U^2 = gH\frac{\Delta\rho}{4\rho_0}$ is used. This is the phase speed of a long wave in a two-layer fluid with equal depths of $H/2$, density jump $\Delta\rho$

and mean density value ρ_0, as discussed in Appendix A. The appendix also demonstrates how this choice of velocity scale is appropriate even when the pycnocline is not centered in the domain, provided it does not lie extremely close to either boundary. The natural interpretation of the time scale $T = H/U$ is the time it would take a long internal wave crest to traverse a distance equal to the fluid depth.

With the chosen velocity scale, it is natural to define the density scaling $R = \Delta\rho/4$. This makes the dimensionless density jump across the fluid roughly four. The buoyancy frequency, expressed as $N(z)$, is defined by $N^2(z) = -(g/\rho_0)d\bar{\rho}/dz$. The dimensionless buoyancy frequency is then $\hat{N}^2(\hat{z}) = T^2N^2(z)$. In terms of the dimensionless background density, $\hat{N}^2(\hat{z}) = -d\hat{\bar{\rho}}/d\hat{z}$. The buoyancy $b = (g/\rho_0)\rho' = \frac{U^2}{H^2}\hat{\rho}'$ has dimensionless equivalent $\hat{b} = \hat{\rho}'$.

Finally, for notational simplicity, all hats are dropped from the dimensionless variables. It is understood that unless otherwise stated, in the equations immediately below and all those that follow, the quantities are dimensionless. The Boussinesq equations become

$$u_t + uu_x + wu_z - fv = -p_x \tag{2.3a}$$

$$v_t + uv_x + wv_z + fu = 0 \tag{2.3b}$$

$$w_t + uw_x + ww_z = -p_z - \rho \tag{2.3c}$$

$$\rho_t + u\rho_x + w\rho_z = 0 \tag{2.3d}$$

$$u_x + w_z = 0 \tag{2.3e}$$

$$-\infty < x, y < \infty, 0 \leq z \leq 1.$$

This dimensionless set of equations is the foundation upon which this thesis is built.

The y-independence of these equations allows for introduction of the streamfunction ψ such that $(u, w) = (-\psi_z, \psi_x)$. The incompressibility condition (2.3e) is then automatically satisfied. Taking the curl of the x and z momentum equations yields the equation for the streamfunction

$$\frac{\partial}{\partial t}\nabla^2\psi + J(\psi, \nabla^2\psi) + fv_z = -b_x, \tag{2.4}$$

where the Jacobian operator is defined by $J(A, B) = A_xB_z - A_zB_x$. The equation for density can then be written

$$\frac{\partial b}{\partial t} + J(\psi, b) - N^2(z)\psi_x = 0. \tag{2.5}$$

Differentiating (2.4) with respect to t and simplifying reveals the following set of equations:

$$\nabla^2\psi_{tt} + f^2\psi_{zz} + N^2(z)\psi_{xx} = -\tfrac{\partial}{\partial t}J(\psi, \nabla^2\psi) + f\tfrac{\partial}{\partial z}J(\psi, v) + \tfrac{\partial}{\partial x}J(\psi, b) \tag{2.6a}$$

$$v_t + J(\psi, v) - f\psi_z = 0 \tag{2.6b}$$

$$b_t + J(\psi, b) - N^2(z)\psi_x = 0. \tag{2.6c}$$

These equations are more convenient for the derivation of resonant triad interactions.

2.1.2 Multiple-Scales Analysis

Large amplitude wave interactions are highly nonlinear processes and difficult to analyze. A more modest approach is to study the interactions of small amplitude waves. While this seems quite restrictive, it turns out that with the present choice of dimensionless parameters, small amplitude waves are still very interesting. With the analysis centered on equation (2.6a), small amplitude waves are just those for which $\{|\psi|, |b|, |v|\} \ll 1$. Physically, these are waves where the magnitudes of the induced velocity fields are small compared with the phase speed of a long wave in the equivalent two-layer fluid.

To analyze the small waves, suppose ψ is $O(\epsilon)$, where $\epsilon \ll 1$. Define slow space and time variables $\{X, T\} = \{\epsilon x, \epsilon t\}$. The variables ψ, v, and b are expanded as power series in ϵ so that

$$\begin{aligned} \psi &= \epsilon\psi^{(0)} + \epsilon^2\psi^{(1)} + \epsilon^3\psi^{(2)} + \cdots \\ v &= \epsilon v^{(0)} + \epsilon^2 v^{(1)} + \epsilon^3 v^{(2)} + \cdots \\ b &= \epsilon b^{(0)} + \epsilon^2 b^{(1)} + \epsilon^3 b^{(2)} + \cdots \end{aligned} \tag{2.7}$$

At any order j, the terms $\{\psi^{(j)}, v^{(j)}, b^{(j)}\}$ are functions of x, X, t, and T.

Substituting the series expansions into equations (2.6), carefully treating the derivatives, and noting nonlinear terms such as $J(\psi, \nabla^2\psi)$ are $O(\epsilon^2)$, simplifies the problem. Collecting like powers of ϵ reveals the $O(\epsilon)$ problem:

$$\begin{gathered} \nabla^2\psi^{(0)}_{tt} + f^2\psi^{(0)}_{zz} + N^2(z)\psi^{(0)}_{xx} = 0 \\ v^{(0)}_t - f\psi^{(0)}_z = 0 \\ b^{(0)}_t - N^2(z)\psi^{(0)}_x = 0. \end{gathered} \tag{2.8}$$

The equation for $\psi^{(0)}$ admits wave-like solutions of the form $\psi^{(0)} = g(z)\exp(i(kx - \sigma t))$, provided $g(z)$, k, and σ satisfy the equation

$$\begin{gathered} g''(z) + k^2\left(\frac{N^2(z)-\sigma^2}{\sigma^2-f^2}\right)g(z) = 0 \\ g(0) = g(1) = 0. \end{gathered} \tag{2.9}$$

The boundary conditions arise because $w = \psi_x$ must be zero at the rigid boundaries. Treating k as a parameter, this represents an eigenvalue problem that can be rewritten in

Sturm-Liouville form (see Section 2.3). The eigenvalues are simply the admissible frequencies σ, and when treated as a function of k, define the dispersion relation $\sigma(k)$. Solving the eigenvalue problem requires finding values of both σ and $g(z)$.

When $N^2(z) - f^2 > 0$ for $0 \leq z \leq 1$, the problem is of regular Sturm-Liouville type (see Zettl [78, Chapter 3]). This point is discussed carefully in Section 2.3, but for now it is assumed. At each k there is a countable infinity of eigenvalues that can be ordered $\sigma_1^2(k) > \sigma_2^2(k) > \cdots > 0$. The corresponding eigenfunctions are real and continuous. These ideas suggest rewriting the eigenvalue problem in the form

$$\begin{gathered} g_n''(z,k) + k^2 \left(\tfrac{N^2(z)-f^2}{\sigma_n^2(k)-f^2} - 1 \right) g_n(z,k) = 0, \\ g_n(0,k) = g_n(1,k) = 0, \end{gathered} \tag{2.10}$$

where the index n, known as the vertical mode number, has been associated with each eigenvalue and eigenfunction. In addition, the parameter k has been included as an argument of g_n to highlight the eigenfunction dependence on k.

The natural orthogonality condition for two eigenfunctions at the same value of k takes the form

$$\int_0^1 (N^2(z) - f^2) g_m(z,k) g_n(z,k)\, dz = \begin{cases} 1 & \text{if } m = n \\ 0 & \text{otherwise.} \end{cases} \tag{2.11}$$

These properties, and many others, are discussed by Zettl [78]. In Section 2.3 additional properties specific to the internal gravity wave problem are also developed.

Returning to (2.8) and the linear problem for $\psi^{(0)}$, consider a solution consisting of a superposition of three waves in the form

$$\psi^{(0)} = \sum_{p=1}^{3} \left(a_p e^{i\theta_p + i\frac{\pi}{2}} + a_p^* e^{-i\theta_p - i\frac{\pi}{2}} \right) g_{n_p}(z, k_p), \tag{2.12}$$

where p is a counting index, $\theta_p = k_p x - \omega_p t$, and $\omega_p = \sigma_{n_p}(k_p)$ lies on the mode-n_p dispersion curve. The factors of $\exp(i\pi/2)$ are chosen for algebraic convenience. The slowly varying complex-valued wave envelopes, denoted by a_p, are functions of X and T. The asterisk is used to denote the complex conjugate so that $\psi^{(0)}$ is real. In addition to satisfying (2.10), the wavenumbers and frequencies are assumed to obey the resonance condition (Craik [14, Chapter 5]):

$$\begin{aligned} k_1 + k_2 + k_3 &= 0 \\ \omega_1 + \omega_2 + \omega_3 &= 0, \end{aligned} \tag{2.13}$$

so that $\theta_1 + \theta_2 + \theta_3 = 0$ for all x, t. It may be extremely rare or even impossible that waves can be found satisfying (2.13) for a given stratification. For now this concern is simply ignored. The restrictiveness of the resonance condition will be relaxed shortly.

Given the proposed form of $\psi^{(0)}$, solutions for $v^{(0)}$ and $b^{(0)}$ can be readily obtained through (2.8). The complete $O(\epsilon)$ solution is

$$\begin{aligned}
\psi^{(0)} &= \sum_{p=1}^{3} \left(a_p e^{i\theta_p + i\frac{\pi}{2}} + a_p^* e^{-i\theta_p - i\frac{\pi}{2}} \right) g_{n_p}(z, k_p) \\
v^{(0)} &= f \sum_{p=1}^{3} \left(i\frac{a_p}{\omega_p} e^{i\theta_p + i\frac{\pi}{2}} - i\frac{a_p^*}{\omega_p} e^{-i\theta_p - i\frac{\pi}{2}} \right) g'_{n_p}(z, k_p) \\
b^{(0)} &= -N^2(z) \sum_{p=1}^{3} \left(\frac{k_p}{\omega_p} a_p e^{i\theta_p + i\frac{\pi}{2}} + \frac{k_p}{\omega_p} a_p^* e^{-i\theta_p - i\frac{\pi}{2}} \right) g_{n_p}(z, k_p),
\end{aligned} \tag{2.14}$$

where $g'_{n_p}(z, k_p) = dg_{n_p}(z, k_p)/dz$.

The next task is to consider the $O(\epsilon^2)$ problem so that evolution equations can be found for each wave envelope. Substituting the series form of each variable into (2.6) and collecting like terms yields the $O(\epsilon^2)$ equation:

$$\begin{aligned}
\nabla^2 \psi_{tt}^{(1)} + f^2 \psi_{zz}^{(1)} + N^2(z) \psi_{xx}^{(1)} = \; & -2 \left(\frac{\partial^2}{\partial t^2} \frac{\partial^2}{\partial x \partial X} + \nabla^2 \frac{\partial^2}{\partial t \partial T} \right) \psi^{(0)} \\
& -2N^2(z) \frac{\partial^2}{\partial x \partial X} \psi^{(0)} - \frac{\partial}{\partial t} J(\psi^{(0)}, \nabla^2 \psi^{(0)}) \\
& + f \frac{\partial}{\partial z} J(\psi^{(0)}, v^{(0)}) + \frac{\partial}{\partial x} J(\psi^{(0)}, b^{(0)}),
\end{aligned} \tag{2.15}$$

and

$$\begin{aligned}
v_t^{(1)} - f\psi_z^{(1)} &= -v_T^{(0)} - J(\psi^{(0)}, v^{(0)}), \\
b_t^{(1)} - N^2(z)\psi_x^{(1)} &= -b_T^{(0)} + N^2(z)\psi_X^{(0)} - J(\psi^{(0)}, b^{(0)}).
\end{aligned} \tag{2.16}$$

At this point the analysis becomes tedious because the Jacobian terms lead to lengthy expressions involving sums and differences of phases. The key observation, however, is that for waves satisfying the resonance conditions (2.13), the right hand side of (2.15) contains terms proportional to $\exp(i\theta_p)$ and $\exp(-i\theta_p)$ for $p = 1, 2, 3$. These terms could resonantly force the $O(\epsilon^2)$ solution, eventually breaking the ordering of the asymptotic expansion. The envelope functions a_p must be chosen to obey certain equations that prevent the resonant forcing.

In Appendix B, the detailed calculations are presented. The end result is a set of coupled partial differential equations that the envelope functions must satisfy to preserve asymptotic ordering. The equations take the form

$$\begin{aligned}
\frac{\partial a_1}{\partial T} + v_1 \frac{\partial a_1}{\partial X} &= \gamma_1 a_2^* a_3^*, \\
\frac{\partial a_2}{\partial T} + v_2 \frac{\partial a_2}{\partial X} &= \gamma_2 a_1^* a_3^*, \\
\frac{\partial a_3}{\partial T} + v_3 \frac{\partial a_3}{\partial X} &= \gamma_3 a_1^* a_2^*.
\end{aligned} \tag{2.17}$$

These equations are henceforth referred to as the resonant triad interaction equations. It is shown in Section 2.3 that the advection coefficients, v_p exactly match the group velocity

for the underlying waves. The interaction coefficients γ_p are real, and in Appendix B they are shown to agree with the results of Hu [34] and Lamb [41] when $N^2(z)$ is constant.

In Section 2.2 many important properties of these equations will be explored. First, however, the effects of relaxing the resonance condition (2.13) are considered.

2.1.3 Near-Resonant Interactions

The above theory describes the evolution of wave envelopes for three waves that satisfy the resonance condition (2.13) exactly. For an arbitrary background density profile, it may be impossible to find three waves obeying this condition. Even in situations where it is possible, the wavenumbers and frequencies involved may not be of physical interest. To counter these problems, a relaxed form of the resonance conditions is considered. Suppose that

$$\begin{aligned} k_1 + k_2 + k_3 &= \epsilon\hat{k}, \\ \omega_1 + \omega_2 + \omega_3 &= \epsilon\hat{\omega}, \end{aligned} \tag{2.18}$$

where $\hat{k}$, and $\hat{\omega}$ are at most $O(1)$. Triads meeting these conditions are referred to as near-resonant, or inexact triads. This loosening of the resonance condition significantly increases the applicability of the theory.

Much like a pendulum forced at near-resonance, the relaxed condition (2.18) still leads to growing waves. Like the exact case, wave envelopes must be chosen so that resonant growth does not occur on the fast space and time scales. As shown in Appendix B, the interaction equations for near-resonant triads take the form

$$\begin{aligned} \tfrac{\partial a_1}{\partial T} + v_1 \tfrac{\partial a_1}{\partial X} &= \gamma_1 a_2^* a_3^* e^{-i(\hat{k}X - \hat{\omega}T)}, \\ \tfrac{\partial a_2}{\partial T} + v_2 \tfrac{\partial a_2}{\partial X} &= \gamma_2 a_1^* a_3^* e^{-i(\hat{k}X - \hat{\omega}T)}, \\ \tfrac{\partial a_3}{\partial T} + v_3 \tfrac{\partial a_3}{\partial X} &= \gamma_3 a_1^* a_2^* e^{-i(\hat{k}X - \hat{\omega}T)}. \end{aligned} \tag{2.19}$$

The reduction to equation set (2.17) when $\hat{k} = \hat{\omega} = 0$ is apparent.

While the allowance for inexactness greatly improves the applicability of the theory, it does lead to more complicated evolution equations. In addition to being nonlinear and coupled, interactions now depend on variable coefficients. Even with this complication many interesting properties of the wave envelopes can be found, as described in the next section.

2.2 Properties of the Interaction Equations

The triad interaction equations (2.17) and their near-resonant cousins (2.19) determine the rate of growth or decay of the wave envelopes in a particular interaction. The amplitude

of a wave train is dictated by the shape of its envelope, so these equations describe the stability of the underlying waves. This section presents some of the important properties of the equations and their implications for stability of waves.

2.2.1 Preliminary Discussion

Informally, some features of the solutions to the evolution equations (2.17) and (2.19) can be discerned. When all three γ values are zero or none of the wave envelopes are overlapping, waves do not interact and the envelopes simply travel at a constant velocity with speed and direction determined by the group velocity values. Wave energy must travel with the envelopes, as there can only be waves where the envelope is non-zero. The calculations presented in Section 2.3 and Appendix B confirm that the velocity coefficients match the group velocity for the underlying waves. This matches the expected result that wave energy travels with the group velocity.

The effect of two wave envelopes interacting is to increase or decrease the local amplitude of the third envelope, depending on the sign of its γ value. The presence of the third wave then leads to interactions that modify the first and second envelopes, and a complicated process of energy transfers ensues. The initial behaviour of this energy transfer is described in upcoming subsections.

Another observation is that the three interaction coefficients cannot all have the same sign. If they did, unbounded growth could result for all three wave envelopes. Such interactions are referred to as explosive resonant triads, and require an energy source (such as a background sheared flow) to occur. Craik and Adam [16] have demonstrated the possibility of explosive resonance in a three-layer Kelvin-Helmholtz flow. Becker and Grimshaw [5] show that for explosive resonance to occur for a triad in a shear flow a critical layer is required. Explosive resonance is also discussed by Craik [14].

When a triad consists of two relatively fast moving waves and a slow moving wave, the slow wave will be present at locations beyond what could be achieved by a stationary source. The two fast waves continually generate and interact with the third wave as they propagate. In addition, two rightward propagating waves could interact to produce a leftward propagating wave (provided the resonance condition can be met). In contrast, under linear theory a given wave can only be found at distances dictated by its group velocity.

A more exotic form of the above phenomenon occurs in the exact resonant case when three solutions are locked together. Certain special envelope shapes have the remarkable property that they remain unchanged through the continuous interaction process and travel as a group. Such solutions are known as solitons, and are sometimes referred to as bright-

bright-dark, or simulton solutions. Families of solutions possessing these properties are described by Degasperis et al. [18], but this topic is not pursued further here.

2.2.2 Conservation Laws and Exact Solutions

A detailed discussion of conservation laws and exact solutions for the interaction equations is given by Craik [14, Chapter 5]. The discussion given here is loosely based on that presentation.

Both forms of the interaction equations (2.17) and (2.19) possess exact solutions and conservation laws. Conservation laws are generally found by multiplying the equation for a_n by the complex conjugate a_n^* and integrating from $X = -\infty$ to $+\infty$. With minor algebraic manipulations and the boundary conditions $|a_n| \to 0$ as $|x| \to \infty$, an energy conservation law of the form

$$\frac{\partial}{\partial T} \int_{-\infty}^{\infty} \gamma_2\gamma_3|a_1|^2 + \gamma_1\gamma_3|a_2|^2 - 2\gamma_1\gamma_2|a_3|^2 \; dX = 0 \tag{2.20}$$

is immediately found. The fact that one of the interaction coefficients must have a different sign from the other two ensures that each term in the above conservation law has the same sign. This conservation law also explains how an explosive resonant triad could lead to all three waves growing unboundedly. If one of the terms in (2.20) differs in sign from the other two there is no bounding constraint on how large the envelope amplitudes can become.

A set of three more conservation laws, known as the Manley-Rowe relations, are found by taking differences of the interaction equations (see Craik [14, page 130]. The laws take the form

$$\begin{array}{l} \frac{\partial}{\partial T} \int_{-\infty}^{\infty} \gamma_2|a_1|^2 - \gamma_1|a_2|^2 \; dX = 0, \\ \frac{\partial}{\partial T} \int_{-\infty}^{\infty} \gamma_3|a_1|^2 - \gamma_1|a_3|^2 \; dX = 0, \\ \frac{\partial}{\partial T} \int_{-\infty}^{\infty} \gamma_3|a_2|^2 - \gamma_2|a_3|^2 \; dX = 0. \end{array} \tag{2.21}$$

An important special case occurs when the wave trains under analysis are assumed to be spatially uniform. In this case the derivatives with respect to X vanish. The conservation law (2.20) and the Manley-Rowe relations do not change in form except for the absence of the integrals. For spatially uniform waves the exact interaction equations are solvable in terms of Jacobi's elliptic functions. As discussed by Craik [14], these equations were actually first solved by Euler in his studies of rigid body motion.

The initial value problem for the exact interaction equations are also solvable by means of the Inverse Scattering Transform (IST). The IST approach is discussed by Craik [14], and considered in particular detail by Ablowitz and Segur [2]. It is unclear if the IST could be extended to the near-resonant interaction equations, but this open question is not addressed here.

2.2.3 Near-Resonant Stability Conditions

A stability analysis for waves governed by the near-resonance interaction equations (2.19) is now presented. The results found here are directly applicable to the exact resonance case. To simplify analysis, the transformation $a_p = b_p \exp(-i\Delta/3)$ for $p = 1, 2, 3$ is used, where $\Delta = \hat{k}X - \hat{\omega}T$. This reduces the near-resonant interaction equations to a set of coupled equations with constant coefficients:

$$\begin{aligned} \tfrac{\partial b_1}{\partial T} + v_1 \tfrac{\partial b_1}{\partial X} - i\tfrac{(\hat{k}v_1 - \hat{\omega})}{3} b_1 &= \gamma_1 b_2^* b_3^*, \\ \tfrac{\partial b_2}{\partial T} + v_2 \tfrac{\partial b_2}{\partial X} - i\tfrac{(\hat{k}v_2 - \hat{\omega})}{3} b_2 &= \gamma_2 b_1^* b_3^*, \\ \tfrac{\partial b_3}{\partial T} + v_3 \tfrac{\partial b_3}{\partial X} - i\tfrac{(\hat{k}v_3 - \hat{\omega})}{3} b_3 &= \gamma_3 b_1^* b_2^*. \end{aligned} \tag{2.22}$$

Let (p, q, r) denote the indices of three waves satisfying these equations and the near-resonance conditions (2.18). Suppose the largest amplitude (primary) wave is indexed by p, and small (parasitic) waves q and r perturb it. The linear stability of the primary wave in the presence of this disturbance is determined by the growth or decay of the two smaller waves. If the parasitic waves grow in time, the primary wave is unstable to their presence.

Suppose waves q and r have amplitudes of order μ, and let $a_p = A + O(\mu)$, where $\mu \ll A$ and A is constant. This mimics the physical situation where the parasitic waves perturb the relatively uniform primary wave in some small region. To leading order, waves q and r satisfy

$$\begin{aligned} \tfrac{\partial b_q}{\partial T} + v_q \tfrac{\partial b_q}{\partial X} - i\tfrac{(\hat{k}v_q - \hat{\omega})}{3} b_q &= \gamma_q A^* b_r^*, \\ \tfrac{\partial b_r}{\partial T} + v_r \tfrac{\partial b_r}{\partial X} - i\tfrac{(\hat{k}v_r - \hat{\omega})}{3} b_r &= \gamma_r A^* b_q^*. \end{aligned} \tag{2.23}$$

For the index n, define the operator $L_n = \partial/\partial T + v_n \partial/\partial X - i\frac{(\tilde{k}v_n - \tilde{\omega})}{3}$. Applying the complex conjugate operator L_r^* to the evolution equation for b_q reduces the system to:

$$L_r^*(L_q(b_q)) = \gamma_q \gamma_r A^* A b_q. \tag{2.24}$$

Next, consider how a plane wave component of b_q evolves. Substituting $b_q = \exp(i(KX - \Omega T))$ into (2.24) reveals

$$\left(\Omega - \left(v_r K + \frac{(\hat{k}v_r - \hat{\omega})}{3}\right)\right)\left(\Omega - \left(v_q K - \frac{(\hat{k}v_q - \hat{\omega})}{3}\right)\right) = -\gamma_q \gamma_r |A|^2. \tag{2.25}$$

This equation is quadratic in Ω, and its roots dictate whether or not wave q will grow in time. Let $d_q = v_q K - (v_q \hat{k} - \hat{\omega})/3$ and $d_r = v_r K + (v_r \hat{k} - \hat{\omega})/3$. The polynomial in Ω can be factored to yield

$$\Omega = \frac{(d_q + d_r) \pm \sqrt{(d_q - d_r)^2 - 4\gamma_q \gamma_r |A|^2}}{2}. \tag{2.26}$$

Clearly Ω is complex when the discriminant is negative. It follows that $\gamma_q\gamma_r > 0$ is a necessary condition for wave p to be unstable. The discriminant is negative whenever

$$\left(K - \left(\frac{(v_q + v_r)\hat{k} - 2\hat{\omega}}{3(v_q - v_r)}\right)\right)^2 < \frac{4\gamma_q\gamma_r|A|^2}{(v_q - v_r)^2}. \tag{2.27}$$

The results of this linear stability analysis are summarized in the following theorem.

Theorem 1. *Consider waves p, q, r satisfying the near-resonance conditions* (2.18) *and interaction equations* (2.19)*. Suppose that the primary wave p is perturbed by parasitic waves q and r. The following statements are true:*

1. *If $\gamma_q\gamma_r \leq 0$ the primary wave p is linearly stable to disturbances of parasitic waves q and r.*

2. *If $\gamma_q\gamma_r > 0$, the plane wave component $\exp(i(KX - \Omega T))$ of waves q and r grows in time whenever condition* (2.27) *holds.*

In view of this theorem, it is clear that if two of the waves in the triad have similar velocities, a much broader range of K values for the third wave will lead to instabilities. This demonstrates that triad interaction behaviour depends delicately on the shapes of the underlying wave envelopes, not just their relative amplitudes.

2.2.4 Early Evolution of Parasitic Waves

The linear stability conditions derived in the previous subsection give no indication about how the initial parasitic wave disturbances grow. In this subsection an interesting connection between the early growth of the parasitic waves and the Klein-Gordon equation is explored. Though the analysis and discussion presented here were derived independently, the main results were later found to be a special case of the "pump-wave" analysis presented by Craik and Adam [15].

As before, suppose that the primary wave is $O(A)$ with parasitic waves that are $O(\mu)$ where $\mu \ll A$. To leading order the evolution of the two parasitic waves is governed by the equations

$$\begin{aligned} \tfrac{\partial}{\partial T}a_q + v_q\tfrac{\partial}{\partial X}a_q &= \gamma_q a_r^* A^* e^{-i(\hat{k}X - \hat{\omega}T)}, \\ \tfrac{\partial}{\partial T}a_r + v_r\tfrac{\partial}{\partial X}a_r &= \gamma_r a_q^* A^* e^{-i(\hat{k}X - \hat{\omega}T)}. \end{aligned} \tag{2.28}$$

Using the transformations $a_q = B\exp(-i(\hat{k}X - \hat{\omega}T)/2)$ and $a_r^* = C\exp(i(\hat{k}X - \hat{\omega}T)/2)$, these reduce to the set of equations

$$\begin{aligned} B_T + v_q B_X + i\Delta_q B &= \gamma_q A^* C, \\ C_T + v_r C_X - i\Delta_r C &= \gamma_r A B, \end{aligned} \tag{2.29}$$

where $\Delta_n = (-v_n\hat{k} + \hat{\omega})/2$ for $n = q, r$. Subscripts of X and T are now used to indicate partial derivatives.

Consider first the exact resonance case where $\Delta_q = \Delta_r = 0$. When $v_q = v_r$ Fourier transforms can be used. The result is a simple system of two ODEs that is directly solvable. Generally $v_q \neq v_r$, so the resulting system of equations is too complicated to invert, and more consideration is required. A helpful approach is to define a new coordinate $\chi = X - \left(\frac{v_q+v_r}{2}\right) T$. Then, in the new coordinate system, the equations reduce to

$$\begin{aligned} B_T + vB_\chi &= \gamma_q A^* C, \\ C_T - vC_\chi &= \gamma_r AB, \end{aligned} \tag{2.30}$$

where $v = (v_q - v_r)/2$. Applying the operator $\partial_T - v\partial_\chi$ to the first equation yields

$$B_{TT} - v^2 B_{\chi\chi} = \gamma_q \gamma_r |A|^2 B. \tag{2.31}$$

This is a form of the well-known Klein-Gordon equation (see Knobel [35, Chapter 6]). It is important to note that the term on the right-hand side could have positive or negative sign. Initial profile shapes for a_q and a_r are required to properly define the initial conditions on B and B_T. For this informal discussion these details are ignored.

It is natural to expect that a similar evolution equation will govern the initial growth of a parasitic wave in a near-resonant interaction. Returning to equation (2.29), using the transformation from X to χ as before, and applying the operator $\partial_T - v\partial_\chi - i\Delta_r$ to the equation for B reveals the evolution equation

$$B_{TT} + i(\Delta_q - \Delta_r)B_T - iv(\Delta_q + \Delta_r)B_\chi - v^2 B_{\chi\chi} + \Delta_q \Delta_r B = \gamma_q \gamma_r |A|^2 B. \tag{2.32}$$

Finally, the transformation $B = \hat{B} \exp\left[i\left(\frac{-(\Delta_q+\Delta_r)\chi/v + (\Delta_r - \Delta_q)T}{2}\right)\right]$ reduces (2.32) to the following Klein-Gordon equation for $\hat{B}$:

$$\hat{B}_{TT} - v^2 \hat{B}_{\chi\chi} = \left(-2\Delta_q \Delta_r + \gamma_q \gamma_r |A|^2\right) \hat{B}. \tag{2.33}$$

The above analysis shows that, in a coordinate frame moving at the average velocity of the two parasitic waves, the underlying growth of the parasitic waves is governed by a Klein-Gordon equation initial value problem. This is true for both exact and near-resonant interactions.

These Klein-Gordon equations can be used to explain the conditions needed for solutions to grow. To see this, multiply (2.31) by $B(\chi, T)$, then integrate from $\chi = -\infty$ to $\chi = \infty$. Note that $BB_{TT} = \frac{1}{2}\partial_{TT}(B^2) - B_T^2$ and $BB_{\chi\chi} = \frac{1}{2}\partial_{\chi\chi}(B^2) - B_\chi^2$. Then, after minor manipulation, and assuming the initial disturbance is localized so that $|B| \to 0$ as $|\chi| \to \infty$, it follows that

$$\frac{\partial^2}{\partial T^2} \int_{-\infty}^{\infty} B^2 \, d\chi - 2\gamma_q \gamma_r |A|^2 \int_{-\infty}^{\infty} B^2 \, d\chi = 2 \int_{-\infty}^{\infty} B_T^2 - v^2 B_\chi^2 \, d\chi. \tag{2.34}$$

This is an evolution equation for $\int_{-\infty}^{\infty} B^2 \, d\chi$, a quantity that represents the size of the parasitic disturbance. Both sides of the equation only depend on T, and the right-hand side can be expanded as a power series about $T = 0$. The result is that, if $\gamma_q \gamma_r > 0$, then $\int_{-\infty}^{\infty} B^2 \, d\chi$ must initially grow exponentially in T, with a growth rate of $\sqrt{2\gamma_q \gamma_r}|A|$. If, on the other hand, $\gamma_q \gamma_r < 0$, solutions to (2.34) will be oscillatory, and $\int_{-\infty}^{\infty} B^2 \, d\chi$ will not initially grow in time. This is in agreement with the statement of Theorem 1.

More elaborate methods could be used to study how the parasitic disturbances grow under the Klein-Gordon equations (2.31) and (2.33). However, from a physical perspective the exact initial conditions are usually not known, it is more important to understand the conditions under which growth can occur.

2.3 The Linear Eigenvalue Problem

This section presents a technical discussion of the linear eigenvalue problem that arises for internal gravity waves under the Boussinesq approximation. The linear eigenvalue problem plays an essential role in the dynamics of internal gravity waves, determining both the vertical shape of a linear wave and the dispersion relationship. The dispersion relationship has great importance: it relates a wave's frequency to its wavenumber, and from it the phase speed and group velocity are derived.

Recall the eigenvalue problem (2.9) derived above. Minor rearrangement shows that this eigenvalue problem is of Sturm-Liouville type. To demonstrate this, (2.9) can be rewritten in the form

$$\frac{d}{dz}\left(p(z)\frac{d}{z}g(z)\right) - q(z)g(z) + \lambda r(z)g(z) = 0 \tag{2.35}$$

where $p(z) = 1$, $q(z) = k^2$, $r(z) = N^2(z) - f^2$, and $\lambda = 1/(\sigma^2(k) - f^2)$. This follows the notation of Boyce and DiPrima [10, Chapter 11]. Sturm-Liouville theory has been developed extensively, and many deep results that go far beyond the needs of this discussion are known. The interested reader is referred to the more advanced treatments by Naylor and Sell [53, Chapter 7], or Zettl [78] for a comprehensive discussion of the field including an extensive set of references.

Provided $N^2(z) - f^2 > 0$ for $0 \leq z \leq 1$ and $N^2(z)$ is continuous, equation (2.35) is one of the simplest types of Sturm-Liouville problems. The three most important results needed here, interpreted for use with (2.9), are as follows.

1. For a given value of k, a countably infinite set of real, distinct eigenvalues $\sigma_1^2(k) > \sigma_2^2(k) \cdots > f^2$ exists. This comes from the standard result for (2.35) combined with the definition $\lambda = 1/(\sigma^2 - f^2)$.

2. The corresponding eigenfunctions g_n are real and linearly independent, and they form an orthonormal basis in the Hilbert space $L^2([0,1], N^2(z) - f^2, dz)$.

3. The eigenfunction g_n has exactly $n-1$ isolated zeros in the interval $0 < z < 1$.

These properties suggest writing the problem in the form:

$$\begin{gathered} \frac{d^2}{dz^2} g_n(z,k) + k^2 \left(\frac{N^2(z) - f^2}{\sigma_n^2(k) - f^2} - 1 \right) g_n(z,k) = 0, \\ g_n(0,k) = g_n(1,k) = 0. \end{gathered} \tag{2.36}$$

The eigenfunctions are now expressed as functions of both z and k.

Many of the important properties of the eigenfunctions and dispersion relation are illustrated by the special case $N^2(z) = N_0^2$. In that instance, the (non-normalized) eigenfunctions are found to be

$$g_n(z,k) = \sin(n\pi z), \tag{2.37}$$

which do not depend on k. The statements about the distributions of the zeros of $g_n(z,k)$ are readily confirmed. The dispersion relation is found from

$$\sigma_n^2(k) = \frac{k^2 N_0^2 + f^2 n^2 \pi^2}{k^2 + n^2 \pi^2}. \tag{2.38}$$

In what follows, important properties of the eigenfunctions, dispersion relation, group velocity, and phase speed are discussed. Unless explicitly stated otherwise, the assumption $N^2(z) - f^2 > 0$ for $0 \le z \le 1$ is made throughout this section. Some of the properties described below are summarized by LeBlond and Mysak [43, page 74] and derived by Yih [76, Chapter 2], [77, page 263-290]. Yanowitch [75] has also studied related phase speed problems for heterogeneous fluids with a free surface.

2.3.1 An Alternative Formulation

A different approach to the eigenvalue problem has been suggested by Poulin [60]. Starting from the equation for the leading order behaviour of the streamfunction (2.8), solutions of the form $\psi^{(0)} = \psi \exp(i\sigma t)$ are sought. Substitution reveals

$$\sigma^2 \nabla^2 \psi = f^2 \psi_{zz} + N^2(z) \psi_{xx} \tag{2.39}$$

Now consider two solution pairs (ψ_1, σ_1) and (ψ_2, σ_2) that satisfy the boundary conditions $\psi(x,0) = 0$ and $\psi(x,1) = 0$. In addition assume that $\psi_1, \psi_2, \partial_x \psi_1$, and $\partial_x \psi_2$ are periodic on $0 \le x \le L$. Define the inner product

$$\langle \psi_1, \psi_2 \rangle = \int_0^1 \int_0^L \psi_1 \psi_2^* \, dx \, dz, \tag{2.40}$$

with the asterisk denoting the complex conjugate. The shorthand notation $\langle \psi_1, \psi_2 \rangle = \int\int_A \psi_1 \psi_2^* \, dA$ is used below. Define the self-adjoint operator $L = \partial_{xx} + \partial_{zz}$ so that

$$\langle L\psi_1, \psi_2 \rangle = -\int\int_A (\nabla \psi_1) \cdot (\nabla \psi_2^*) \, dA, \tag{2.41}$$

and

$$\langle L\psi_1, \psi_1 \rangle = -\int\int_A |\nabla \psi_1|^2 \, dA. \tag{2.42}$$

Define the self-adjoint operator $M = f^2 \partial_{zz} + N^2(z) \partial_{xx}$ so that

$$\langle M\psi_1, \psi_2 \rangle = -f^2 \int\int_A (\nabla \psi_1) \cdot (\nabla \psi_2^*) \, dA - \int\int_A (N^2 - f^2) \partial_x \psi_1 \partial_x \psi_2^* \, dA. \tag{2.43}$$

Then

$$\begin{aligned} \sigma_1^2 \langle L\psi_1, \psi_2 \rangle - \sigma_2^2 \langle \psi_1, L\psi_2 \rangle &= (\sigma_2^2 - \sigma_1^2) \int\int_A (\nabla \psi_1) \cdot (\nabla \psi_2^*) \, dA, \\ &= \langle M\psi_1, \psi_2 \rangle - \langle \psi_1, M\psi_2 \rangle, \\ &= 0. \end{aligned} \tag{2.44}$$

So, if $\sigma_1 \neq \sigma_2$ then $\int\int_A (\nabla \psi_1) \cdot (\nabla \psi_2^*) \, dA = 0$. Since L is self-adjoint, this implies that

$$\int\int_A (N^2 - f^2) \partial_x \psi_1 \partial_x \psi_2^* \, dA = 0. \tag{2.45}$$

This is a more general form of the orthogonality condition found below.

Next, since $\sigma_1^2 \langle L\psi_1, \psi_1 \rangle = \langle M\psi_1, \psi_1 \rangle$, it follows that

$$\sigma^2 \int\int_A |\nabla \psi_1|^2 \, dA = f^2 \int\int_A |\partial_x \psi_1|^2 \, dA + \int\int_A N^2(z) |\partial_x \psi_1|^2 \, dA. \tag{2.46}$$

Each integral is strictly positive, so provided a solution exists, it satisfies $\sigma^2 > 0$. When $N^2(z) - f^2 > 0$ everywhere, this expression implies that $\sigma^2 \geq f^2$. However, if $N^2(z) - f^2 < 0$ for some z then it is possible that $\sigma^2 < f^2$.

2.3.2 The Eigenfunctions and Dispersion Relation

Even without explicit knowledge of their form, certain important properties of the eigenfunctions can be ascertained. For instance, an orthogonality condition can be derived with ease. Holding k fixed, consider (2.36) for mode-m and mode-n solutions. Multiplying the equation for g_n by g_m and vice-versa, then integrating both from $z = 0$ to $z = 1$ leads to a pair of coupled equations. Applying integration by parts once on the first terms and subtracting the result gives:

$$k^2 \left(\frac{1}{\sigma_m^2 - f^2} - \frac{1}{\sigma_n^2 - f^2} \right) \int_0^1 \left(N^2(z) - f^2 \right) g_m(z,k) g_n(z,k) \, dz = 0. \tag{2.47}$$

The eigenvalues of the Sturm-Liouville problem are distinct, so if $m \neq n$, $\sigma_m(k) \neq \sigma_n(k)$. It is then natural to scale eigenfunctions so that

$$\int_0^1 \left(N^2(z) - f^2\right) g_m(z,k) g_n(z,k)\, dz = \begin{cases} 0 & \text{if } m \neq n \\ 1 & \text{if } m = n. \end{cases} \tag{2.48}$$

It is important to point out that this condition only holds for two eigenfunctions at the same value of k. However, when $N^2(z)$ is constant the eigenfunctions do not depend on k, so the orthogonality condition always holds.

An expression for the dispersion relation is found from the eigenvalue problem (2.36) by multiplying both sides by $g_n(z,k)$, and integrating with respect to z. Using integration by parts on the first term and applying the orthogonality condition (2.48) reveals the expression

$$\frac{k^2}{\sigma_n^2 - f^2} = I_1 + k^2 I_2 \tag{2.49}$$

where $I_1 = \int_0^1 \left(\frac{\partial}{\partial z} g_n(z,k)\right)^2\, dz$, and $I_2 = \int_0^1 g_n^2(z,k)\, dz$. This expression can be directly solved for σ_n to yield

$$\sigma_n(k) = \pm\sqrt{f^2 + \frac{k^2}{I_1 + k^2 I_2}}. \tag{2.50}$$

Evidently the dispersion relation has two branches. By convention, the positive square root is taken.

The above expression for $\sigma_n(k)$ illustrates the intimate connection between the dispersion relation and the eigenfunctions $g_n(z,k)$. In general, the eigenvalue problem must be solved numerically. The standard approach is to discretize the differentiation operator and then solve for the eigenvalues and eigenfunctions simultaneously. This is explained in detail in Chapter 3.

As an illustrative example, consider the buoyancy frequency

$$N^2(z) = \operatorname{sech}^2\left(\frac{z - 0.25}{0.2}\right). \tag{2.51}$$

The resulting eigenvalue problem is considered with $f = 0$ and $f = 0.01$, so that in both cases $N^2(z) - f^2 > 0$ holds throughout the domain. The first three modes of the dispersion relation (with $f = 0$) are plotted in Figure 2.1. Frequencies appear to increase with wavenumber and decrease with vertical mode number. Plots with nonzero f values are included later.

The mode one, two, and three eigenfunctions at $k = 1$ (dashed lines) and $k = 100$ (dotted lines) are plotted in Figure 2.2. Eigenfunctions are scaled to unit amplitude for

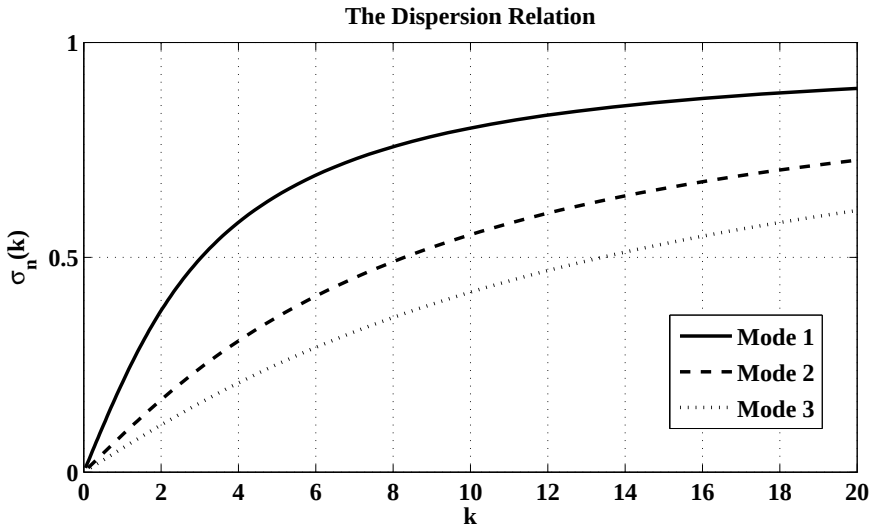

Figure 2.1: The mode 1–3 dispersion relation for $N^2(z)$ given by equation (2.51). The dispersion relation appears to increase with k and decrease with vertical mode number. For this plot $f = 0$.

aesthetic reasons. Included in each subplot is the corresponding eigenfunction for the buoyancy profile $N^2(z) = 1$ (solid lines). Not surprisingly, the oscillatory behavior of the eigenfunctions for $N^2(z)$ is localized to the vicinity of $z = 0.25$. The dependence of the eigenfunctions on k is clearly evident. The eigenfunctions for $k = 100$ are much more localized about the point $z = 0.25$ where $N^2(z)$ achieves its maximum.

In this thesis, eigenfunctions are frequently referred to by their vertical mode number (the subscript on σ). When $N^2(z)$ is constant the mode number has a very natural interpretation, since a mode-n eigenfunction is of the form $\sin(n\pi z)$. When $N^2(z)$ is not constant, the mode number still has an important meaning, it indicates how oscillatory the eigenfunction is. More precisely, a mode-n eigenfunction has exactly $n-1$ zeros in the interval $0 < z < 1$. This is evident in Figure 2.2.

2.3.3 The Group Velocity and Phase Speed

The group velocity for a mode-n plane wave is denoted by $v_n(k)$ and defined by

$$v_n(k) := \frac{d\sigma_n}{dk}. \tag{2.52}$$

For the problems considered here, each mode of the dispersion relation $\sigma_n(k)$ is in fact a continuous and differentiable function of the wavenumber k (see Zettl [78, Chapter 4] and the references therein).

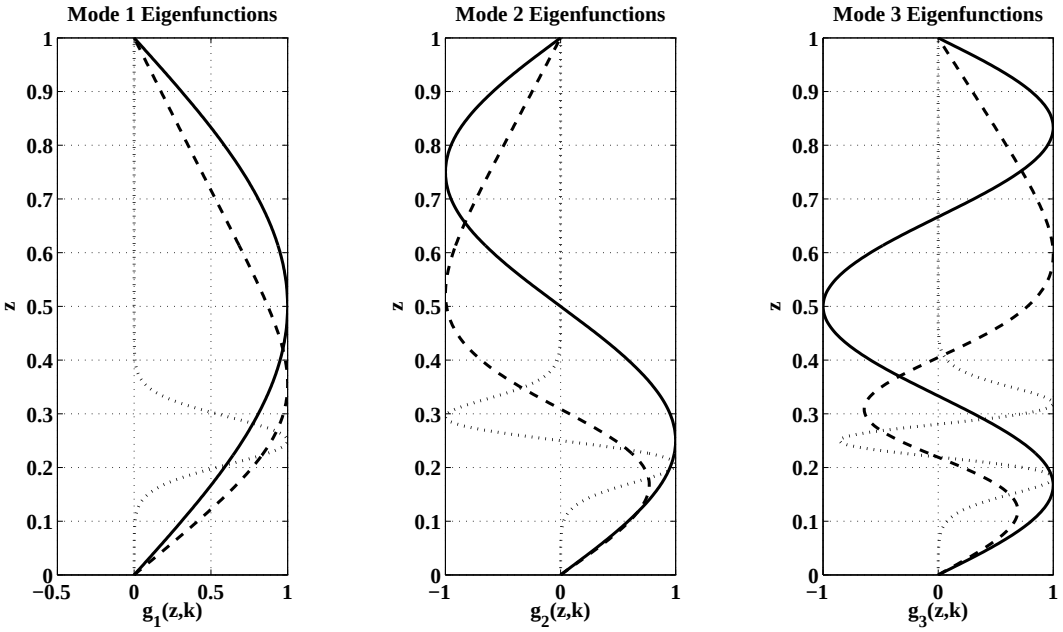

Figure 2.2: The mode one (left subplot), mode two (middle subplot), and mode three (right subplot) eigenfunctions, re-scaled to unit-amplitude, for $N^2(z)$ given in equation (2.51). Solid lines mark the eigenfunctions for the related linear stratification $N^2(z) = 1$, dashed lines depict the eigenfunctions for $k = 1$, and dotted lines portray the eigenfunctions for $k = 100$. Note the localization of the oscillatory behaviour as k increases.

The group velocity has an important physical meaning, it is the velocity at which energy propagates for linear waves (see below). This is also demonstrated by the asymptotic analysis of Chapter 5.

With the notation presented in the previous subsection, expressions for the group velocity can be found. While not truly in closed form, the formulas given in the following theorem are useful because I_1 and I_2 are strictly positive.

Theorem 2. *The group velocity can be expressed in the equivalent forms*

$$\frac{d\sigma_n}{dk} = \frac{(\sigma_n^2 - f^2)}{\sigma_n k} - \frac{(\sigma_n^2 - f^2)^2}{\sigma_n k} \int_0^1 g_n^2(z,k)\, dz, \tag{2.53}$$

and

$$\frac{d\sigma_n}{dk} = \frac{(\sigma_n^2 - f^2)^2}{\sigma_n k^3} \int_0^1 \left(\frac{\partial}{\partial z} g_n(z,k) \right)^2 dz. \tag{2.54}$$

Proof. Differentiating expression (2.49) with respect to k and solving for $d\sigma_n/dk$ leads to

$$\frac{d\sigma_n}{dk} = \frac{(\sigma_n^2 - f^2)}{\sigma_n k} - \frac{(\sigma_n^2 - f^2)^2}{\sigma_n k} I_2 - \frac{(\sigma_n^2 - f^2)^2}{2\sigma_n k^2}\left(\frac{dI_1}{dk} + k^2 \frac{dI_2}{dk}\right). \tag{2.55}$$

This reduces to (2.53) because $dI_1/dk + k^2 dI_2/dk = 0$. To see this, note that $dI_2/dk = 2\int_0^1 g_n \frac{\partial g_n}{\partial k}\, dz$, and, after using integration by parts and the boundary conditions, $dI_1/dk = -2\int_0^1 \frac{\partial^2 g_n}{\partial z^2}\frac{\partial g_n}{\partial k}\, dz$. Therefore

$$\begin{aligned} \tfrac{dI_1}{dk} + k^2 \tfrac{dI_2}{dk} &= -2\int_0^1 \left(\tfrac{\partial^2 g_n}{\partial z^2} - k^2 g_n\right)\tfrac{\partial g_n}{\partial k}\, dz \\ &= -\tfrac{2}{\sigma_n^2 - f^2}\int_0^1 (N^2(z) - f^2) g_n \tfrac{\partial g_n}{\partial k}\, dz \\ &= -\tfrac{1}{\sigma_n^2 - f^2}\tfrac{\partial}{\partial k}\int_0^1 (N^2 - f^2) g_n^2\, dz \\ &= -\tfrac{1}{\sigma_n^2 - f^2}\tfrac{\partial}{\partial k} 1 \\ &= 0. \end{aligned} \tag{2.56}$$

The second expression for the group velocity is found by substituting the identity $I_2 = 1/(\sigma_n^2 - f^2) - I_1/k^2$ into the first. □

These expressions both reduce to the expected result when $N^2(z)$ is constant. In addition, note that equation (2.53) matches the equation for the advection coefficient in the triad interaction equations (derived in Appendix B). This proves that the energy of a linear internal gravity wave train, which must travel with the wave envelope, travels at the group velocity of the underlying wave. An immediate consequence of expression (2.54) is the monotonicity of $\sigma_n(k)$, as summarized in the following corollary.

Corollary 1. *For each mode number n, the dispersion relation $\sigma_n(k)$ is a monotonically increasing function of k when $k \geq 0$.*

The monotonic nature of the frequency has been proved by Yih [77] for non-Boussinesq fluids with or without an upper rigid boundary.

The phase speed of a mode-n wave is denoted by $c_n(k)$ and defined by

$$c_n(k) := \frac{\sigma_n(k)}{k}. \tag{2.57}$$

The phase speed is an important physical quantity that describes the speed at which wave crests propagate. An important property of the phase speed and its relation to the magnitude of the group velocity is given in the next lemma.

Lemma 1. *The phase speed for internal gravity waves is a strictly decreasing function of k for $k \geq 0$. At a fixed value of k, the phase speed $c_n(k)$ is an upper bound for the group velocity.*

Proof. By definition, $dc_n(k)/dk = \frac{1}{k}\frac{d\sigma_n}{dk} - \frac{\sigma_n}{k^2}$. Using expression (2.53), it follows that

$$\begin{aligned} \frac{dc_n(k)}{dk} &= \frac{\sigma_n^2 - f^2}{\sigma_n k^2} - \frac{(\sigma_n^2 - f^2)^2}{\sigma_n k^2} I_2 - \frac{\sigma_n}{k^2} \\ &= -\frac{f^2}{\sigma_n k^2} - \frac{(\sigma_n^2 - f^2)^2}{\sigma_n k^2} I_2 \\ &\leq 0, \end{aligned} \tag{2.58}$$

which proves the first statement.

To show the phase speed is an upper bound for the magnitude of the group velocity, write $dc_n/dk = \frac{1}{k}\left(\frac{d}{dk}\sigma_n(k) - c_n(k)\right)$, and since $dc_n/dk \leq 0$ it immediately follows that $c_n(k) \geq d\sigma_n/dk$. □

The above argument can be readily modified to show that when $f \neq 0$ the phase speed is strictly decreasing when $k \leq 0$, since $c_n(k)$ is an odd function. Likewise, if $f = 0$, $c_n(k)$ is an even function, so the phase speed achieves its maximum at $k = 0$. The proof of Lemma 1 is direct, but Yih [76, Chapter 2] has also derived this result using the Sturm comparison theorem.

Figure 2.3 depicts the phase speeds for the mode 1–3 waves as a function of wavenumber for $N^2(z)$ given by equation (2.51). The left subplot shows the phase speeds for $f = 0$, the right subplot shows phase speeds for $f = 0.01$. The curves are qualitatively similar away from $k = 0$. As $k \to 0^+$ the phase speed tends to $+\infty$ for $f \neq 0$.

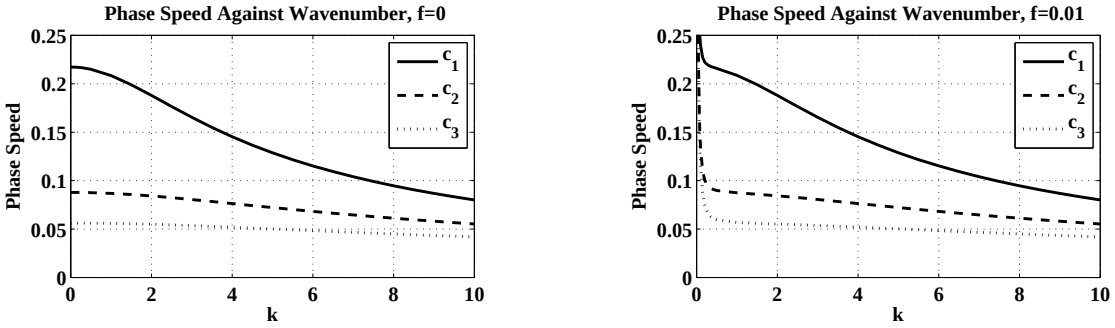

Figure 2.3: Dimensionless phase speeds for the mode 1–3 waves for $N^2(z)$ give by equation (2.51). In the left subplot $f = 0$, in the right subplot $f = 0.01$. Note the phase speeds are strictly decreasing with wavenumber, in agreement with Lemma 1. Phase speeds also decrease with vertical mode number. For $f \neq 0$, the phase speed tends to ∞ as $k \to 0^+$.

Intuitively, one would expect that in the short wave limit ($k \to \infty$) both the phase speed and group velocity tend to zero. This is indeed true, and can be viewed as an immediate consequence of Proposition 1 below.

2.3.4 The Dispersion Relation Revisited

In this section several important properties of the dispersion relation are established. The methods developed here provide a means for making comparisons of the dispersion relations for internal waves in fluids with different stratifications. These techniques reveal properties of $\sigma_n(k)$ in important limits.

The definitions

$$N^2_{\max} = \max_{0\le z\le 1} N^2(z), \quad \text{and} \quad N^2_{\min} = \min_{0\le z\le 1} N^2(z) \tag{2.59}$$

are useful in the analysis that ensues.

Proposition 1. *Suppose $N^2(z) - f^2 > 0$ for $0 \le z \le 1$. For $k \ge 0$, the dispersion relation satisfies $f \le \sigma_n(k) \le N_{\max}$, and $\lim_{k\to 0} \sigma_n(k)$ and $\lim_{k\to\infty} \sigma_n(k)$ both exist.*

Proof. Integrating the eigenvalue problem (2.36) against $g_n(z,k)$, using integration by parts and rearranging reveals

$$\int_0^1 \left(\frac{N^2(z)-f^2}{\sigma_n^2(k)-f^2} - 1\right) g_n^2(z,k)\, dz = \frac{1}{k^2}\int_0^1 \left(\frac{\partial}{\partial z} g_n(z,k)\right)^2 dz. \tag{2.60}$$

The right hand side of this equation is strictly positive. For the left hand side to be positive, $\sigma_n(k)$ must satisfy $f \le \sigma_n(k) \le N_{\max}$.

From Corollary 1, $\sigma_n(k)$ is a strictly increasing function of k for $k \ge 0$, and since it is bounded above, $\lim_{k\to\infty} \sigma_n(k)$ must exist. The analogous argument shows $\lim_{k\to 0} \sigma_n(k)$ also exists.

□

The bounded, monotonic nature of $\sigma_n(k)$ implies that as $k \to \infty$ the phase speed and group velocity tend to zero.

Proposition 1 ensures that the limits as $k \to 0$ and $k \to \infty$ of $\sigma_n(k)$ exist, but provides no information about what the two limits in question actually are, or how to find them. Determining the limits is somewhat challenging, and is the focus of the remainder of this subsection. Some insight is gained by studying numerical examples. As seen in Figure 2.4, the dispersion curves for the buoyancy frequency $N^2(z) = \operatorname{sech}^2((z-0.25)/0.2)$ (see equation (2.51)) appear to be approaching the value $N_{\max} = 1$ as k increases. This hints at the possible value of the short-wave limit. In Figure 2.5, the first three modes of the dispersion relation are plotted for the same buoyancy frequency, with $f = 0$ in the left subplot and $f = 0.01$ in the right subplot. As $k \to 0^+$ the curves appear to approach f, suggesting the long-wave limit.

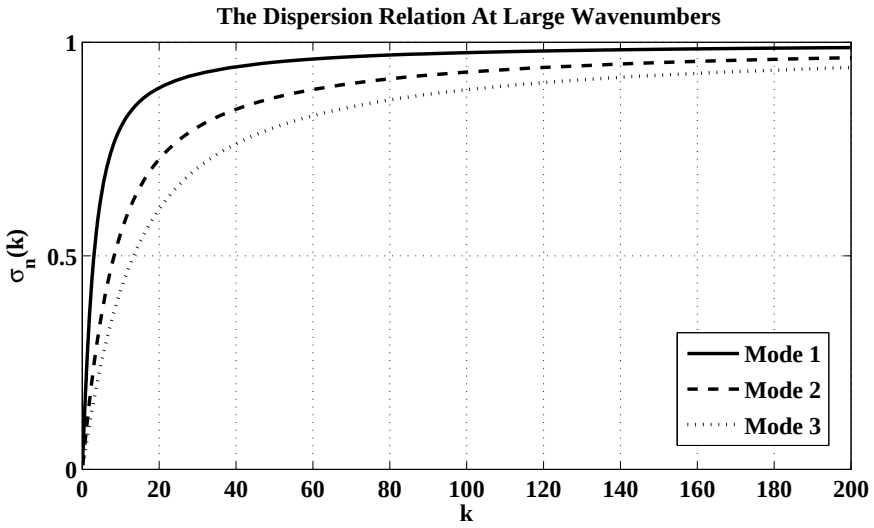

Figure 2.4: The mode 1–3 dispersion relation for $N^2(z)$ given by (2.51) at large wavenumbers, with $f = 0$. All three dispersion curves appear to be approaching the value $N_{\max} = 1$.

The approach used here for determining the limit of $\sigma_n(k)$ as $k \to 0$ and $k \to \infty$ is not straightforward. The intermediate step of analyzing how the dispersion relation changes with $N^2(z)$ is required first. This is developed in two different ways. First, a perturbation argument is used to infer the result. Then, a more direct approach is used.

To understand the behaviour of the dispersion relation as $N^2(z)$ changes the perturbation technique explained by Courant and Hilbert [13, Chapter 5] and Richards [61, Chapter 10]) can be used. Define the operator $L = (1/k^2)d^2/dz^2 - 1$. The eigenvalue problem (2.36) can be rewritten so that the eigenvalues $\sigma_n^2(k)$ and eigenfunctions $g_n(z,k)$ obey

$$Lg_n + \frac{N^2(z) - f^2}{\sigma_n^2(k) - f^2} g_n = 0 \tag{2.61}$$

with the boundary conditions $g_n(0,k) = 0 = g_n(1,k)$. Now consider the perturbed problem by setting $\tilde{N}^2(z) = N^2(z) - \epsilon h(z)$, with $0 < \epsilon \ll 1$ and $h(z) \geq 0$, such that $h(z)$ is continuous. The corresponding eigenvalues are denoted by $\tilde{\sigma}_n^2(k)$ with eigenfunctions $\tilde{g}_n(z,k)$. These perturbed quantities satisfy

$$L\tilde{g}_n + \frac{\tilde{N}^2(z) - f^2}{\tilde{\sigma}_n^2(k) - f^2} \tilde{g}_n = 0 \tag{2.62}$$

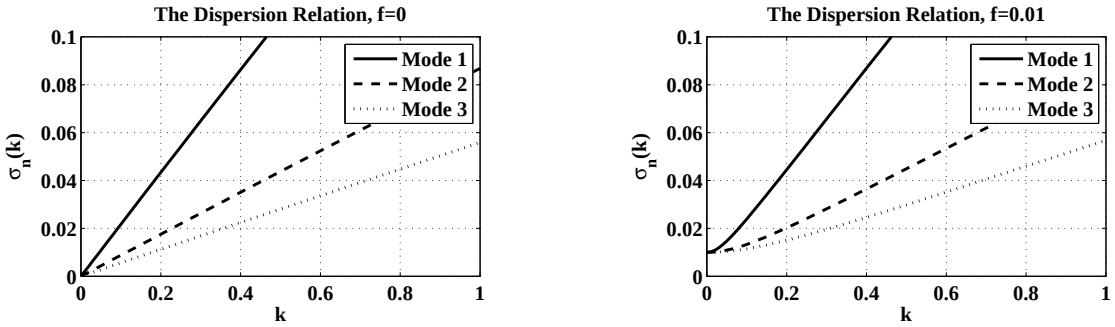

Figure 2.5: The dispersion relation at small wavenumbers when $f = 0$ (left subplot) and $f = 0.01$ (right subplot). $N^2(z)$ is given by (2.51).

which can be rearranged to the form

$$L\tilde{g}_n + \frac{N^2(z) - f^2}{\sigma_n^2(k) - f^2}\tilde{g}_n = \left(\frac{N^2(z) - f^2}{\sigma_n^2(k) - f^2} - \frac{\tilde{N}^2(z) - f^2}{\tilde{\sigma}_n^2(k) - f^2}\right)\tilde{g}_n. \tag{2.63}$$

Multiplying both sides by g_n and integrating with respect to z from 0 to 1 leads to significant simplifications. After using integration by parts twice, the left hand side is plainly zero. Therefore

$$(\tilde{d}_n - d_n)\int_0^1 (N^2(z) - f^2)g_n\tilde{g}_n \, dz = \epsilon\tilde{d}_n \int_0^1 h(z)g_n\tilde{g}_n \, dz, \tag{2.64}$$

where $d_n = 1/(\sigma_n^2 - f^2)$ and $\tilde{d}_n = 1/(\tilde{\sigma}_n^2 - f^2)$ for notational convenience. Now, on the assumption that ϵ is small, expand $\tilde{d}_n = d_n + \epsilon d_n^{(1)} + O(\epsilon^2)$ and $\tilde{g}_n = g_n + \epsilon g_n^{(1)} + O(\epsilon^2)$. Collecting terms to $O(\epsilon)$ and applying the orthogonality condition shows that

$$d_n^{(1)} = d_n \int_0^1 h(z)g_n^2(z) \, dz. \tag{2.65}$$

With $h(z) \geq 0$, the immediate conclusion is that $\tilde{\sigma}_n(k) \leq \sigma_n(k)$.

The above arguments motivate the statement of the following theorem, though the proof used below is quite different and does not rely on perturbation arguments.

Theorem 3. *Consider the continuous profile $N^2(z) > f^2$ with corresponding mode-n dispersion relation $\sigma_n(k)$, and a second continuous profile $\hat{N}^2(z) > f^2$ with corresponding dispersion relation $\hat{\sigma}_n(k)$. Suppose $\hat{N}^2(z) \leq N^2(z)$ for all $z \in [0, 1]$. Then for each $k \geq 0$ and mode number n, $\hat{\sigma}_n(k) \leq \sigma_n(k)$.*

Proof. Consider the buoyancy frequency

$$\tilde{N}^2(z, s) = N^2(z) + sp(z) \tag{2.66}$$

where the new variable s has been introduced. Assume $p(z)$ is a continuous function. Provided $\tilde{N}^2(z,s) > f^2$ and is continuous, the corresponding eigenvalue problem at a given value of s is of Sturm-Liouville type and possesses the properties discussed in Section 2.3.2. The corresponding eigenfunctions $\tilde{g}_n(z,k,s)$ must depend on k and s in addition to z, and are normalized by the equation

$$\int_0^1 (\tilde{N}^2(z,s) - f^2)\tilde{g}_n^2(z,k,s)\ dz = 1. \tag{2.67}$$

Next, consider the corresponding eigenvalues $\tilde{\sigma}_n^2(k,s)$. Rearranging equation (2.49), these are determined by the expression

$$\tilde{\sigma}_n^2(k,s) = f^2 + \frac{k^2}{\tilde{I}_1 + k^2\tilde{I}_2}, \tag{2.68}$$

where $\tilde{I}_1$ and $\tilde{I}_2$ must depend on k and s. Just as σ_n is a continuous and differentiable function of k, the results stated in Zettl [78, Chapter 4] ensure that σ_n is a continuous, differentiable function of s.

Differentiating with respect to s and simplifying reveals

$$\frac{\partial\tilde{\sigma}_n}{\partial s} = -\frac{(\tilde{\sigma}_n^2 - f^2)^2}{2\tilde{\sigma}_n k^2}\left(\frac{\partial\tilde{I}_1}{\partial s} + k^2\frac{\partial\tilde{I}_2}{\partial s}\right). \tag{2.69}$$

Next, expand

$$\begin{aligned}
\tfrac{\partial\tilde{I}_1}{\partial s} + k^2\tfrac{\partial\tilde{I}_2}{\partial s} &= 2\textstyle\int_0^1 \left(\tfrac{\partial\tilde{g}_n}{\partial z}\tfrac{\partial^2\tilde{g}_n}{\partial z\partial s} + k^2\tilde{g}_n\tfrac{\partial\tilde{g}_n}{\partial s}\right)\ dz \\
&= -2\textstyle\int_0^1 \left(\tfrac{\partial^2\tilde{g}_n}{\partial z^2} - k^2\tilde{g}_n\right)\tfrac{\partial\tilde{g}_n}{\partial s}\ dz \\
&= \tfrac{k^2}{\tilde{\sigma}_n^2 - f^2}\textstyle\int_0^1 (\tilde{N}^2(z,s) - f^2)\tfrac{\partial}{\partial s}\tilde{g}_n^2\ dz \\
&= \tfrac{k^2}{\tilde{\sigma}_n^2 - f^2}\left[\textstyle\int_0^1 \tfrac{\partial}{\partial s}\left((\tilde{N}^2(z,s) - f^2)\tilde{g}_n^2\right)\ dz\right. \\
&\quad \left. - \textstyle\int_0^1 \tfrac{\partial\tilde{N}^2(z,s)}{\partial s}\tilde{g}_n^2\ dz\right] \\
&= \tfrac{k^2}{\tilde{\sigma}_n^2 - f^2}\left[\tfrac{\partial}{\partial s}1 - \textstyle\int_0^1 p(z)\tilde{g}_n^2\ dz\right] \\
&= -\tfrac{k^2}{\tilde{\sigma}_n^2 - f^2}\textstyle\int_0^1 p(z)\tilde{g}_n^2(z,k,s)\ dz.
\end{aligned} \tag{2.70}$$

Therefore

$$\frac{\partial\tilde{\sigma}_n}{\partial s} = \frac{\tilde{\sigma}_n^2 - f^2}{2\tilde{\sigma}_n}\int_0^1 p(z)\tilde{g}_n^2(z,k,s)\ dz. \tag{2.71}$$

It follows that if $p(z) \leq 0$ for all $0 \leq z \leq 1$ then $\tilde{\sigma}_n(k,s)$ is a decreasing function of s. Similarly, if $p(z) \geq 0$ then $\tilde{\sigma}_n(k,s)$ is an increasing function of s.

To complete the proof, set $p(z) = \hat{N}^2(z) - N^2(z)$ so that $\tilde{N}^2(z,0) = N^2(z)$ and $\tilde{\sigma}_n(k,0) = \sigma_n(k)$. In addition, $\tilde{N}^2(z,1) = \hat{N}^2(z)$ and $\tilde{\sigma}_n(k,1) = \hat{\sigma}_n(k)$. Clearly $p(z) \leq 0$ and is a continuous function, so for s increasing from 0 to 1, $\sigma(k,s)$ must decrease. Therefore $\hat{\sigma}_n(k) \leq \sigma_n(k)$.

□

As a simple check of the theorem, consider the case when N^2 and $\hat{N}^2$ are constant. As can be seen directly from the dispersion relation (2.38), if $N^2 \geq \hat{N}^2$ then $\sigma_n^2(k) \geq \hat{\sigma}_n^2(k)$, in confirmation of the theorem.

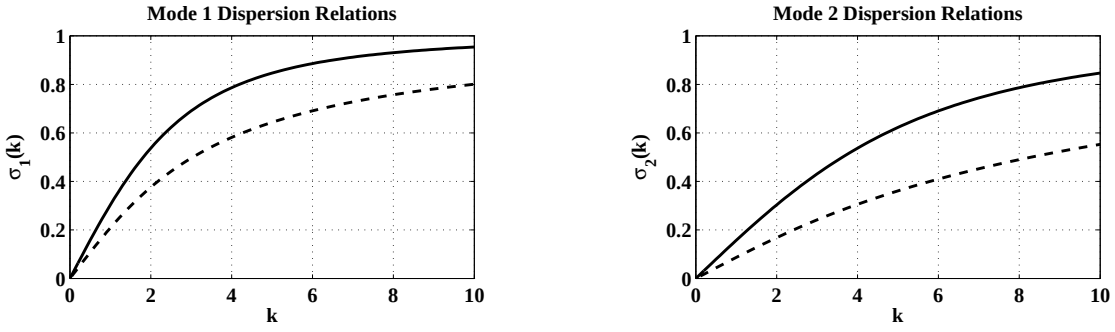

Figure 2.6: The mode one (left subplot) and mode two (right subplot) dispersion relations for the buoyancy frequencies $N_0^2(z) = 1$ (solid lines) and $N^2(z)$ given by (2.51). For both plots $f = 0$.

To demonstrate Theorem 3, Figure 2.6 shows the modes one and two dispersion relations for the the buoyancy frequencies $N_0^2(z) = 1$ and $N^2(z) = \text{sech}^2((z-0.25)/0.2)$ (see equation (2.51)). Since $N^2(z) \leq N_0^2(z)$, Theorem 3 dictates that the dispersion curves for $N^2(z)$ lie below those of $N_0^2(z)$. This is evident in the figure.

Unfortunately, the dependence of $\partial\tilde{\sigma}_n/\partial s$ is subtle, so directly applying formula (2.71) is generally not possible. Even so, Theorem 3 provides the necessary result for determining the limits as $k \to \infty$ and $k \to 0$ of $\sigma_n(k)$, as witnessed in the proof of the next theorem.

Theorem 4. *Consider a stratified fluid with continuous profile $N^2(z) > f^2$ and mode-n dispersion relation $\sigma_n(k)$. Then*

$$\lim_{k\to 0} \sigma_n(k) = f, \tag{2.72}$$

and

$$\lim_{k\to\infty} \sigma_n(k) = N_{\max}. \tag{2.73}$$

Proof. This proof utilizes the notation developed in the proof of Theorem 3. Set $p(z) = N_{\max}^2 - N^2(z)$. Then $\tilde{N}^2(z,0) = N^2(z)$ and $\tilde{N}^2(z,1) = N_{\max}^2$ is constant. Since $p(z) \geq 0$ is

continuous, $\tilde{\sigma}_n(k,0) \leq \tilde{\sigma}_n(k,1)$. The dispersion relation for a fluid with constant buoyancy frequency is known:

$$\tilde{\sigma}_n^2(k,1) = \frac{k^2 N_{\max}^2 + f^2 n^2 \pi^2}{k^2 + n^2 \pi^2}. \tag{2.74}$$

It is then easy to verify that $\lim_{k\to 0} \tilde{\sigma}_n(k,1) = f$, so Theorem 3 implies f is an upper bound for $\sigma_n(k)$ as $k \to 0$. By Proposition 1, f is also a lower bound for $\sigma_n(k) = \tilde{\sigma}_n(k,0)$, so the squeeze theorem implies that $\lim_{k\to 0} \sigma_n(k) = f$.

The proof of the second limit is more subtle and involves analyzing the zeros of the mode-n eigenfunction for a different buoyancy frequency function. To proceed, let $\epsilon > 0$, but require that $\epsilon < N_{\max}^2 - N_{\min}^2$. First, suppose $N^2(z)$ does not achieve a unique global maximum at $z = 0$ or $z = 1$. By the continuity of $N^2(z)$, it is possible to find $a(\epsilon)$ and $b(\epsilon)$ where $0 \leq a < b \leq 1$, such that $N^2(a) = N^2(b) = N_{\max}^2 - \epsilon$, and for $a < z < b$, $N^2(z) \geq N_{\max}^2 - \epsilon$. If the maximum of $N^2(z)$ does occur at $z = 0$ or $z = 1$, a or b can be replaced with that endpoint as appropriate. Define $\hat{N}_\epsilon^2(z)$ to be a continuous function such that on the interval $a \leq z \leq b$, $\hat{N}_\epsilon^2(z) = N_{\max}^2 - \epsilon$, while outside of this interval $f^2 < \hat{N}_\epsilon^2(z) < N^2(z)$. It is not necessary to explicitly define $\hat{N}_\epsilon^2(z)$ outside of the interval $a \leq z \leq b$.

Denote the mode-n eigenfunctions corresponding to $N_\epsilon^2(z)$ by $\hat{g}_n(z,k)$ and the dispersion relation by $\hat{\sigma}_n(k)$. Since $\hat{N}_\epsilon^2(z)$ is strictly positive and continuous, the standard results of Sturm-Liouville theory apply to the eigenfunctions and eigenvalues. Most importantly, $\hat{g}_n$ has exactly $n-1$ simple zeros in the interval $0 < z < 1$.

In the interval $a \leq z \leq b$ the eigenfunctions satisfy

$$\hat{g}_n'' + \mu_n^2 \hat{g}_n = 0 \tag{2.75}$$

where differentiation is with respect to z, and $\mu_n = k\sqrt{\frac{N_{\max}^2 - \epsilon - f^2}{\hat{\sigma}_n^2(k) - f^2} - 1}$. In this interval, the eigenfunctions must take the form $\hat{g}_n(z,k) = d_1 \sin(\mu_n(z-a)) + d_2 \cos(\mu_n(z-a))$, where the constants d_1 and d_2 are determined by matching conditions at a and b. The constants cannot both be zero because the zeros of Sturm-Liouville eigenfunctions are discrete. Suppose $d_1 \neq 0$, the argument when $d_1 = 0$ is analogous. The eigenfunction $\hat{g}_n(z,k)$ has zeros in the interval $a \leq z \leq b$ whenever

$$\tan(\mu_n(z-a)) = -\frac{d_2}{d_1}. \tag{2.76}$$

In the interval $[0, m\pi)$, the function $\tan(z)$ intersects any horizontal line exactly m times. Therefore, if $\mu_n > m\pi/(b-a)$, $\hat{g}_n(z,k)$ must have m zeros in $a \leq z \leq b$.

Now for the contradiction. Assume $\lim_{k\to\infty} \hat{\sigma}_n^2(k) = L < N_{\max}^2 - \epsilon$. Then $\mu_n >$

$k\sqrt{\frac{N_{\max}^2-\epsilon-f^2}{L-f^2}-1}$, so for any finite k satisfying

$$k > \frac{m\pi}{(b-a)\sqrt{\frac{N_{\max}^2-\epsilon-f^2}{L-f^2}-1}}, \tag{2.77}$$

$\hat{g}_n(z,k)$ must have at least m zeros in the interval $a < z < b$. Taking $m > n$, for sufficiently large but finite k the mode-n eigenfunction must have more than n zeros in the interval $0 < z < 1$. This contradicts the fact that the mode-n eigenfunction of a Sturm-Liouville problem should have exactly $n-1$ zeros in the interval $0 < z < 1$. The assumption $L < N_{\max}^2 - \epsilon$ must be false, so, with the aide of Proposition 1, it follows that $\lim_{k\to\infty} \hat{\sigma}_n^2(k) = N_{\max}^2 - \epsilon$.

The results of Theorem 3 can now be applied. Since $N^2(z) \geq \hat{N}^2(z)$ and both functions are continuous, at any $k \geq 0$, $\sigma_n(k) \geq \hat{\sigma}_n(k)$. Therefore $\lim_{k\to\infty} \sigma_n^2(k) \geq N_{\max}^2 - \epsilon$. The limit exists and is bounded above by $N_{\max}^2$ as proved in Proposition 1, and since $\epsilon > 0$ is arbitrary it follows that $\lim_{k\to\infty} \sigma_n^2(k) = N_{\max}^2$.

□

Theorem 4 holds for any finite mode number n. For the eigenvalue problem (2.36), if σ is viewed as the parameter and k as the eigenvalue, Theorem 4 guarantees that an infinite number of wavenumbers can be found, provided $f < \sigma < N_{\max}$. This is interesting because from that perspective, the problem is no longer of regular Sturm-Liouville type, since the weight function is indefinite.

The result that $\lim_{k\to\infty} \sigma_n(k) = N_{\max}$ is intuitive from a physical perspective. The buoyancy frequency has the interpretation of being the frequency at which an infinitesimally displaced particle would oscillate. A particle at the z level where $N(z) = N_{\max}$ should oscillate at the peak buoyancy frequency, and displacing a single particle in a fluid column is certainly a short-wave disturbance.

2.3.5 The Fastest Phase Speed Problem

In this subsection an original solution to an interesting problem related to long wave limits is presented. The purpose of this discussion is to determine an upper bound for the phase speed of internal waves in a fluid, as well as the stratification needed to achieve that bound. This analysis is limited to the case $f = 0$, as phase speeds become infinite in the long wave limit otherwise.

Consider the dimensional form of the Sturm-Liouville eigenvalue problem that defines the dispersion relation:

$$\frac{d^2}{dz^2}\phi_n(z,k) + k^2\left(\frac{N^2(z)}{\sigma_n^2(k)} - 1\right)\phi_n(z,k) = 0, \tag{2.78}$$

with boundary conditions $\phi_n(0,k) = 0 = \phi_n(H,k)$. In this discussion the eigenfunctions are written as ϕ_n instead of g_n to emphasize the dimensional form and avoid confusion with the gravitational constant g.

In the long wave limit, $k \to 0$ and the differential equation reduces to the simpler eigenvalue problem

$$\phi_n''(z) + \frac{N^2(z)}{c_n^2}\phi_n(z) = 0, \tag{2.79}$$

where $c_n = \lim_{k\to 0} \sigma_n(k)/k$ is the mode-n long wave phase speed. This problem is also of Sturm-Liouville type, and when $N^2(z)$ is continuous a countably infinite set of eigenfunctions exists and forms an orthonormal basis for the Hilbert space $L^2([0,H], N^2(z), dz)$. As proved in Lemma 1, the long wave phase speed for a given mode is in fact the maximum possible phase speed that a linear wave can attain.

Suppose the density jump $\Delta\rho$ across the fluid is fixed. Consider the density stratification $\rho(z) = \rho_0 + \bar{\rho}(z)$ satisfying the density jump constraint, so that the buoyancy frequency satisfies $\int_0^H N^2(z)\, dz = (g/\rho_0)(\rho(0) - \rho(H)) = g\Delta\rho/\rho_0$. It is assumed in this analysis that the eigenfunctions are normalized such that $\int_0^H N^2(z)\phi_n^2(z)\, dz = 1$.

While the optimal buoyancy frequency could perhaps be found through variational arguments, little progress was made with that approach. The solution presented here relies on a novel application of the Green's function. Green's functions can be a powerful tool for studying linear differential equations in many different contexts, the reader is referred to Duffy [22] for an introduction to their use. In this setting they are useful because they allow the eigenfunctions to be expressed in the form of an integral equation.

It is necessary to construct the Green's function $G(z,\xi)$ for the simplified equation

$$\frac{d^2}{dz^2}G(z,\xi) = -\delta(z-\xi) \tag{2.80}$$

with boundary conditions $G(0,\xi) = 0 = G(H,\xi)$. The jump condition on the derivative of the Green's function is

$$\frac{d}{dz}G(z,\xi)\Big|_{z=\xi-}^{z=\xi+} = -1. \tag{2.81}$$

It then follows that

$$G(z,\xi) = \begin{cases} \frac{(H-\xi)}{H}z & \text{for } 0 \le z \le \xi \\ \frac{\xi}{H}(H-z) & \text{for } \xi \le z \le H. \end{cases} \tag{2.82}$$

This function is illustrated in Figure 2.7.

The solution to the long wave eigenvalue problem (2.79) can then be expressed in the form:

$$c_n^2\phi_n(z) = \int_0^H G(z,\xi)N^2(\xi)\phi_n(\xi)\, d\xi. \tag{2.83}$$

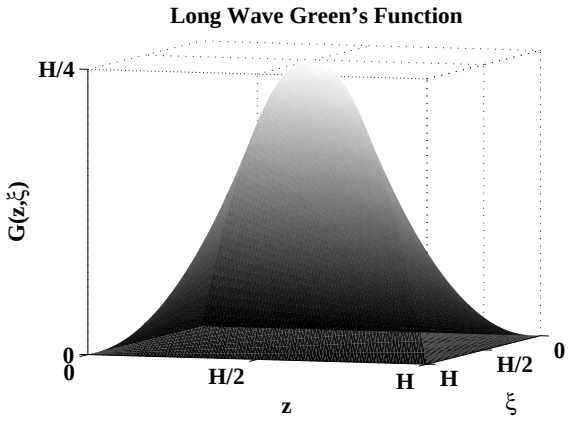

Figure 2.7: The Green's function $G(z,\xi)$ for the long wave problem. Note the maximum occurs at $(z,\xi) = (H/2, H/2)$, as can be shown with simple calculus arguments.

Multiplying both sides by $N^2(z)\phi_n(z)$, integrating against z and using the normalization condition reveals

$$c_n^2 = \int_0^H \int_0^H G(z,\xi) N^2(\xi)\phi_n(\xi) N^2(z)\phi_n(z)\ d\xi\ dz. \tag{2.84}$$

Clearly $|G(z,\xi)| \leq H/4$, with equality only holding when $z = \xi = H/2$. Therefore the phase speed must satisfy the inequality

$$c_n^2 \leq \frac{H}{4}\left(\int_0^H N^2(z)|\phi_n(z)|\ dz\right)^2. \tag{2.85}$$

The remaining integral can be bounded by the Cauchy-Schwarz inequality. The result is

$$c_n^2 \leq \frac{H}{4}\int_0^H N^2(z)\ dz \int_0^H N^2(z)\phi_n^2(z)\ dz. \tag{2.86}$$

Simplifying the first integral with the density jump condition and making use of the normalization condition on the second integral reveals

$$c_n^2 \leq \frac{H}{4}\frac{g\Delta\rho}{\rho_0}. \tag{2.87}$$

Notably, the right hand side of this equation is c_{LW}^2, the square of the long wave phase speed for a wave in a two-layer fluid with equal depths of $H/2$, density jump $\Delta\rho$, and mean density ρ_0 (see Appendix A). The derivation of this inequality also makes it clear that no

other stratification could yield phase speeds equal to c_{LW}. This is because $|G(z,\xi)| < H/4$ away from $z = H/2$, so the buoyancy frequency must be localized at $z = H/2$ or the phase speed is reduced. This analysis proves the following theorem.

Theorem 5. *Consider a Boussinesq fluid with depth H, reference density ρ_0, and density jump $\Delta\rho$. The long wave speed*

$$c_{LW} := \sqrt{\frac{H}{4}\frac{g\Delta\rho}{\rho_0}} \tag{2.88}$$

is an upper bound for the phase speed of a linear wave in the fluid. This phase speed is only achieved in a two-layer fluid with equal layer depths of $H/2$.

This upper bound on phase speeds could be useful for selecting bounds for time-steps for numerical simulations of the Boussinesq equations. With the aid of Theorem 5 it is not necessary to numerically solve the long wave eigenvalue problem prior to simulations. In addition, this analysis supports the choice of the velocity scale chosen for the dimensional analysis used throughout this thesis. The small parameter expansion used in the derivation of the resonant interaction equations holds when the induced velocity values are small in comparison with the fastest possible linear wave phase speed.

Theorem 5 provides a bound on the phase speed for any mode number, but it can only be achieved by mode-1 waves in a limiting stratification. Following the approach used by Yanowitch [75], a tighter, mode number dependent bound for the phase speed can be derived. Yanowitch's method requires some basic concepts from functional analysis. Define the inner product of two functions $a(z)$ and $b(z)$ by

$$\langle a(z), b(z)\rangle = \int_0^H a(z)N^2(z)b(z)\ dz. \tag{2.89}$$

The operator trace is another important quantity that plays an essential role here. Naylor and Sell [53, pages 389-392] present a discussion of the trace of a linear operator L using the definition:

$$\mathrm{tr}(L) = \sum_{n=1}^{\infty}\langle Lx_n, x_n\rangle, \tag{2.90}$$

where $\{x_n\}$ is any set of functions forming an orthonormal basis for the underlying Hilbert space. This definition bears a clear resemblance to the trace of a finite dimensional matrix.

As mentioned before, the Green's function derived above allows for solutions to the long wave eigenvalue problem to be written in the form of a linear integral equation. Notation is simplified by defining the linear integral operator K such that

$$K\phi = \int_0^H G(z,\xi)N^2(\xi)\phi(\xi)\ d\xi. \tag{2.91}$$

Now consider the trace of the linear operator K. For any eigenfunction $\phi_n(z)$, the equation $K\phi_n = c_n^2\phi_n$ holds. In addition, the set of eigenfunctions $\{\phi_n\}$ forms an orthonormal basis for $L^2([0,H], N^2(z), dz)$. So,

$$\mathrm{tr}(K) = \sum_{n=1}^{\infty} \langle K\phi_n, \phi_n\rangle = \sum_{n=1}^{\infty} \langle c_n^2\phi_n, \phi_n\rangle = \sum_{n=1}^{\infty} c_n^2. \tag{2.92}$$

On the other hand, this can be written in the form:

$$\mathrm{tr}(K) = \sum_{n=1}^{\infty} \int_0^H \int_0^H G(z,\xi)N^2(\xi)\phi_n(\xi)N^2(z)\phi_n(z)\ dz\ d\xi. \tag{2.93}$$

This expression can be simplified because $G(z,\xi)$ is continuous and can be projected onto the orthonormal basis. That is, $G(z,\xi) = \sum_{n=1}^{\infty}\langle G(z,\xi), \phi_n(z)\rangle\phi_n(z)$. This allows $\mathrm{tr}(K)$ to be written in the form:

$$\begin{aligned}
\mathrm{tr}(K) &= \int_0^H N^2(\xi)\left[\sum_{n=1}^{\infty}\left(\int_0^H G(z,\xi)N^2(z)\phi_n(z)\ dz\right)\phi_n(\xi)\right]\ d\xi, \\
&= \int_0^H N^2(\xi)\left[\sum_{n=1}^{\infty}\langle G(z,\xi),\phi_n(z)\rangle\phi_n(\xi)\right]\ d\xi, \\
&= \int_0^H G(\xi,\xi)N^2(\xi)\ d\xi.
\end{aligned} \tag{2.94}$$

It follows that

$$\begin{aligned}
\sum_{n=1}^{\infty} c_n^2 &= \int_0^H G(\xi,\xi)N^2(\xi)\ d\xi, \\
&\le \tfrac{H}{4}\int_0^H N^2(\xi)\ d\xi, \\
&\le \tfrac{Hg\Delta\rho}{4\rho_0}.
\end{aligned} \tag{2.95}$$

Now, since $nc_n^2 \le \sum_{j=1}^{n} c_j^2 \le \sum_{j=1}^{\infty} c_j^2$, the above inequality implies that:

$$c_n^2 \le \frac{1}{n}\frac{Hg\Delta\rho}{4\rho_0}. \tag{2.96}$$

This derivation proves the following theorem.

Theorem 6. *Consider a Boussinesq fluid with depth H, reference density ρ_0, and density jump $\Delta\rho$. Suppose the buoyancy frequency $N(z)$ is strictly positive and continuous. The long wave mode-n phase speed c_n is bounded by*

$$c_n \le \sqrt{\frac{1}{n}\frac{H}{4}\frac{g\Delta\rho}{\rho_0}}. \tag{2.97}$$

It is interesting to note that, as shown by Bender and Orszag [6, Section 10.1], the eigenvalues for a Sturm-Liouville problem of the form (2.79) decay like $1/n^2$ as $n \to \infty$. This implies that for a continuous stratification the long-wave phase speeds should decay like $1/n$. It is not immediately obvious if the method used in the derivation of Theorem 6 could be modified to derive a better bound. This discussion motivates a search for the stratification that leads to the fastest mode-n phase speed.

2.3.6 Summary

Several properties of the linear eigenvalue problem (2.10) and the associated phase speed and group velocity have been explored. Some of these are well-known and intuitive, but others are novel. The analysis in this section has been based on the assumption that $N^2(z) - f^2 > 0$ for $0 \leq z \leq 1$. Under that assumption, the major results of this section are as follows.

1. The dispersion relation is monotonically increasing and satisfies $f \leq \sigma_n(k) \leq N_{\max}$. These properties are well-known.

2. The phase speed of an internal wave decreases with wavenumber, and provides an upper bound on the magnitude of the group velocity. This was derived in a very different manner by Yih [76, Chapter 2].

3. Given two buoyancy profiles defined by $\hat{N}^2(z)$ and $N^2(z)$ satisfying $\hat{N}^2(z) \leq N^2(z)$, the corresponding dispersion relations satisfy $\hat{\sigma}_n(k) \leq \sigma_n(k)$. This result is a direct consequence of the Sturm comparison theorem.

4. In the long-wave limit $k \to 0$, $\sigma_n(k) \to f$. This is a well-known property, but the proof given in Theorem 4 is original.

5. In the limit $k \to \infty$, $\sigma_n(k) \to N_{\max}$. The result is intuitive and should be well-known, but the proof in Theorem 4 is original.

6. The fastest phase speed attainable in a Boussinesq fluid with $f = 0$ and rigid lids is achieved in a two-layer fluid of equal layer depths. The derivation of Theorem 5 is original. Independently, Yanowitch [75] used an argument involving a Green's function to show that the fastest phase speed for a fluid of depth h with a free surface is $\sqrt{gh}$. Yanowitch's approach was used in the derivation of Theorem 6, showing that $c_n \leq \sqrt{gH\Delta\rho/(4n\rho_0)}$.

Chapter 3

Numerical Methods and Analysis

Studying the resonant interactions described in the previous chapter with numerical experiments requires careful consideration. The numerical methods needed to simulate and analyze the interactions are interesting in their own right and worthy of discussion. This chapter provides that discussion, acting as the bridge between the theory discussed thus far and the simulations presented in the next chapter.

The numerical methods described here can be loosely grouped into two categories; those that are used to simulate the equations of interest, and those that are used to analyze the resulting data. Naturally there is a large overlap between the two groups, and some of the methods are essential in both areas. In Section 3.1 the method used to solve the linear eigenvalue problem (2.10) is presented, along with a description of how candidate triads are found for a given stratification. The two numerical models used for solving the Boussinesq equations are described in Section 3.2. Section 3.3 explains how energy in a stratified fluid is calculated. The definition of energy leads to a curious energy spectrum shape that is explained in Section 3.4. The chapter ends with an introduction to numerical forcing theory in Section 3.5. This is the final ingredient necessary for simulating waves in variable density stratifications, and is the precursor to Chapter 5.

3.1 Preliminary Calculations

Designing resonant triad interaction experiments requires significant preliminary work. Simple questions, such as what wavelengths will be produced by a given forcing frequency must be answered. Knowing which waves to expect through resonant interactions also necessitates a search for possible triad candidates. As discussed in Section 3.5, the shape of the eigenfunction for a given forcing frequency is also needed to properly generate the desired waves. Many of these issues are addressed through the numerical solution of the

underlying linear eigenvalue problem, which is presented in the next subsection. Then, with the dispersion relation and eigenfunctions in hand, candidate triads can be determined, as explained in Section 3.1.2.

3.1.1 Solving the Linear Eigenvalue Problem

Recall the dimensionless linear eigenvalue problem (2.10) governing the dispersion relation $\sigma_n(k)$ and corresponding eigenfunctions $g_n(z,k)$:

$$\frac{\partial^2}{\partial z^2} g_n(z,k) + k^2 \left(\frac{N^2(z) - f^2}{\sigma_n^2(k) - f^2} - 1 \right) g_n(z,k) = 0, \tag{3.1}$$

with boundary conditions $g_n(0,k) = 0 = g_n(1,k)$. Given $N^2(z)$, it is generally not possible to solve this problem analytically, though many properties of the solutions are known (see Section 2.3). Approximate solutions can be constructed numerically with relative ease, however. The usual method of approximating the differential equation as a system of algebraic equations is employed here.

The basic scheme is to split the interval $0 \leq z \leq 1$ using $M+1$ equi-spaced points $z_j = j/M$, with $j = 0, 1, \ldots, M$. The eigenfunction $g_n(z,k)$ is then approximated with the vector $\hat{g}_n$ defined at those points. The term $\partial_z^2 g_n(z,k)$ is approximated with the matrix-vector product $D_2 \hat{g}_n$, where D_2 is the second derivative matrix operator discussed below. This approach converts the continuous eigenvalue problem into a generalized algebraic eigenvalue problem of the form

$$(D_2 - k^2 I)\hat{g} = \frac{k^2}{\sigma^2 - f^2} \mathrm{Diag}(N^2(z) - f^2)\hat{g}, \tag{3.2}$$

where I is the $(M+1)\times(M+1)$ identity matrix and $\mathrm{Diag}(N^2(z)-f^2)$ is the $(M+1)\times(M+1)$ diagonal matrix whose j^{th} diagonal entry is $N^2(z_j)-f^2$. The Dirichlet boundary conditions on $\hat{g}$ are imposed by deleting the first and last row and column of each matrix in (3.2).

Equation (3.2) is more easily recognized as a generalized eigenvalue problem by rewriting it in the form $A\hat{g} = \lambda B\hat{g}$, where $A = D_2 - k^2 I$, $B = k^2 \mathrm{Diag}(N^2(z) - f^2)$, and $\lambda = 1/(\sigma^2 - f^2)$. In some instances it is preferable to solve the eigenvalue problem (3.2) with σ treated as the parameter and k the eigenvalue. In that case, simple rearrangement reveals the new generalized eigenvalue problem $\tilde{A}\hat{g} = \tilde{\lambda}\tilde{B}\hat{g}$, where $\tilde{A} = D_2$, $\tilde{B} = \mathrm{Diag}(N^2(z) - f^2)/(\sigma^2 - f^2) - I$, and $\tilde{\lambda} = k^2$. In both situations, the eigenfunctions and eigenvalues are found simultaneously through the Matlab "eig" function, which makes use of the QR algorithm (see Demmel [19, Chapters 4-5] for an introduction).

The result of this process is a collection of $M-1$ eigenvectors and eigenvalues, sorted by eigenvalue magnitude and assigned indices. To determine the full dispersion relation,

or study the eigenfunction dependence on k, the problem must be solved over the desired range of wavenumbers. This can be costly as the underlying factorization algorithm requires $O(M^3)$ operations.

A variety of differentiation matrices D_2 could be used to approximate the second derivative. Finite differences are an obvious choice, but for high precision the Fourier differentiation methods provided in the Matlab toolbox by Weideman and Reddy [72], and discussed extensively by Trefethan [67], are used.

The Fourier differentiation matrices require periodicity of the underlying functions and continuity of the derivatives at the boundaries. A modification is therefore necessary to compute the eigenfunctions with odd mode numbers. To understand why, recall from Section 2.3 that a mode-n eigenfunction has precisely $n-1$ zeros in the interval $(0,1)$. It follows that if n is odd and $g_n(z,k) \geq 0$ as $z \to 0^+$ then $g_n \geq 0$ as $z \to 1^-$, so $\partial_z g_n|_{z=0} \neq \partial_z g_n|_{z=1}$.

This problem is corrected using the following process. First, the second derivative matrix $\hat{D}_2$ is constructed for the interval $0 \leq z \leq 2$ using the $2M+1$ grid points $z_j = j/M$, $j = 0, 1, \cdots 2M$. Then, odd-symmetry about $z = 1$ is enforced for matrix-vector products. This is done by defining the $(M-1) \times (M-1)$ matrix $D_2^* = \hat{D}_2(2:M, 2:M) - \hat{D}_2(2:M, 2M-1:M+1)$, where standard Matlab notation is being used. Using D_2^* in (3.2) allows for computation of even and odd-numbered eigenmodes on $0 \leq z \leq 1$.

3.1.2 Finding Candidate Triads

Once the dispersion relation has been constructed numerically, candidate triads can be determined through a brute-force search. Looping over the wavenumbers, every possible pair of waves is considered. If the sum of their wavenumbers and frequencies match another wave in the data set (to within a desired tolerance), the data is saved as a candidate triad. To save time, triads are only sought within the first few modes of the dispersion relation. Even then, a data set consisting of m wavenumbers and frequencies requires $O(m^2)$ calculations. Run-time is reduced in some cases by constraining one of the three waves in the triad to have a fixed frequency (such as tidal frequency or a desired paddle frequency).

Once all possible triad candidates of interest have been found it is necessary to compute the group velocities and interaction coefficients . This is done using equation (B.23):

$$v_p = \frac{(\omega_p^2 - f^2)}{\omega_p k_p} - \frac{(\omega_p^2 - f^2)^2}{\omega_p k_p} \int_0^1 g_p^2(z)\, dz, \tag{3.3}$$

and equation (B.25):

$$\gamma_p = \left(\frac{\omega_p^2 - f^2}{2k_p^2 \omega_p} \right) \int_0^1 \left(F_{pqr} + G_{pqr} + H_{pqr} \right) g_p(z) dz, \tag{3.4}$$

with the underlying quantities defined in the appendix. The integral expressions are approximated by Riemann sums over the same grids where the numerical eigenfunctions are defined.

Finally, the strength of the candidate triads is evaluated by considering products of the interaction coefficients. When the product is larger (in absolute value) the interaction is stronger. This allows for the triads to be sorted by strength, which in turn guides the design of numerical experiments.

3.2 Solving the Boussinesq Equations

Numerically solving the Boussinesq equations is essential to this study of resonant triad interactions. Developing a code to solve the fully nonlinear equations is a significant undertaking. Many subtle issues must be addressed, and a range of compromises must be made to balance the needs of accuracy, stability, and running-time efficiency. Fortunately, others have devoted significant time and effort to such endeavors. The SPINS model, developed by Subich [64], is used for all of the nonlinear simulations.

Early experiments with the SPINS model demonstrated some unexpected behaviour. Even at small amplitudes, efforts to force individual internal waves often resulted in noisy wave fields, and the energy spectrum possessed a curious shape. These peculiarities motivated the development of a linear solver for basic forcing and energy investigations. The Matlab code used for this purpose is described in Section 3.2.1, and the SPINS model is discussed in Section 3.2.2.

3.2.1 The Linear Matlab Solver

The Matlab solver described here works with the linearized version of the streamfunction formulation of the Boussinesq equations (2.6a). Taking $f = 0$, the underlying equation that must be solved is

$$\nabla^2 \psi_{tt} + N^2(z) \psi_{xx} = F(x, z, t) \tag{3.5}$$

with initial conditions $\psi(x, z, 0) = 0$, $\psi_t(x, z, 0) = 0$, periodic boundary conditions in x, and $\psi(x, 0, t) = \psi(x, 1, t) = 0$. The forcing function $F(x, z, t)$ must be chosen to be compatible with the desired forcing for the nonlinear equations. As described in Section

3.5, a forcing function $F_2(x,z,t)$ is used to force the vertical momentum equation for the nonlinear problem. With that choice, it is necessary to take $F(x,z,t) = \frac{\partial^2}{\partial x \partial t} F_2(x,z,t)$. In general, the linear solver uses

$$F(x,z,t) = A\cos(\omega_F t + \vartheta) f(x) h(z), \tag{3.6}$$

and care must be taken in the choice of $f(x)$ and $h(z)$ to compare against nonlinear simulations.

Numerically solving the linearized streamfunction equation is advantageous because it allows for easy use of the Fast Fourier Transform (FFT). From the solution ψ, the linearized density perturbation ρ' can be reconstructed by the relation $\rho'_t = -\psi_x d\bar{\rho}/dz$. The horizontal and vertical velocity components are found through $(u,w) = (-\psi_z, \psi_x)$.

An approximate solution to (3.5) is sought in the form of a partial Fourier series. The truncated solution is found with continuous x and z, then sampled on a discrete set of evenly spaced grid points. Suppose the domain has horizontal length L, the discrete x samples are given by $x_j = jL/N_x,\ j = 0, \ldots N_x - 1$, where N_x specifies the number of grid points in the horizontal direction. Similarly, the vertical coordinate is given by $z_j = j/N_z$, where N_z defines the number of points used to discretize the vertical coordinate. The approximate solution then takes the form

$$\psi(x,z,t) = \sum_{m=-N_f}^{N_f-1} \sum_{n=1}^{N_M} \hat{a}_{m,n}(t) \exp(ik_m x) g_n(z, k_m). \tag{3.7}$$

Here

$$k_m = \frac{2\pi m}{L} \text{ and } N_f = N_x/2 \tag{3.8}$$

define the resolvable wavenumbers for a domain of length L. In the approximate solution (3.7) only the first N_M vertical modes are kept as simulations of interest generally only involve low vertical mode numbers. The unknown coefficients $\hat{a}_{m,n}(t)$ must be determined to construct the numerical solution.

Substituting the approximate form (3.7) into the governing linear equation (3.5) leads to a sum of ODEs governing the growth of the unknown coefficients. With the assumed forcing shape, the coefficients satisfy

$$\sum_{m,n} \left[\frac{k_m^2}{\omega_{m,n}^2} \left(\hat{a}''_{m,n} + \omega_{m,n}^2 \hat{a}_{m,n} \right) \exp(ik_m x) \right] N^2(z) g_n(z, k_m) = -A\cos(\omega_F t + \vartheta) f(x) h(z), \tag{3.9}$$

where $\omega_{m,n} = \sigma_n(k_m)$. Suppose that $f(x)$ decays to zero quickly enough at the boundaries so that it can be represented as a continuous periodic function. Then $f(x)$ can be

decomposed in the form:

$$f(x) = \sum_{m=-N_f}^{N_f-1} f_m \exp(ik_m x). \tag{3.10}$$

In addition, define

$$h_{m,n} = \int_0^1 h(z) g_n(z, k_m)\, dz, \tag{3.11}$$

which can be computed numerically as a Riemann sum. It follows that

$$\hat{a}''_{m,n}(t) + \omega^2_{m,n}\hat{a}_{m,n}(t) = -f_m h_{m,n} \frac{\omega^2_{m,n}}{k_n^2} A\cos(\omega_F t + \vartheta)). \tag{3.12}$$

The initial conditions $\hat{a}_{m,n}(0) = \hat{a}'_{m,n}(0) = 0$ lead to the solution

$$\begin{aligned} \hat{a}_{m,n}(t) = -\tfrac{\omega^2_{m,n}}{k_m^2}\tfrac{A f_m h_{m,n}}{\omega^2_{m,n}-\omega_F^2} \quad & \Big(\cos(\omega_F t + \vartheta) - \cos(\vartheta)\cos(\omega_{m,n} t) \\ & + \tfrac{\omega_F}{\omega_{m,n}} \sin(\vartheta)\sin(\omega_{m,n} t) \Big). \end{aligned} \tag{3.13}$$

It is assumed that $\omega_F \neq \omega_{m,n}$ for all m, n so that the above solution is valid. The transcendental nature of the $\omega_{m,n}$ makes this a reasonable assumption unless a pathological value of ω_F is chosen.

Using expression (3.13), the series solution (3.7) can be directly constructed. For the applications of interest here, only small vertical mode numbers are considered. The sum over the vertical modes is typically truncated to just the first three terms. With these limitations the linear Matlab solver is primarily used as a diagnostic tool in this chapter. Results generated with the code are discussed in the sections that follow.

3.2.2 The SPINS Solver

The SPINS solver is a C++ code developed by Chris Subich. The program is capable of solving the full Navier-Stokes equations in two or three dimensions, and can also be used to solve the Boussinesq equations. SPINS is specifically designed for studying geophysical processes such as internal waves. Important features of the code are discussed here. A complete description of SPINS is found in the associated thesis [64].

The SPINS model uses a mixed explicit-implicit time-stepping scheme. Diffusive and viscous terms are treated implicitly, while advection and forcing terms are handled explicitly. The scheme used is globally third-order. The explicit terms are treated with the third-order Adams-Bashforth method, a multi-step method involving data from the current time level and previous two time levels. Multi-step methods are problematic for

initial time-steps because data from previous time levels does not exist. SPINS counters this problem with a technique based on Richardson extrapolation. The method preserves the overall third-order accuracy of the time-stepping procedure.

SPINS approximates continuous functions on a discrete set of grid points. Spectral collocation methods are used to approximate derivatives, and functionality for both Chebyshev and Fourier differentiation is available (though only Fourier differentiation is used in this investigation). This is advantageous because the differentiation operation simply becomes an algebraic operation in Fourier space. With the assistance of the FFT, conversions to and from Fourier space are made at very low cost. Build-up of energy at high wavenumbers is problematic for spectral solvers, and to counter this SPINS uses a 2/3 low-pass filter. Essentially, energy at all wavenumbers greater than 2/3 of the Nyquist frequency are exponentially filtered out.

SPINS runs in parallel and makes use of the MPI protocol. Typical simulations presented here involved eight processors, though scaling tests have been performed by Subich on much larger systems. SPINS creates a binary output file for the vertical and horizontal velocity fields, as well as the density field, at pre-determined save times. In addition, the x and z grid coordinates are stored. The code also creates a Matlab script that is used for importing all of the necessary data into Matlab.

Setting up experiments with the SPINS model is also a simple process. All of the necessary parameters are set in a single main-driver file. This seemingly minor detail is actually a major convenience as it reduces errors that occur from modifying multiple input files. The only externally-set parameter is the number of processors to use at runtime, but this is simply set at the command line.

There are, of course, alternatives to the SPINS model. These include the spectral flow_solve model by Winters, Mackinnon, and Mills [73], and the IGW finite volume code written by Lamb [38]. The IGW model would be particularly useful for simulations involving topography interactions, though topography functionality has recently been added to SPINS as well.

3.3 The Energy Decomposition

Making effective use of the data collected with the SPINS model or linear Boussinesq solver is critical to the understanding of resonant triad interactions. The key question that must be answered from analyzing simulation data is: how much energy lies in each wave at a given time? This section explains the energy decomposition approach necessary to resolve that question.

3.3.1 Energy in a Stratified Fluid

The energy in a stratified fluid can be decomposed into a sum of kinetic and potential energy. However, a different quantity, known as the available potential energy (APE) is of particular interest because it represents the amount of potential energy that can actually be converted into useful work, such as mixing or heat (through dissipation). The sum of kinetic and available potential energy is referred to as pseudo-energy, and the concept and calculation of this quantity are discussed extensively by Lamb [39]. The linearized expression for pseudo-energy density is given by

$$E = \frac{\rho_0}{2}\left(u^2 + w^2\right) + \frac{1}{2}\frac{g^2}{\rho_0}\frac{\rho'^2}{N^2(z)} \tag{3.14}$$

see Gill [29, page 139] or Bühler [12, Chapter 6], for instance. This energy density depends on x, z, and t, and must be integrated over the domain to determine the total energy. The first term involving velocity components is the kinetic energy (KE) density. The term involving ρ' in (3.14) is the leading order contribution of the APE density, but it is exact when $N^2(z)$ is constant. In essence, to calculate the APE contribution exactly the difference between the disturbed and undisturbed state must be integrated over the domain.

Expression (3.14) is in dimensional form. Using the scalings defined in Chapter 2, this equation can be expressed in terms of dimensionless variables as

$$E = RU^2\left[\frac{\hat{\rho}_0}{2}(\hat{u}^2 + \hat{w}^2) + \frac{\hat{\rho}_0}{2}\frac{\hat{\rho}'^2}{\hat{N}^2(\hat{z})}\right]. \tag{3.15}$$

Here $R = \Delta\rho/4$, $\hat{\rho}_0 = \rho_0/R$, and $U^2 = Hg\Delta\rho/(4\rho_0)$. This dimensionless form must be used for pseudo-energy computations with the Matlab solver.

As already mentioned, the total pseudo-energy of the fluid must be found by integrating E over the domain. This could be done by directly integrating the SPINS (or linear solver) output data with relative ease. However, to understand energy transfers in wave interactions, it is necessary to project the total energy onto the different vertical modes at each horizontal wavenumber. The method used for that projection is now described.

3.3.2 The Velocity and Density Fields

To make use of the energy formula above, the data u, w, ρ' and ψ (if the Matlab solver is used) must be projected onto horizontal wavenumbers and eigenfunctions. At each wavenumber and frequency a sum of left and rightward propagating waves with different phases is possible. The decomposition must account for this.

Let $\sum_{m,n} A_{m,n} = \sum_{m=-N_f}^{N_f-1} \left(\sum_{n=1}^{\infty} A_{m,n} \right)$ for a given quantity $A_{m,n}$. Then the natural decomposition for the vertical velocity field takes the form:

$$w(x,z,t) = \sum_{m,n} a_{m,n}(t) \exp(ik_m x)\, g_n(z,k_m). \tag{3.16}$$

The incompressibility condition suggests the decomposition

$$u(x,z,t) = \bar{u}(z) + i \sum_{m,n} \frac{a_{m,n}(t)}{k_m} \exp(ik_m x)\, \frac{d}{dz} g_n(z,k_m), \tag{3.17}$$

where $\bar{u}(z)$ is the background mean flow induced by the waves (the contribution from $k = 0$). Note that this expression involves the same coefficients $a_{m,n}$ used in the decomposition of u. This is important and useful; the dependence of u on the derivatives of the vertical eigenmodes makes it difficult to directly decompose u. The incompressibility of the data field allows for the decomposition to be done without actually working with the u data. For decomposing the density, the linearized equation $\partial\rho'/\partial t + w d\bar{\rho}/dz = 0$ suggests the appropriate form:

$$\rho'(x,z,t) = \frac{\rho_0}{g} N^2(z) \sum_{m,n} \frac{b_{m,n}(t)}{\omega_{m,n}} \exp(ik_m x)\, g_n(z,k_m). \tag{3.18}$$

When the linear Matlab solver is used, the streamfunction must be decomposed. This is done using the expression

$$\psi(x,z,t) = \sum_{m,n} \hat{a}_{m,n}(t) \exp(ik_m x)\, g_n(z,k_m), \tag{3.19}$$

where $\hat{a}_{m,n}(t)$ is given explicitly by (3.13).

Since the underlying data fields are real, the coefficients in each decomposition satisfy an important property. The coefficient corresponding to k_{-m} is just the complex conjugate of the coefficient for k_m. That is, $a_{-m,n} = a^*_{m,n}$, and similarly for $b_{m,n}$ and $\hat{a}_{m,n}$. Quick inspection of the eigenvalue problem also reveals that the eigenfunctions satisfy $g_n(z,k_m) = g_n(z,k_{-m})$.

3.3.3 Expressions for the Total Pseudo-Energy

With the above decompositions it is possible to express the pseudo-energy in terms of the coefficients $a_{m,n}$, $b_{m,n}$, and $\hat{a}_{m,n}$. As mentioned earlier, (3.14) represents the pseudo-energy density at a point, so integrations over the domain must be performed to find the total pseudo-energy.

A General Expression for Energy

To determine the total kinetic and available potential energy integration of the decomposed signals is required. The total kinetic energy is given by

$$KE = \frac{\rho_0}{2} \int_0^H \int_0^L \left(u^2 + w^2\right)\ dx\ dz. \tag{3.20}$$

For shorthand, the notation: $\delta_{mn} = 1$ if $m = n$ and 0 otherwise, is used. Suppose that k_m and k_n are among the resolvable frequencies. Direct integration reveals

$$\int_0^H \int_0^L w^2\ dx\ dz = L \sum_{m,n,q} \left[a_{m,n} a_{-m,q} \int_0^H g_n(z, k_m) g_q(z, k_m)\ dz \right]. \tag{3.21}$$

Similarly

$$\begin{aligned} \textstyle\int_0^H \int_0^L u^2\ dx\ dz &= L \textstyle\int_0^1 \bar{u}^2(z)\ dz \\ &\quad + L \textstyle\sum_{m,n,q} \left[a_{m,n} a_{-m,q} \int_0^H \frac{1}{k_m^2} \frac{d}{dz} g_n(z, k_m) \frac{d}{dz} g_q(z, k_m)\ dz \right]. \end{aligned} \tag{3.22}$$

Using integration by parts and the definition of the eigenfunction, it is possible to show that $\int_0^1 \frac{1}{k_m^2} \frac{d}{dz} g_n(z, k_m) \frac{d}{dz} g_q(z, k_m)\ dz = \frac{\delta_{nq}}{\omega_{m,n}^2} - \int_0^H g_n(z, k_m) g_q(z, k_m)\ dz$. This simplifies the expression for the total kinetic energy to:

$$KE = \frac{\rho_0 L}{2} \int_0^H \bar{u}^2(z)\ dz + \frac{\rho_0 L}{2} \sum_{m,n} \frac{|a_{m,n}|^2}{\omega_{m,n}^2}. \tag{3.23}$$

The contribution from the mean flow $\bar{u}(z)$ is discussed below.

The net contribution of available potential energy is

$$APE = \frac{1}{2} \frac{g^2}{\rho_0} \int_0^H \int_0^L \frac{\rho'^2}{N^2(z)}\ dx\ dz. \tag{3.24}$$

Substituting in the series solution for ρ' from equation (3.18), directly integrating, and making use of the eigenfunction orthogonality condition reveals

$$APE = \frac{\rho_0 L}{2} \sum_{m,n,q} \frac{|b_{m,n}|^2}{\omega_{m,n}^2}. \tag{3.25}$$

Summing equations (3.23) and (3.25) reveals that the total linearized pseudo-energy in the fluid is

$$E = \frac{\rho_0 L}{2} \int_0^H \bar{u}^2(z)\ dz + \frac{\rho_0 L}{2} \sum_{m=-N_f/2}^{N_f/2-1} \left(\sum_{n=0}^{\infty} \frac{|a_{m,n}|^2 + |b_{m,n}|^2}{\omega_{m,n}^2} \right). \tag{3.26}$$

This is the expression that is used to determine the pseudo-energy after a simulation is complete. The equation can be immediately interpreted in terms of contributions of specific vertical modes at different horizontal wavenumbers. The pseudo-energy of a mode-n wave at a non-zero wavenumber k_m is

$$E_{m,n} = \frac{\rho_0 L}{2}\left(\frac{|a_{m,n}|^2 + |b_{m,n}|^2}{\omega_{m,n}^2}\right). \tag{3.27}$$

The Mean Flow Contribution

The first term in (3.26) represents the energy due to the mean flow. Decomposing this into different vertical modes requires special attention. In the limit $k \to 0$, the dominant balance in the linear eigenvalue problem (2.10) is between g_n'' and $(k^2/\sigma_n^2)N^2(z)g_n$, since $\sigma \to 0$. As discussed in Section 2.3.5, the resulting eigenvalue problem can be written as

$$g_n''(z) + \frac{N^2(z)}{c_n^2} g_n(z) = 0, \tag{3.28}$$

with boundary conditions $g_n(0) = g_n(H) = 0$. The eigenvalue c_n is the phase speed in the long-wave limit. The natural orthogonality condition on two eigenfunctions is once again $\int_0^H N^2(z) g_m(z) g_n(z)\ dz = \delta_{mn}$. This suggests the decomposition $\bar{u}(z) = \sum_{n=1}^{\infty} \alpha_n N(z) g_n(z)$, so that

$$\int_0^H \bar{u}^2(z)\ dz = \sum_{n=1}^{\infty} \alpha_n^2. \tag{3.29}$$

This implies that the energy contribution from the mode-n mean flow component is $\rho_0 L \alpha_n^2/2$.

The Streamfunction Calculation

For the Matlab solver, only the streamfunction ψ is computed. The density perturbation field can be reconstructed for data visualization, but an exact expression for the total pseudo-energy is possible directly from the streamfunction data.

When the streamfunction is decomposed as in (3.19) the expression for kinetic energy becomes $KE = \frac{\rho_0 L}{2} \sum_{m,n} \frac{k_m^2 |\hat{a}_{mn}|^2}{\omega_{mn}^2}$, with $\hat{a}_{m,n}$ defined by (3.13). The density perturbation field can be extrapolated from ψ, and written in the form (3.18) with $\hat{b}_{m,n}$ in place of $b_{m,n}$, and no factor of ρ_0/g. The coefficient $\hat{b}_{m,n}$ is given by

$$\begin{aligned}\hat{b}_{m,n}(t) = -\tfrac{\omega_{m,n}^3}{k_m^2}\tfrac{A f_m g_{m,n}}{\omega_{m,n}^2 - \omega_F^2} \quad & \Big(\tfrac{\sin(\omega_F t + \vartheta)}{\omega_F} - \tfrac{\cos(\vartheta)}{\omega_{m,n}} \sin(\omega_{m,n} t) \\ & + \tfrac{\omega_F}{\omega_{m,n}^2}\sin(\vartheta) - \tfrac{\omega_F}{\omega_{m,n}^2}\sin(\vartheta)\cos(\omega_{m,n} t)\Big),\end{aligned} \tag{3.30}$$

where $\rho'(x,z,0) = 0$ is assumed. The available potential energy is once again $APE = \frac{\rho_0 L}{2}\sum_{m,n}\frac{|\hat{b}_{m,n}|^2}{\omega_{m,n}^2}$. The total pseudo-energy in a mode-n wave at wavenumber k_m is then

$$E_{m,n} = \frac{\rho_0 L}{2} k_m^2 \left(\frac{|\hat{a}_{m,n}|^2 + |\hat{b}_{m,n}|^2}{\omega_{m,n}^2} \right), \tag{3.31}$$

where each quantity in the expression is dimensionless.

While working with the Matlab linear solver no mean flow calculations are required. This is because all of the simulations presented here are done with a quiescent background state, and a mean flow can only be generated through nonlinear interactions.

3.3.4 Decomposing the Simulation Data

The discussion above suggests the useful features of the data that are needed in order to determine the energy content of different flows. In particular, the determination of the Fourier coefficients $a_{m,n}$ and $b_{m,n}$ are required. This subsection describes the techniques used to obtain the coefficients. The methods described here are specific to the analysis of output from the SPINS model, analysis of data from the Matlab solver follows naturally.

Suppose a simulation is run with N_x horizontal grid points and N_z vertical grid points. The computational domain has height H and length L. The data fields for velocity and density at each time step consist of a $N_x \times N_z$ array of data values.

The SPINS model collects data on a staggered grid at coordinates specified by $\hat{x}, \hat{z}$. The data points lie at

$$\begin{aligned} \hat{x}_i &= (i - 1/2)\tfrac{L}{N_x}, \quad i = 1, \ldots, N_x, \\ \hat{z}_j &= (j - 1/2)\tfrac{H}{N_z}, \quad j = 1, \ldots, N_z. \end{aligned} \tag{3.32}$$

For analysis purposes, the vertical velocity and density data fields are interpolated onto the new set of grid points aligned with the boundaries and given by

$$\begin{aligned} x_i &= i\tfrac{L}{N_x}, \quad i = 0, \ldots, N_x - 1 \\ z_j &= j\tfrac{H}{N_z}, \quad j = 0, \ldots, N_z. \end{aligned} \tag{3.33}$$

Dirichlet boundary conditions on w and ρ are imposed at $z = 0, H$. The set of resolvable horizontal wavenumbers for the interpolated data take the form

$$k_j = \frac{2\pi j}{L}, \text{ with } -N_f \le j \le N_f - 1, \text{ and } N_f = \frac{N_x}{2}. \tag{3.34}$$

The Nyquist frequency, which is the largest resolvable frequency is $2\pi N_f/L$, or simply $\pi N_x/L$.

Let W be the $N_x \times N_z$ matrix such that $W_{i,j}$ denotes the value of the vertical velocity field at the coordinate (x_i, z_j) Applying the FFT to each column of W (that is, with respect to x), yields a new matrix whose i^{th} row gives the z-dependence of W at the wavenumber k_i. This must be further decomposed by projecting each row of $\hat{W}$ onto the vertical modes associated with each wavenumber.

To accomplish the decomposition, a projection matrix is found beforehand. At each of the resolvable wavenumbers, the eigenvalue problem (2.10) is solved numerically using the methods of Section 3.1.1. The first N_{modes} vertical modes are stored at each wavenumber, and typically the value $N_{modes} = 5$ is used. The vertical eigenmodes are used to construct the block-diagonal matrix P of the form

$$P = \begin{pmatrix} P^{(1)} & 0 & \dots & 0 \\ 0 & P^{(2)} & \dots & \vdots \\ \vdots & \dots & \ddots & \vdots \\ 0 & \dots & \dots & P^{(N_f)} \end{pmatrix}, \tag{3.35}$$

where P is a $(N_{modes} \cdot N_f) \times (N_z \cdot N_f)$. The j^{th} block matrix $P^{(j)}$ is the $N_{modes} \times N_z$ matrix whose element at index (m, n) is $N^2(z_n) g_m(z_n, k_m)$.

For multiplication with P, the first N_f columns of $\tilde{W}$ are concatenated into a single column vector of length $N_f \cdot N_z$. The product $P\tilde{W}$ creates a new column vector of length $N_{modes} \cdot N_f$, that is refolded into a $N_{modex} \times N_f$ matrix of pseudo-energy values. The (i, j) entry of this matrix is the pseudo-energy in the i^{th} vertical mode number at wavenumber k_j.

3.4 Exploring the Pseudo-Energy Spectrum

Armed with the energy decomposition techniques described above, simulation data can be effectively interpreted. However, a cursory glance at the energy spectrum for basic simulations of forced waves suggests some peculiarities that are worth exploring. In this section, the shape of the energy spectrum is explained. In addition, some difficulties in the energy decomposition of modulated long waves are considered.

3.4.1 Holes in the Energy Spectrum

Figure 3.1 depicts the mode 1 pseudo-energy decomposition for a simple forced wave simulation at $t = 10$ and $t = 50$ seconds. The data was generated using the SPINS model, and comes from test L1 described in Section 4.1. The experiment involves forcing a mode

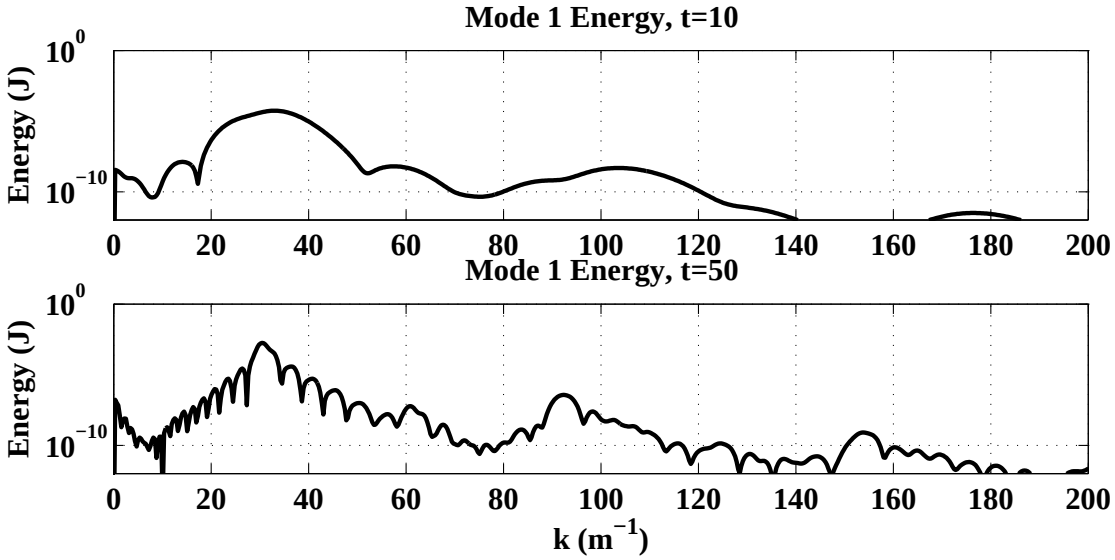

Figure 3.1: An example of holes in the mode 1 pseudo-energy spectrum at $t = 10$ seconds (top subplot) and $t = 50$ seconds (bottom subplot). Initially only a few cusps are visible but even by $t = 50$ s, a substantial number of kinks are visible in the pseudo-energy curve. This plot depicts data from test L1, described in Section 4.1.

1 wave at $k = 30.9$ m^{-1} with period 2.8 seconds. Note the expected peak at the forced wavenumber. At both values of t, the pseudo-energy spectrum appears to have sharp trough-like cusps where the energy spikes downwards at select wavenumbers. The lower subplot, corresponding to $t = 50$, has a much more complicated spectrum, and is riddled with pseudo-energy spikes. Although Figure 3.1 only depicts the pseudo-energy for mode 1, similar results are visible in plots of the pseudo-energy for higher mode numbers.

When viewed as an animation, the troughs traverse the figure. The troughs appear from both the left and right sides of the spectrum, and migrate towards the forced wavenumber. As they approach the forced wavenumber some of the troughs appear to slow down and accumulate. This accumulation is evident in the bottom subplot of Figure 3.1, where the spacing between troughs is significantly decreased. Even after very long simulation times new troughs are visible modifying the spectrum. These curious results are not limited to nonlinear simulations. Consider Figure 3.2, which depicts the kinetic and available potential energy contributions found with the linear Matlab solver. Although the variables are dimensionless, the simulation was performed using the same stratification and forcing frequency as the test L1. Both curves exhibit the trough structure seen in the nonlinear simulation.

The key hypothesis for understanding the spectrum shape is that, if the KE and APE

decompositions were performed over a continuum of wavenumbers, the spectrum troughs would actually be zeros. If this is the case, then the troughs in the pseudo-energy spectrum are simply the locations where the zeros of the KE and APE are approximately aligned.

To test this idea, consider the expression for the pseudo-energy in the mode-n component at wavenumber k_m given in equation (3.31). This expression is valid in the limit as wave amplitudes approach zero. For the mode-n pseudo-energy to be zero at a given wavenumber it is necessary that $\hat{a}_{m,n} = \hat{b}_{m,n} = 0$. This requires

$$\cos(\omega_F t + \vartheta) - \cos(\vartheta)\cos(\omega_{mn} t) + \sin(\vartheta)\frac{\omega_F}{\omega_{mn}}\sin(\omega_{mn} t) = 0, \tag{3.36}$$

and

$$\frac{\sin(\omega_F t + \vartheta)}{\omega_F} - \frac{\cos(\vartheta)}{\omega_{m,n}}\sin(\omega_{m,n} t) + \frac{\omega_F}{\omega_{m,n}^2}\sin(\vartheta) - \frac{\omega_F}{\omega_{m,n}^2}\sin(\vartheta)\cos(\omega_{m,n} t) = 0. \tag{3.37}$$

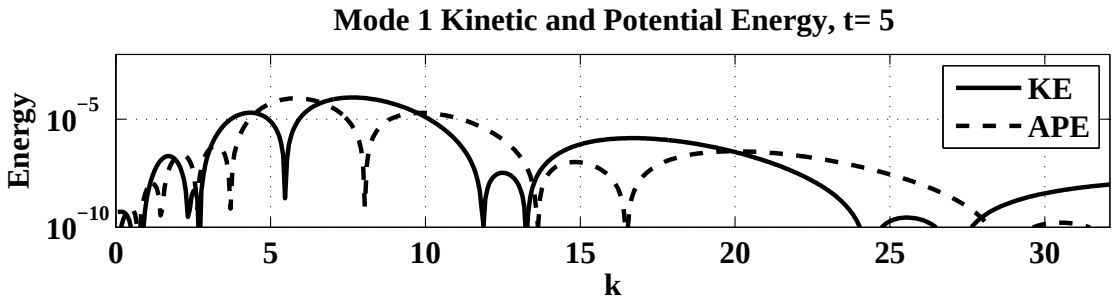

Figure 3.2: The mode 1 KE (solid line) and APE (dashed line) spectrum. This simulation was conducted with the linear Matlab solver. All variables are dimensionless. Note the energy troughs in the two curves do not line up perfectly.

To simplify the analysis, suppose $\vartheta = 0$, the results for general ϑ are more complicated algebraically. Now consider t to be a fixed value, and observe that the kinetic energy contribution is zero at frequencies $\tilde{\omega}_{m,n}$ satisfying

$$\tilde{\omega}_{m,n} = -\omega_F + \frac{2\pi j}{t}, \quad \text{or} \quad \tilde{\omega}_{m,n} = \omega_F + \frac{2\pi j}{t}, \tag{3.38}$$

where $j = 0, \pm 1, \pm 2, \pm 3, \ldots$. These conditions hold at wavenumbers $\tilde{k}^{\pm}$ defined by

$$\tilde{k}^{+} = \sigma_n^{-1}\left(\omega_F + \frac{2\pi j}{t}\right), \quad \text{and} \quad \tilde{k}^{-} = \sigma_n^{-1}\left(-\omega_F + \frac{2\pi j}{t}\right). \tag{3.39}$$

These zeros, or holes, in the KE traverse the spectrum as time increases. In fact, simple calculation shows that a zero at the wavenumber k^* travels with velocity

$$v = -\frac{2\pi j}{t^2 v_n(k^*)} \tag{3.40}$$

where $v_n(k^*)$ is the mode-n group velocity. The speed of propagation of the zeros through the spectrum decreases quickly with time and location. In addition, the holes defined by $\tilde{k}^+$ always lie to the right of the forced wavenumber. The holes defined by $\tilde{k}^-$ when $j > 0$ do pass through the forced wavenumber and also cross $k = 0$. In Figure 3.3 the predicted holes in the KE spectrum are marked. All of the troughs are accounted for, with vertical dashed lines denoting holes of the form $\tilde{k}^+$ and vertical dotted lines indicating the wavenumbers $\tilde{k}^-$.

Next, consider the APE. At fixed t, the energy is zero at the roots of the transcendental equation

$$\omega \sin(\omega_F t) = \omega_F \sin(\omega t). \tag{3.41}$$

This equation must be solved numerically for ω, and then the dispersion relation must be inverted to find the corresponding wavenumbers. Provided that $\omega_F > 1/t$ this equation always has at least one root and as t increases so does the number of roots. For each root of this equation, the corresponding discrete value $\omega_{m,n}$ closest to ω will lead to a wavenumber at which the APE is very small.

As time increases, the number of zeros (or near misses) in the KE and APE spectrum must also increase, and their spacing decreases. The pseudo-energy is just the sum of KE and APE, so as the holes in the two spectrums become more frequent the likelihood of them overlapping also increases. It is the overlap of holes in the KE and APE spectrum that leads to the troughs visible in the pseudo-energy spectrum. In Figure 3.4 the predicted positions for holes in the pseudo-energy are marked with vertical lines. Holes in the pseudo-energy are predicted by simply averaging the locations of nearby KE and APE holes.

The analysis for the problem with multiple forcing frequencies becomes substantially more complicated. Transcendental equations for both the KE and APE spectrum zeros will become increasingly difficult to solve as the number of forcing frequencies increases. In light of this, it is only possible to apply this analysis heuristically for analyzing the spectrums of nonlinear simulations. Nonlinear terms act as sources, and the spread of energy across the spectrum means a vast number of forcing terms are present. The simple analysis presented here can only help predict the early onset of zeros in the energy spectrum for nonlinear simulations. Even without precise predictive power for the nonlinear case the analysis does explain why these features are present.

For both linear and nonlinear simulations the zeros in the energy spectrum can cause confusion. At certain times the zeros may pass through the forcing wavenumber which can

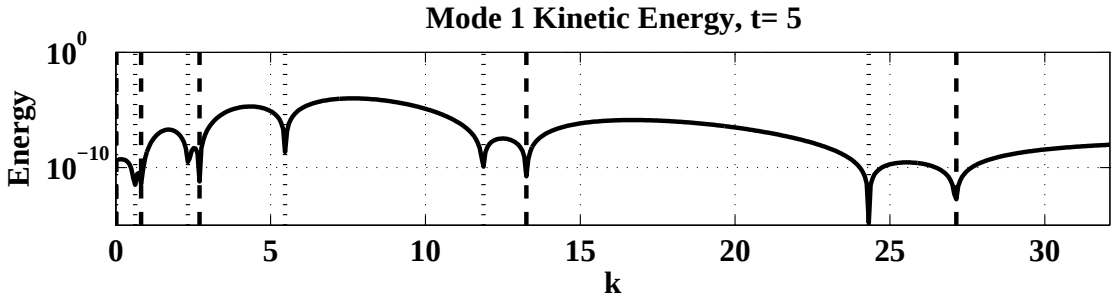

Figure 3.3: The mode 1 kinetic energy spectrum, computed with the linear Matlab solver. Vertical dashed lines mark the expected positions $\tilde{k}^{+}$, vertical dotted lines mark the positions of the expected zeros at $\tilde{k}^{-}$. All variables are dimensionless.

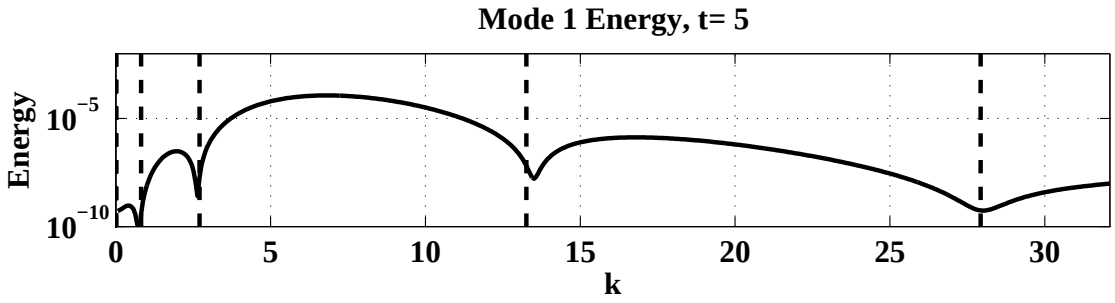

Figure 3.4: The mode 1 pseudo-energy spectrum from the linear Matlab solver. Vertical dashed lines mark the positions of expected zeros in the spectrum. Predictions are made by averaging the locations of adjacent holes in the KE and APE spectrums when both have similar zeros. Wavenumber, energy, and time are dimensionless.

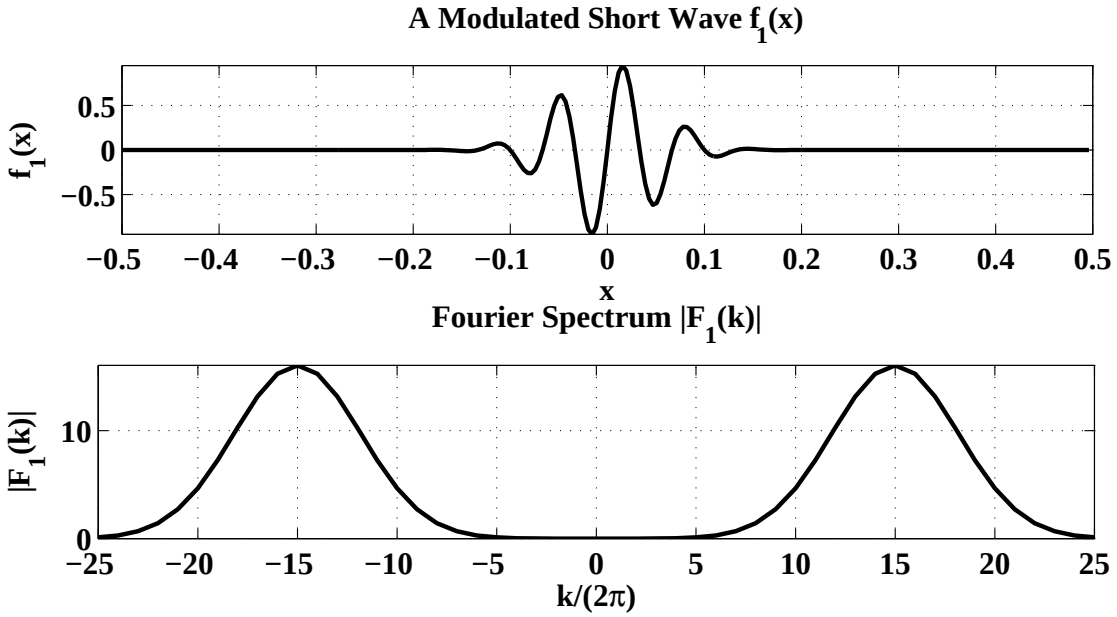

Figure 3.5: The modulated short wave. In the top subplot several wavelengths are visible within the wave packet. The absolute value of the Fourier coefficients, plotted in the bottom subplot, contains two peaks at the expected wavenumbers $k/(2\pi) = \pm 15$.

give the misleading impression that there is little or no energy in the forced wave. This problem can be avoided by time-averaging the spectrum. The problem with the averaging approach is that it may hide the presence of short-lived features of short duration. For resonant interactions this could be particularly damaging as the source of an energy peak may be averaged out.

3.4.2 Long Wave Energy Problems

Determining the energy content of long waves, whether forced directly, or generated through other processes, can be a subtle problem. When the wave in question is modulated by an envelope of relatively short width, Fourier decompositions are complicated because the energy peaks may lie at unexpected wavenumbers. This idea is explained through a simple analysis. The analysis used here involves Gaussian envelope functions. Numerically generated waves are modulated by a variety of envelope shapes, but the Gaussian is a useful analytical tool that captures many of the properties of other modulating functions.

On the infinite domain, consider the wave $s(x) = \cos(mx + \phi)$ on the domain $-\infty < x < \infty$. Suppose that the wave is localized to some region near $x = 0$ by modulation

with the Gaussian envelope $g(x) = \exp(-Dx^2)$. The long wave, limited by the envelope, is expressed as the signal $f(x) = s(x)g(x)$. The size of D determines the extent of the region where $f(x)$ attains significant values. The Fourier transform of $f(x)$ is given by $F(k) = \int_{-\infty}^{\infty} f(x)\exp(-ikx)\,dx$ (this is explained in detail in Chapter 5). Using similar notation for the transforms of $s(x)$ and $g(x)$, it follows that:

$$\begin{aligned} S(k) &= 2\pi\left[\exp(-i\phi)\delta(k+m) + \exp(i\phi)\delta(k-m)\right], \\ G(k) &= \sqrt{\tfrac{\pi}{D}}\exp\left(-\tfrac{k^2}{4D}\right), \\ F(k) &= 2\pi\sqrt{\tfrac{\pi}{D}}\left[\exp(i\phi)\exp\left(-\tfrac{(k-m)^2}{4D}\right) + \exp(-i\phi)\exp\left(-\tfrac{(k+m)^2}{4D}\right)\right]. \end{aligned} \tag{3.42}$$

Computing $S(k)$ involves the convolution theorem (see Haberman [30, Chapter 10]).

For a spatially uniform wave ($D \to 0$), all the wave energy lies at $k = \pm m$. For finite D, the energy peaks are shifted and depend on D and ϕ. The reason for the shift in energy peaks is because the two Gaussians composing $S(k)$ overlap when D is large and positive. Depending on the value of ϕ, these could shift the peaks towards $k = 0$ or away from it.

These simple arguments are now used to explain the numerical results on a periodic domain. Consider the domain $-1/2 \leq x \leq 1/2$. Periodic waves of the form described above exist provided $m = 2\pi n$ for integer values of n. The longest wave supported on the domain is that corresponding to $n = 1$, with wavelength $\lambda = 1$. Continuous Fourier transforms are replaced by their discrete analogues, and the decompositions still lead to shifted peaks.

As a concrete example, consider the modulated short wave $f_1(x)$ and modulated long wave $f_2(x)$ defined by:

$$f_1(x) = \cos(30\pi x + \pi/2)\exp(-20x^2),\;\; f_2(x) = \cos(2\pi x + \pi/2)\exp(-20x^2). \tag{3.43}$$

The modulated short wave is depicted in the top subplot of Figure 3.5. The modulated long wave is plotted in the top subplot of Figure 3.6. In the bottom subplot of each figure the power spectrum is plotted against $k/2\pi$. The spectrum for the short wave has two distinct peaks located at $k = 30\pi$. The peaks for the long wave, on the other had, do not coincide with $k = \pm 2\pi$. Instead, they are shifted to $k = 6\pi$. Had the phase ϕ in the underlying signal been set to zero, the long wave spectrum would have a single peak centered at $k = 0$.

In numerical simulations the phase ϕ of a generated wave is unknown. This means the presence of the modulated envelope could shift the energy peaks in either direction along the k-axis. It is therefore impossible to determine exactly where the long wave energy lies. To avoid these problems, D should be sufficiently small that $\exp(-m^2/4D)$ is negligible. It is not possible to simply set D, however, as it is the width measure of the wave packet in a simulation. Instead, this analysis suggests that simulations must be run for significant

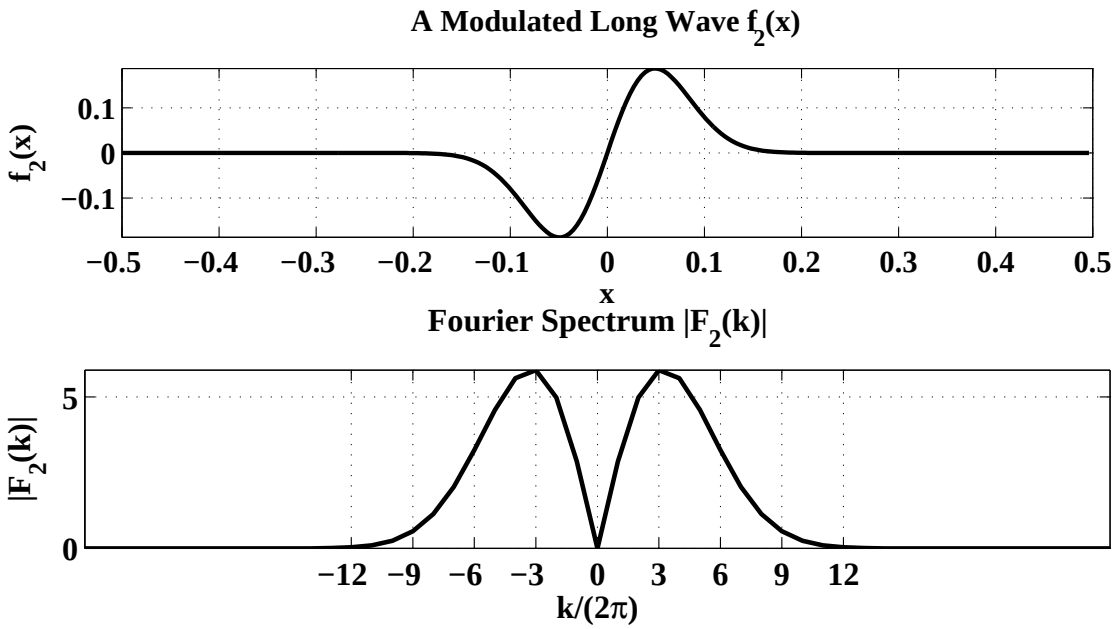

Figure 3.6: The modulated long wave. The wavelength is comparable to the envelope width, as evident in the top subplot. In the bottom subplot the absolute value of the Fourier coefficients are plotted against $k/2\pi$. The two visible peaks lie at $k/(2\pi) = \pm 3$ instead of $k/(2\pi) = \pm 1$.

amounts of time for the long wave energy decomposition to be trustworthy. For simulations where the wave packet is of short extent the long wave energy decomposition is skewed, and while the presence of long waves are assured it is not possible to determine their exact wavenumber.

3.5 Numerical Forcing Theory

Initial attempts at numerically forcing waves led to some unexpected results. While energy decompositions of the data did show a peak at the expected location, it was often found that waves of different wavenumber and vertical mode number had significant energy levels, in some cases even exceeding those of the forced wave. The reasons for this are connected with the eigenvalue problem (2.10), and can be explained through linear analysis, as shown below.

3.5.1 Forcing the Vertical Momentum Equation

Forcing the vertical momentum equation is a natural choice for generating internal gravity waves. The reasons for this are twofold. First, forcing the vertical momentum equation mimics the effects of a vertically oscillating paddle in a fluid. Second, for linear waves the vertical velocity w of an internal wave depends on the eigenfunction solution of (2.10), not its derivative. This provides some guidance as to how to choose the shape of the vertical forcing function. There are, of course, alternatives to forcing the vertical momentum equation. For instance, Fringer and Street [26] force the horizontal momentum equation with a function that follows the wave. Their forcing approach was used to induce wave-breaking, whereas the intent here is to generate clean waves of moderate amplitudes.

The basic strategy here is to force the vertical momentum equation with a spatially localized signal that varies sinusoidally in time at a desired frequency ω_F. Intuitively, this should preferentially produce waves at the forcing frequency and corresponding wavenumbers. If the horizontal and vertical forcing shape are chosen appropriately, it should be possible to generate a clean wave field dominated by waves of the desired frequency and wavenumber. The issue is then reduced to choosing a forcing shape that generates the desired wave.

Following these ideas, forcing functions of the form

$$F_2(x,z,t) = A_0 \sin(\omega_F t + \vartheta)\phi(x)h(z) \tag{3.44}$$

are studied. The subscript on F reflects the fact that the vertical momentum equation is forced. With reference to Section 3.2.1, the equivalent linear forcing in the vorticity

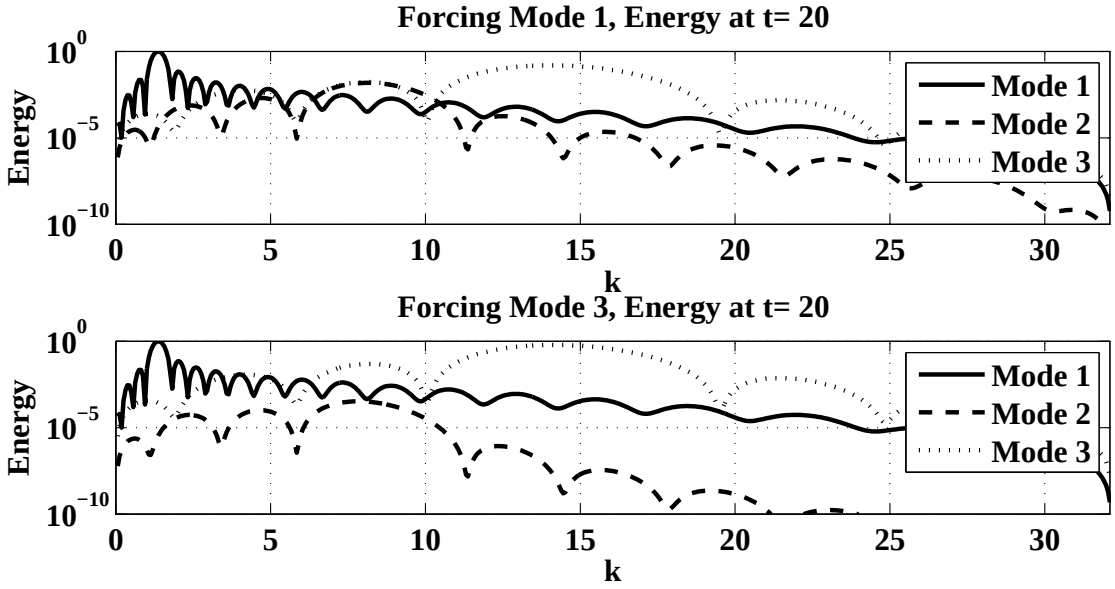

Figure 3.7: An example of bad forcing results from two linear simulations. For both simulations the forcing frequency $\omega = 2\pi/8$ is used. In the top subplot, the mode-1 wave at $k \approx 1.4$ is forced, but significant energy resides in the mode-3 spectrum near $k \approx 14.6$. In the bottom subplot, the mode-3 wave at $k \approx 14.6$ is forced, but the mode-1 wave near $k \approx 1.4$ has slightly more energy.

equation takes the form

$$\frac{\partial^2}{\partial x \partial t} F_2(x, z, t) = A \cos(\omega_F t + \vartheta) f(x) h(z), \tag{3.45}$$

where $A = \omega_F A_0$ and $f(x) = \phi'(x)$.

The natural first guess for the horizontal forcing shape is to choose $\phi(x)$ to be some localized function such as a Gaussian or sech profile. This is reasonable because it imitates the action of a paddle of finite dimension. Choosing the appropriate vertical forcing shape $h(z)$ is a more subtle issue. A natural first guess is to set $h(z) = g_n(z, k_F)$, where n is the vertical mode number and $k_F = \sigma_n^{-1}(\omega_F)$ is the desired wavenumber.

Early experiments with this horizontal and vertical forcing shape revealed a woeful inadequacy. In particular, when forcing a mode one wave, the pseudo-energy observed in other odd-numbered modes was undesirably large. Similar results were found for even-numbered modes. In certain cases, it was even found that the peak energy in the system did not always reside with the forced mode. To demonstrate this flaw, consider the forcing shapes

$$f(x) = -\frac{1}{D} \operatorname{sech}\left(\frac{x}{D}\right) \tanh\left(\frac{x}{D}\right), \quad \text{and} \quad h(z) = g_n(z, k_F), \tag{3.46}$$

used with the linear solver on the stratification defined for the lab-scale experiments of Chapter 4. The horizontal shape is derived from $\phi(x) = \text{sech}(x/D)$. In Figure 3.7 the pseudo-energy decomposition from two simple experiments is depicted. In both experiments the dimensionless frequency $\omega_F = 2\pi/8$ was used. In the top subplot, forcing with $h(z) = g_1(z, k_F)$ was intended to primarily excite mode-1 waves at $k_F \approx 1.4$. The mode-3 energy at $k \approx 14.6$ is comparable, however. In the bottom subplot, $h(z) = g_3(z, k_F)$ was used in an attempt to generate mode-3 waves at $k_F \approx 14.6$. The mode-1 energy peak at $k \approx 1.4$ is actually larger than the intended mode-3 peak. In both cases an undesired amount of energy was pumped into waves of the forcing frequency but at the wrong vertical mode. This is explained through the linear analysis below.

3.5.2 Analysis on a Periodic Domain

A simple linear analysis explains the poor results illustrated above and suggests the necessary fix. Consider the dimensionless streamfunction formulation of the Boussinesq equations (2.6a). Eliminating nonlinear terms and including the forcing term F_2 in the vertical momentum equation yields the linear equation

$$\frac{\partial^2}{\partial t^2}\nabla^2\psi + N^2(z)\psi_{xx} = \frac{\partial^2}{\partial x \partial t}F_2(x, z, t). \tag{3.47}$$

The domain is bounded by $0 \leq z \leq 1$, with boundary conditions $\psi(x, 0, t) = \psi(x, 1, t) = 0$. The streamfunction is periodic in the x direction on a domain of length L. The initial conditions are $\psi(x, z, 0) = \psi_t(x, z, 0) = 0$. From the discussion above, the right-hand side becomes

$$\frac{\partial^2}{\partial x \partial t}F_2(x, z, t) = A\cos(\omega_F t + \vartheta)f(x)h(z), \tag{3.48}$$

with $f(x) = \phi'(x)$ and $A = \omega_F A_0$.

Separation of variables provides the necessary insight into how to choose $F_2(x, z, t)$. First, consider $F_2 = 0$, and let $\psi = X(x)Z(z)T(t)$. Minor manipulation reveals that

$$-\frac{T''Z''}{T''Z + TN^2(z)Z} = \frac{X''}{X} = -k_m^2. \tag{3.49}$$

This implies $X(x)$ is a linear combination of $\exp(ik_m x)$ and $\exp(-ik_m x)$ where $k_m = 2\pi n/L$ so that the solution is periodic. Another manipulation reveals

$$\frac{k_m^2 N^2(z)Z}{Z'' - k_m^2 Z} = \frac{T''}{T} = -\omega_m^2, \tag{3.50}$$

where ω_m must be a real eigenvalue depending on k_m such that

$$Z'' + k_m^2\left(\frac{N^2(z)}{\omega_m^2} - 1\right)Z = 0, \tag{3.51}$$

and $Z(0) = 0 = Z(1)$. This is, of course, the Sturm-Liouville problem discussed at length in Chapter 2. At each k_m, a countably infinite set of solutions $\omega_{m,n} = \sigma_n(k_m)$ exist. For notational consistency, let $Z(z) = g_n(z, k_m)$ be the mode-n eigenfunction corresponding to the frequency $\omega_{m,n}$ and wavenumber k_m.

The separation of variables approach for the unforced problem extends naturally to the forced case. The key idea is to use an eigenfunction expansion of the form

$$\psi = \sum_{m=-\infty}^{\infty} \sum_{n=1}^{\infty} T_{m,n}(t) \exp(ik_m x) g_n(z, k_m). \tag{3.52}$$

Substituting this into the governing equation (3.47) and using the definition of $g_n(z, k_m)$ reveals

$$\begin{aligned} \sum_{m=-\infty}^{\infty} \sum_{n=1}^{\infty} \; & \tfrac{k_m^2}{\omega_{m,n}^2} (T''_{m,n} + \omega_{m,n}^2 T_{m,n}) \exp(ik_m x) N^2(z) g_n(z, k_m) \\ & = -A \cos(\omega_F t + \vartheta) f(x) h(z). \end{aligned} \tag{3.53}$$

The x-dependence is eliminated by integrating both sides against $\exp(-ik_m x)$ from $x = -L/2$ to $x = L/2$. The remaining z-dependence is removed by integrating both sides against the eigenfunction $g_n(z, k_m)$ and making use of the orthogonality condition (2.48). Next, suppose $f(x)$ decays rapidly to zero by the domain boundaries so that a periodic continuation $f(x) = \sum_{m=-\infty}^{\infty} f_m \exp(ik_m x)$ can be used, and define

$$h_{m,n} = \int_0^1 h(z) g_n(z, k_m) \, dz. \tag{3.54}$$

It follows that

$$T''_{m,n} + \omega_{m,n}^2 T_{m,n} = -A \frac{\omega_{m,n}^2}{k_m^2} f_m h_{m,n} \cos(\omega_F t + \vartheta), \tag{3.55}$$

with $T_{m,n}(0) = T'_{m,n}(0) = 0$. This equation describes the temporal evolution of the mode-n wave at wavenumber k_m, and some important observations can be made. First, note that waves at each wavenumber k_m and corresponding frequency $\omega_{m,n}$ experience some forcing effects provided $f_m \neq 0$ and $h_{m,n} \neq 0$. Second, any waves with frequencies $\omega_{m,n}$ close to ω_F will be forced in near-resonance.

In light of these simple observations, the goal of forcing a desired wave cleanly can be achieved. Suppose the desired wave has wavenumber k_F and vertical mode number n_F, so that $\omega_F = \sigma_{n_F}(k_F)$. The functions $f(x)$ and $h(z)$ should be chosen using the following guidelines:

1. The Fourier coefficients f_m should only be large at indices m where the corresponding k_m values are close to $\pm k_F$. Away from this range of indices the Fourier coefficients should be as small as possible.

2. The vertical shape $h(z)$ should be designed so that, for wavenumbers k_m near $\pm k_F$, h_{m,n_F} is large. For the same range of wavenumbers, $h_{m,n}$ should be small when $n \neq n_F$.

To satisfy the first condition, some knowledge of the continuous Fourier transform is helpful. Ideally, the function $f(x)$ has a spectrum that is narrow-banded about the wavenumber k_F. A useful starting point is $f(x) = \exp(-x^2/D)$. This is a Gaussian that depends on a width parameter D, and has Fourier transform $F(k) = \sqrt{\pi D}\exp(-k^2 D/4)$. Notably this is also a Gaussian in k with width measure inversely proportional to the width in physical space. The function $F(k)$ is centered about $k = 0$, but the peak can be shifted to $\pm k_F$ by using the modified function $\bar{f}(x) = \cos(k_F x)\exp(-x^2/D)$. To achieve a narrow spectrum about $k = k_F$, the parameter D must be relatively large. This is made more precise below.

To satisfy the second condition, the choice $h(z) = N^2(z)g_{n_F}(z, k_F)$ is appropriate. The orthogonality condition (2.48) ensures that near $k = k_F$ only the mode n_F wave is excited strongly. Since the orthogonality condition only holds exactly for eigenfunctions corresponding to the same wavenumber, some waves near k_F at undesired vertical mode numbers will always be excited. This cannot be avoided unless $N^2(z)$ is constant so that the eigenfunctions do not depend on the wavenumber.

With these considerations, numerical simulations are conducted with:

$$F_2(x, z, t) = A\sin(\omega_F t + \vartheta)\sin(k_F x)\mathrm{sech}\left(\frac{x}{D}\right)N^2(z)g_{n_F}(z, k_F). \tag{3.56}$$

The spatial oscillatory component $\sin(k_F x)$ could be replaced with $\cos(k_F x)$. The final issue is to determine an appropriate value for the width parameter D. The answer lies in equation (3.55). Clearly any wave of frequency $\omega_{m,n}$ near ω_F will be excited in near-resonance when f_m is non-zero. This is because $h_{m,n}$ will generally be non-zero due to the non-orthogonality of eigenfunctions at different wavenumbers. Suppose the wavenumber of the mode-n wave with frequency ω_F is denoted by $k_{F,n}$. The width D must be chosen so that the spectrum of $f(x)$ is extremely small at distances $|k_{F,n_F} - k_{F,n_F\pm 1}|$ away from $\pm k_{F,n}$. This ensures that for all the waves with frequency near ω_F, only the one one with vertical mode number n_F will be strongly excited.

To demonstrate the effects of using the appropriate forcing function, recall the example of Figure 3.7. The calculations were repeated using

$$f(x) = -\frac{1}{D}\sin(k_F x)\mathrm{sech}\left(\frac{x}{D}\right)\tanh\left(\frac{x}{D}\right) + k_F\cos(k_F x)\mathrm{sech}\left(\frac{x}{D}\right), \tag{3.57}$$

and $h(z) = N^2(z)g_n(z, k_F)$ for $n = 1, 3$. The results are shown in Figure 3.8. In the top subplot, the intended mode-1 wave at $k_F \approx 1.4$ is nearly five orders of magnitude larger

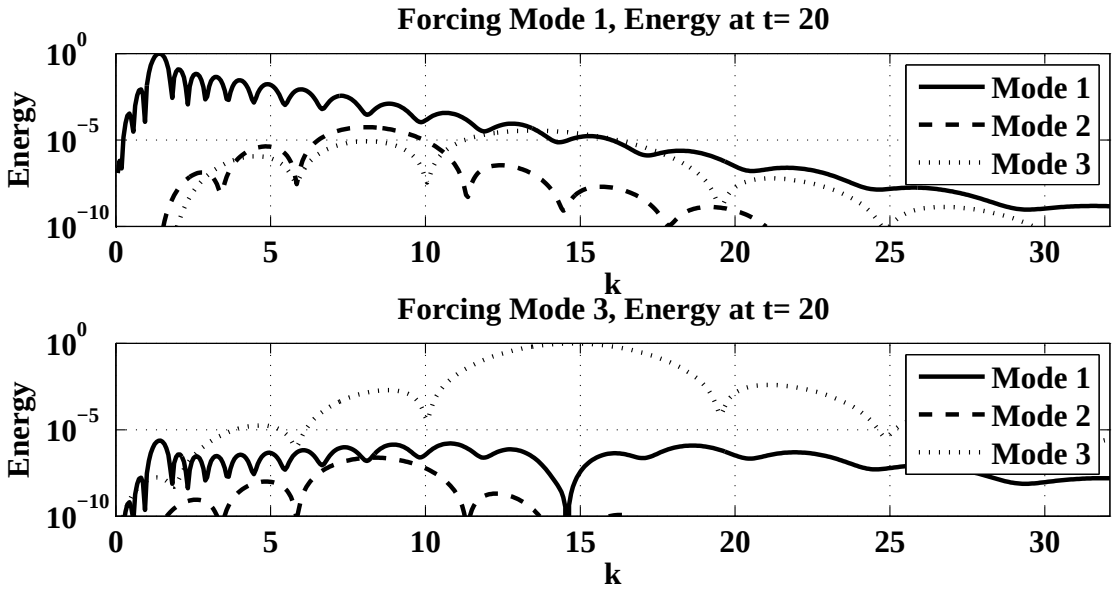

Figure 3.8: An example of improved forcing results. In both linear solver experiments the frequency $\omega_F = 2\pi/8$ was used. In the top subplot, the mode-1 wave at $k \approx 1.4$ is forced. In the bottom subplot, the mode-3 wave at $k \approx 14.6$ is forced. Contrast this with Figure 3.7.

than the peaks in the higher modes. Similarly, in the bottom subplot the intended peak in the mode-3 spectrum at $k_F \approx 14.6$ is dominant.

The structure of the forcing function for the vertical momentum equation (3.56) suggests that unidirectional waves can be generated with only minor modifications. This is seen from the simple trigonometric identity

$$\sin(\omega_F + \vartheta)\sin(k_F x) = \frac{\cos(k_F x - \omega_F t - \vartheta)}{2} - \frac{\cos(k_F x + \omega_F t + \vartheta)}{2}. \tag{3.58}$$

This is a sum of leftward and rightward-propagating waves (depending on the signs of k_F and ω_F). To generate unidirectional waves, then, the term $\sin(\omega_F + \vartheta)\sin(k_F x)$ in (3.56) can be replaced by $\cos(k_F x - \omega_F t - \vartheta)$. This is useful as it reduces the computational domain size needed to investigate a propagating wave. However, the theory is linear so it must be tested to evaluate its practicality for the fully nonlinear Boussinesq equations.

3.5.3 A Force Scaling Rule

The form of the forcing function (3.56) leads to a simple but useful scaling law for generating waves. The horizontal forcing dependence can be written in the general form $\phi(x) = \sin(k_F x)p(x/D)$, where $p(x/D) = \operatorname{sech}(x/D)$. More generally p could be any localized function, not necessarily centered at the origin, but the result is the same. For linear analysis, the forcing function $f(x) = \phi'(x)$ is used. The growth of the forced wave is dependent on the Fourier coefficient f_m, where

$$f_m = \int_{-L/2}^{L/2} \exp(-ik_m x)\phi'(x)\, dx. \tag{3.59}$$

Assume $p(x)$ is localized so that $|\phi(x)| \ll 1$ as $|x| \to L/2$. Integration by parts reveals that

$$\begin{aligned} f_m &= \exp(-ik_m x)\phi(x)\big|_{-L/2}^{L/2} + ik_m \textstyle\int_{-L/2}^{L/2} \exp(-ik_m x)\phi(x)\, dx, \\ &\approx ik_m \textstyle\int_{-L/2}^{L/2} \exp(-ik_m x)\phi(x)\, dx, \\ &\approx ik_m \textstyle\int_{-\infty}^{\infty} \exp(-ik_m x)\phi(x)\, dx. \end{aligned} \tag{3.60}$$

The final step of extending the integration bounds to $\pm\infty$ does not significantly affect the value of the integral because it is assumed that $|\phi(x)| \ll 1$ for $|x| > L/2$. The final integral in (3.60) is just $\Phi(k_m)$, the continuous Fourier transform of $\phi(x)$ evaluated at $k = k_m$ (see Section 5.1.1). Since $\phi(x) = \sin(k_F x)p(x/D)$ the convolution theorem can be applied to show that

$$\begin{aligned} \Phi(k) &= i\pi\left(\delta(k + k_f) - \delta(k - k_F)\right) \star \mathcal{F}\{p(x/D)\} \\ &= i\pi D\left[P(-Dk_F) - P(Dk_F)\right], \end{aligned} \tag{3.61}$$

where $P(k)$ is the Fourier transform of $p(x)$. This shows that the Fourier coefficient f_m with k_m closest to k_F is approximately proportional to D. Therefore, if two experiments are conducted with forcing widths D_1 and D_2, the forcing amplitudes A_1 and A_2 must be scaled so that

$$D_1 A_1 = D_2 A_2 \tag{3.62}$$

in order to generate waves of the same amplitude. This scaling rule is important for nonlinear simulations where the forcing width in Fourier space affects which nonlinear interactions can occur. The rule is verified for nonlinear simulations in Chapter 4.

Chapter 4

Numerical Simulations

In this chapter, numerical simulations of resonant triad interactions are presented. The simulations described here were performed using the SPINS model (see Section 3.2.2). There are two main objectives of these experiments. First, to observe fully nonlinear resonant wave interactions, and second, to test the validity of the linear forcing theory. Simulations involving laboratory scale parameters are presented in Section 4.1. A set of simulations with ocean-like parameters are described in Section 4.2. Some of the interesting features observed in the simulation data are explained in Section 4.3, and insights on the applicability of linear theory are given.

All of the simulations presented in this chapter were performed on a Mac Pro with two 2.8 GHz Intel Xeon Quad-core processors, and a total of 4 GB of RAM. Experiments were designed to illustrate interesting phenomena in relatively short run-time. Most experiments were performed on a grid consisting of 4096 points in the horizontal and 256 points in the vertical. The lab-scale experiments typically took less than 3 hours. The ocean-scale simulations were usually completed in less than 6 hours, with the collision experiments lasting roughly 18 hours.

4.1 Lab-Scale Simulations

In this section simulations involving lab-scale parameters are presented. The intention is that, if so inclined, an experimentalist could repeat these experiments in a tank of reasonable length using a stratification of fresh and salty water. For the experiments conducted here, the tank is taken to be 20 cm deep, and 10, 20, or 40 meters long. These values are feasible in light of existing lab equipment used by Martin et al. [49] or Troy and Koseff [68].

For the lab-scale experiments, the background density stratification:

$$\rho_0(z) = \rho_0 - \frac{\Delta\rho}{2}\tanh\left(\frac{z - z_p}{L_p}\right) \tag{4.1}$$

is used. The reference density value is set to $\rho_0 = 1020$ kg/m^3, and the top-to-bottom density jump is fixed at $\Delta\rho = 40$ kg/m^3. The vertical coordinate lies in the interval $0 \leq z \leq 0.2$ m, and the pycnocline center is set at $z_p = 0.14$ m. The width parameter is taken to be $L_p = 4.72 \cdot 10^{-3}$ m so that 99% of the density jump occurs over a distance of 2.5 cm. This stratification models a thin density interface separating well-mixed layers of fresh and salty water, and is quite similar to the stratification used by Troy and Koseff [68].

The lab-scale experimental parameters are summarized in Table 4.1. In Figure 4.1 the density profile and buoyancy frequency are plotted. The pycnocline is identifiable as the transition zone in the density subplot and the region near the peak of $N^2(z)$ in the buoyancy subplot. The maximum value of the buoyancy frequency is $N(0.14) \approx 6.38$ s^{-1}, and at the boundaries $N(0.2) \approx 3.9 \cdot 10^{-5}$ s^{-1}, and $N(0) \approx 1.7 \cdot 10^{-12}$ s^{-1}.

Lab-scale Experimental Parameters

Parameter	Value
H	0.2 m
$\rho_0, \Delta\rho$	1020, 40 (kg/m^3)
z_p, L_p	0.14, 0.00472 (m)
$\max N(z)$	6.375 s^{-1}
N_x, N_z	4096, 256
U	0.13916 m/s

Table 4.1: Simulation parameters for the lab-scale experiments. Tank lengths are specified for each experiment. The number of horizontal and vertical grid points is specified by N_x and N_z. The velocity U is used for the dimensional analysis.

Preliminary calculations showed that a vast number of near-resonant interactions are possible for the chosen stratification. To illustrate some of the important concepts, two of these triads have been selected for demonstration purposes. To simplify the discussion that follows, the waves in triads A and B are referred to by their index in the table where they are defined. Triad A consists of two mode-1 waves interacting with a mode-2 wave, all propagating in the same direction. Waves A_2 and A_3 have wavelengths of about $3 - 4$ cm, which is comparable to the pycnocline width. Triad B also consists of two mode-1 waves and a mode-2 wave, but the long mode-1 wave (B_1) propagates in the opposite direction of B_2 and B_3. The wavelengths of all three waves in triad B are significantly longer than the

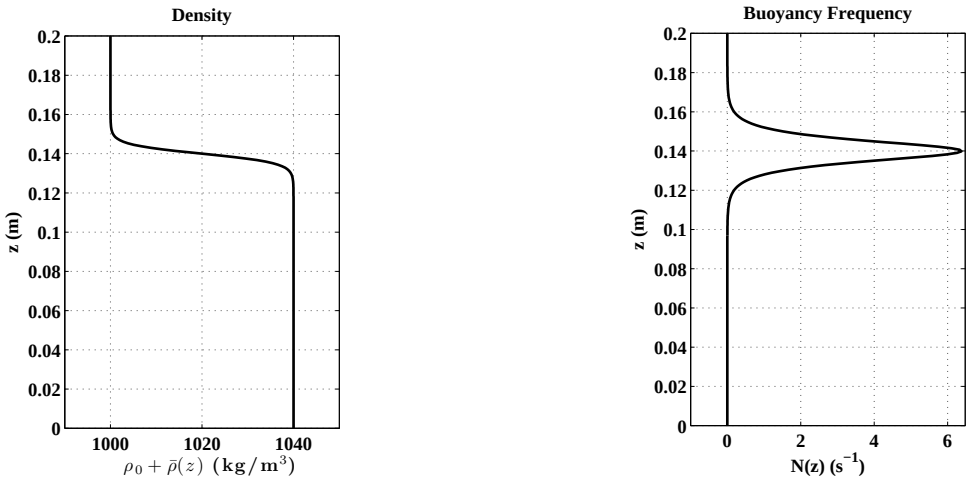

Figure 4.1: Background density (left subplot) and buoyancy frequency (right subplot) for the lab-scale simulations. The pycnocline is centered at $z = 0.14$ m, and has a 99% density jump width of 2.5 cm.

pycnocline width, and the longest wavelength is about three times as long as the depth of the fluid.

Important data for triad A is summarized in Table 4.2, and the data pertaining to triad B is summarized in Table 4.3. Data for triads A and B is plotted along with the dispersion relation in Figure 4.2. The differences in scales between the two triads is apparent in the figure. From Figure 4.2 and the data tables, it is clear that the wavelengths and periods could readily be generated in the laboratory.

Triad A

Wave	Mode	ω (s^{-1})	T (s)	k (m^{-1})	λ (cm)	v (cm/s)	γ
A_1	1	2.24	2.8	30.9	20.3	3.6	$-2.92 \cdot 10^3$
A_2	2	2.24	2.8	166.0	3.8	0.86	$-1.17 \cdot 10^2$
A_3	1	-4.42	1.42	-195.2	3.2	0.59	$5.83 \cdot 10^2$

$\delta_\omega = 7 \cdot 10^{-2}$ (s^{-1}) $\qquad$ $\delta_k = 1.7$ (m^{-1})

Table 4.2: Physical data for triad A. From left-to-right, the columns are as follows: wave name, vertical mode number, frequency, period, wavenumber, wavelength, group velocity, interaction coefficient. Error in the frequency resonance condition is given by δ_ω, and error in the wavenumber resonance condition is given by δ_k.

Experiments with triads A and B were conducted by forcing one or two of the waves in the triad using the approach described in Section 3.5. In particular, the vertical momentum

Triad B

Wave	Mode	ω (s^{-1})	T(s)	k (m^{-1})	λ (cm)	v (cm/s)	γ
B_1	1	1.05	6.0	9.47	66.4	9.0	126.3
B_2	1	-1.63	3.85	17.48	36.0	-5.9	-124.3
B_3	2	0.545	11.54	-28.22	22.3	-1.8	-39.2

$\delta_\omega = -4.2 \cdot 10^{-2}$ (s^{-1}) $\qquad$ $\delta_k = -1.3$ (m^{-1})

Table 4.3: Physical data for triad B. From left-to-right, the columns are as follows: wave name, vertical mode number, frequency, period, wavenumber, wavelength, group velocity, interaction coefficient. Error in the frequency resonance condition is given by δ_ω, and error in the wavenumber resonance condition is given by δ_k.

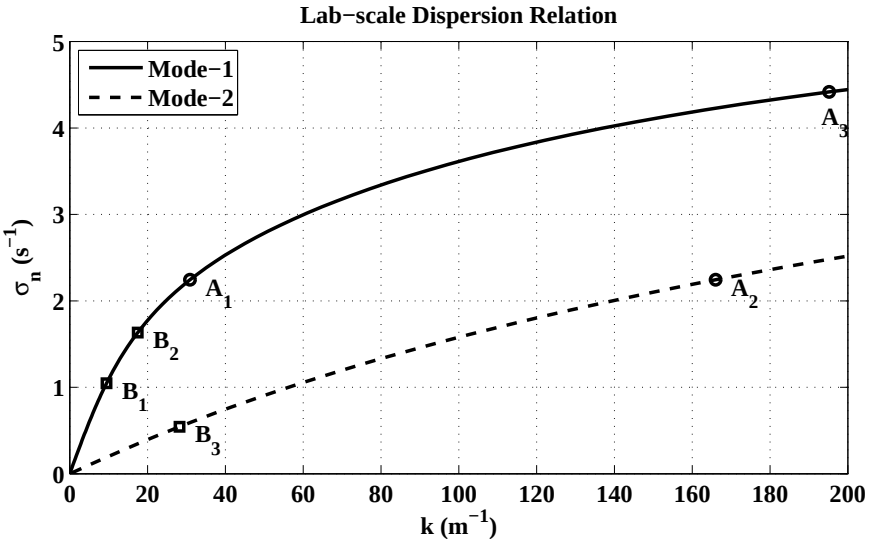

Figure 4.2: The dispersion relation for lab-scale experiments. Waves from triad A are marked with circles, waves from triad B are marked with squares.

equation is forced with a function of the form

$$F_2(x,z,t) = a_0 \text{sech}\left(\frac{x-x_0}{w_0}\right)\cos(kx)\cos(\omega t)N^2(z)\phi_n(z;k). \tag{4.2}$$

Here $\phi_n(z;k)$ is the dimensionless mode-n eigenfunction at wavenumber k, and $\omega = \sigma_n(k)$. The forcing amplitude, center, and width measure are given by a_0, x_0, and w_0, respectively. To generate multiple waves simultaneously, a superposition of these forcing functions is used, with forcing centers, amplitudes, and width regions defined as needed. Since $N^2(z)$ has dimensions of s^{-2}, the forcing amplitude a_0 has units of meters for dimensional consistency.

A range of experiments performed on triads A and B are now described. Some of the experiments were conducted simply to test the usefulness of the bidirectional forcing theory and width scaling rule. Other experiments give a detailed picture of how the resonant interactions unfold.

4.1.1 Preliminary Tests

A large number of preliminary tests were conducted to study the basic dynamics of internal waves. As an initial study, consider the problem of generating wave A_1 and A_2. It is prudent to check the force scaling rule of Section 3.5.3, and it is worth verifying that density contour diagrams, energy decompositions, and wave propagation speeds match expected results. Tests L1 – L4 are used as simple benchmark tests for this purpose, and each test uses a tank of length 20 m. The necessary parameters are found in Table 4.4.

Tests L1 – L3 consist of forcing wave A_1 at different forcing amplitudes and widths, chosen so that $w_0 a_0$ remains constant. From the theory of Section 3.5.3, each test should produce a wave train of the same amplitude and wavenumber. In Figure 4.3, the density contours are plotted for test L1 at $t = 60$ s. With a group velocity of roughly 3.6 cm/s, the wavefront is expected to have traveled slightly less than 2.2 m. This is in visual agreement with the plot, when leading transients and the non-compact forcing shape are accounted for. The plotted contours appear to be smooth, suggesting very little short-wave noise is present. The peak-to-trough isopycnal displacements in the main body of the wave train are about 1.1 cm. The magnitude of the maximum induced velocity in the flow is about 1.4 cm/s. As shown in the final column of Table 4.1), the ratio of maximum induced velocity to phase speed of the underlying wave satisfies $\max(\mathbf{u})/c \leq 0.23$ for each of tests L1 – L3. These relatively small steepness measures suggest the waves are within the linear regime.

As a test of the force scaling rule of Section 3.5.3, the pseudo-energy decomposition for tests L1 – L3 is shown in Figure 4.4. The pseudo-energy depicted in the plot was found by averaging over 20 data sets in the time interval $50.5 \leq t \leq 60$ s. From the mode-1 energy

Lab-scale Preliminary Experiments

Test	Wave	a_0 (m)	w_0 (m)	max(**u**)/c
L1	A_1	0.5	0.1	0.20
L2	A_1	0.25	0.2	0.19
L3	A_1	1.0	0.05	0.23
L4	A_2	0.01	0.1	0.24

Table 4.4: Data for the preliminary lab-scale experiments. Each experiment involves forcing the single specified wave. The forcing amplitude and forcing width are defined in the third and fourth column. For each of these tests a tank length of 20 m was used, and 4096 horizontal and 256 vertical grid points were used.

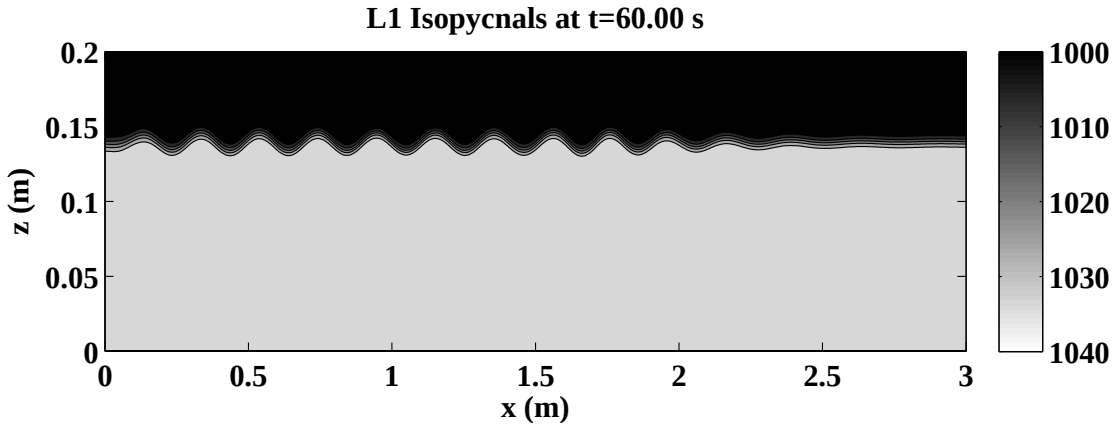

Figure 4.3: Density contours for test L1 at $t = 60$ s. It is expected that the waves reach a distance of $v \cdot t \approx 2.16$ m. The forcing function is not compact in x and there are transients to consider, but the predicted result is consistent with the plot. The peak-to-trough isopycnal displacements in the main body of the wavetrain are about 1.1 cm.

decomposition (top subplot), the peak for each test is seen to lie at the expected forced wavenumber of $k = 30.9$ m^{-1}. The amplitudes of the energy peaks at that wavenumber are in agreement to several digits, supporting the result in Section 3.5.3. The expected result that increasing the forcing width in physical space decreases the width of the spectrum about the forced peak is also apparent.

In the mode-2 pseudo-energy decomposition (bottom subplot) certain features are common to all three tests. For each test, a large peak in the mode-2 spectrum lies near $k = 62$ m^{-1}. This is double the forced wavenumber and hence this is likely the result of a self-interaction of the forced mode-1 wave. For the lab-scale stratification $\sigma_2(61.8) \approx 1.05$ s^{-1} is far from the required value of 4.48 s^{-1} needed for resonance, so the self-interaction is not resonant. The largest peak in the mode-2 spectrum for each of tests L1 – L3 lies at $k \approx 0.31$ m^{-1}. A possible explanation for this is a form of resonant interaction that is classified as the induced diffusion mechanism (see Müller et al. [51]). This mechanism involves two waves of similar frequency and wavenumber interacting to produce a third wave of much smaller frequency and wavenumber. Calculations revealed that resonant interactions for waves near the forced mode-1 peak are possible. However, the different forcing widths used in L1 – L3 ensure that if induced diffusion were responsible for the buildup of low wavenumber mode-2 energy, then the peaks at $k \approx 0.31$ m^{-1} would have different amplitudes. In fact, these long-wave mode-2 peaks have the same amplitude to several digits of agreement, thus ruling out induced diffusion interactions as the source. A more likely cause for this energy peak is discussed in Section 4.3.

To further study the energy contributions, the kinetic and linear available potential energy decompositions in mode-1 and mode-2 are plotted for test L1 in Figure 4.5. The plotted signals are again averaged over 20 data sets spaced evenly in the interval $50.5 \leq t \leq 60$ s. The magnitudes of the energy components are rather small, but this is expected because the maximum induced speed in the fluid is roughly 1.4 cm/s, and the fast-moving fluid only occupies a small portion of the domain. The kinetic and available potential energy curves in the figure, marked by solid and dashed lines respectively, closely follow each other in shape. In the mode-1 decomposition the two components of energy are almost indistinguishable for moderate wavenumbers. A peak is clearly visible in both curves at the expected wavenumber $k = 30.9$ m^{-1}.

Test L4 is similar to test L1, except wave A_2 (a mode-2 wave) is forced. The group velocity of the forced wave is 0.86 cm/s, so after 60 seconds the wave is expected to have traveled slightly more than 50 cm. This is visible in Figure 4.6, where the density contours appear smooth and have the expected wavelength of 3.8 cm. The waves are clearly mode-2, as troughs in the lower half of the pycnocline align with crests in the upper half. The waves are very small in amplitude, with peak-to-trough isopycnal displacements of about 1 mm. The aspect ratio of the plot should be emphasized: the wavelength of the forced wave is actually less than twice the width of the pycnocline. Only a small wave is illustrated here,

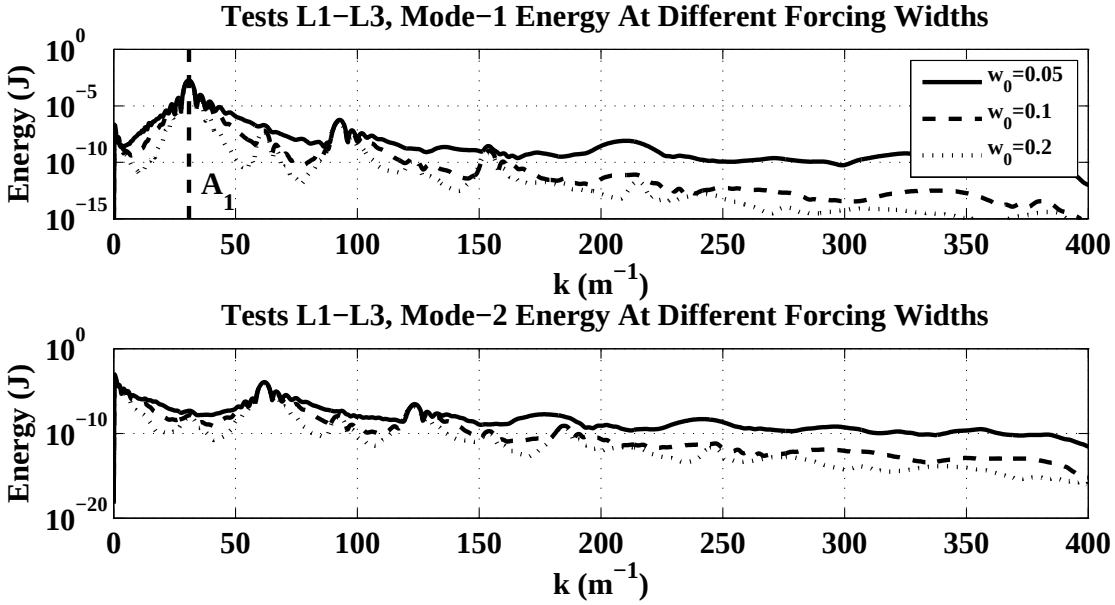

Figure 4.4: The mode-1 and mode-2 pseudo-energy decomposition for tests L1 – L3. Data is averaged over twenty data sets in the interval $50.5 \leq t \leq 60$ s. The solid line corresponds to a forcing width of 0.05 m (test L3), the dashed line involves a forcing width of $w = 0.1$ m (test L1), and the dashed line corresponds to a forcing width of $w = 0.2$ m (test L2). Note the narrower forcing width creates a broader mode-1 spectrum, but all three tests have the same peak amplitude at the expected wavenumber $k = 30.9$ m^{-1}. There is also a buildup of energy in the low-wavenumber range of mode-2 for each test. Wave A_1 is marked with the vertical dashed line.

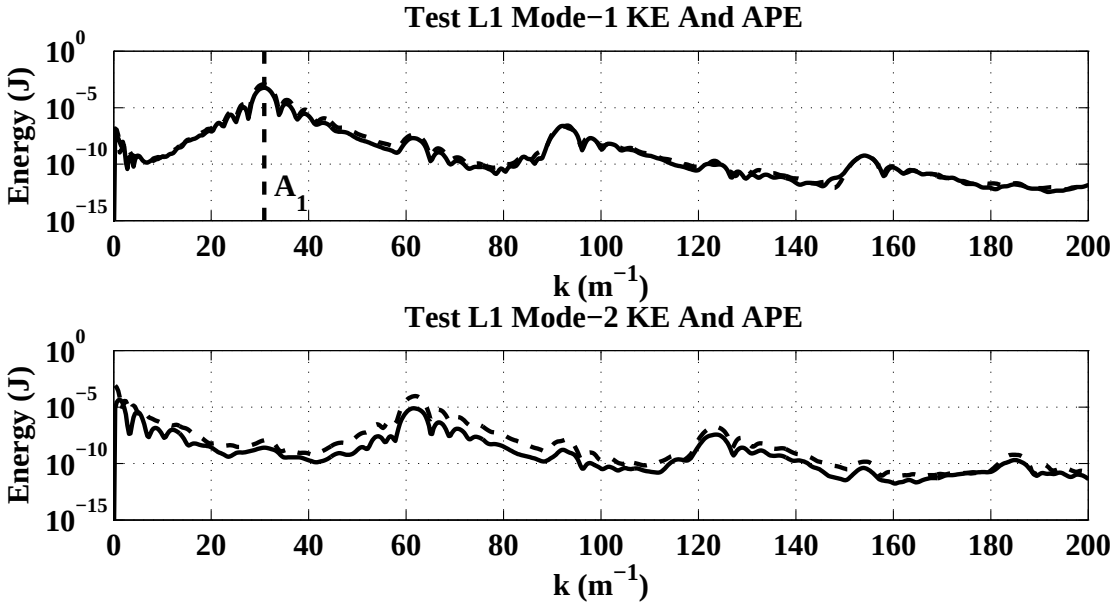

Figure 4.5: The mode-1 and mode-2 kinetic energy (solid lines) and linear available potential energy (dashed lines) for test L1. Data is averaged over twenty data sets in the interval $50.5 \leq t \leq 60$ s. Only minor differences exist in the mode-1 spectrum. More significant differences are visible in the mode-2 spectrum but the curves follow each other qualitatively. The vertical dashed line in the top subplot indicates the location of wave A_1.

and a discussion of some of the difficulties involved in forcing larger-amplitude mode-2 waves is given in Section 4.3.

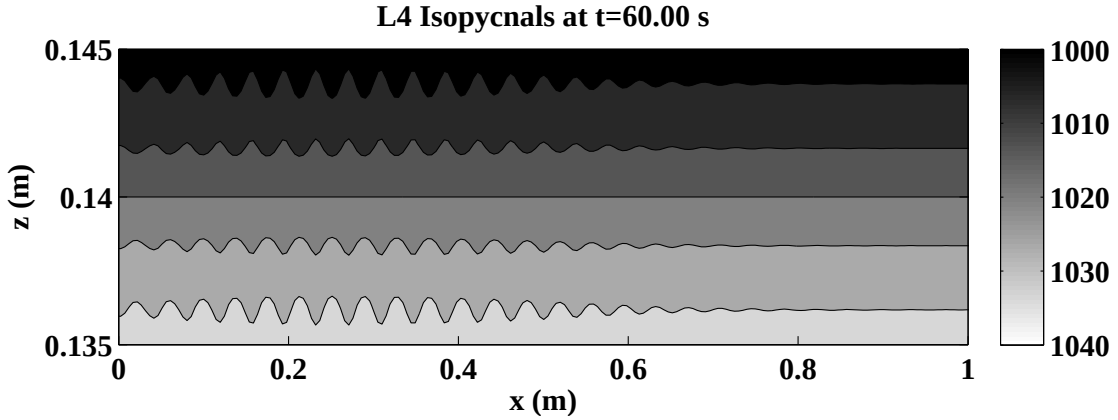

Figure 4.6: Density contours for experiment L4. The expected mode-2 wave appears to be a clean sinusoid, but is small, with peak-to-trough isopycnal displacements of about 1 mm. The expected wavelength of 3.8 cm matches the picture.

The mode-2 pseudo-energy decomposition for experiment L4 is shown in Figure 4.7. The dominant peak lies at $k \approx 166$ m^{-1}, the expected forced wavenumber for A_2. A secondary peak is also visible at twice this value, due to a non-resonant self-interaction of the forced wave, and there is a buildup of energy at low wavenumbers as well. Comparing orders of magnitude, however, shows that the forced wave is by far the dominant signal in the system.

4.1.2 Wave Collison Experiments

In this subsection experiments are presented for triad A and B to demonstrate how a resonant interaction unfolds as wave trains pass through each other. The experiments are facilitated by the differences in group velocities of the underlying waves, allowing collisions to take place in reasonable computational time. For these experiments, two of the waves in a triad were forced at different locations for specified time intervals. The forcing width used for each wave is 0.1 m. The precise details are provided in Table 4.5. The second from last column of the table indicates the start and stop time for the forcing of each wave.

Test L5. Experiment L5 involves a train of wave A_1 (a mode-1 wave) passing through a train of A_2 (a mode-2 wave). To achieve this, a small packet of wave A_2 is forced for 30 seconds and allowed to propagate away from the forcing region. After 50 seconds without

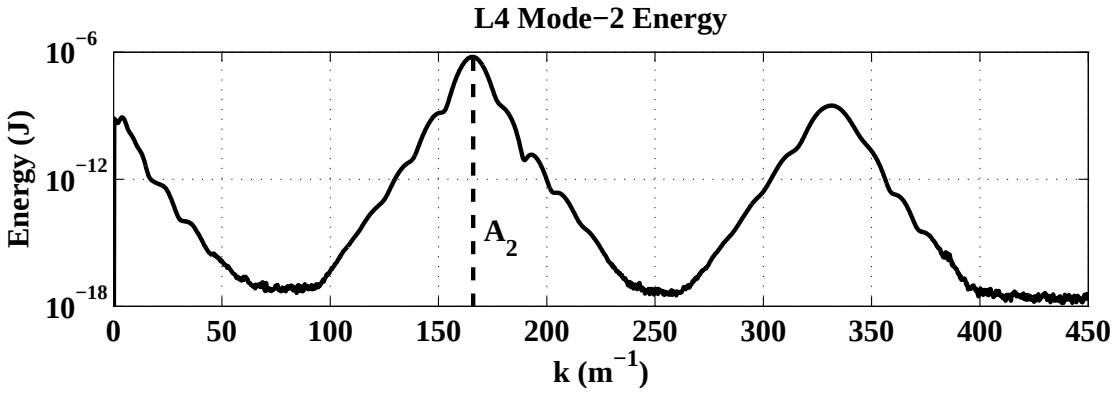

Figure 4.7: The pseudo-energy decomposition for test L4, averaged over $50.5 \leq t \leq 60$ s. The vertical dashed line marks the location of wave A_2. The dominant peak lies at the expected wavenumber $k = 166.0$ m^{-1}, corresponding to wave A_2. A secondary peak near $k = 332$ m^{-1} is visible, as is an accumulation of energy at low wavenumbers.

Lab-scale Collision Experiments

Test	Waves	a_1, a_2 (m)	x_1, x_2 (m)	$[t_{1i}, t_{1f}]$, $[t_{2i}, t_{2f}]$ (s)	L (m)
L5	A_1, A_2	0.5, 0.01	0, 0	$[80, 120]$, $[0, 30]$	10.0
L6	B_1, B_2	1.5, 0.5	2.5, -2.5	$[0, 45]$, $[0, 45]$	40.0

Table 4.5: Data for lab-scale collision experiments. From left-to-right, the columns specify: the name of the experiment, waves being forced, forcing amplitudes, forcing centers, time intervals of forcing, and tank length. For each experiment 4096 horizontal and 256 vertical grid points were used. Forcing widths of $w_0 = 0.1$ m were used for each wave.

any forcing, wave A_1 is forced at moderate amplitude for 40 seconds. Forcing is switched off at $t = 120$ seconds, and the A_1 waves passes through the A_2 waves.

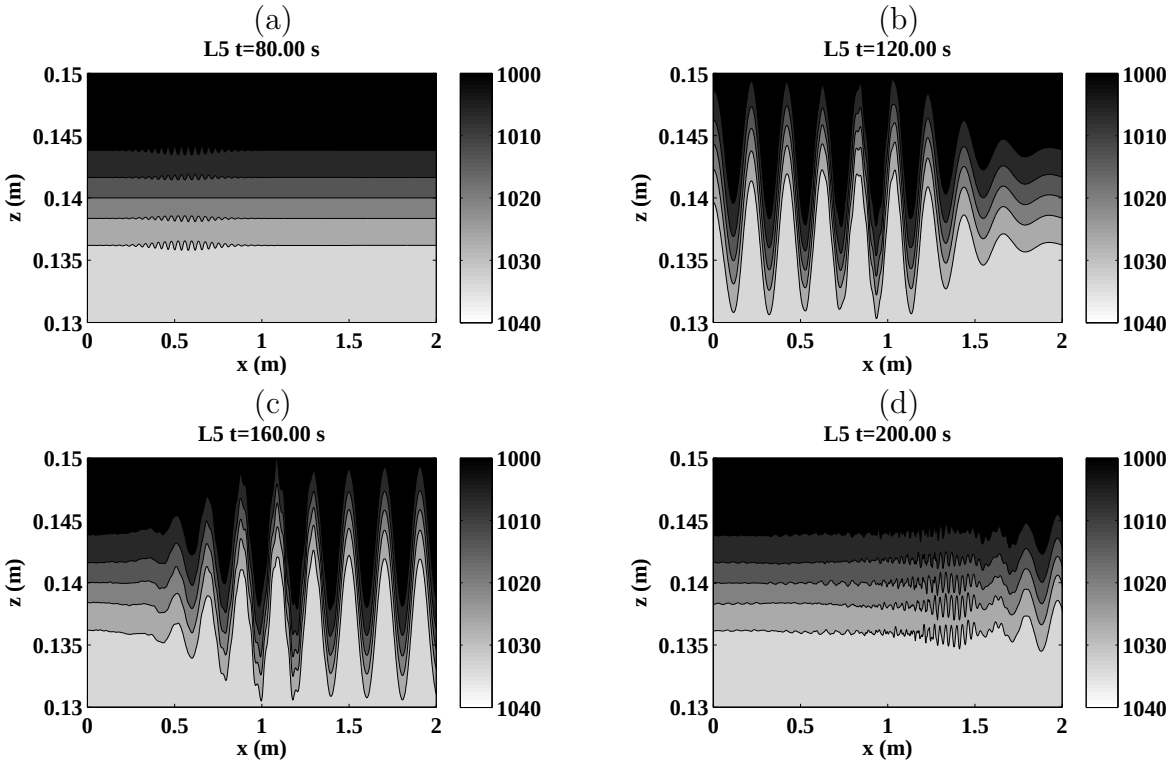

Figure 4.8: Evolution of isopycnals for experiment L5. In panel (a), at $t = 80$ s, a small-amplitude mode-2 wave train of A_2 lies between $x = 0.4$ m and $x = 0.75$ m. In panel (b), at $t = 120$ s, the forced mode-1 wave A_1 is passing through A_2. In panel (c), $t = 160$ s and wave A_1 has almost passed through A_2, but minor distortions are visible. In panel (d), at $t = 200$ s, wave A_1 has passed through A_2 and a coherent wake is apparent.

In Figure 4.8, the density contours are plotted for L5 at four different times. In panel (a), contours are shown at $t = 80$ s, immediately before wave A_1 is forced. Wave A_2 is small, with peak-to-trough isopycnal displacements of about 1 mm, and its trailing edge has travelled about 43 cm. The forcing width is 0.1 m, so wave A_2 lies outside of the forcing region. For $80 \leq t \leq 120$ s, wave A_1 is forced, and in panel (b) the density contours are shown at $t = 120$ s. The peak-to-trough isopycnal displacements of A_1 are about 1.1 cm. In panel (c), the contours are shown at $t = 160$ s. Minor distortions are visible in the contours, but the presence of A_2 is mostly hidden. Finally, density contours at $t = 200$ s are shown in panel (d). Wave A_1 has passed through A_2, and clearly visible in the noisy wake is a regular mode-1 signal of short wavelength.

A magnified view of the contours at $t = 200$ s is shown in Figure 4.9. The waves

visible in the figure are mostly of mode-1 vertical structure and appear to have a regular wavelength of slightly more than 3 cm. This matches the expected wavelength of wave A_3. The peak-to-trough isopycnal displacements of this regular mode-1 wave are greater than 2 mm.

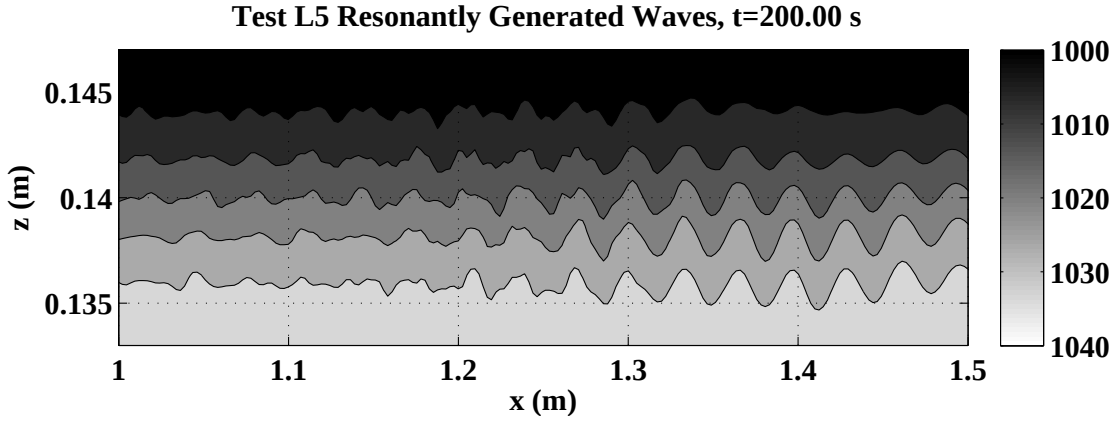

Figure 4.9: A magnified view of the resonantly generated wave train for test L5. Towards the right side of the contour plot a very regular mode-1 wave is visible, with the expected wavelength of about 3.2 cm, indicating it is in fact wave A_3.

An energy decomposition for test L5 is plotted in Figure 4.10. In the top subplot the dominant peak lies at $k = 30.9$ m^{-1}, and corresponds to wave A_1. The second largest peak in the mode-1 spectrum corresponds to wave A_3 and lies at $k \approx 195$ m^{-1}. It is the result of the near-resonant interaction. In the bottom subplot of Figure 4.10 the mode-2 energy decomposition is shown. A peak near $k \approx 166$ m^{-1} indicates the presence of wave A_2, but there is more energy in the peaks near $k = 62$ m^{-1} and $k \approx 0.3$ m^{-1}. The peak near $k = 62$ m^{-1} was observed in tests L1 – L3 and is likely due to the self-interaction of forced wave A_1. The shift to long wave energy is an important effect that occurs in many of the experiments presented here. Possible mechanisms explaining the shift are discussed in Section 4.3.

As a final illustration of the resonant interaction occurring in L5, consider the Hovmöller diagrams shown in Figure 4.11. To construct each diagram, the density field is sampled at a fixed z value at each time step. The amplitudes of the density are then plotted as a contour diagram with time running on the vertical axis. A different shading scheme is used in each plot to emphasize the desired features. This style of plot cleanly visualizes the propagation of wave crests and wave packets. In the left subplot, the weakly forced wave A_2 is visible as a beam emanating from the origin. The forcing of the large amplitude wave A_1 for $80 \leq t \leq 120$ seconds is also visible. The two beams intersect and the resonant

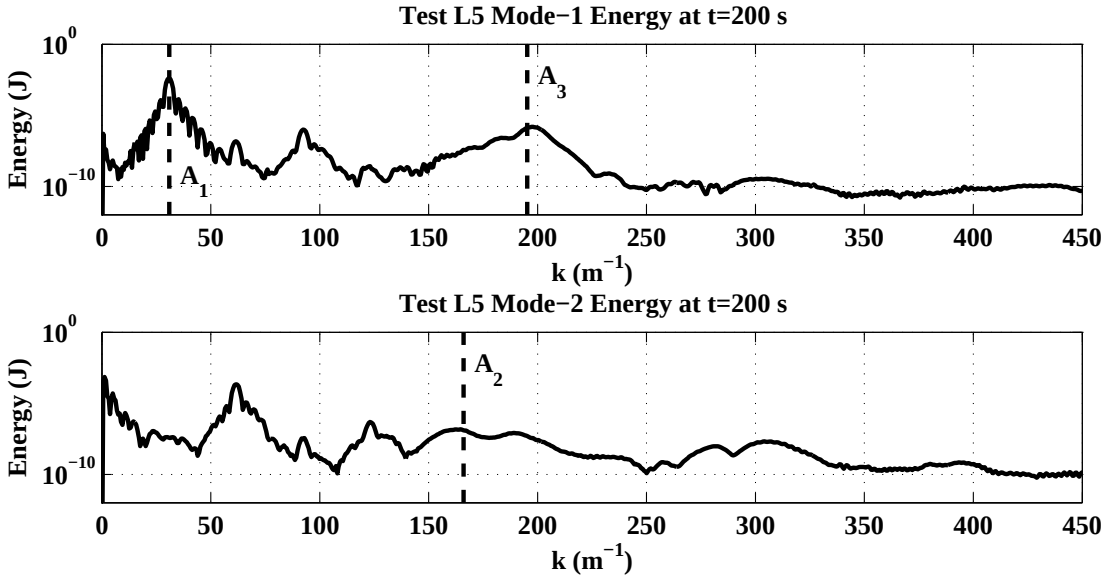

Figure 4.10: The pseudo-energy decomposition for test L5 averaged over $190.5 \leq t \leq 200$ seconds. Vertical dashed lines mark the locations of A_1, A_2, and A_3. In the mode-1 decomposition the dominant peaks lie near $k = 30.9$ m^{-1}and $k = 195$ m^{-1}, corresponding to waves A_1 and A_3. Another large peak near $k = 90$ m^{-1} is visible, though it is unaccounted for. In the bottom subplot the mode-2 decomposition is shown. Wave A_2 has a moderate, broad energy peak but there is actually more energy in long waves near $k \approx 0.3$ m^{-1}.

interaction occurs. In the right subplot a magnified view near the end of simulation time is shown. Clearly leaving the main A_1 packet is a new packet of A_3. The slopes of the stripes in the wavepackets indicate phase speeds, and the group velocities can be estimated by the position of the packet as a whole at different times.

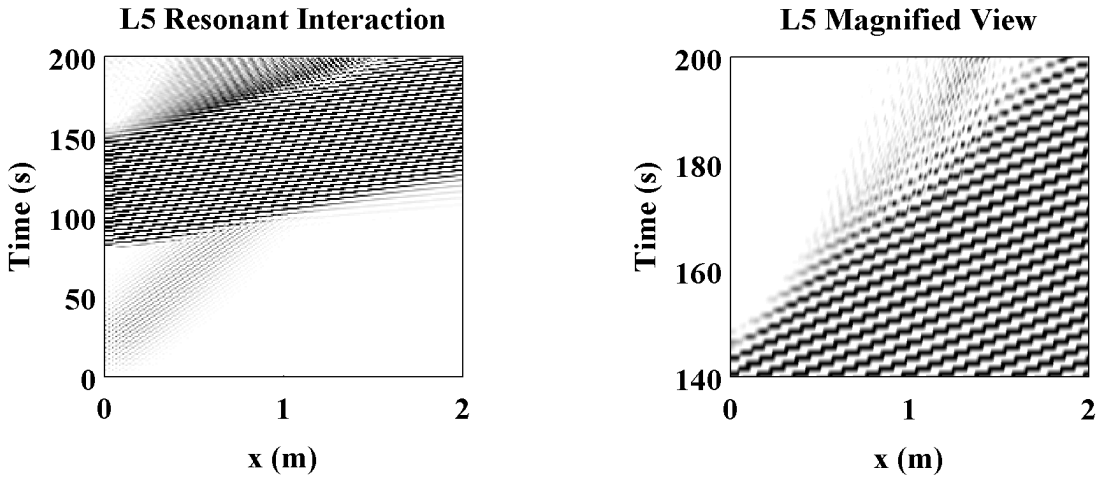

Figure 4.11: Hovmöller diagrams for test L5. Wave A_2 is visible as the weak beam stemming from the origin in the left subplot. Wave A_1 is the large beam visible in both plots, originating in the interval $80 \leq t \leq 120$ on the vertical axis. In the right subplot a magnified view shows that a small packet of waves has separated from the wave A_1, this is the expected wave A_3. A different shading scheme is used in the two subplots to emphasize the presence of the waves.

Test L6. In experiment L6 waves B_1 and B_2 are forced simultaneously for 45 seconds at a distance of 5 meters apart. The forcing is then shut off, and the mode-1 wave trains pass through each other. Both waves are generated with a forcing width of $w_0 = 0.1$ m. An important difference between test L5 and L6 is that test L6 involves waves propagating in opposite directions, so the interaction occurs over a shorter time period. Another important difference between L5 and L6 is that the waves involved in L6 (from triad B) are much longer than those used in L5 (from triad A). The expected result for L6 is that B_1 and B_2 will interact to produce B_3, a rightward-propagating mode-2 wave.

Density contours for experiment L6 are plotted at four different times in Figure 4.12. In panel (a), at $t = 20$ s, the forcing of waves B_1 and B_2, centered at $x = 2.5$ m and $x = -2.5$ m respectively, is visible. The wavefronts are still more than 1 meter apart. The wave source is switched off at $t = 45.0$ s for both waves. In panel (b), at $t = 60$ s, the wave packets have left the forcing sites and are overlapping near $x = 0$. In panel (c), $t = 120$ s, and the two wave trains have almost fully separated, but it appears a wave field has been excited between them. Panel (d) depicts the contours at $t = 180$ s. There, wave B_1 has fully passed through B_2 and a wake involving regular structure is visible. The excited

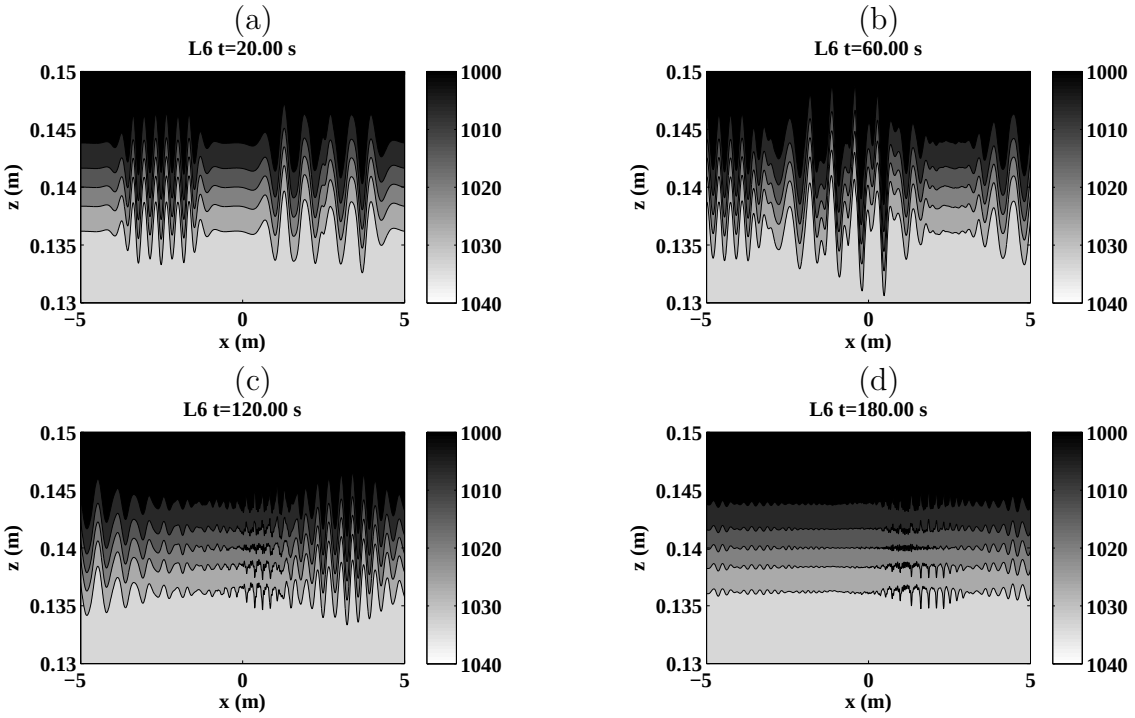

Figure 4.12: Isopycnals for the collision experiment L6 at four different times. In panel (a), $t = 20.0$ s, and mode-1 waves B_1 and B_2 are visible, centered at $x = +2.5$ m and $x = -2.5$ m, respectively. The forcing is switched off at $t = 45.0$ s, and the waves are allowed to pass through each other. In panel (b), at $t = 60.0$ s, the waves are seen to overlap. In panel (c), at $t = 120.0$ s, the wave trains have almost passed through each other. Panel (d) shows the isopycnals at $t = 180$ s, and the wave trains have separated. A coherent packet of mode-2 waves is visible.

waves lying approximately in the interval $0 \leq x \leq 3$ m appear to be primarily mode-2. Comparing the subplots for $t = 120$ s and $t = 180$ s, it appears that the excited waves are moving rightward. This is confimed when the evolution of density contours is viewed as an animation. The group velocity of the excited waves must be less than that of B_2 because they have been left behind.

A magnified view of the resonantly generated waves is provided in Figure 4.13. From the figure, the excited waves are mostly of mode-2 structure, with a wavelength of about 22 cm towards the right edge of the plot. This is the expected wavelength for B_3. Closer inspection reveals a small component of short mode-1 waves towards the left side of the plot. In addition, the mode-2 waves at the left edge of the wave train appear to be smaller in amplitude and have a wavelength of roughly 30 cm. Under linear theory these longer waves should travel faster than the B_3 waves to their right. However, the waves are clearly

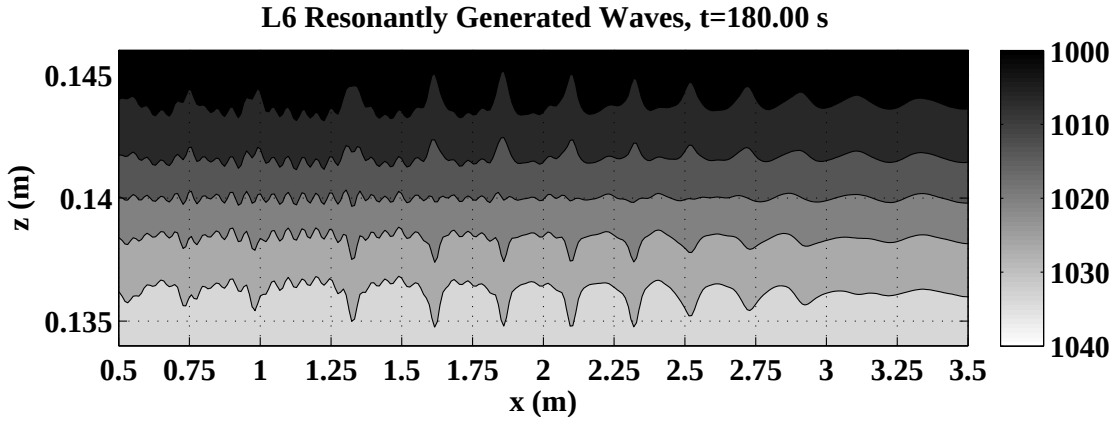

Figure 4.13: A magnified view of the resonantly generated waves in experiment L6. The wave field is mostly of mode-2 structure, but not sinusoidal. Troughs are significantly broadened, and crests are steep. The wavelength of the mode-2 waves near the right side of the plot is about 22 cm, but towards the left side it is closer to 30 cm. A small-amplitude short mode-1 wave is visible in the left side of the wave train. The pycnocline appears to be compressed by the mode-2 waves.

not sinusoidal in shape and may be closer in structure to solitary waves. For solitary waves, it is expected that larger amplitude waves travel faster, which would explain the relative locations of the two groups of mode-2 waves in the figure. The complicated horizontal structure of these waves is problematic because the energy decompositions that are used, as well as the underlying interaction theory, are based on the assumption of sinusoidal shape. The shape of these mode-2 waves and the impact on the energy decomposition are investigated in more detail in Section 4.3.

A Hovmöller diagram for test L6 is shown in Figure 4.14. The B_1 and B_2 wave trains are visible as beams originating from $x = \pm 2.5$ m. The forcing functions generate waves in both directions, as is visible in the plot. The forced waves intersect near $x = 0$, and from the intersection region a third beam is visible, extending upwards and to the right. The third beam is traveling in the positive x direction, and has a slower speed than the two forced waves. This resonantly generated beam corresponds to wave B_3 and other smaller excited waves.

The pseudo-energy decomposition for test L6 is depicted in Figure 4.15. The energy decomposition is plotted for $t = 200$ s after averaging over ten data sets in the interval $191 \leq t \leq 200$ s. The two dominant peaks in the mode-1 spectrum, near $k = 9.5$ m^{-1} and $k = 17.5$ m^{-1}, correspond to the forced waves B_1 and B_2, respectively. In the mode-2 spectrum, the dominant peak is expected to be due to wave B_3 and should lie near $k = 28.2$ m^{-1}. A peak does lie near $k = 27$ m^{-1}, but is actually the third largest peak in

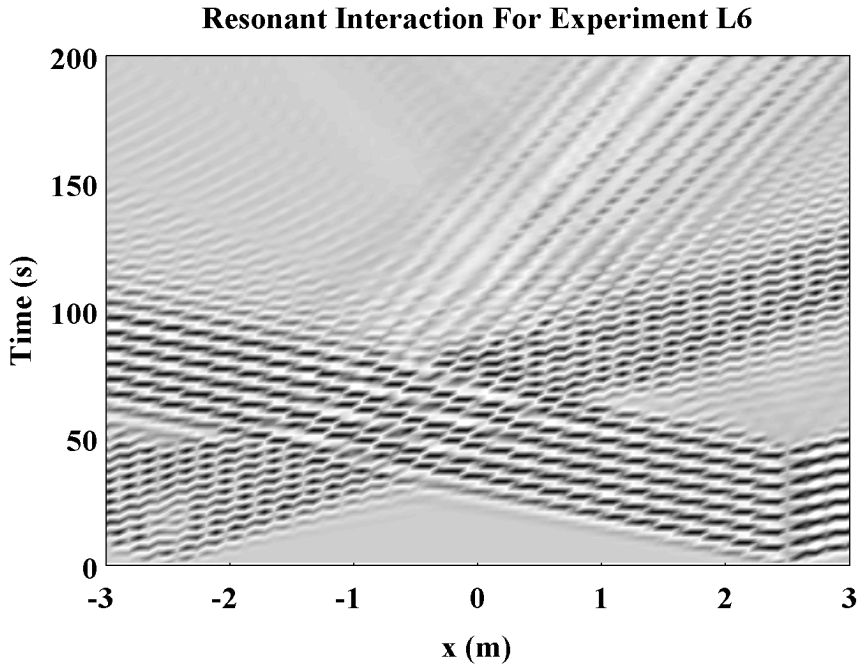

Figure 4.14: A Hovmöller diagram for test L6. The forced mode-1 waves are generated at sites centered at $x = \pm 2.5$ m. The waves collide near $x = 0$ and pass through each other. A third beam is visible emanating from the interaction site, and travels more slowly than wave B_1 or B_2. It corresponds to wave B_3 and the other excited waves.

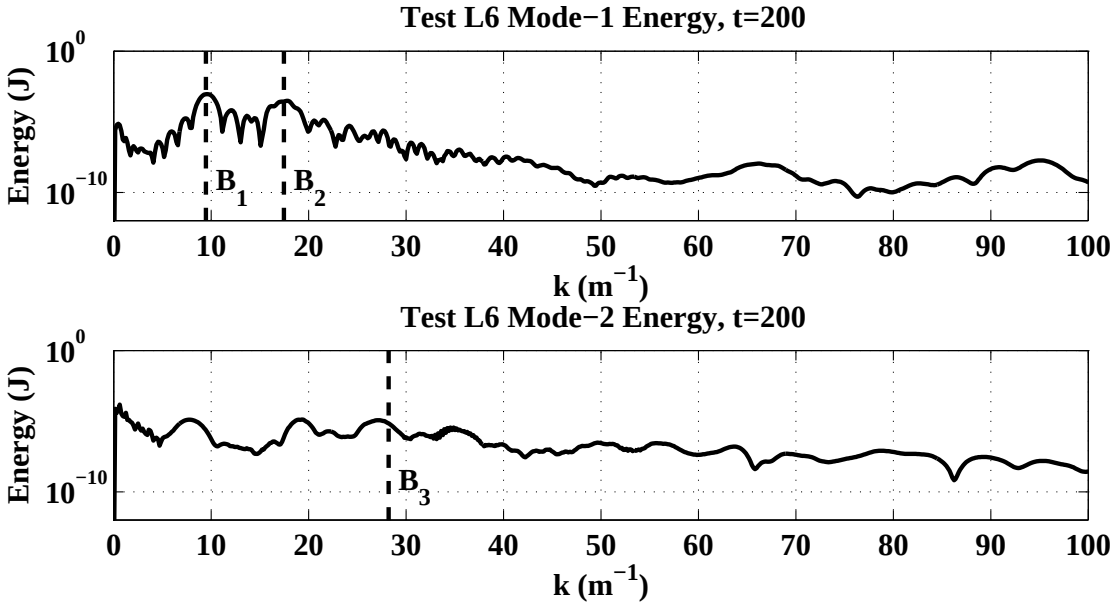

Figure 4.15: The pseudo-energy decomposition for test L6 averaged over $191 \leq t \leq 200$ s. In the top subplot the mode-1 decomposition demonstrates the two peaks at the forced wavenumbers $k = 9.47$ m^{-1} (wave B_1) and $k = 17.47$ m^{-1} (wave B_2). In the bottom subplot the mode-2 decomposition shows peaks near $k \approx 28$ m^{-1} and $k \approx 19.3$ m^{-1}, but the strongest energy signal lies in long mode-2 waves near $k \approx 0.63$ m^{-1}.

the mode-2 spectrum. The largest mode-2 peak is found near $k = 0.628$ m^{-1}, and another peak at $k = 19.1$ m^{-1} also exceeds the energy content of wave B_3. Forcing experiments involving just wave B_1 also produced a peak near $k = 19.1$ m^{-1}, and as it is nearly twice the wavenumber of wave B_1 it is likely due to a self-interaction. The peak at $k = 19.1$ m^{-1} corresponds to a wave with wavelength 32.9 cm. This is the wave that was identified in the left edge of the magnified view of Figure 4.13, but its source is unaccounted for. It is interesting that the mode-2 peak that should lie at $k = 28.2$ m^{-1}(corresponding to wave B_3) lies closer to $k = 27$ m^{-1}. This could be a result of a slightly different triad interaction occuring, or an artifact of the non-sinusoidal nature of the underlying wave.

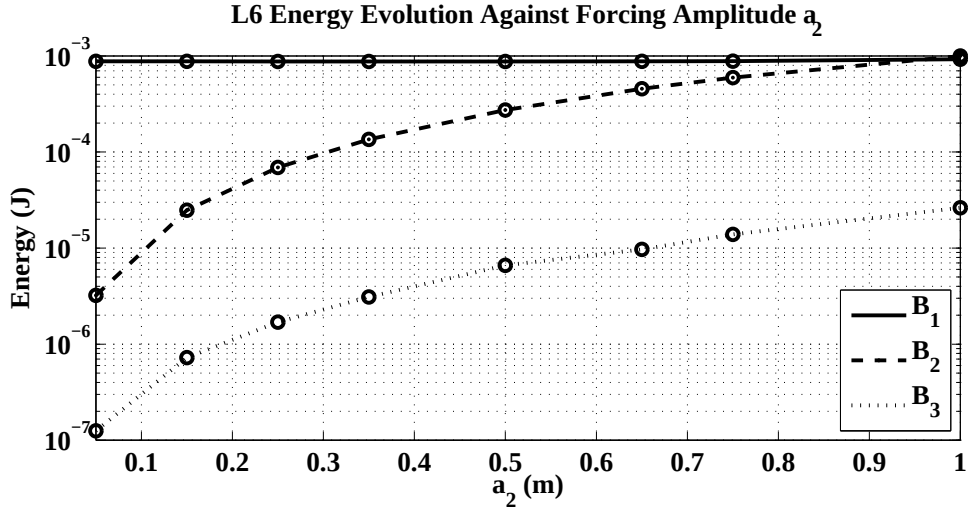

Figure 4.16: The evolution of the amplitude of energy in waves B_1 – B_3 as the forcing amplitude a_2 of wave B_2 is varied. The forcing amplitude of wave B_1 is held fixed at $a_1 = 1.5$ m. Energy data is averaged over twenty data sets in the interval $181 \leq t \leq 200$ s.

Experiment L6 was repeated with different forcing amplitudes a_2 for wave B_2, while the forcing amplitude $a_1 = 1.5$ m for B_1 was held fixed. The energy content for each of waves B_1 – B_3 is shown in Figure 4.16. The energy was computed by averaging data over the interval $181 \leq t \leq 200$ s. As seen in the plot, the energy of wave B_1 remains relatively unchanged as a_2 varies. Wave B_2 grows with the forcing amplitude a_2 as expected, and wave B_3 grows in a very similar fashion, but the energy level is lower.

Experiments L5 and L6 demonstrate that resonant interactions can occur for waves travelling in the same direction, or in opposite directions. Both experiments were successful in generating the expected third wave in the triad. However, the wave field generated by the interactions is much more complicated than the weakly-nonlinear theory predicts. Not only are unexpected waves present in the wake of interactions, the expected waves do not

have a clean sinusoidal shape. The presence of unexpected waves could be the result of interactions taking place that were not considered in the a priori calculations, or could involve higher-order interactions. The finite-amplitude effects observed for the small wave amplitudes is a problem that limits the applicability of the weakly-nonlinear resonant interaction theory. Confidence in the energy decomposition, which uses sinusoidal basis functions, is also diminished by the finite-amplitude effects.

4.2 Deep Ocean Simulations

In this section numerical experiments involving deep ocean-like parameters are presented. Two different models of the oceanic stratification are used. The first is a simple model analogous to the one used for lab-scale experiments. The second model is similar, but the pycnocline lies slightly deeper and the bottom layer of fluid is uniformly (but weakly) stratified.

In many of the tests conducted here a wave of M_2 tidal frequency is used (see Mellor [52]). The M_2 tidal frequency is $\omega_2 = 1.4075 \cdot 10^{-4}$ s^{-1}, and corresponds to a period of 12.4 hours. The generation of internal waves through interactions of barotropic tidal flow with topography is an important source of internal waves (see Garrett and Kunze [27]), which motivates this choice.

4.2.1 A Continuous Two-Layer Model

Now consider the background density profile defined by

$$\rho_0(z) = \rho_0 - \frac{\Delta\rho}{2} \tanh\left(\frac{z - z_p}{L_p}\right), \tag{4.3}$$

with $\rho_0 = 1025$ kg/m^3, and density jump $\Delta\rho = 10$ kg/m^3. This models seawater with a moderate density variation across its depth. The fluid depth is taken to be $H = 2$ km, and the pycnocline is centered 200 meters below the surface, at $z_p = 1800$ m. The density width parameter $L_p \approx 56.7$ m is chosen so that the 99% density jump occurs across a distance of 300 m in the interval $1650 \leq z \leq 1950$ m. The peak buoyancy frequency is 0.0289 s^{-1}, corresponding to a period of roughly 216.7 seconds.

Simulations involving this stratification were performed on domains with lengths of 2000 – 4000 km. The parameters for these ocean simulations are summarized in Table 4.6. The density profile and buoyancy frequency are plotted in Figure 4.17. Simulations performed using this stratification are assigned names with the prefix "DC", an abbreviation for "Deep Ocean Continuous Two-Layer Model".

DC Experimental Parameters

Parameter	Value
H	2 km
$\rho_0, \Delta\rho$	1025, 10 kg/m^3
z_p, L_p	1800, 56.7 m
$\max N(z)$	0.0289 s^{-1}
N_x, N_z	4096, 256
U	6.91 m/s

Table 4.6: Simulation parameters for the continuous two-layer ocean experiments.

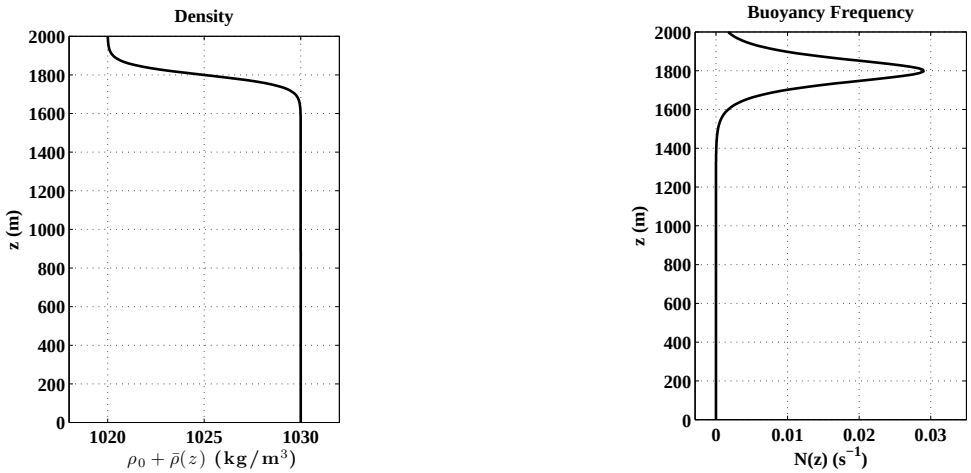

Figure 4.17: Background density (left subplot) and buoyancy frequency (right subplot) for the DC simulations. The center of the pycnocline lies at $z_p = 1800$ meters, and has a 99% density jump width of 300 meters.

As discussed above, M_2 tidal frequency waves play a fundamental role in the ocean scale simulations presented here. For the DC stratification, the mode-1 M_2 tidal wave has a wavelength of approximately 172.1 km. Only triads involving this wave were sought. Another constraint on the triads under consideration was that the second and third waves must be of a similar scale to the M_2 wave. While it may be possible for the M_2 tidal wave to interact with waves of significantly different scales, such interactions are difficult to simulate. Even with these constraints, a large number of candidates were found, and one was chosen for demonstration purposes here.

A triad involving waves of roughly the same scale as the M_2 wave, and with relatively strong interaction coefficients, is presented in Table 4.7. The triad is referred to as triad C, and involves an interaction between a mode-1, 2, and 3 wave. Waves C_1 and C_2 are

Triad C

Wave	Mode	ω (s^{-1})	T (hr)	k (m^{-1})	λ (km)	v (m/s)	γ
C_1	1	$1.4 \cdot 10^{-4}$	12.4	$3.65 \cdot 10^{-5}$	172.1	3.86	-0.015
C_2	2	$-1.07 \cdot 10^{-4}$	16.3	$-1.06 \cdot 10^{-4}$	59.5	1.01	0.0027
C_3	3	$-3.9 \cdot 10^{-5}$	44.3	$6.43 \cdot 10^{-5}$	97.6	0.61	-0.0012

$\delta_\omega = -5.6 \cdot 10^{-6}$ (s^{-1}) $\quad$ $\delta_k = -4.8 \cdot 10^{-6}$ (m^{-1})

Table 4.7: Parameters for triad C, investigated for the DC experiments. From left-to-right, the columns are as follows: wave name, vertical mode number, frequency, period, wavenumber, wavelength, group velocity, interaction coefficient.

rightward-propagating, and C_3 is leftward-propagating. The triad, along with the first three modes of the dispersion relation for the DC model, is plotted in Figure 4.18. All three waves in triad C are long relative to the fluid depth and pycnocline width, and in this regime the dispersion curves are almost linear.

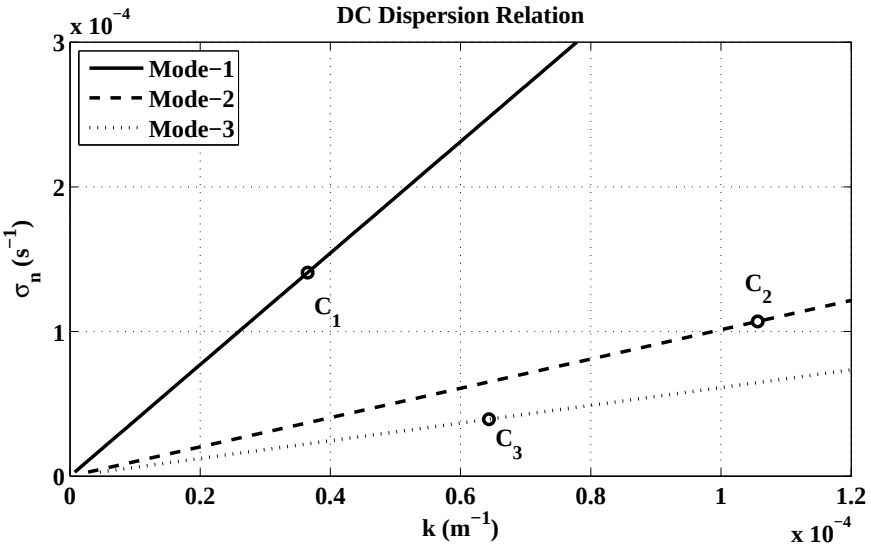

Figure 4.18: The dispersion relation for the DC experiments. The absolute values of the k and ω values for the waves in triad C are marked with circles. The dispersion relation is almost linear in this regime.

Monochromatic Forcing Experiments

It turns out that the simple problem of forcing a single wave from triad C yields interesting results, so monochromatic forcing experiments are considered before an attempt is made

at producing a resonant interaction. In addition to using bidirectional forcing shapes like that described by equation (4.2), unidirectional forcing is also tested here. Unidirectional forcing is achieved by forcing the vertical momentum equation using the technique proposed in Section 3.5. In particular, the forcing shape is taken to be

$$F_2(x,z,t) = a_n \text{sech}\left(\frac{x-x_n}{w_n}\right)\cos(kx-\omega t)N^2(z)\phi_n(z;k). \tag{4.4}$$

The simple experiments conducted on the DC model are described in Table 4.8. Experiments involving unidirectional forcing are marked explicitly in the table with a superscript right-arrow, such as DC3$^{\rightarrow}$.

DC Monochromatic Forcing Experiments

Test	Wave	a_0 (m)	x_0 (km)	w_0 (km)	L (km)	max(**u**)/c
DC1	C_1	2.0	0.0	30.0	4000.0	0.019
DC2	C_1	5.0	0.0	30.0	4000	0.099
DC3$^{\rightarrow}$	C_1	1.0	-1000	30.0	3000	0.026
DC4$^{\rightarrow}$	C_2	0.2	-1000	30.0	3000	0.12

Table 4.8: Monochromatic forcing experiments with the DC model. The domain length L, forcing width w_0, and forcing center x_0 are specified in km. The final column, max(**u**)/c, gives the ratio of the maximum magnitude of the velocity to the phase speed of the underlying wave, and is a measure of wave steepness. The maximum velocity is computed over the duration of the experiment.

In tests DC1 – DC3$^{\rightarrow}$, wave C_1 (the M_2 wave) is forced at various amplitudes on a domain of two different lengths. The forcing amplitudes were chosen so that the resulting wave amplitudes would be small relative to the fluid depth, pycnocline width, and wavelength. In experiment DC4 wave C_2 was forced so that the behaviour of a mode-2 wave can be studied. The ratio of the maximum induced velocity to the phase speed of the underlying forced wave, denoted by max(**u**)/c, is given in the rightmost column of Table 4.8. In each experiment this dimensionless steepness parameter is significantly smaller than the equivalent parameter for the waves in the lab-scale experiments.

Density contours for DC1 and DC2 are displayed in Figure 4.19 at $t = 62.2$ hours (slightly more than five forcing periods). Test DC2 is identical to DC1 except that the forcing amplitude is 2.5 times larger. In the left subplot a regular wave train is visible, but the waves have clearly steepened, particularly towards the wavefront (right edge). The troughs in the M_2 wave outpace the crests and the waves steepen from behind. This is even more pronounced in the right subplot, which illustrates the density contours for DC2 at the same time. In addition to steepening, a series of oscillations has developed on the back sides of the waves near the leading edge. When viewed as an animation, the waves

appear to steepen from behind until they are almost vertical, then small oscillations grow. These oscillations actually significantly alter the peak-to-trough isopycnal displacements. For comparison purposes, the peak-to-trough isopycnal displacements are about 8 m for DC1 and roughly 18 m for DC2 away from the oscillations. In steep oscillatory regions, the peak-to-trough isopycnal displacements are about 23 m for DC2. In Figure 4.20 a

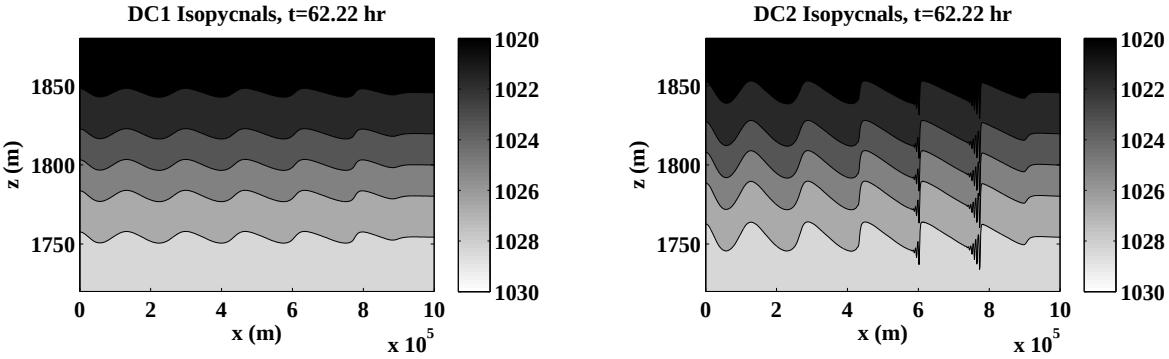

Figure 4.19: Isopycnal contour diagrams for DC1 and DC2 after 62.2 hours. Steepening is visible in both plots. The horizontal plot length is 1000 km, the vertical plot length is 180 m.

magnified view of a single isopycnal at $t = 62.2$ hours is plotted for DC2. The shape bears striking resemblance to the undular bores studied by Lamb and Yan [42], and is discussed further in Section 4.3. The oscillations in the right portion of Figure 4.20 have had one extra M_2 period to develop and, as a result, are larger and there are more of them. Further investigation reveals the wavelength of the oscillations to be about 7 km. These experiments indicate that there will be a difficulty studying resonant wave interactions involving the mode-1 M_2 tidal wave in the DC stratification. Even at modest amplitudes and wave steepness (for DC2 $\max(\mathbf{u})/c \approx 0.099$), the M_2 wave of interest loses its sinusoidal shape within just a few periods (about 2.5 days).

An energy decomposition for DC2 is shown in Figure 4.21. The peak at the forced wavenumber $k_{M_2} = 3.65 \cdot 10^{-5}$ m^{-1} is dominant, but a regular set of peaks at higher harmonics is also evident. The undular bores visible in Figure 4.20 have a wavelength of about 7 km, corresponding to a wavenumber of $k \approx 9 \cdot 10^{-4}$ m^{-1}. No distinct peak is evident at that location but there is a broad rise of the spectrum in that region.

Experiment DC3$^{\rightarrow}$, like DC1 and DC2, involves forcing the M_2 tidal wave, but unidirectional forcing is tested. The resulting density contour plot at $t = 111.1$ hours is shown in Figure 4.22. The forcing center for DC3$^{\rightarrow}$ is at $x_0 = -1000$ km, and there does not appear to be any significant wave motion to the left of that point. The peak-to-trough isopycnal displacements in this experiment are about 6-7 meters, which is very small in comparison with the wavelength and pycnocline width. Even so, the M_2 waves have visibly

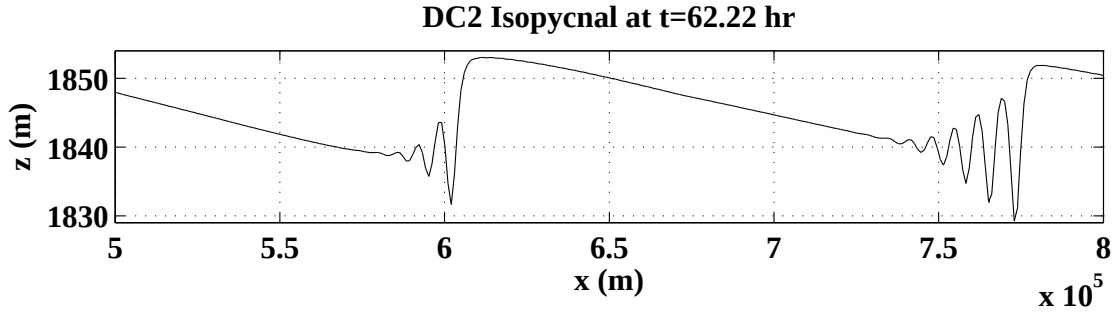

Figure 4.20: Wave steepening in experiment DC2. The troughs move faster than the crests so the waves steepen from behind. Eventually the backs of the waves become so steep that undular bores form. The oscillations visible in this figure are well-resolved, there are about 7 points per wavelength.

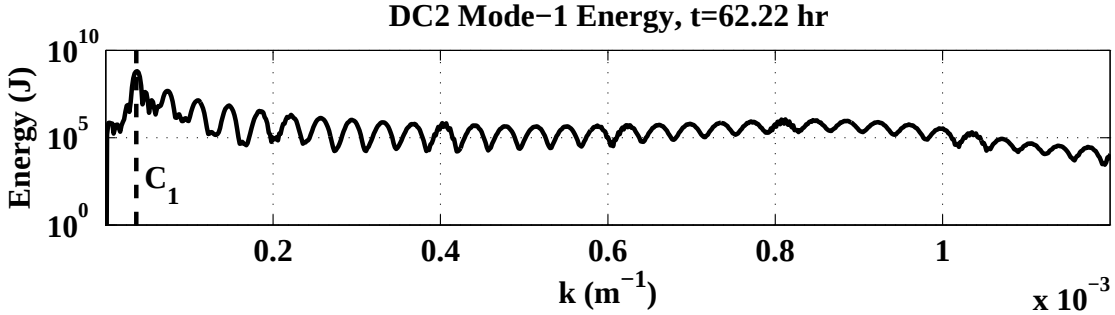

Figure 4.21: The mode-1 pseudo-energy decomposition for DC2. The expected peak lies at $k = 3.6 \cdot 10^{-5}$ m^{-1}, corresponding to wave C_1. Data is averaged over 8 data sets in the interval $54.4 \leq t \leq 62.2$ hr. Wave C_1 is marked with a vertical dashed line.

steepened towards the leading edge, and some small undular bores appear to be growing.

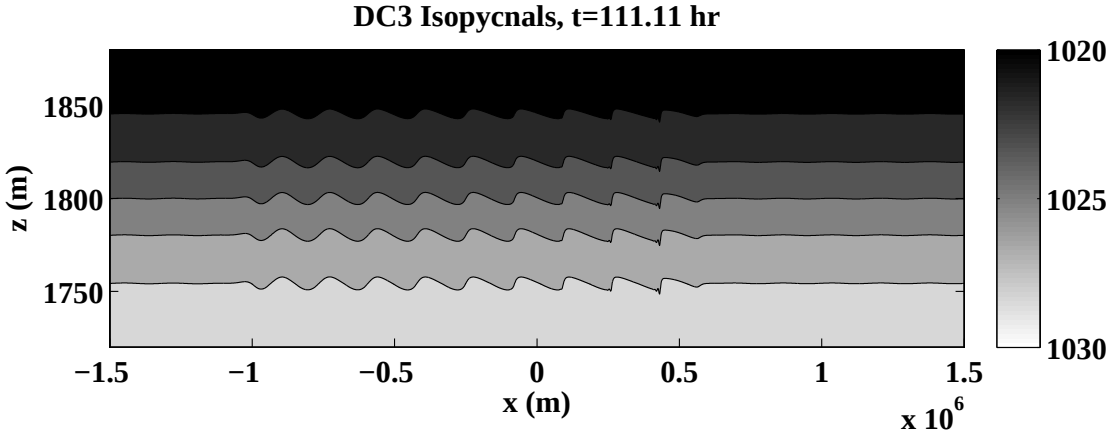

Figure 4.22: Isopycnal displacements for test DC3$^{\rightarrow}$ after 111 hours. Unidirectional forcing is used and only a small amount of leftward-propagating waves are created. Peak-to-trough isopycnal displacements are about 6-7 meters, but even for these small waves steepening is noticeable. Small undular bores are forming in the troughs near the wavefront.

As a further illustration of the propagation characteristics of the M_2 wave, consider Figure 4.23. Hovmöller diagrams are shown for tests DC2 and DC3$^{\rightarrow}$. The unidirectional nature of the forcing is evident in the right subplot, where only a trace of leftward-propagating waves are visible. In the left subplot the lines of constant phase extend from the forcing center in both directions. For both subplots, these lines of constant phase are visually parallel to the propagation of the wave beam as a whole. This is because in the long-wave limit the phase speed tends to the group velocity. As shown in Section 2.3, the phase speed is an upper bound for the group velocity, so it can be expected that the lines of constant phase for shorter waves will be rotated clockwise from the direction of propagation of the beam as a whole. The short wavelength undular bores seen in the contour plots for DC2 are not visible in the Hovmöller diagram.

Test DC4$^{\rightarrow}$ involves small amplitude, unidirectional forcing of wave C_2 (a mode-2 wave). A plot of density contours for DC4$^{\rightarrow}$ is shown in Figure 4.24. The isopycnal displacements for the mode-2 waves are very small, about 4 meters in peak-to-trough amplitude. Towards the right edge of the figure oscillations are visible in the waves. These are similar to those observed for test DC2, however they have a shorter wavelength of about 2.7 km. With the parameters used for this experiment there are about 4 grid points per wavelength in the oscillations, so they are not well-resolved. Mode-2 wave steepening effects related to test DC4$^{\rightarrow}$ are discussed in more detail in Section 4.3.

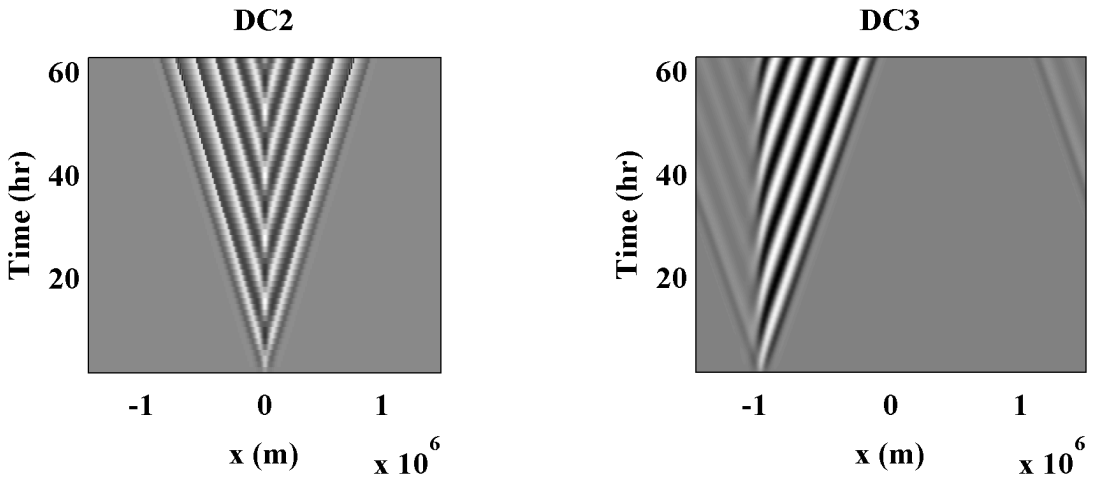

Figure 4.23: Hovmöller diagrams for tests DC2 and DC3$^{\rightarrow}$. Test DC3$^{\rightarrow}$ involves unidirectional forcing so only rightward propagating waves are visible. The stripes indicate lines of constant phase. The undular bores seen in Figure 4.20 are not visible here.

A Collision Experiment

In experiment DC5 an attempt is made to resonantly generate wave C_3 by allowing a packet of wave C_1 to pass through a packet of wave C_2. Waves C_1 and C_2 are forced simultaneously at the same location for $0 \leq t \leq 83.2$ hours. The forcing is then switched off so that any resonantly generated waves are more visible. Waves C_1 and C_2 are rightward-propagating, and are expected to produce a leftward-propagating C_3 wave. The basic data for the experiment is given in Table 4.9.

Interaction Experiment DC5

Test	Waves	a_1, a_2 (m)	x_0 (km)	w_0 (km)	L (km)	Forcing Interval
DC5	C_1, C_2	1.5, 0.3	-666.7	30.0	2000.0	$0 \leq t \leq 83.2$ hr

Table 4.9: Interaction experiment DC5. Waves C_1 and C_2 are forced at the same location, and for the same time interval. The domain length L, forcing center x_0, and width measure w_0 are given in kilometers.

Density contour diagrams are shown for DC5 at $t = 13.9$ and $t = 111.1$ hours in Figure 4.25. In the left subplot the contours are depicted after slightly more than one M_2 tidal period. Wave C_2 is only visible as a minor distortion in the body of wave C_1. In the right subplot, contours are shown at $t = 111.1$ hours. Wave C_1 has fully passed through C_2, and both exhibit strongly nonlinear characteristics. There is no obvious presence of wave C_3 visible.

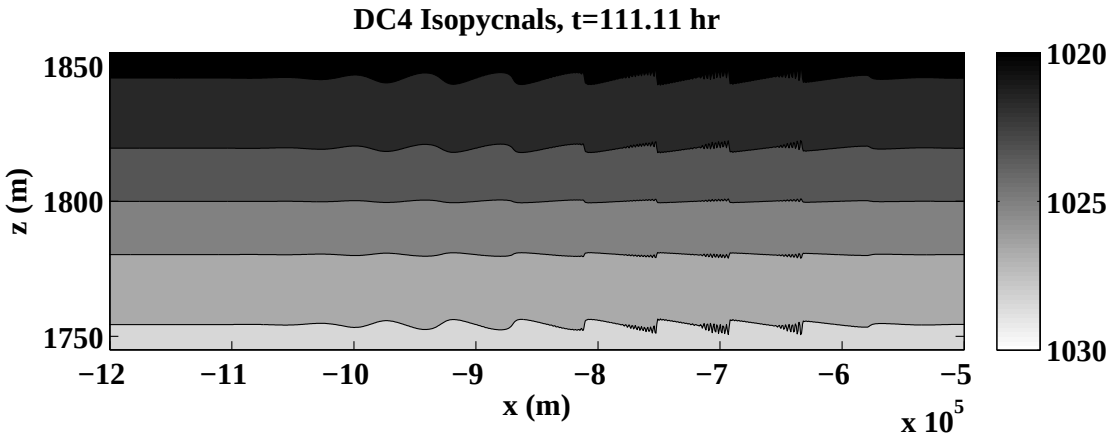

Figure 4.24: Isopycnal displacements for test DC4$^{\rightarrow}$ after 111 hours. Unidirectional forcing is used and only a small amount of leftward-propagating waves are created. Peak-to-trough isopycnal displacements are about 4-5 meters. Steepening and oscillations are noticeable near the right edge of the mode-2 wave train.

Figure 4.26 depicts the modes 1 – 3 pseudo-energy decompositions for test DC5. In the top subplot, mode-1 is shown, and the dominant peak lies at $3.6 \cdot 10^{-5}$ m^{-1}, corresponding to wave C_1. There are many other peaks, however, and these are the signature of the nonlinear wave shape. The mode-2 spectrum (middle subplot) has its dominant peak near $k = 1 \cdot 10^{-4}$ m^{-1}, corresponding to wave C_2, but many other peaks are visible due to the nonlinear nature of the waves. In the bottom subplot, there is a broad mode-3 peak centered at $k = 6.2 \cdot 10^{-5}$ m^{-1} (wave C_3 has a wavenumber of $k = 6.4 \cdot 10^{-5}$ m^{-1}). However, this wave signal is not visible in the associated contour diagrams.

Figure 4.27 shows a Hovmöller diagram for DC5 in the left subplot. The domain is short enough that waves have passed through the right edge by the final plot time. In the right subplot a magnified view of the mode-1 waves that have passed through the boundary is shown. At this point the undular bores are so well developed that they are clearly visible in the plot. They appear as small striations in the major lines of constant phase.

While this experiment shows that an energy signal is present for the resonantly generated wave C_3, the wave is not visible in contour diagrams. Its energy is several orders of magnitude smaller than either wave C_1 or C_2. The nonlinear developments in the waves C_1 and C_2 appear to influence the progress of the interaction.

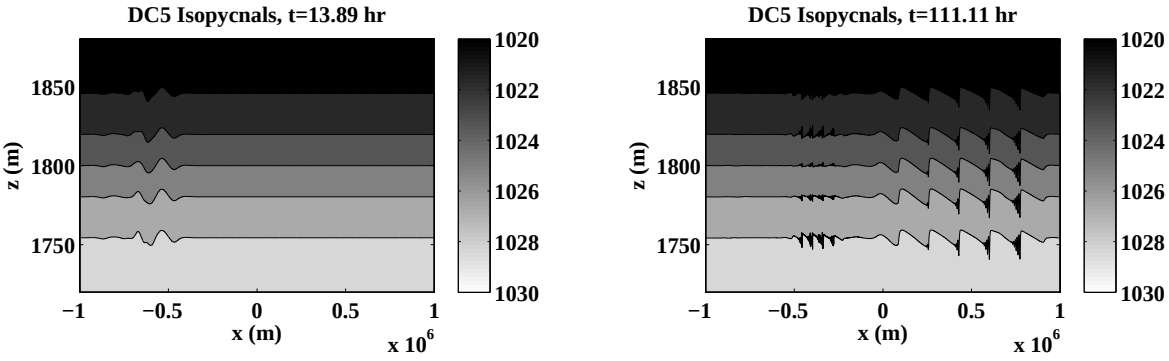

Figure 4.25: Density contours for test DC5 at $t = 11$ hours and $t = 111$ hours. Waves C_1 and C_2 are forced at the same location but separate due to the difference in group velocity.

4.2.2 A More Realistic Stratification Model

The oceanic stratification considered in the previous subsection uses a hyperbolic tangent density profile as a model of a continuous two-layer fluid. Each layer is nearly homogeneous, as the buoyancy frequency values decay exponentially away from the pycnocline. As a first approximation this model is acceptable, but some simple modifications can make it a more accurate representation of the oceanic stratification. The main flaw in the DC model is that it represents the deep ocean as a nearly homogeneous fluid. In reality, the buoyancy frequency in the deep ocean is about $N(z) \approx 10^{-3}$ s^{-1} (see Kundu and Cohen [37] or LeBlond and Mysak [43]).

This motivates the study of a slightly different stratification. The background density profile $\rho_0 + \bar{\rho}(z)$ is used with $\rho_0 = 1027.5$ kg/m^3 and:

$$\bar{\rho}(z) = \begin{cases} -\frac{\Delta\rho}{2}\tanh\left(\frac{z^*-z_p}{L_p}\right) - \frac{\rho_0}{g}10^{-6}(z-z^*) & \text{for } z \le z^*, \\ -\frac{\Delta\rho}{2}\tanh\left(\frac{z-z_p}{L_p}\right) & \text{for } z^* \le z \le H. \end{cases} \tag{4.5}$$

The corresponding buoyancy frequency $N(z)$ satisfies

$$N^2(z) = \begin{cases} 10^{-6} & \text{for } z \le z^*, \\ \frac{g}{\rho_0}\frac{\Delta\rho}{2L_p}\operatorname{sech}^2\left(\frac{z-z_p}{L_p}\right) & \text{for } z^* \le z \le H. \end{cases} \tag{4.6}$$

The ocean depth $H = 2$ km is used again, the pycnocline is centered at $z_p = 1700$ m (100 meters deeper than in the previous model), and the same pycnocline width measure of $L_p = 56.7$ m is used. The parameter $z^* \approx 1489.5$ m is chosen so that $N^2(z)$ is continuous at z^*. A more modest density jump, measured roughly by $\Delta\rho = 5$ kg/m^3, is used. The

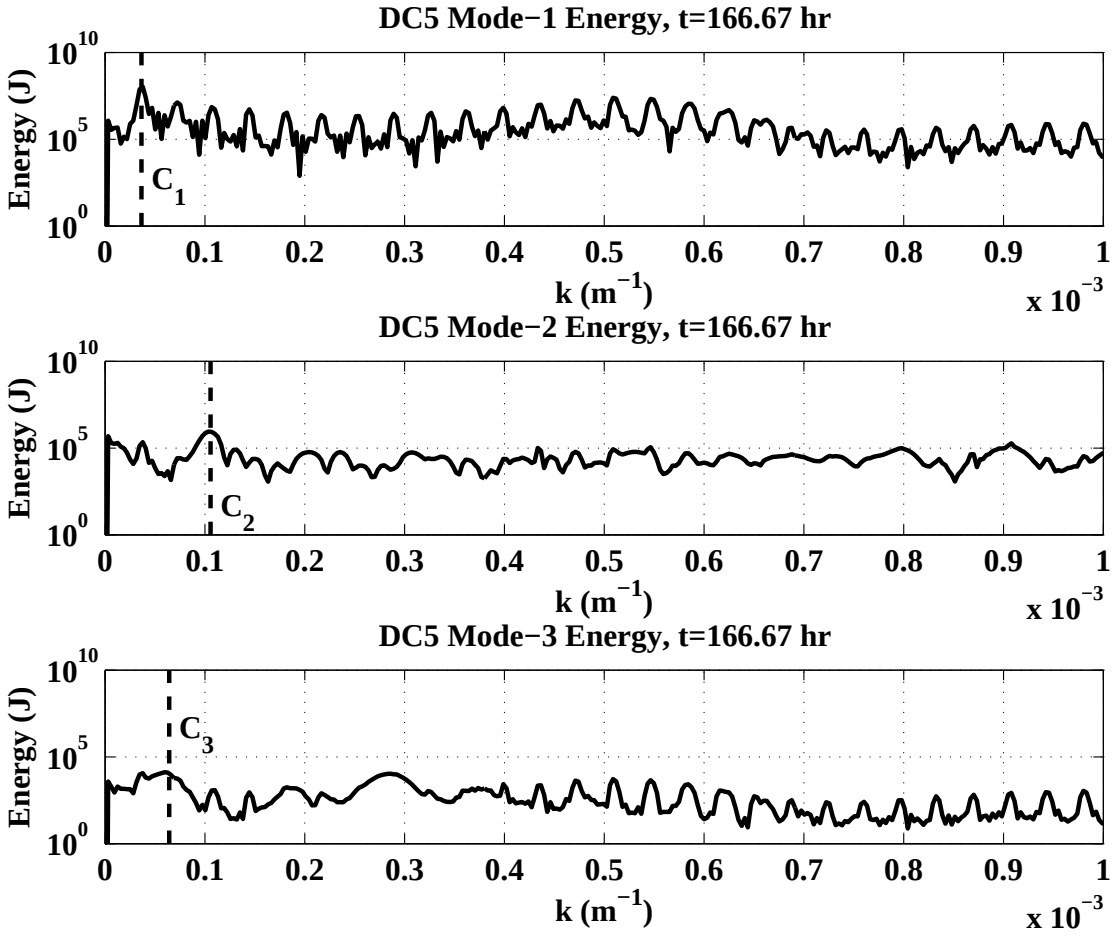

Figure 4.26: Pseudo-energy decomposition for DC5. The mode-1 peak (top subplot) lies near $k = 2.4 \cdot 10^{-5}$ m^{-1}, corresponding to wave C_1, but many other peaks are present due to the non-sinusoidal shape of the wave. In the middle subplot, the mode-2 energy peak lies near $k = 10^{-4}$ m^{-1}, corresponding to wave C_2. In the bottom subplot, the dominant mode-3 peak lies near $k = 6.2 \cdot 10^{-5}$ m^{-1}, corresponding to wave C_3. The vertical dashed lines mark the k values corresponding to waves C_1, C_2, and C_3.

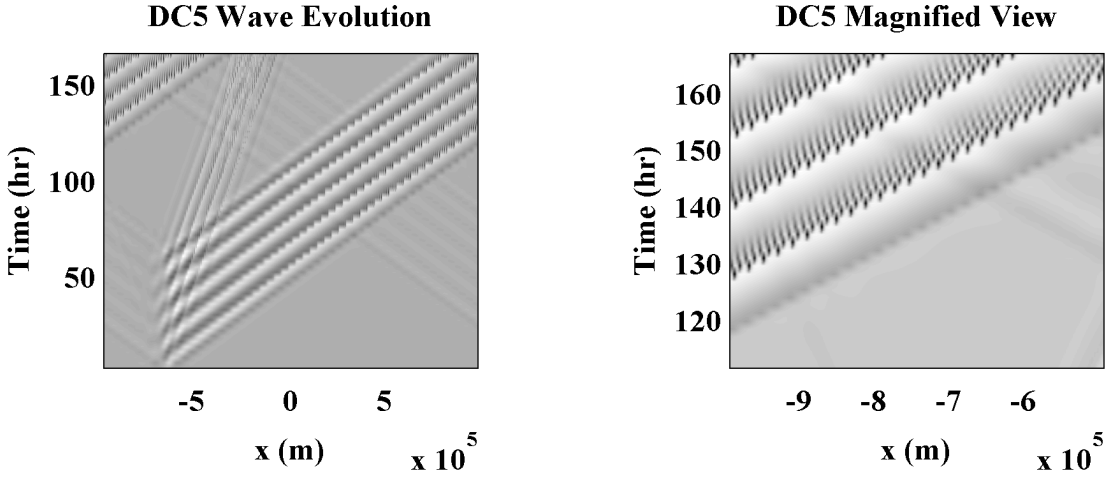

Figure 4.27: Hovmöller diagrams for test DC5. The simulation is run long enough that waves pass through the boundary. In the right subplot, a magnified view is shown, and the undular bores visible in the density contour diagram appear as striations in the lines of constant phase.

addition of a linearly varying term alters the top-to-bottom density change. With the parameters used here, the background density varies from 1025 kg/m^3 to 1030.15 kg/m^3, with 96% of the density jump occurring in the interval $1550 \leq z \leq 1850$ m. In Figure 4.28 the density profile and buoyancy frequency are plotted. The center of the pycnocline is seen to lie at $z = 1700$ meters, and the uniform stratification below $z = 1490$ m is apparent. Experiments using this stratification are prefixed by "DR", an abbreviation for "Deep Ocean Realistic Stratification".

Using the methods described in Section 3.1, a large number of candidate resonant triads were found. The list of possible candidates was reduced by using the same constraints as for the DC model. Table 4.10 provides the data for triad D, a triad that is investigated here. In triad D, the mode-1 M_2 wave (D_1) has a wavelength of roughly 147.4 km, about 25 km shorter than the wavelength of wave C_1. Unlike triad C, triad D consists of two mode-1 waves and a mode-2 wave. Waves D_1 and D_2 are rightward-propagating, and wave D_3 is leftward propagating. The first two modes of the dispersion relation for the DR stratification are plotted in Figure 4.29. Waves D_1 – D_3 are marked on the figure. Like triad C investigated above, the waves in triad D are very long relative to the pycnocline width and fluid depth.

Experiments with triad D cannot be directly compared against experiments with triad C because the underlying waves are of different mode numbers and wavelengths. However, if triad C had been chosen as a triad consisting only of mode-1 and 2 waves, it is likely the results would not have changed significantly. As described below, the steepening effects

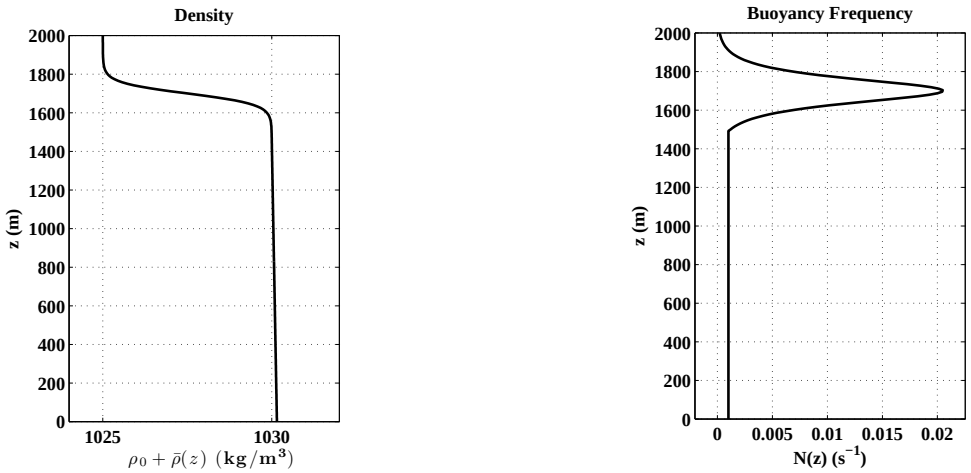

Figure 4.28: Background density (left subplot) and buoyancy frequency (right subplot) for the more realistic ocean scale simulations. The center of the pycnocline lies at $z = 1700$ m, and 96% of the density jump occurs across the interval $1550 \leq z \leq 1850$ m.

Triad D

Wave	Mode	ω (s^{-1})	T (hr)	k (m^{-1})	λ (km)	v (m/s)	γ
D_1	1	$1.4 \cdot 10^{-4}$	12.4	$4.3 \cdot 10^{-5}$	147.4	3.3	$-7.2 \cdot 10^{-4}$
D_2	2	$-5.2 \cdot 10^{-5}$	33.5	$-7.0 \cdot 10^{-5}$	90.33	0.75	$1.9 \cdot 10^{-4}$
D_3	1	$-8.7 \cdot 10^{-5}$	20.0	$2.6 \cdot 10^{-5}$	237.8	3.3	$-3.2 \cdot 10^{-3}$

$\delta_\omega = 1.4 \cdot 10^{-6}$ (s^{-1}) $\qquad$ $\delta_k = 5.1 \cdot 10^{-10}$ (m^{-1})

Table 4.10: Parameters for triad D, investigated for the DR experiments. From left-to-right, the columns are as follows: wave name, vertical mode number, frequency, period, wavenumber, wavelength, group velocity, interaction coefficient.

that plagued the DC experiments are due to the length of the waves and the proximity of the pycnocline to the surface. Therefore, experiments involving the M_2 tidal wave but different modes would have given similar results.

Monochromatic Forcing Experiments

Two monochromatic forcing experiments are included here. These are important because they give some insight into the basic evolution of the underlying waves in triad D. The experimental parameters are summarized in Table 4.11. Test DR1$^{\rightarrow}$ is used to demonstrate the evolution of wave D_1, and DR2$^{\rightarrow}$ is used to study the evolution of wave D_2. Test DR2$^{\rightarrow}$ has four times the horizontal resolution of DR1$^{\rightarrow}$, and, due to the smaller time steps required, took about 2.5 days to complete.

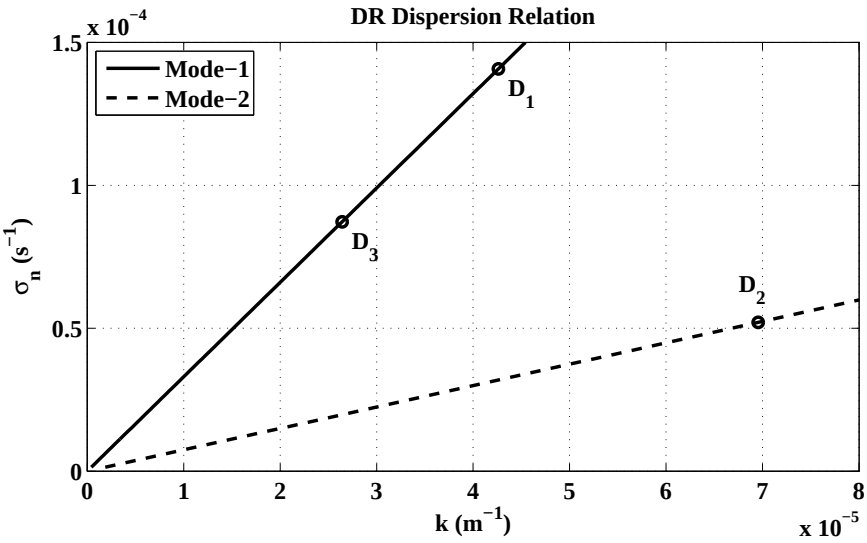

Figure 4.29: The dispersion relation for DR experiments. The waves in triad D are marked with circles (absolute values of wavenumbers and frequencies are plotted).

DR Monochromatic Forcing Experiments

Test	Wave	a_0 (m)	x_0 (km)	w_0 (km)	L (km)	max(**u**)/c
DR1$^{\rightarrow}$	D_1	0.25	-500	30.0	2000	0.048
DR2$^{\rightarrow}$	D_2	0.1	-150	30.0	500	0.43

Table 4.11: Monochromatic forcing experiments for triad D with the DR model. The final column, max(**u**)/c, gives the ratio of the maximum magnitude of the velocity to the phase speed of the underlying wave, and is a measure of wave steepness. Both experiments use 4096 horizontal grid points and 256 vertical grid points.

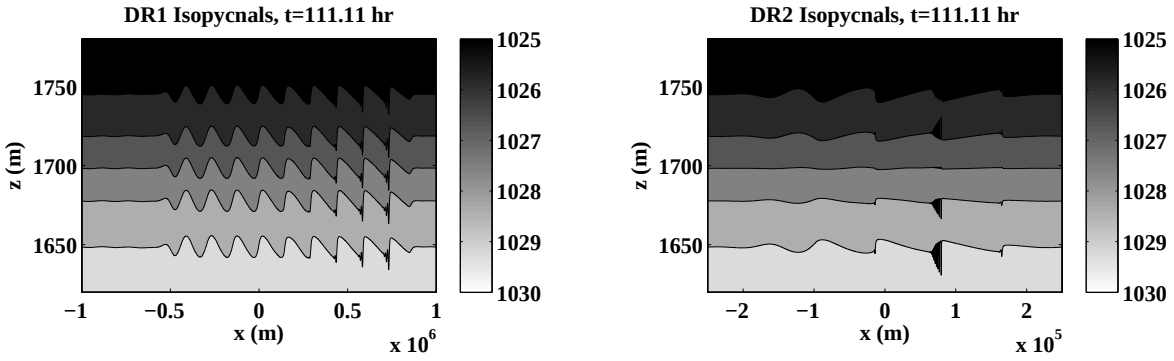

Figure 4.30: Density contour diagrams for tests DR1$^{\rightarrow}$ and DR2$^{\rightarrow}$. Wave steepening is visible within just a few wavelengths of the forcing center for wave D_1 in the left subplot. Small undular bores are visible in the waves to the right. In the right subplot, steepening of the mode-2 wave D_2 is visible within just one wavelength, and large undular bores are visible in the right portion of the figure.

In Figure 4.30, density contour diagrams are shown for tests DR1$^{\rightarrow}$ and DR2$^{\rightarrow}$ at $t = 111$ hours. The peak-to-trough isopycnal displacements for the mode-1 wave D_1 in test DR1$^{\rightarrow}$ are about 11 meters (away from the undular bores). Near the leading edge of the wave train small undular bores are forming on the steepened waves. The undular bores have a wavelength of about 11 km and are well-resolved. In test DR2$^{\rightarrow}$ the mode-2 wave D_2 was forced, and the resulting isopycnal contours are displayed in the right subplot of Figure 4.30. Away from the short-wavelength oscillations, the peak-to-trough isopycnal displacements for wave D_2 are about 8 – 9 meters. In the oscillatory regions the peak-to-trough isopycnal displacements are about 20 m. The wavelength of these undular bores varies from about 1.6 km to 2.6 km, and they have mode-2 vertical structure.

In the rightmost column of Table 4.11, the wave steepness parameter $\max(\mathbf{u})/c$ is given. For test DR1$^{\rightarrow}$ this value is very small. However, for test DR2$^{\rightarrow}$ the steepness measure is about 0.43. This relatively large value is due to the short wavelength oscillations. Away from these undular bores, $\max(\mathbf{u})/c$ is about 0.12. Further discussion of the wave steepening process for tests DR1$^{\rightarrow}$ and DR2$^{\rightarrow}$ is given in Section 4.3 below.

A Collision Experiment

Like test DC5, experiment DR3 is an attempt to observe a resonant wave interaction. The important parameters for the experiment are listed in Table 4.12. The forcing amplitudes were chosen to avoid the formation of undular bores in wave D_2.

Density contours for DR3 are plotted at $t = 33.3$ hours (left subplot) and $t = 166.7$ hours (right subplot) in Figure 4.31. The steepening effects are visible in the latter plot.

Collision Experiment for DR Stratification

Test	Waves	a_1, a_2 (m)	x_1, x_2 (km)	w_0 (km)	L (km)	Forcing Interval
DR3	D_1, D_2	0.2, 0.03	-1000, -500	30.0	3000.0	$0 \leq t \leq 55.5$ hr

Table 4.12: Experiment DR3. Waves D_1 and D_2 are forced with amplitudes a_1 and a_2, centered at locations x_1 and x_2. Both waves are forced with the same width measure w_0.

There is no visible evidence of a leftward-propagating wave resulting from an interaction. In Figure 4.32, a Hovmöller diagram for test DR3 is shown. The diagram shows the passage of waves D_1 through D_2, and the two waves overlap in the time interval given approximately by $40 \leq t \leq 120$ hours. Even with the long duration of overlapping, no evidence of wave D_3 is present. If D_3 were generated, a leftward-propagating beam would be seen emanating from the interaction region.

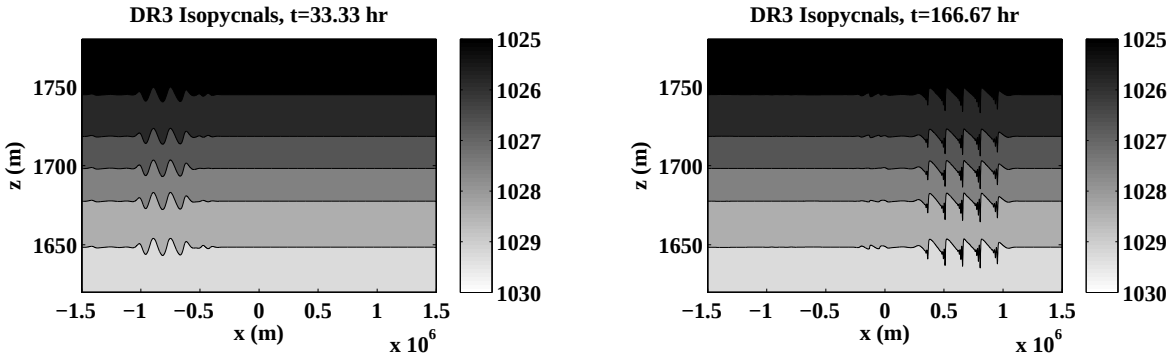

Figure 4.31: Density contour diagrams for collision experiment DR3. In the left subplot, $t = 33.3$ hours and slightly less than three M_2 tidal periods have elapsed. The small mode-2 wave is visible slightly to the right of the mode-1 waves. In the right subplot$t = 166.7$ hours, and the M_2 wave train has passed through wave D_2.

A pseudo-energy decomposition for DR3 is depicted in Figure 4.33. The dominant peaks in the mode-1 and mode-2 spectrum correspond to waves D_1 and D_2. There is a small peak near $2.6 \cdot 10^{-4}$ m^{-1} in the mode-1 spectrum that corresponds to wave D_3. The failure to generate a strong copy of wave D_3 through a resonant interaction is likely due to the steepening effects altering the underlying sinusoidal structure of waves D_1 and D_2. This is also what was observed in test DC5. In the next section this and other problems are investigated further.

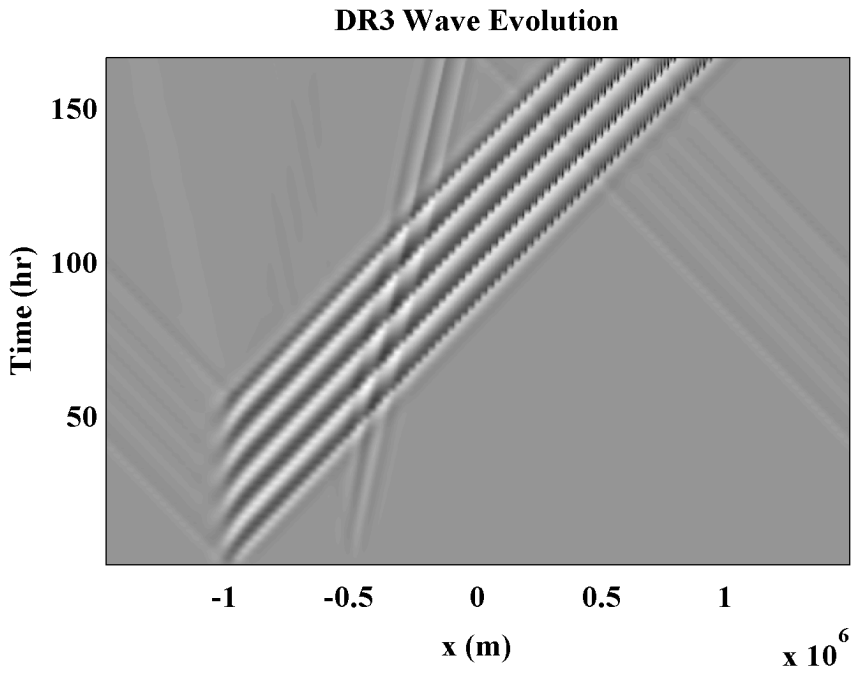

Figure 4.32: A Hovmöller diagram for test DR3. Wave D_1 starts to the left of wave D_2, they pass through each other, but no third wave is visible emanating from the interaction region.

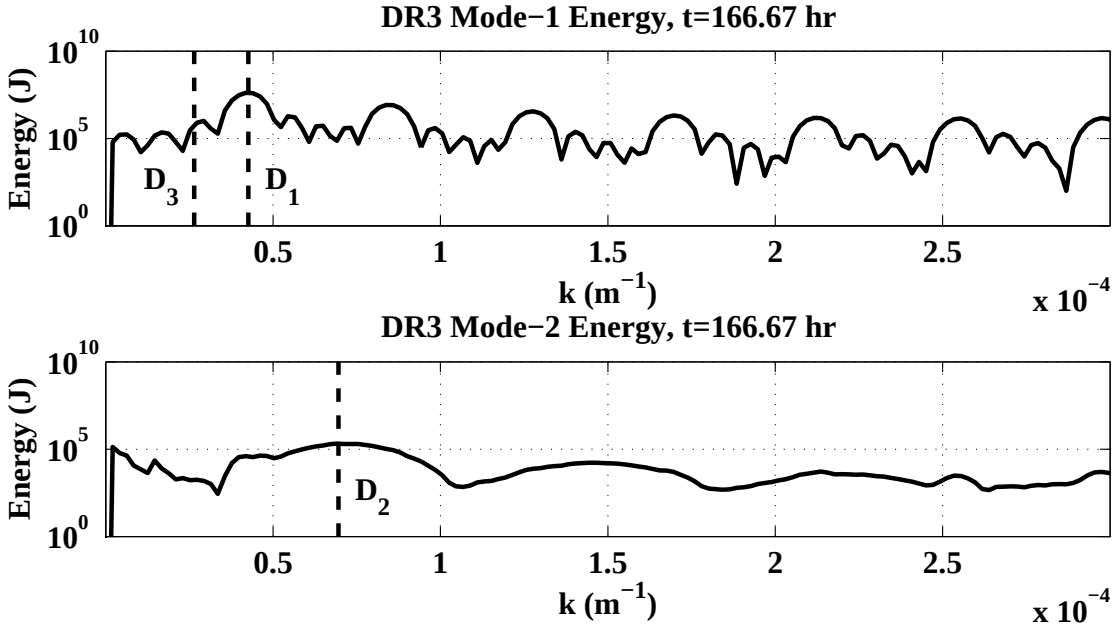

Figure 4.33: Energy decomposition for test DR3. The largest mode-1 peak lies at $k = 4 \cdot 10^{-5}$ m^{-1}, and the mode-2 peak corresponds to the forced wave D_2. There is only a small peak near $2.6 \cdot 10^{-5}$ m^{-1}in in the mode-1 spectrum corresponding to wave D_3. The wavenumbers of D_1, D_2, and D_3 are marked with vertical dashed lines.

4.3 Discussion

In this section some of the interesting results observed through simulations with the SPINS model are explored in more detail. Finite-amplitude effects are the focus of this discussion as they played an important role in many of the simulations presented above. Two different variants of finite-amplitude effects are considered, and some general conclusions about resonant interactions in the deep ocean are drawn.

4.3.1 Mode-2 Cnoidal Waves and Energy

In experiment L6, the interaction of waves B_1 and B_2 produced wave B_3, but the result was not a clean sinusoidal wave train. The troughs in Figure 4.13 are much broader than the crests. In the lone lab-scale test devoted to producing a mode-2 wave (L4), the desired result was achieved but the wave amplitude was very small. Other simulations not included above revealed that generating moderate amplitude mode-2 waves with clean sinusoidal shape is difficult if not impossible.

To further emphasize this point, consider Figure 4.34. The figure illustrates density isopycnals in an experiment attempting to generate wave B_3 with forcing amplitude $a_3 =$ 0.1 N. The wavelength for B_3 is about 22 cm, and the amplitude of the generated waves is less than 2 mm peak-to-trough but the waves do not have a sinusoidal shape. The wave steepness measure for this experiment is $\max(\mathbf{u})/c \approx 0.36$. The difficulty of generating mode-2 waves does not appear to be a flaw in the linear forcing theory. Figures 4.6 and 4.7 demonstrate that, at small enough amplitudes, it is possible to generate the desired waves. The observed waveforms at larger amplitudes must be the result of finite-amplitude effects.

In fact, the waves observed in Figure 4.13 and Figure 4.34 bear resemblance to the cnoidal wave sketched in the top subplot of Figure 4.35. The cnoidal waves plotted in that figure are defined by

$$s(x) = -\frac{1}{2} + \mathrm{cn}^2\left(\frac{x}{2K(m)\lambda}\right), \quad \text{where} \quad K(m) = \int_0^{\pi/2} \frac{dx}{\sqrt{1 - m^2\sin^2(x)}}. \tag{4.7}$$

Here *cn* is the Jacobian elliptic function, and λ is the wavelength. For an introduction to these functions the reader is referred to Drazin and Johnson [20, Chapter 2]. In Figure 4.35, the values $\lambda = 2\pi$ and $m = 0.995$ are used. These values were chosen so that the relative widths of the crests and troughs in the cnoidal wave train appear similar those in Figure 4.34. The power spectrum for the cnoidal wave is plotted in the bottom subplot of the figure. In contrast to the equivalent spectrum for a cosine wave of the same period, the cnoidal wave spectrum involves a shift of energy to the mean, as well as higher harmonics.

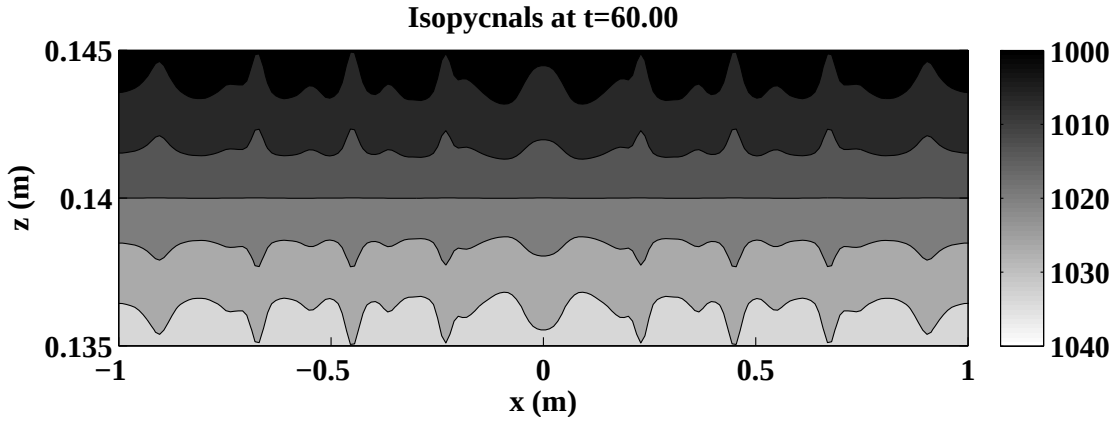

Figure 4.34: An example of B_3 waves formed from small amplitude mode-2 forcing. The waves appear to have a similar shape to the resonantly generated waves in Figure 4.13.

For a cnoidal wave train modulated by a long envelope, these sharp energy peaks become smeared out, and a significant portion of the energy may lie at low wavenumbers.

The energy shift to long waves, and eventually a mean flow, can be partially explained by a Stokes drift analysis. Stokes drift is well-known for surface waves, and is described by Kundu and Cohen [37, Chapter 7]. The essence of Stokes drift is that, on average, fluid particles in finite amplitude waves experience a non-zero horizontal Lagrangian velocity. The actual calculations are somewhat complicated for internal waves in nonuniform stratifications. Appendix C contains a detailed derivation. The analysis given there is similar to early work done by Thorpe [65], and the interested reader is also referred to research by Bretherton [11]. The mathematics reveals that within a train of monochromatic internal waves of amplitude a the mean Eulerian velocity is zero. However, the average height of an isopycnal is modified at $O(a^2)$. In particular, the averaged height of an isopycnal initially at z_0 in the undisturbed fluid is located at

$$\langle z \rangle = z_0 + a^2 \frac{1}{4\omega^2 N^2(z_0)} \frac{d(\phi_n^2 N^2)}{dz}\bigg|_{z_0}. \tag{4.8}$$

As a result of this, in the body of the wave train the stratification appears different from the quiescent background state. The time-averaged, modified stratification takes the form

$$\langle \rho_0(z) \rangle = \rho_0 + \bar{\rho}(z) + a^2 \frac{\rho_0}{g} \frac{1}{4\omega^2} \frac{d(\phi_n^2 N^2)}{dz}. \tag{4.9}$$

Therefore, when a wave train impinges on a quiescent region of fluid, the average isopycnal locations and stratification in front of and behind the wave are different. The isopycnals

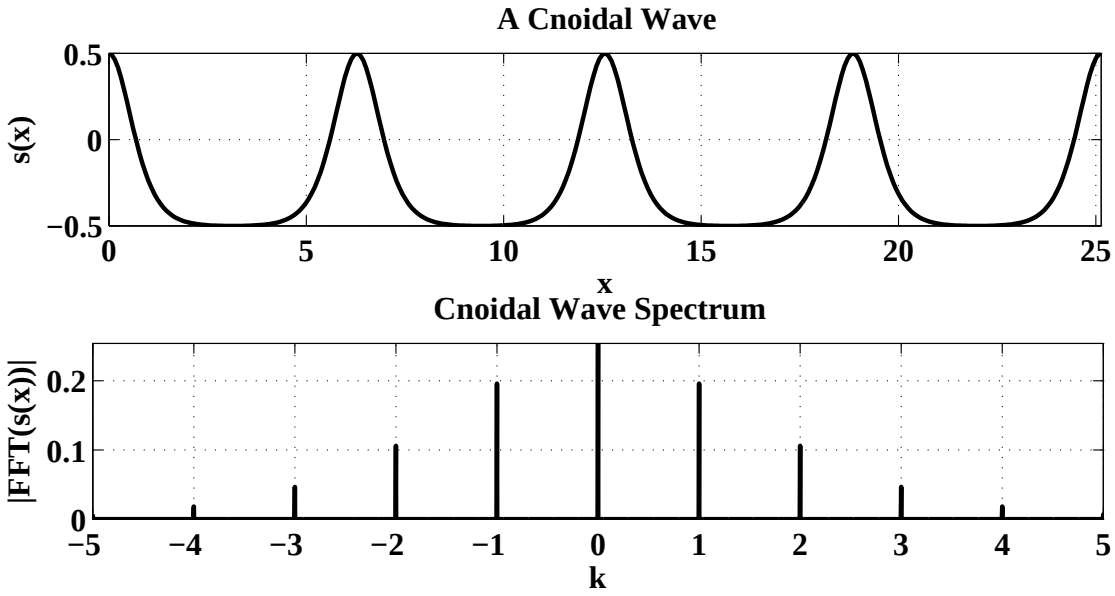

Figure 4.35: A cnoidal wave and its spectrum. The elliptic parameter $m = 0.995$, and the period is 2π. Note the broadened troughs and observe the spread of energy in the spectrum.

must then, on average, be tilted, and a flow ensues. When the wavy region is of finite extent the modified isopycnal heights will appear as long waves in the energy spectrum. The modal structure of the wave will determine the mode numbers at which the long wave energy appears. This discussion provides a possible explanation for the bottom subplot of Figure 4.4, where there is a clear indication of long mode-2 wave energy.

4.3.2 The Long Wave Steepening Process

The wave steepening observed in the ocean-scale simulations is the result of a different mechanism than that described above. Long wave steepening was observed for mode-1 and mode-2 waves, and instead of a cnoidal wave shape, undular bores (short wavelength oscillations) were observed. The reasons for this are now considered.

The shapes of steep long waves from different parts of the pycnocline are illustrated in Figure 4.36. In the left panels, isopycnals from test DC2 are plotted. Panel (a) shows an isopycnal from near the top of the pycnocline, and panel (b) shows an isopycnal from near the bottom of the pycnocline. The mode-1 wave has steepened along the leading edge of each trough. In panels (c) and (d), similar plots show isopycnals from DC4 (a mode-2 experiment). In contrast to the mode-1 case, the mode-2 wave travels as a bulge on the

pycnocline. The outer edges of the mode-2 bulge appear to travel fastest, so the waves are steepening on the front side.

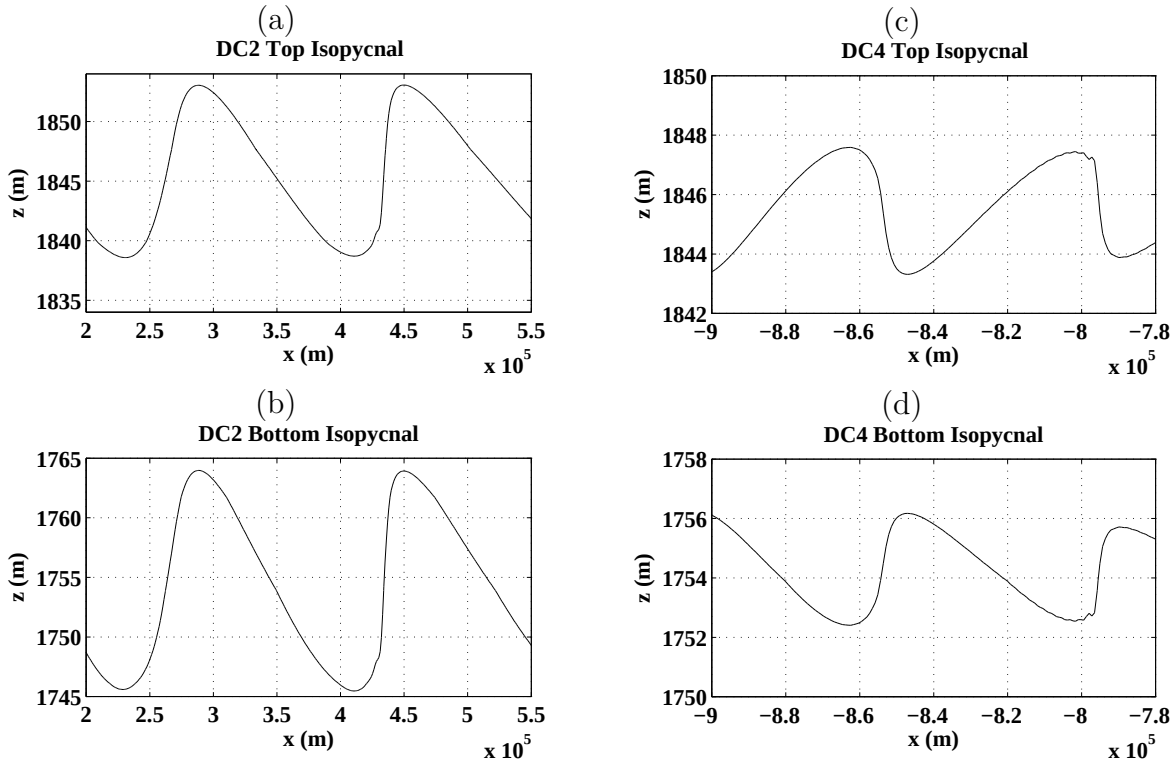

Figure 4.36: Mode-1 (panels (a) and (b)) and mode-2 (panels (c) and (d)) long wave steepening. Panels (a) and (b) are taken from test DC2 at $t = 62.2$ hours, panels (c) and (d) are taken from DC4 at $t = 111.1$ hours. The top panels show an isopycnal from the upper portion of the pycnocline, the bottom panels show an isopycnal from the lower portion of the pycnocline. Mode-1 waves appear to steepen from behind. The mode-2 waves propagate as a bulge on the pycnocline.

An explanation for the left portion of Figure 4.36 is as follows. When the pycnocline lies above the mid-depth of the fluid, internal solitary waves are waves of depression, and their speed increases with amplitude. As a result of this, mode-1 troughs travel faster than crests, so the waves steepen along the leading edge of the troughs.

The isopycnals illustrated in Figure 4.36 are taken prior to the onset of undular bores (see Figure 4.20). To convince the reader that the bores that arise are not due to Gibbs phenomena, consider Figure 4.37. In that figure, a magnified view of the isopycnal contours is shown for test DR1$^{\rightarrow}$. The contours are smooth, and there are about 22 horizontal grid points per bore wavelength, so the bores are very well-resolved.

In Figure 4.38, a magnified view of the isopycnals from test DR2$^{\rightarrow}$ is presented. The

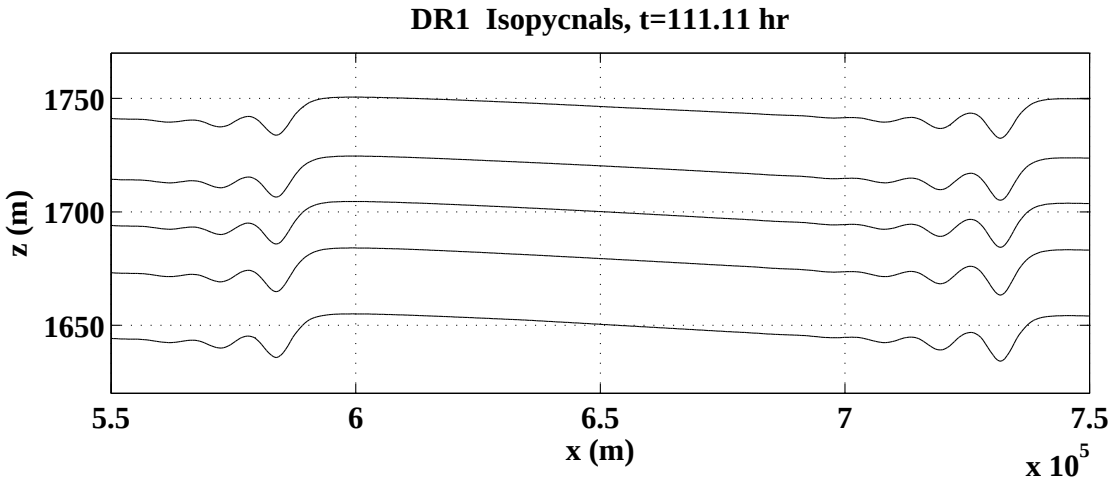

Figure 4.37: A magnified view of the isopycnals for test DR1$^{\rightarrow}$. The short undular bore oscillations are well-resolved with about 22 grid points per wavelength.

undular bores possess a mode-2 vertical shape and are strongly cnoidal in their horizontal structure. The cnoidal waves have a wavelength of about 1.6 km at the left of the undular bores, and about 2.6 km at the right. The horizontal grid spacing is about 122 m, so the bores are well-resolved. The narrow peaks of the cnoidal waves do cause resolution issues, and simulations involving grid spacings of 250 m fell victim to Gibbs oscillations. This demonstrates a difficulty in simulating large-amplitude, long mode-2 waves. The number of grid points required to resolve the sharp cnoidal peaks to avoid numerical instabilities may lead to prohibitively slow computations.

Lamb and Yan [42] compared mathematical theory with numerical simulations of undular bore formation in long internal waves. Their work shows that accurate modeling of the bores requires inclusion of all second-order nonlinear and dispersive terms in the model equations. Such an undertaking is beyond the scope of the present work, the interested reader is directed to their paper.

Physical causes for the nonlinear behaviour observed in the ocean simulations can be found by comparing the lab and ocean-scale experiments. One factor that can be ruled out is the relative thickness of the pycnocline. The ratio of the 99% width measure to the fluid depth for the lab and ocean-scale experiments is 0.125 and 0.15, respectively. These values are quite similar, and thus not likely to be a major factor in steepening and bore formation. Other possible factors include the Froude number, wave steepness, wavelength of the forced waves, and proximity of the pycnocline to the surface. These possibilities are now considered. A comparison of dimensionless wave parameters for the lab and ocean-scale experiments is presented in Tables 4.13 and 4.14. In Table 4.13 mode-

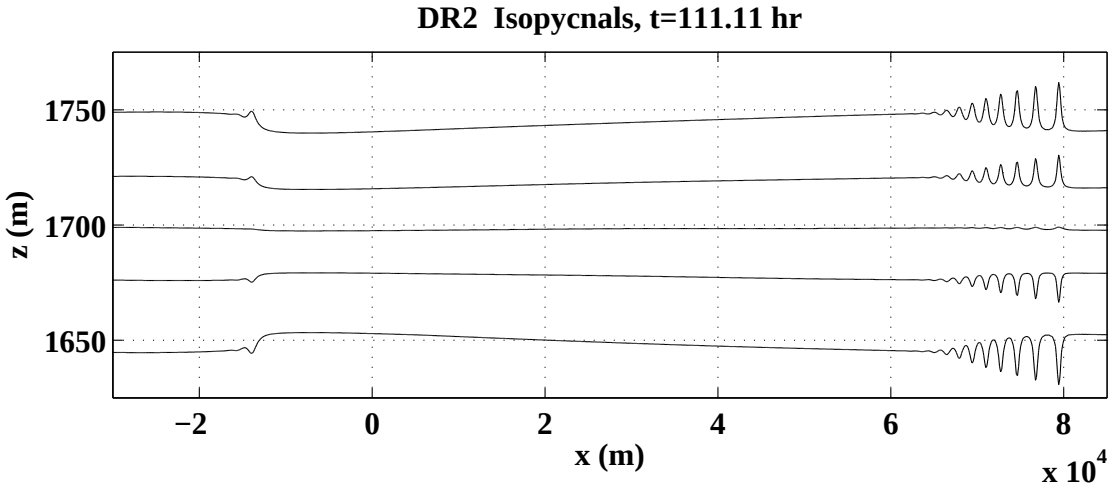

Figure 4.38: A magnified view of isopycnals for test DR2$^{\rightarrow}$. The undular bores have a mode-2 vertical structure and have a cnoidal horizontal shape. The cnoidal waves do not have a constant wavelength, with longer waves appearing on the right. There are at least 12 horizontal grid points per undular bore.

Comparison of Mode-1 Dimensionless Wave Parameters

Experiment	Wave	ka	$k\delta$	Fr
L1	A_1	0.16	0.77	0.2
DC2	C_1	$4 \cdot 10^{-4}$	0.01	0.099
DR1$^{\rightarrow}$	D_1	$2.5 \cdot 10^{-4}$	$7.5 \cdot 10^{-3}$	0.025

Table 4.13: Comparison of dimensionless steepness parameters of representative mode-1 experiments. The wavenumber k corresponds to that of the wave specified in each row. The wave amplitude a is taken to be half the observed peak-to-trough value, and the pycnocline thickness δ is taken as the 99% width measure (96% in DR experiments). In the final column, the Froude number Fr=max(**u**)/c gives the ratio of the maximum induced velocity to the phase speed of the underlying wave during the simulation.

1 experiments are compared. In each of the three dimensionless parameters reported in the table, the lab-scale experiment L1 has the largest value. However, waves in test L1 were observed to be sinusoidal. In Table 4.14 the dimensionless parameters for mode-2 experiments are presented. The large Froude number for DR2$^{\rightarrow}$ is somewhat misleading because it is due to the high velocities in the vicinity of the short-wavelength undular bores. Prior to the onset of undular bores, the Froude number was about 0.13 for test DR2$^{\rightarrow}$. Taking this into account, dimensionless parameters for the lab-scale experiment L4 exceed those of both ocean-scale experiments in the table. No steepening or bore formation was observed for either of the lab-scale experiments in the tables. This suggests that the major factors controlling steepening and bore formation must be a combination of wavelength and pycnocline proximity to the surface.

Comparison of Mode-2 Dimensionless Wave Parameters

Experiment	Wave	ka	$k\delta$	Fr
L4	A_2	0.08	4.15	0.24
DC4$^{\rightarrow}$	C_2	$2.7 \cdot 10^{-4}$	0.032	0.12
DR2$^{\rightarrow}$	D_2	$3.2 \cdot 10^{-4}$	0.02	0.43

Table 4.14: Comparison of dimensionless wave parameters of representative mode-2 experiments. The wavenumber k corresponds to that of the wave specified in each row. The wave amplitude a is taken to be half the observed peak-to-trough value, and the pycnocline thickness δ is taken as the 99% width measure (96% in DR experiments). In the final column, the Froude number Fr=max($\mathbf{u}$)/c gives the ratio of the maximum induced velocity to the phase speed of the underlying wave during the simulation.

Indeed, in a given stratification longer waves generally experience weaker dispersion. This is expected because dispersive models describing long internal waves involve high-order derivatives in the spatial coordinate. As the wavelength increases, nonlinear effects will deform a wave to a much greater degree before dispersion becomes important. The nonlinear effects are further enhanced when the pycnocline lies close to the surface. To illustrate this point, consider Figure 4.39. The figure depicts the density isopycnals at $t = 66.7$ hours for a wave with wavelength 172 km in a stratification identical to the DC model, except that the pycnocline is centered at $z_p = 1400$ m. The chosen wavelength is the same as that of wave C_1, and the relative depth of the pycnocline is equivalent to that used for the lab-scale experiments. Peak-to-trough isopycnal displacements are about 10-11 m for the mode-1 wave, about 60% larger than those seen in experiment DC1. The steepening effects observed in experiment DC1 are not as pronounced in Figure 4.39 even though the waves are of larger amplitude. Using the KdV equation as the model for long dispersive internal waves in the DC stratification, it is found that moving the pycnocline depth from 200 m to 600 m decreases the nonlinearity coefficient by about a factor of three. Similarly, the dispersive coefficient increases by a factor of about three.

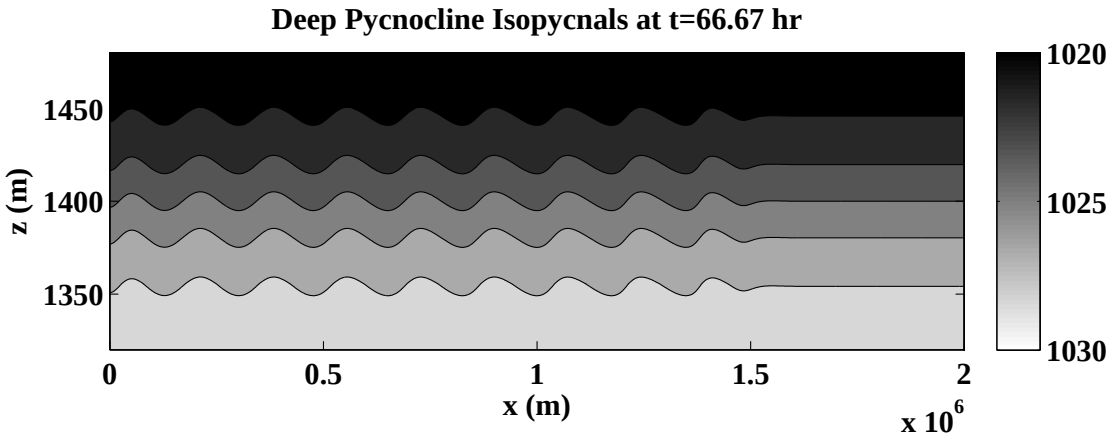

Figure 4.39: Density contours for a mode-1 wave with wavelength 172 km on a pycnocline 600 m below the surface in a fluid of depth 2 km. Steepening effects are visible in the sixth period and onwards.

The KdV equation can be used to construct estimates for the wave steepening time. Since only a rough approximation is desired, the KdV equation for interfacial waves in a two-layer fluid is used here:

$$\eta_t + c_0\eta + \frac{3}{2}\left(\frac{h_1 - h_2}{h_1 h_2}\right) c_0\eta\eta_x + \frac{1}{6}c_0 h_1 h_2 \eta_{xxx} = 0. \tag{4.10}$$

This equation is derived and discussed in detail by Gerkema and Zimmerman [28, Chapter 8], for instance. Here $\eta(x,t)$ gives the interface height, g' is the reduced gravity, h_1 and h_2 are the layer depths, and $c_0 = \sqrt{g'h_1h_2/(h_1+h_2)}$ is the long-wave phase speed (see Appendix A). To estimate breaking times, a gradient catastrophe analysis is performed. The analysis closely follows Knobel [35, Chapter 18]. To simplify the calculation, the dispersive term in (4.10) is ignored and the coefficient of the nonlinear term is denoted by v. Thus the inviscid Burger's equation

$$\eta_t + c_0\eta + v\eta\eta_x = 0, \tag{4.11}$$

is considered, and the initial condition $\eta(x,0) = A\sin(kx) = \eta_0(x)$ is taken. Analyzing the characteristic curves provides the estimate for the breaking time of the initially sinusoidal wave train. The characteristic curves are defined implicitly by $x(t) = (c_0 + v\eta_0(x_0))t + x_0$, and wave breaking occurs when characteristics intersect, so that η_x becomes infinite. Since the exact solution to (4.11) is simply $\eta(x,t) = \eta_0(x_0)$, it follows that $\eta_x = \eta_0'(x_0)\partial x_0/\partial x$, where:

$$\frac{\partial x_0}{\partial x} = \frac{1}{1 + vt\eta_0'(x_0)}. \tag{4.12}$$

From this, it is clear that breaking first occurs for an initially sinusoidal wave at time

$$t_B = -\frac{1}{vAk}. \tag{4.13}$$

As expected, this suggests that larger amplitude waves break more rapidly.

For the DC stratification, the M_2 tidal wave of 9 meter amplitude (corresponding to test DC1) has a breaking time of about $t_B = 32$ hours. For the interaction experiment DC5, the expected breaking time for the M_2 tidal wave is about 41 hours. Following the discussion in Chapter 2, waves q and r perturbing wave p in a triad grow like $\exp(\sqrt{\gamma_q \gamma_r}\epsilon t)$. For experiment DC5 wave C_3 then has an e-folding time of about 5 hours. Similarly, for experiment DR3$^{\rightarrow}$, the breaking time for the M_2 wave is about 100 hours, while the e-folding time for the interaction is about 5 hours. In both experiments the interaction time scale is significantly shorter than the steepening time scale.

4.3.3 Implications

The strong tendency for waves to demonstrate nonlinear behaviour, through the formation of cnoidal waves or undular bores, is problematic for the resonant interaction theory developed in this thesis. The theory presented in Chapter 2 was derived using sinusoidal functions to describe the horizontal shape of waves. Clearly this is not the case for waves of modest amplitudes on the stratifications considered in this chapter. In addition, the pseudo-energy decomposition that was developed in Chapter 3, and used extensively above, is based on a decomposition onto sinusoidal basis functions. The complicated horizontal structure of the finite amplitude waves diminishes the value of this pseudo-energy analysis. As a result, the energy plots presented in this chapter should only be used as rough, approximate descriptions of wave energy content.

These problems highlight a shortcoming of the weakly-nonlinear theory, and motivate the study of a more descriptive model. Work done by Osborne [56] suggests that it may be possible to extend the weakly-nonlinear analysis to a theory for triad interactions among cnoidal waves. Similarly, improved data decompositions, based on nonlinear Fourier transform techniques, could be of benefit. These extensions would involve considerable mathematical challenges, and they are not pursued here.

The simulations involving the DC and DR stratifications suggest that long internal waves (near M_2 tidal wavelength) of modest amplitude steepen rapidly, hindering the progress of near-resonant interactions. At smaller amplitudes nonlinear effects are reduced, but the time scale of wave interactions increases. Numerical experiments conducted by Lamb [41] show that in regions of the ocean where the stratification is weaker or more uniform, and hence nonlinear effects are less pronounced, resonant interactions can play a strong role.

The significance of the ocean-scale simulations must be tempered by the fact that rotational effects were not included. The importance of rotation in the experiments can be estimated by considering the Rossby number, U/fL. For instance, using the maximum induced flow velocity for U and the wavelength of wave C_1 for L, the Rossby number for test DC1 at 30° latitude is $O(10^{-2})$. This small value demonstrates that rotation is very important. As discussed by Farmer et al. [25], Helfrich and Grimshaw [31]), and others, rotational dispersive effects tend to inhibit the steepening process. This reduction in steepening could enable the expected interactions to unfold as predicted. To properly quantify the importance of near-resonant interactions among long waves in the ocean it is therefore necessary to conduct further experiments using the f-plane model.

As mentioned above, in the absence of rotation the weakly-nonlinear theory is not appropriate for describing long wave interactions. In certain regions of the oceans, however, the theory may still provide important insights. In shallow waters where the pycnocline lies closer to the mid-depth level, the strength of the nonlinear coefficient for long wave models is reduced (see equation (4.10)). In addition, the M_2 tidal wavelength decreases as water depth decreases, increasing the importance of dispersion. It can be expected that wave trains of tidal frequency propagating through shallow water would not steepen so dramatically. In such regions the desired resonant interactions might unfold as predicted by the weakly nonlinear-theory.

Finally, it might be profitable to analyze interactions involving the undular bores associated with the long waves. These bores are of moderate wavelength, and their modification through resonant triad interactions would in turn alter the balance of dispersion and nonlinearity in the accompanying long wave. The ensuing wave evolution process would be very interesting to observe.

Chapter 5

Asymptotic Analysis of Forced Wave Equations

In this chapter analytical techniques for studying forced wave problems are presented. This investigation was initially inspired by the early failures in attempts to numerically force internal gravity waves. The solution described in Section 3.5 produced satisfactory results in numerical tests, but a broader question remained. Given a wave equation on an infinite domain and an oscillatory source localized in a region, what waves can be expected to propagate from the forcing zone? What amplitude, phase, and wavelength do the waves possess? Even for simple wave equations these questions are difficult to answer, and asymptotic methods become essential tools.

While the initial goal was to analyze forced internal gravity waves, the problem was found too difficult, and a sequence of easier problems was tackled. The study of simpler problems allows for the development of a repertoire of useful techniques. In Section 5.1 the notation and asymptotic analysis used to study the wave equations is presented. As a first illustration of the solution method, the forced linear Korteweg-de Vries (KdV) problem is studied in Section 5.2. Then the linear Benjamin-Bona-Mahony (BBM) equation is studied in Section 5.3. The asymptotic methods are then applied to investigate the internal gravity wave (IGW) problem in Section 5.4. The intricate details of the steepest descents analysis for each wave equation is found in Appendix D. This chapter concludes with a brief discussion in Section 5.5.

5.1 Solution Techniques and Notation

In this section the methods and notation used to analyze forced wave equations are presented. After briefly discussing the Fourier transform, a discussion of how to deform

integration contours that pass through singularities is presented. An introduction to some useful techniques for the asymptotic expansions of integrals is then provided.

5.1.1 The Fourier Transform

The Fourier transform plays a vital role in the analysis of partial differential equations and wave phenomena. It has many applications, and a broad range of examples are given by Duffy [23]. Slight variants and different notation for the transform are used in different branches of Mathematics. In this document, the following conventions are used. A function $G(k)$ is defined as the Fourier transform of $g(x)$ when

$$G(k) = \mathcal{F}\{g(x)\} = \int_{-\infty}^{\infty} g(x) \exp(-ikx)\ dx. \tag{5.1}$$

The function $g(x)$ is determined from $G(k)$ by the inverse Fourier transform formula

$$g(x) = \mathcal{F}^{-1}\{G(k)\} = \frac{1}{2\pi} \int_{-\infty}^{\infty} G(k) \exp(ikx)\ dk. \tag{5.2}$$

The operator $\mathcal{F}$ is used to represent the transform, and $g(x)$ and $G(k)$ are said to be a Fourier transform pair.

The Fourier transform is generally used to decompose a function of a physical variable, such as the position, x, into its constituent wave components. The variable k represents the wavenumber, and is related to the wavelength λ of the corresponding wave by the relation $k = 2\pi/\lambda$.

It frequently occurs that the integrand in the inverse Fourier transform has singularities lying on the real axis. Since integration cannot be carried out directly through a singularity, a modified definition of the inverse Fourier transform is required. The inverse formula takes the more general form

$$g(x) = \frac{1}{2\pi} \int_{C} G(k) \exp(ikx)\ dk, \tag{5.3}$$

where C is a contour whose real part ranges from $-\infty$ to $+\infty$ and traverses the real line, but is deformed around the singularities of the integrand. The procedure for determining how to indent the contour C is now discussed.

5.1.2 Avoiding Poles on the Path of Integration

The contours of integration that arise from inverting Fourier solutions to PDEs must be chosen so as to avoid directly passing through singularities of the integrand. Physical

arguments dictate how the contour must be indented around any poles lying on the real k axis. Once it has been determined that the contour should be indented below (above) a given pole, the pole will only contribute a residue to integrals closed in the upper (lower) half-plane.

To determine whether to indent a contour above or below a particular pole, two lines of physical reasoning are considered here, both are discussed briefly by Voisin [71]. In the first approach the wave equation is modified with a dissipative term, and the behaviour of the pole is studied in the dissipative limit. In the second approach, following a method constructed by Lighthill [45], the behaviour of the pole is studied for the related forced problem where the forcing amplitude is ramped up from $t = -\infty$. Both methods express the same physical constraint, known as the Sommerfeld radiation condition, that waves cannot propagate inwards from infinity. As a rule, contours are deformed below poles that approach the real axis from the upper half-plane, and above poles that approach from the lower half-plane.

As will be seen, the Fourier-space solutions to forced wave equations have poles that lie at wavenumbers k satisfying

$$\sigma(k) + \omega = 0. \tag{5.4}$$

Here ω is the forcing frequency and $\sigma(k)$ is the dispersion relation. In the analysis that follows, the poles on the real k axis are assumed to be roots of (5.4).

The Dissipative Approach

Consider a function $u(x,t)$ governed by a linear PDE with constant coefficients, represented by the operator L. Then

$$Lu = A\exp(i\omega t)f(x) \tag{5.5}$$

is the forced problem of interest. Only $t \geq 0$ is considered, but for this analysis, boundary and initial conditions are not important. Substituting $u = \exp(i(kx - \sigma t))$ into the homogeneous problem ($A = 0$) leads to the dispersion relation $\sigma(k)$. This is defined implicitly through the algebraic equation

$$D(\sigma, k) = 0, \tag{5.6}$$

and multiple roots for $\sigma(k)$ may exist.

Now restrict attention to operators that are first-order in time. If a dissipative term is added to the homogeneous problem then

$$Lu = \epsilon u_{xx}. \tag{5.7}$$

This leads to a modified dispersion relationship $\hat{\sigma}(k)$ defined through the equation

$$D(\hat{\sigma}, k) = -\epsilon k^2. \tag{5.8}$$

For ϵ sufficiently small, the expansion

$$\hat{\sigma}(k) = \sigma(k) + \epsilon\sigma_1(k) + O(\epsilon^2) \tag{5.9}$$

is assumed valid. Substituting this expansion into $D(\hat{\sigma}, k) = -\epsilon k^2$ and collecting like terms reveals

$$D(\sigma, k) + \epsilon\left(\sigma_1 \frac{\partial D}{\partial \sigma} + k^2\right) + O(\epsilon^2) = 0, \tag{5.10}$$

where $\partial D/\partial\sigma = D_\sigma$ for shorthand. For equality to hold, the coefficient of each power of ϵ must be zero. Then, setting the coefficient of ϵ to zero requires

$$\sigma_1(k) = -\frac{k^2}{D_\sigma}. \tag{5.11}$$

Now turn to the solution of the equation $\sigma(k) + \omega = 0$, whose roots define the poles of the integrand. Suppose $k = k_0$ is a root. The corresponding root $\hat{k}$ for the dissipative problem must satisfy

$$\hat{\sigma}(\hat{k}) + \omega = 0. \tag{5.12}$$

The dissipation is assumed so small that $\hat{k}$ and k_0 are close, so that the expansion $\hat{k} = k_0 + \epsilon k_1 + O(\epsilon^2)$ is valid. Substituting this series into (5.12), expanding $\hat{\sigma}$, and collecting like powers of ϵ yields

$$\sigma(k_0) + \omega + \epsilon\big(k_1\sigma'(k_0) + \sigma_1(k_0)\big) + O(\epsilon^2) = 0, \tag{5.13}$$

where the prime symbol represents differentiation with respect to k. By the definition of σ and k_0, the leading order term is zero. Equating the coefficient of ϵ to zero requires

$$k_1 = \frac{k_0^2}{D_\sigma \sigma'(k_0)}. \tag{5.14}$$

A few observations are in order. Under the assumption that the PDE is first-order in time, the derivative $D_\sigma = -i$. The first-order correction to the root at k_0 is then

$$k_1 = i\frac{k_0^2}{\sigma_0'(k_0)}. \tag{5.15}$$

Since the root behaves like $k_0 + \epsilon k_1$ in the dissipative limit, the sign of the group velocity at k_0 dictates how the corresponding pole is approached in the complex plane. When the group velocity is positive, the pole is approached from the upper half-plane. When the group velocity is negative, the pole is approached from the lower half-plane. By considering the underlying PDE as the limit of a dissipative system, it is logical to deform contours of

integration to pass below poles that approach the real k axis from the upper half-plane, and above those that approach from the lower half-plane.

This approach to finding the proper way to deform integration contours can be difficult to apply for more complicated equations. When the underlying PDE involves higher order derivatives in time, special care must be taken in the form of the dissipative term that is used. Simply analyzing $Lu = \epsilon u_{xx}$ is not appropriate. For example, if L consists of only even ordered derivatives then D and all of its derivatives with respect to σ will be real, as will group velocities at the roots of $\sigma(k) + \omega = 0$. The higher-order corrections to the roots will then always be real, so the contour deformation cannot be determined.

Lighthill's Method

Lighthill presents an alternative means of determining how poles approach the real axis in a physical limit [45, Chapter 4]. Instead of modifying the dispersion relationship through dissipation, an alternative, ramped forcing problem is considered. The basic idea is to adjust the forcing frequency ω to include a small imaginary component, and consider the problem starting from $t = -\infty$. This shifts the poles off the real axis in a manner that is now described in more detail.

Once again, consider the general form of the impulsively forced problem given by equation (5.5). Suppose the solution is to be expressed as an integral and the contour must be determined near a pole. Assume that the pole of interest lies at $k = k_0$ and satisfies $\sigma(k_0) + \omega = 0$. The analysis proceeds by considering the related problem where the forcing begins at $t = -\infty$, but is ramped-up from zero initial amplitude by the use of a complex frequency $\omega - i\epsilon$, where $0 < \epsilon \ll 1$. The corresponding pole $\hat{k}$ for the modified problem satisfies

$$\sigma(\hat{k}) + \omega - i\epsilon = 0. \tag{5.16}$$

Using the expansion $\hat{k} = k_0 + \epsilon k_1 + O(\epsilon^2)$, substituting it in to (5.16), performing a Taylor expansion, and collecting like powers of ϵ reveals

$$\sigma(k_0) + \omega + \epsilon\left(k_1\sigma_0'(k_0) - i\right) + O(\epsilon^2) = 0. \tag{5.17}$$

The leading order term is zero by the definition of k_0. Equating the coefficient of ϵ to zero requires

$$k_1 = \frac{i}{\sigma'(k_0)}. \tag{5.18}$$

Note that k_1 represents the first-order correction to the pole at k_0 as $\epsilon \to 0^+$. Therefore the pole k_0 approaches the real axis from the upper half-plane when the group velocity of the forced wave is positive, and from the lower half-plane when the group velocity is negative.

The modified problem can be used to determine how to deform contours as follows. If the forced problem were ramped up from $t = -\infty$, at $t = 0$, only rightward-propagating waves should be found to the right of the forcing region, and only leftward-propagating waves should be found to the left of the forcing region. Therefore contours of integration must be deformed below poles at wavenumbers with positive group velocity and above poles at wavenumbers with negative group velocity.

Lighthill's approach agrees with the dissipative argument presented above, however it requires less effort. Unlike the dissipative argument, the modified problem does not change the dispersion relation $\sigma(k)$, so the required expansions are easier to perform. In addition, Lighthill's method can also be applied to equations with higher-order time derivatives with ease.

Discussion

Both the dissipative argument and Lighthill's approach suggest the appropriate criteria for deforming the contour of integration when expressing the solution to impulsively forced wave equations with the inverse Fourier transform. The integration contour must be deformed below poles corresponding to wavenumbers with positive group velocity and above poles corresponding to wavenumbers with negative group velocity.

A problem arises when a pole of the integrand corresponds to a wave with zero group velocity. In that situation both techniques discussed here can lead to a pole that approaches from both the top and bottom half of the complex plane. However, if the intent is to study traveling waves far from the forcing region such pathological cases are not a problem: the contribution from the pole can simply be ignored. Waves with zero group velocity cannot escape the forcing region. Parameter choices that lead to such waves may be of interest, however, as the build-up of waves in the forcing region would cause the breakdown of the validity of the linearized model.

5.1.3 Forcing with Point Sources

The Dirac-delta function is used throughout this chapter to represent point sources. This generalized function is denoted by $\delta(x)$ and is particularly useful in Fourier analysis. More general forcing functions $f(x)$ introduce difficulties because their Fourier transforms can be poorly behaved in the complex plane. For instance, the Fourier transform of the Gaussian $f(x) = \exp(-x^2)$ is $F(k) = \sqrt{\pi}\exp(-k^2/4)$. Although $f(x)$ is well behaved on the real line, $F(k)$ grows super-exponentially in the sectors of the complex k-plane bounded by angles $\pi/4 < \theta < 3\pi/4$ and $5\pi/4 < \theta < 7\pi/4$.

While point sources are useful for analysis, they are difficult to work with numerically. This leads to problems when comparing numerical and asymptotic solutions. There is, however, a simple way to use the point source solution to determine the leading order behaviour for a more general forced problem. The method works when $f(x)$ is a localized function, as seen below.

Suppose u satisfies the linear PDE $Lu = \exp(i\omega t)\delta(x)$. Then the solution of $Lv = \exp(i\omega t)f(x)$ is given by $v = f \star u$, where '$\star$' denotes the convolution operator. This is apparent by applying L to the convolution integral. The function u is actually the Green's function in the spatial coordinate (see Duffy [22]).

Now consider the situation when the problem is so difficult that only an asymptotic solution u_a can be found as $t \to \infty$. With $u \sim u_a$, it follows that $v \sim f \star u_a$. In general, the convolution cannot be computed directly because $u_a(x,t)$ may involve complicated terms with ratios of x/t. It is often the case, however, that the leading order behaviour of u_a is given by $u_a(x,t) \sim A\exp(i(k_0x - \omega t))$, valid in the interval $0 \leq x \leq a$, as $t \to \infty$. It is then possible to determine a simple expression and region of validity for the leading-order behaviour of v.

To show this, assume

$$u_a(x,t) = A\exp(i(k_0x - \omega t)) + O(t^{-\alpha}) \tag{5.19}$$

holds for $0 < x < a$, with $\alpha > 0$, as $t \to \infty$. For $x > a$, assume that u_a is $O(t^{-\alpha})$. Rewrite u_a as

$$u_a(x,t) = A\exp(i(k_0x - \omega t))\left(1 - \mathcal{H}(-x) - \mathcal{H}(x-a)\right) + O(t^{-\alpha}), \tag{5.20}$$

where $\mathcal{H}(x)$ is the Heaviside step function. The leading-order behaviour of v is found by taking the convolution of $f(x)$ with $u_a(x,t)$. Using the definition of the convolution integral (see Haberman [30, Chapter 10]) implies that

$$\begin{array}{rcl} v & \sim & f(x) \star u_a(x,t) \\ & \sim & AF(k_0)\exp(i(k_0x - \omega t)) \\ & & -A\exp(i(k_0x - \omega t))\int_{-\infty}^{\infty} f(X)\exp(-ik_0X)\mathcal{H}(X - x)\ dX \\ & & -A\exp(i(k_0x - \omega t))\int_{-\infty}^{\infty} f(X)\exp(-ik_0X)\mathcal{H}(x - a - X)\ dX \\ & & +O(t^{-\alpha}). \end{array} \tag{5.21}$$

Now assume that $f(x)$ is localized in the interval $c < x < d$, centered about $c_0 = (c+d)/2$. To be precise, suppose that $|f(x)|$ is $O(e^{-\mu|x-c_0|})$ for some $\mu > 0$, whenever $x < c$ or $x > d$. In addition, assume that enough time has passed so that $a + c > d$. Then

$$\int_{-\infty}^{\infty} f(X)\exp(-ik_0X)\mathcal{H}(X - x)\ dX = \int_{x}^{\infty} f(X)\exp(-ik_0X)\ dX \tag{5.22}$$

must be $O(e^{-\mu|x-c_0|})$ for $x > d$. Similarly

$$\int_{-\infty}^{\infty} f(X)\exp(-ik_0X)\mathcal{H}(x-a-X)\ dX = \int_{-\infty}^{x-a} f(X)\exp(-ik_0X)\ dX, \tag{5.23}$$

must be $O(e^{-\mu|x-c_0|})$ when $x < a + c$.

The above argument shows that, provided $f(x)$ is sufficiently small outside of $c < x < d$, the leading-order solution for the point source problem and the more general forced problem only differ by the multiplicative constant $F(k_0)$. That is,

$$v(x,t) \sim AF(k_0)\exp(i(k_0x - \omega t)) + O(e^{-\mu|x-c_0|}) + O(t^{-\alpha}), \tag{5.24}$$

valid in $d < x < a + c$ as $t \to \infty$. In essence, the forcing shape function only alters the character of the asymptotic solution in the forcing region and at the wavefront as $t \to \infty$.

5.1.4 Asymptotic Expansions of Integrals

The field of asymptotic analysis can be loosely described as a collection of techniques used to approximate solutions to problems involving small or large parameters. Within that field, the study of asymptotic expansions of integrals represents an important subdiscipline. This is true in part because a broad range of physical problems have solutions that can be represented in integral form. Standard methods for solving differential equations, such as Green's functions, Laplace, Fourier, or Hankel transforms, all lead to solutions that are expressed as integrals (see Duffy [23] or any introductory text on transform methods for solving PDEs).

While some integrals can be computed analytically, in many cases this is not possible. Even if an integral can be computed exactly, the expressions that are found may be so complicated that they obscure the meaning of the result. In addition, for many physical processes an approximate solution for a limited parameter range is adequate.

In this very brief introduction to the asymptotic expansion of integrals, the important aspects of Laplace's method and the method of steepest descents are provided. The key feature of these methods is that the difficult global problem of integrating a function over an interval or contour is reduced to the study of the local behaviour of the function near a few critical points.

This discussion is largely an adaptation of the excellent presentation given by Ablowitz and Fokkas [1]. Other useful references include Bender and Orszag [6], and Bleistein and Handelsman [8]. The purpose of this section is simply to provide a quick reference and brief overview of the techniques that will be used in the analysis of forced wave equations in this chapter.

Laplace's Method

Integrals of the form

$$I(t) = \int_a^b f(s)e^{-\phi(s)t}\, ds, \tag{5.25}$$

where $\phi(s)$ and $f(s)$ are real, are known as integrals of Laplace-type. These arise frequently in applications such as the Laplace transform. The stipulation that $f(s)$ be real is not limiting, if $f(s)$ were complex then (5.25) could be split into two integrals of Laplace type.

Laplace's method reduces the integration problem to the study of the integrand in the neighborhood of points where $\phi(s)$ achieves its minimum. This is intuitively reasonable because away from such points the factor $\exp(-\phi(s)t)$ is so small as $t \to \infty$ that the contributions to the integral are negligible. If the minimum is not unique, it is the set of points where ϕ achieves its minimum that provide the dominant contributions to $I(t)$.

Once the minimum of $\phi(s)$ has been determined, say at $s = c$, series expansions of $\phi(s)$ and $f(s)$ are found in the neighborhood of c. These series are then substituted into the integral (5.25), and an approximation is found. How this is actually performed in practice depends on the nature of $\phi(s)$.

An important special case is $\phi(s) = s$. In this situation the source of dominant contributions to $I(t)$ is the left endpoint $s = a$. A very useful result, known as Watson's lemma, can then be used. The following statement of Watson's lemma is taken directly from Ablowitz and Fokkas [1, page 427-8], with only minor notation modifications.

Lemma 2. (Watson's Lemma)

Let

$$I(t) = \int_0^b f(s)e^{-st}\, ds, \ \textit{with } b > 0. \tag{5.26}$$

Suppose $f(s)$ is integrable in $(0, b)$ and has the series expansion

$$f(s) = s^\alpha \sum_{n=0}^{\infty} a_n s^{\beta n}, \ \textit{as } s \to 0^+ \tag{5.27}$$

where $\alpha > -1, \beta > 0$. Then

$$I(t) \sim \sum_{n=0}^{\infty} a_n \frac{\Gamma(\alpha + \beta n + 1)}{t^{\alpha+\beta n+1}} \ \textit{as } t \to \infty. \tag{5.28}$$

This lemma has important implications for a broad class of functions $\phi(s)$, and is the foundation for Laplace's method and the method of steepest descents. The proof of Watson's lemma is not difficult but is omitted here.

To see how Watson's lemma can be used, suppose $\phi(s)$ is monotonically increasing in $a \leq s \leq b$. Defining the new variable $\psi = \phi(s) - \phi(a)$, the inverse of ϕ can be used to find $s(\psi) = \phi^{-1}(\psi + \phi(c))$ and $I(t)$ can be expressed as

$$I(t) = e^{-\phi(a)t} \int_0^{\phi(b)-\phi(a)} \hat{f}(\psi) e^{-\psi t} \, d\psi, \tag{5.29}$$

where

$$\hat{f}(\psi) = \left. \frac{f(s)}{\phi'(s)} \right|_{s(\psi)}. \tag{5.30}$$

Provided f and ϕ are sufficiently smooth, a series expansion for $\hat{f}(\psi)$ can be found as $\psi \to 0^+$ and Watson's Lemma can be applied. A similar argument treats the situation when $\phi(s)$ is monotonically decreasing.

Next, suppose $\phi(s)$ has a unique minimum at c where $a < c < b$, and $\phi''(c) > 0$. As shown by Ablowitz and Fokkas [1], when ϵ is a small but finite positive number such that $a < c - \epsilon$ and $c + \epsilon < b$,

$$I(t) \sim \int_{c-\epsilon}^{c+\epsilon} f(s) e^{-\phi(s)t} \, ds \text{ as } t \to \infty, \tag{5.31}$$

with error that is small beyond all orders. With ϵ chosen sufficiently small, $\phi(s) \approx \phi(c) + \phi''(c)(s-c)^2/2$ and $f(s) \approx f(c)$ can be substituted into the integrand. Then

$$I(t) \sim f(c) e^{-\phi(c)t} \int_{c-\epsilon}^{c+\epsilon} \exp\left(-\frac{1}{2} \phi''(c)(s-c)^2 t \right) \, ds. \tag{5.32}$$

Substituting $\psi = \sqrt{\frac{t}{2}\phi''(c)}(s-c)$ into the integral reveals

$$I(t) \sim f(c) e^{-\phi(c)t} \sqrt{\frac{2}{\phi''(c)t}} \int_{-\epsilon\sqrt{\frac{t}{2}\phi''(c)}}^{\epsilon\sqrt{\frac{t}{2}\phi''(c)}} \exp\left(-\psi^2\right) \, d\psi. \tag{5.33}$$

Finally, in the limit $t \to \infty$, the remaining integral is just $\sqrt{\pi}$. Thus

$$I(t) \sim f(c) e^{-\phi(c)t} \sqrt{\frac{2\pi}{\phi''(c)t}}. \tag{5.34}$$

This result, known as Laplace's formula, is very useful. It can be derived rigourously by splitting the integral $\int_a^b = \int_a^c + \int_c^d$. In each of these intervals of integration, $\phi(s)$ is

monotonic and thus, after a suitable transformation of variables, Watson's lemma can be applied. The rigorous approach also determines the error term, and it turns out that

$$I(t) \sim f(c)e^{-\phi(c)t}\sqrt{\frac{2\pi}{\phi''(c)t}} + O\left(\frac{e^{-\phi(c)t}}{t^{3/2}}\right). \tag{5.35}$$

Through its grounding in Watson's lemma, Laplace's method can in principle be used to determine the full asymptotic expansion for $I(t)$. Deriving higher-order terms, however, requires a more careful treatment of the series expansions for $f(s)$ and $\phi(s)$.

The Method of Steepest Descents

The method of steepest descents can be viewed as an extension of Laplace's method to integrals of complex variables. The method is used to approximate integrals of the form

$$I(t) = \int_C f(k)e^{\phi(k)t}\, dk, \tag{5.36}$$

in the limit $t \to \infty$. The contour C lies in the complex k-plane and $f(k)$ and $\phi(k)$ are assumed to be analytic functions in some open neighborhood containing C.

The fundamental idea behind the steepest descents approach is to make use of the analyticity of $f(k)$ and $\phi(k)$ to deform C onto a new contour $\hat{C}$ along which asymptotic contributions can be readily computed. The most natural means of accomplishing this is to choose $\hat{C}$ so that the imaginary part of $\phi(k)$ remains constant. Letting $k = \eta + i\xi$, and splitting $\phi(k) = \phi_R(\eta, \xi) + i\phi_I(\eta, \xi)$, written as $\phi_R(k) + i\phi_I(k)$ for shorthand, equation (5.36) becomes

$$I(t) = e^{i\phi_I t}\int_{\hat{C}} f(k)e^{\phi_R(k)t}\, dk. \tag{5.37}$$

The new contour $\hat{C}$ is a level curve of the function $\phi_I(\eta, \xi)$. At any point along $\hat{C}$, $\nabla\phi_I$ is orthogonal to the tangent at that point. By the Cauchy-Riemann equations, $\nabla\phi_I = (-\partial_\xi\phi_R, \partial_\eta\phi_R)$, which is orthogonal to $\nabla\phi_R$. It follows that the contour $\hat{C}$ represents the curve of most rapid descent or ascent for the function ϕ_R, depending on which direction it is traversed. In general, a path of steepest descent from a point k_0, refers to a path emanating from k_0 along which $\phi_R(k)$ decreases most rapidly (there may be many such paths).

Saddle points, defined as points where $\phi'(k) = 0$, play an important role in steepest descents analysis. Along a path of steepest descent, these are the locations where $\nabla\phi_R = 0$ and thus ϕ_R achieves its maximum (or minimum). When possible, the deformed contour

$\hat{C}$ is chosen as a steepest descents path through one or more saddle points. The reason for this is, as with the analysis of Laplace-type integrals, that $I(t)$ can then be studied through the local behaviour of the integrand about the saddle point.

To analyze the integrand of (5.36) and the structure of the steepest descents path near a saddle point, some discussion is required. A saddle point k_0 is said to be of order N when

$$\frac{d^m}{dk^m}\phi(k)\bigg|_{k=k_0} = 0 \text{ for } m = 1, \ldots, N, \tag{5.38}$$

or referred to as a simple saddle point if $N = 1$. In the immediate neighborhood of k_0, the steepest descents paths can be determined by setting $k = k_0 + |k - k_0|e^{i\theta}$, with $|k - k_0| \ll 1$, and analyzing how $u(k)$ and $v(k)$ behave for different values of θ. Expanding

$$\phi(k) - \phi(k_0) \sim \frac{1}{(N+1)!}\frac{d^{N+1}}{dk^{N+1}}\phi(k)\bigg|_{k=k_0}(k - k_0)^{N+1} \tag{5.39}$$

and writing

$$\frac{1}{(N+1)!}\frac{d^{N+1}}{dk^{N+1}}\phi(k)\bigg|_{k=k_0} = \frac{|\phi^{(N+1)}(k_0)|}{(N+1)!}e^{i\alpha} \tag{5.40}$$

(which implicitly defines α) shows that

$$\phi(k) - \phi(k_0) \sim \frac{|\phi^{(N+1)}(k_0)|}{(N+1)!}|k - k_0|e^{i(\alpha+(N+1)\theta)}. \tag{5.41}$$

As discussed above, along a steepest descents path leaving k_0, the imaginary part of ϕ must remain constant to yield the maximum rate of decrease in the real part of ϕ. To meet this condition,

$$\sin(\alpha + (N+1)\theta) = 0, \text{ and } \cos(\alpha + (N+1)\theta) < 0. \tag{5.42}$$

Therefore, the angles θ corresponding to steepest descent paths from the saddle point k_0 are given by

$$\theta = \frac{-\alpha + (2m+1)\pi}{N+1}, \text{ for } m = 0, 1, 2, \ldots N, \tag{5.43}$$

where α is defined in equation (5.40). In the case of a simple saddle point there are evidently two directions of steepest descent, $\theta = -\alpha/2 + \pi/2$ and $\theta = -\alpha/2 + 3\pi/2$.

Now suppose the initial integration contour C has been deformed onto a new contour $\hat{C}$ which is a path of steepest descent passing through a saddle point at $k = k_0$. The saddle point could be an endpoint of the contour, or $\hat{C}$ could enter k_0 along one path of steepest descent and leave along another. Let the contribution to $I(t)$ along a sub-contour $\hat{C}_n$ corresponding to the steepest descent angle θ_n passing through k_0 be given by

$$I_n(t) = \int_{\hat{C}_n} f(k)e^{\phi(k)t}\, dk. \tag{5.44}$$

Since $u(k)$ is monotonically decreasing along $\hat{C}_n$ and $v(k) = v(k_0)$ remains constant, $\phi(k) - \phi(k_0)$ is real and must be monotonically decreasing along $\hat{C}_n$, and hence has an inverse. Letting $\phi(k) - \phi(k_0) = -\kappa$ and transforming the variable of integration, it is possible to show that $I_n(t)$ can be approximated by the integral

$$I_n(t) \sim -e^{\phi(k_0)t} \int_0^\infty \hat{f}(\kappa) e^{-\kappa t}\, d\kappa, \tag{5.45}$$

where

$$\hat{f}(\kappa) = \left. \frac{f(k)}{\frac{1}{(N+1)!}\phi^{(N+1)}(k)} \right|_{k(\kappa)}, \tag{5.46}$$

with an error that is asymptotically small beyond all orders as $t \to \infty$. In fact, upon comparing the two formulas for $I_n(t)$ it is clear that the only error introduced in (5.45) is through the use of ∞ as the upper bound of integration. As argued in the discussion of Laplace's method, however, this is warranted because the dominant contribution to the integral come from the neighborhood of $\kappa = 0$.

All that remains to be done is a careful expansion of $\hat{f}(\kappa)$ as $\kappa \to 0^+$ so that (5.45) can be estimated using Watson's lemma. This is done explicitly here so that an error bound on the estimate for $I_n(t)$ is clear. The analysis also serves as a demonstration of how steepest descents approximations can be used to find an infinite asymptotic series. Therefore, suppose that k_0 is a N^{th} order saddle point so that as $k \to k_0$,

$$\begin{aligned} \phi(k) \quad &\sim \quad \phi(k_0) + \tfrac{\phi^{(N+1)}(k_0)}{(N+1)!}(k-k_0)^{N+1} + \tfrac{\phi^{(N+2)}(k_0)}{(N+2)!}(k-k_0)^{N+2} \\ &\quad\; + O\left((k-k_0)^{N+3}\right). \end{aligned} \tag{5.47}$$

In the neighborhood of k_0, $\phi'(k)$ can be found by differentiating (5.47):

$$\phi'(k) \sim \frac{\phi^{(N+1)}(k_0)}{N!}(k-k_0)^N + \frac{\phi^{(N+2)}(k_0)}{(N+1)!}(k-k_0)^{N+1} + O\left((k-k_0)^{N+2}\right). \tag{5.48}$$

Further, assume that $f(k)$ is sufficiently smooth so that

$$f(k) \sim f_0(k-k_0)^{\beta-1} + f_1(k-k_0)^\beta + O\left((k-k_0)^{\beta+1}\right) \tag{5.49}$$

as $k \to k_0$, where $Re(\beta) > 0$. If follows that for k near k_0,

$$\begin{aligned} \tfrac{f(k)}{\phi'(k)} \quad &\sim \quad \tfrac{f_0(k-k_0)^{\beta-1} + f_1(k-k_0)^\beta + O((k-k_0)^{\beta+1})}{\frac{\phi^{(N+1)}(k_0)}{N!}(k-k_0)^N + \frac{\phi^{(N+2)}(k_0)}{(N+1)!}(k-k_0)^{N+1} + O((k-k_0)^{N+2})} \\ &\sim \quad \tfrac{f_0(k-k_0)^{\beta-N-1} + f_1(k-k_0)^{\beta-N}}{\frac{\phi^{(N+1)}(k_0)}{N!}} \times \left[1 - \tfrac{\phi^{(N+2)}(k_0)}{(N+1)\phi^{(N+1)}(k_0)}(k-k_0)\right] \\ &\quad\; + O\left((k-k_0)^{\beta-N+1}\right), \end{aligned} \tag{5.50}$$

where after a simple factoring, the denominator has been expanded to leading order as a geometric series. Multiplication yields

$$\begin{aligned}\frac{f(k)}{\phi'(k)} &\sim \frac{f_0 N!}{\phi^{(N+1)}(k_0)}(k-k_0)^{\beta-N-1} \\ &+\left(\frac{f_1 N!}{\phi^{(N+1)}(k_0)} - \frac{N!\phi^{(N+2)}(k_0)}{(N+1)\left(\phi^{(N+1)}(k_0)\right)^2}\right)(k-k_0)^{\beta-N} \\ &+O\left((k-k_0)^{\beta-N+1}\right).\end{aligned} \tag{5.51}$$

To use this in the evaluation of $\hat{f}(\kappa)$ as $\kappa \to 0^+$, $k-k_0$ must be expressed in terms of κ. This is done through the relation $-\kappa = \phi(k) - \phi(k_0)$, which implies

$$-\kappa \sim \frac{\phi^{(N+1)}(k_0)}{(N+1)!}(k-k_0)^{N+1} + \frac{\phi^{(N+2)}(k_0)}{(N+2)!}(k-k_0)^{N+2} + O\left((k-k_0)^{N+3}\right). \tag{5.52}$$

From this, $k-k_0$ can be found as a power series in κ. Expanding $k-k_0 = e^{i\theta}\left(c_0\kappa^{\mu} + c_1\kappa^{\mu+\gamma} + O(\kappa^{\mu+2\gamma})\right)$ reveals that $\mu = \gamma = 1/(N+1)$ and

$$c_0 = \left(\frac{(N+1)!}{|\phi^{(N+1)}(k_0)|}\right)^{\frac{1}{N+1}}, c_1 = \frac{c_0^2\phi^{(N+2)}(k_0)e^{i(N+2)\theta}}{(N+1)(N+2)|\phi^{(N+1)}(k_0)|}. \tag{5.53}$$

Substituting the expansion for $k-k_0$ back into equation (5.51), the binomial theorem can be used to show that as $\kappa \to 0^+$,

$$\hat{f}(\kappa) = a_0\kappa^{\frac{\beta}{N+1}-1} + a_1\kappa^{\frac{\beta+1}{N+1}-1} + O\left(\kappa^{\frac{\beta+2}{N+1}-1}\right) \tag{5.54}$$

where

$$a_0 = -\frac{f_0 e^{i\beta\theta}}{N+1}\left(\frac{(N+1)!}{|\phi^{(N+1)}(k_0)|}\right)^{\frac{\beta}{N+1}}, \tag{5.55}$$

and

$$\begin{aligned}a_1 &= (N+1-\beta)\frac{f_0 N!}{|\phi^{(N+1)}(k_0)|}e^{\beta\theta} \\ &+\left(\frac{f_1 N!}{\phi^{(N+1)}(k_0)} - \frac{N!\phi^{(N+2)}(k_0)}{(N+1)\left(\phi^{(N+1)}(k_0)\right)^2}\right)c_0^{\beta-N}e^{i(\beta-N)\theta}.\end{aligned} \tag{5.56}$$

Finally, using the series expansion for $\hat{f}(\kappa)$ in equation (5.54), Watson's lemma can be directly applied to the definition of $I_n(t)$ in (5.45). The result is

$$I_n(t) \sim \frac{f_0((N+1)!)^{\frac{\beta}{N+1}}e^{i\beta\theta}}{N+1}\frac{e^{\phi(k_0)t}\Gamma\left(\frac{\beta}{N+1}\right)}{(|\phi^{(N+1)}(k_0)|t)^{\frac{\beta}{N+1}}} + O\left(\frac{e^{\phi(k_0)t}}{t^{\frac{\beta+1}{N+1}}}\right) \tag{5.57}$$

In most of the applications of the method considered here, $\beta = 1$ and $N = 1$. Even with those values, the determination of higher-order terms in the asymptotic solution is algebraically challenging.

The final asymptotic expansion for $I(t)$ is found by summing all of the contributions from steepest descent paths through saddle points on $\hat{C}$. In addition, residue contributions from poles encircled in the contour deformation process must also be included. The steepest descents analysis process is summarized in the following steps:

1. Determine the critical points of the integrand. These include saddle points k_0 where $\phi'(k_0) = 0$, endpoints of the integration contour, and singularities.
2. Determine the paths of steepest descent through critical points of interest.
3. Ensure it is possible to deform the original contour C onto one or more of the paths of steepest descent. Take special care to determine if the deformation of C introduces any singularities.
4. Approximate the integral along the new contour $\hat{C}$ using equation (5.57) and any residue contributions that resulted from the deformation process.

These steps have been adapted from Bleistein and Handelsman [8, Chapter 7]. The application of these steps is a somewhat flexible. Interestingly, the final step is typically the easiest to apply since equation (5.57) is known. Determining which critical points to use, qualitative behaviour of the steepest descents paths emanating from them, and ensuring the deformation process is possible are the most time-consuming steps.

5.2 The Forced Linear KdV Equation

Consider the dispersive wave equation

$$\begin{gathered} u_t + c_0 u_x + \nu u_{xxx} = A \exp(i\omega t) f(x), \\ -\infty < x < \infty,\ t \geq 0, \end{gathered} \tag{5.58}$$

with initial condition

$$u(x, 0) = u_0(x), \tag{5.59}$$

and far-field conditions

$$\{u, u_x, u_{xx}\} \to 0 \text{ as } x \to +\infty, \tag{5.60}$$

and assume $c_0 > 0, \nu > 0$. The partial differential equation (5.58) is a linearized form of the well-known Korteweg de Vries equation (see Drazin and Johnson [20]). Among its many applications, it is used to model long surface waves propagating on a shallow channel. The KdV equation is often introduced as a first model of a dispersive partial differential equation.

In this analysis it is the impulsively-forced response that is of primary interest. More specifically, the goal of this investigation is to determine the properties of the waves that are generated by the oscillatory source. The solution method used here is based on the Fourier transform. After discussing the dispersion relation, group velocity, and phase speed the solution in Fourier space is derived. The inverse Fourier transform is then applied, and the solution is seen to be quite complicated. A simpler, more intuitive solution is then derived using the method of steepest descents, and it is compared against a numerical solution.

5.2.1 The Dispersion Relation and Group Velocity

The dispersion relation is found by substituting $u = \exp(i(kx - \sigma t))$ into the homogeneous KdV problem and solving for $\sigma(k)$. This yields

$$\sigma(k) = c_0 k - \nu k^3. \tag{5.61}$$

The phase speed depends on k, and is given by

$$c = \frac{\sigma}{k} = c_0 - \nu k^2. \tag{5.62}$$

The group velocity also depends on k, and satisfies

$$c_g = \frac{d\sigma}{dk} = c_0 - 3\nu k^2. \tag{5.63}$$

Both the phase speed and group velocity become unbounded in the short-wave limit ($k \to \infty$). This is apparent in Figure 5.1, where the dispersion relation and group velocity are plotted. In general, the KdV equation is only an accurate model for long dispersive waves. The unbounded nature of the phase speed and group velocity is important and problematic for numerical solutions of the KdV equation. Numerical solvers often work with modified forms of the KdV equation, such as the BBM equation (see Section 5.3), to counter this problem. In what follows, the impulsively-forced KdV equation (5.58) is studied using exact and asymptotic approaches.

5.2.2 The Spectral Solution

Letting $U(k,t) = \mathcal{F}\{u(x,t)\}$, and $F(k) = \mathcal{F}\{f(x)\}$, the continuous Fourier transform of the linear KdV equation reduces the problem to the ordinary differential equation

$$U_t(k,t) + i\sigma(k)U(k,t) = A\exp(i\omega t)F(k). \tag{5.64}$$

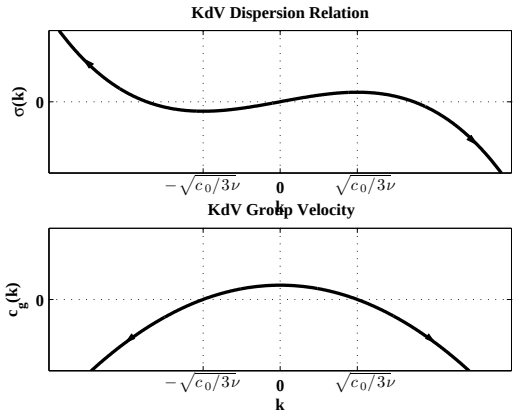

Figure 5.1: The dispersion relation (top subplot) and group velocity (bottom subplot) for the KdV equation.

Then, by use of the integrating factor $\exp(i\sigma t)$, the solution in Fourier space satisfies

$$\frac{d}{dt}\left(\exp\left(i\sigma(k)t\right)U(k,t)\right) = A\exp\left(i(\sigma(k)+\omega)t\right)F(k). \tag{5.65}$$

Integrating equation (5.65) with respect to time from 0 to t and making use of the initial condition $U(k,0) = U_0(k) = \mathcal{F}\{u_0(x)\}$, leads to

$$U(k,t) = U_0(k)e^{-i\sigma(k)t} + AF(k)\left(\frac{e^{i\omega t} - e^{-i\sigma(k)t}}{i(\sigma(k)+\omega)}\right). \tag{5.66}$$

This is the solution in Fourier space. The solution (5.66) is concise, but it does not provide much insight into how waves in the system behave in physical coordinates. It is unclear how transients might decay, and if a regular wave train is produced its frequency and wavenumber are not immediately obvious.

5.2.3 The Physical Solution

The physical solution to the forced linear KdV equation is found by applying the inverse Fourier transform to the spectral solution in equation (5.66). It is important to emphasize that the first term in (5.66) can be attributed to the initial condition, and the second term to the forcing. Linearity of the equations allows for the isolated discussion of each component.

Evolution of the Initial Condition

First, consider the term involving the initial condition:

$$\begin{aligned}\mathcal{F}^{-1}\left\{U_0(k)e^{-i\sigma(k)t}\right\} &= \mathcal{F}^{-1}\left\{U_0(k)e^{-ikc_0t}\right\} \star \mathcal{F}^{-1}\left\{e^{i\nu tk^3}\right\} \\ &= u_0(x-ct) \star \mathcal{F}^{-1}\left\{e^{i\nu tk^3}\right\}.\end{aligned} \tag{5.67}$$

This shows that the evolution of an initial condition governed by the linear KdV equation is described by the convolution of a traveling copy of the initial profile with an undetermined function. The undetermined function $\mathcal{F}^{-1}\{\exp(i\nu k^3 t)\}$ can be computed analytically. To see this, consider the integral form of the Airy function (Haberman [30, Chapter 14]):

$$\mathrm{Ai}(x) = \frac{1}{2\pi}\int_{-\infty}^{\infty} \exp(i(kx + k^3/3))\, dk. \tag{5.68}$$

Letting $k = s/(3\nu t)^{1/3}$ so that $dk = ds/(3\nu t)^{1/3}$, it follows from the definition of the inverse Fourier transform that

$$\begin{aligned}\mathcal{F}^{-1}\left\{\exp(i\nu tk^3)\right\} &= \tfrac{1}{(3\nu t)^{\frac{1}{3}}}\tfrac{1}{2\pi}\int_{-\infty}^{\infty}\exp\left(i\left(s\tfrac{x}{(3\nu t)^{\frac{1}{3}}} + \tfrac{s^3}{3}\right)\right)\, ds \\ &= \tfrac{1}{(3\nu t)^{\frac{1}{3}}}\mathrm{Ai}\left(\tfrac{x}{(3\nu t)^{\frac{1}{3}}}\right).\end{aligned} \tag{5.69}$$

Thus the inverse Fourier transform of the initial condition in (5.66) is

$$\mathcal{F}^{-1}\left\{U_0(k)\exp(i\nu tk^3)\right\} = u_0(x-c_0t) \star \frac{1}{(3\nu t)^{\frac{1}{3}}}\mathrm{Ai}\left(\frac{x}{(3\nu t)^{\frac{1}{3}}}\right), \tag{5.70}$$

or equivalently,

$$\mathcal{F}^{-1}\left\{U_0(k)\exp(i\nu tk^3)\right\} = \frac{1}{(3\nu t)^{\frac{1}{3}}}\int_{-\infty}^{\infty} u_0(X-c_0t)\mathrm{Ai}\left(\frac{x-X}{(3\nu t)^{\frac{1}{3}}}\right)\, dX. \tag{5.71}$$

This complicated formula explains how the initial condition for the linear KdV equation evolves in time and space. It could serve as the basis for the asymptotic analysis of the long-term evolution of an initial disturbance. Since the interest here is primarily in the forced response of the system this idea is not pursued further.

Evolution of the Forced Terms

Consider now the computation of $\mathcal{F}^{-1}\left\{AF(k)\left(\frac{e^{i\omega t}-e^{-i\sigma(k)t}}{i(\sigma(k)+\omega)}\right)\right\}$. Appealing to the convolution theorem, this expression can be simplified to

$$Af(x) \star \mathcal{F}^{-1}\left\{G_1(k) + G_2(k)\right\}, \tag{5.72}$$

where

$$G_1(k) = \frac{\exp(i\omega t)}{i(\sigma(k)+\omega)},\ G_2(k) = -\frac{\exp(-i\sigma(k)t)}{i(\sigma(k)+\omega)}. \tag{5.73}$$

Inverting these terms with the inverse Fourier transform requires careful consideration. The number and nature of the real roots of $\sigma(k)+\omega = 0$ determine the contour of integration required for the inverse transform. Since both $G_1(k)$ and $G_2(k)$ possess the same singularities the same integration contour is used for both inversions.

The integration contour C needed for the inverse Fourier transforms of $G_1(k)$ and $G_2(k)$ is determined by an analysis of the real poles of the integrand. These poles coincide with the roots of $\sigma(k)+\omega = 0$. With $c_0 > 0$, $\nu > 0$, and $\omega > 0$, the polynomial $\sigma(k)+\omega$ could have one, two, or three distinct real roots.

By expanding $\sigma(k)+\omega = -\nu k^3 + c_0 k + \omega$, it is clear that the local extremes occur at $k = \pm\sqrt{c_0/(3\nu)}$. Note that $\sigma(0)+\omega > 0$ and $\sigma'(0) > 0$. Also, $\sigma'(k) < 0$ for $k > \sqrt{c_0/(3\nu)}$ and $\sigma(k) \to -\infty$ as $k \to \infty$. It follows that $\sigma(k)+\omega$ must always have exactly one real positive root. As ω is decreased from a large positive value, negative roots of $\sigma(k)+\omega$ first occur when $\sigma(k)+\omega$ and $\sigma'(k)$ have a common zero. This double root must occur at $k = -\sqrt{c_0/(3\nu)}$. The corresponding critical frequency $\omega = \omega_c$, is given by

$$\omega_c = \frac{2}{3}c_0\sqrt{\frac{c_0}{3\nu}}. \tag{5.74}$$

Physically, the critical cut-off frequency is significant because it corresponds to the forcing frequency required to produce waves with zero group velocity. The exact nature of the generated waves for $\omega > \omega_c$ and $\omega < \omega_c$ will become apparent through asymptotic analysis. For ω values below this critical frequency $\sigma(k)+\omega$ has two distinct first-order negative roots and a first-order positive root. The possible root configurations for $\sigma(k)+\omega = 0$ are summarized in the following three cases:

- Case 1: $\omega < \omega_c$. Here $\sigma(k)+\omega$ has one positive real zero r_1 and two distinct negative zeros r_2 and r_3. These roots are ordered such that $r_3 < -\sqrt{c_0/(3\nu)} < r_2 < 0$ and $\sqrt{c_0/(3\nu)} < r_1$. Each zero is simple, and $\sigma'(r_3) < 0$, $\sigma'(r_2) > 0$, and $\sigma'(r_1) < 0$.

- Case 2: $\omega = \omega_c$. Here $\sigma(k)+\omega$ has one real positive zero denoted by r_1 and satisfying $r_1 > \sqrt{c_0/(3\nu)}$, and a double zero on the negative axis at $r_2 = -\sqrt{c_0/(3\nu)}$. The group velocities of waves at these zeros satisfy $\sigma'(r_1) < 0$, $\sigma'(r_2) = 0$.

- Case 3: $\omega > \omega_c$. Here $\sigma(k)+\omega$ has one real positive zero r_1 satisfying $r_1 > \sqrt{c_0/(3\nu)}$, and a pair of complex conjugate roots r_2, r_2^*. Roots are labeled so that $Im(r_2) > 0$. The group velocity at the real zero satisfies $\sigma'(r_1) < 0$.

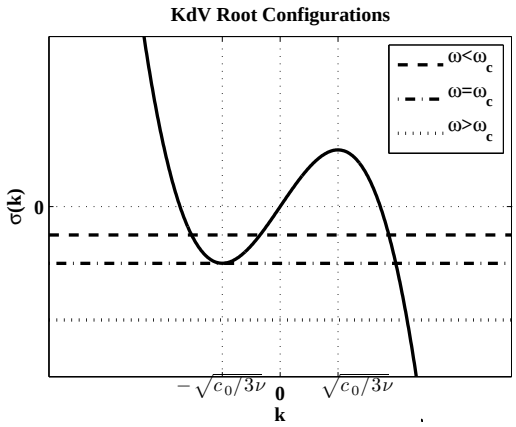

Figure 5.2: Possible root configurations for $\sigma(k) + \omega$. When $\omega < \omega_c$ (dashed line) $\sigma(k)$ intersects $-\omega$ three times. When $\omega = \omega_c$ (dash-dotted line) there are two intersections. When $\omega > \omega_c$ (dotted line) there is just one root. This plot is a magnified view around the origin of Figure 5.1.

A qualitative demonstration of these three cases is given in Figure 5.2. Clearly the regime ω belongs to determines the number and nature of the zeros of $\sigma(k)+\omega$. The group velocity $\sigma'(k)$ at each of the possible roots is also apparent upon consideration of the slopes of the curves.

The above analysis, combined with the discussion in Section 5.1.2, is sufficient to determine the integration contour C needed for the inverse Fourier transforms of $G_1(k)$ and $G_2(k)$. In general, the contour C must traverse the real k-axis from $-\infty$ to $+\infty$. With $\omega < \omega_c$ (Case 1), C must be deformed below the pole at $k = r_2$ and above the poles at $k = r_1$ and $k = r_3$. Case 2 is special because the pole at r_2 corresponds to waves with zero group velocity. With $\omega = \omega_c$, the forcing produces waves that cannot propagate out of the forcing region, therefore the contour C is deformed below the pole at r_2 with the understanding that the residue is not to be included in the analysis of traveling waves. The contour is deformed above the pole at $k = r_1$. When $\omega > \omega_c$ (Case 3), the contour C need only be deformed above the pole at $k = r_1$, since the poles at r_2 and r_2^* lie off the real axis.

The integration contour C for the case 1 scenario is depicted in Figure 5.3. The integration contour lies along the real axis with deformations about the three poles along the axis. As indicated by the arrowheads, the contour is traversed from left to right.

Computing the Inverse Transforms

In finding the exact inverse transforms of (5.72), it is first assumed that $\omega < \omega_c$ (Case 1). The results for Cases 2 and 3 are discussed in the next section. First, consider $g_1(x, t) =$

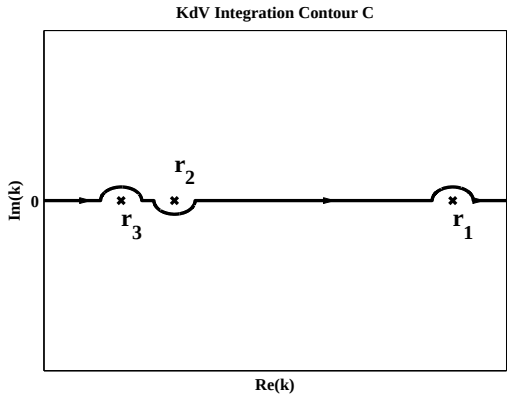

Figure 5.3: The integration contour C when $\omega < \omega_c$ (Case 1). The poles at r_1, r_2, r_3 are marked by 'x' symbols. The direction of the contour is from left to right, indicated by the arrowheads.

$\mathcal{F}^{-1}\{G_1(k)\}$. With the integration contour C described above, $g_1(x,t)$ is defined by

$$g_1(x,t) = \frac{1}{2\pi}\int_C \frac{\exp(i(kx+\omega t))}{i(\sigma(k)+\omega)}\, dk. \tag{5.75}$$

This integral can be computed exactly using residue theory. When $x \geq 0$, the contour of integration can be closed with a semicircular arc in the upper half-plane. The integral along the arc segment tends to zero by Jordan's lemma. In this situation, the closed contour only encloses the pole at $k = r_2$, therefore when $x \geq 0$:

$$g_1(x,t) = -\frac{1}{\nu}\frac{\exp(i(r_2 x+\omega t))}{(r_2-r_1)(r_2-r_3)}. \tag{5.76}$$

Similarly, when $x < 0$ the contour of integration C can be closed with a semicircular arc in the lower half-plane. The integral along the arc is again zero, but the closed contour contains the two poles at r_1 and r_3. Therefore when $x < 0$:

$$g_1(x,t) = \frac{1}{\nu}\left(\frac{\exp(i(r_1 x+\omega t))}{(r_1-r_2)(r_1-r_3)} + \frac{\exp(i(r_3 x+\omega t))}{(r_3-r_1)(r_3-r_2)}\right). \tag{5.77}$$

Observe that these leftward-propagating waves must have a smaller amplitude than the rightward propagating wave found above. This is because $r_3 < r_2 < r_1$, so $|r_1 - r_3| > \max(|r_1-r_2|, |r_2-r_3|)$. The general solution $g_1(x,t)$ can be found by combining the above two results with use of the Heaviside function. That is,

$$\begin{aligned} g_1(x,t) \;=\; & -\tfrac{1}{\nu}\left(\tfrac{\exp(i(r_1x+\omega t))}{(r_1-r_2)(r_1-r_3)} + \tfrac{\exp(i(r_2x+\omega t))}{(r_2-r_1)(r_2-r_3)} + \tfrac{\exp(i(r_3x+\omega t))}{(r_3-r_1)(r_3-r_2)}\right)\mathcal{H}(x) \\ & +\tfrac{1}{\nu}\left(\tfrac{\exp(i(r_1x+\omega t))}{(r_1-r_2)(r_1-r_3)} + \tfrac{\exp(i(r_3x+\omega t))}{(r_3-r_1)(r_3-r_2)}\right). \end{aligned} \tag{5.78}$$

Finding $g_2(x,t) = \mathcal{F}^{-1}\{G_2(k)\}$ is more complicated. The exact expression for $g_2(x,t)$ is

$$g_2(x,t) = -\frac{1}{2\pi}\int_C \frac{\exp(i(kx-\sigma(k)t))}{i(\sigma(k)+\omega)}\,dk. \tag{5.79}$$

The contour C cannot be closed with semicircular arcs in the upper or lower half-plane, regardless of the sign of x. This is apparent because with $k = R\cos(\theta)$ and R large, the exponent behaves like $|\exp(i(kx-\sigma(k)t))| \approx \exp\big(-\nu R^3\sin(3\theta)t\big)$. This is only bounded in the three sectors of the complex plane defined by $0 \le \theta \le \pi/3$, $2\pi/3 \le \theta \le \pi$, and $4\pi/3 \le \theta \le 5\pi/3$. An exact solution for $g_2(x,t)$ can still be found in terms of convolutions, however. By the convolution theorem

$$g_2(x,t) = -\mathcal{F}^{-1}\left\{\frac{\exp(-ic_0kt)}{i(\sigma(k)+\omega)}\right\} \star \mathcal{F}^{-1}\{\exp(i\nu k^3 t)\}. \tag{5.80}$$

The first term is closely related to g_1 and the second term has already been discussed for the evolution of the initial condition. So, it is possible to write

$$g_2(x,t) = -g_1(x-c_0t,0) \star \frac{1}{(3\nu t)^{\frac{1}{3}}}\mathrm{Ai}\left(\frac{x}{(3\nu t)^{\frac{1}{3}}}\right), \tag{5.81}$$

where the convolution integral is with respect to x. The forced terms can now be combined to yield the full solution.

Summary and Interpretation of the Exact Solution

Combining the results from above reveals the full solution to the forced linear KdV equation. The solution can be written as:

$$\begin{aligned} u(x,t) &= u_0(x-c_0t) \star \tfrac{1}{(3\nu t)^{\frac{1}{3}}}\mathrm{Ai}\left(\tfrac{x}{(3\nu t)^{\frac{1}{3}}}\right) \\ &\quad + Af(x) \star \left[g_1(x,t) - g_1(x-c_0t,0) \star \tfrac{1}{(3\nu t)^{\frac{1}{3}}}\mathrm{Ai}\left(\tfrac{x}{(3\nu t)^{\frac{1}{3}}}\right)\right] \end{aligned} \tag{5.82}$$

where $g_1(x,t)$ is defined in equation (5.78). Though exact, (5.82) is cumbersome and difficult to interpret. The primary difficulty lies in the presence of the convolutions. The complicated nature of the Airy function, compounded by the complexity of its argument, further obscures the understanding of how the solution evolves. The only part of (5.82) that can be understood with basic intuition is the first component of the forced response, $f(x) \star g_1(x,t)$. This term is just the convolution of the forcing shape with regular leftward and rightward-propagating waves.

The solution for more general forcing frequencies is now discussed. These expressions for $g_1(x,t)$ and $g_2(x,t)$ are valid even when $\omega > \omega_c$ (Case 3). In that event, the poles at r_2, r_3 in the above solution are replaced by the complex poles r_2, r_2^*. As a result, the corresponding waves associated with these poles decay exponentially with space. The leftward-propagating waves associated with the pole r_1 do not decay in space, as r_1 remains real.

The solution when $\omega = \omega_c$ (Case 2) can also be inferred from the above calculations. Away from the forcing region $f(x) = 0$, so only the leftward propagating waves with wavenumber $k = r_1$ can be found. These must lie to the left of the forcing region. Since the forcing produces waves of zero group velocity, the solution in the forcing region grows as more energy is transferred in, as there is no mechanism to extract it. Eventually, this must lead to the breakdown of the linear model as the wave amplitude increases.

The complicated nature of the exact solution is a strong motivation for seeking an approximate solution. A gain in the meaningfulness of the solution at the cost of a small degree of accuracy is certainly an acceptable compromise.

5.2.4 Asymptotic Analysis

As mentioned above, the exact solution derived for the linear KdV equation is difficult to interpret. A much more understandable, approximate, solution can be found through asymptotic expansion techniques. The method of steepest descents is well-suited to the analysis of the problem, and provides a useful solution in the limit as $t \to \infty$. The details of the calculation are quite technical and can be found in Appendix D.1.

While the method of steepest descents could be used to study the evolution of the initial condition for the KdV problem, the analysis in the appendix is limited to the approximation of the forced response. In fact, the appendix only deals with the approximate inversion of $G_2(k)$ because the form of $g_1(x,t)$ is so simple. To further facilitate the analysis, the restriction $f(x) = \delta(x)$ is made, but in the next section the leading-order solution is verified for a more general $f(x)$.

The steepest descents analysis provides estimates for $u(x,t)$ in different regimes depending on the ratio x/t. When $0 < x/t < c_F$, where $c_F = c_0 - 3\nu r_2^2$ is the group velocity of the forced wave, the approximate solution takes the form:

$$u(x,t) \sim -\frac{A}{\nu}\frac{\exp\left(i(r_2 x + \omega t)\right)}{(r_2 - r_1)(r_2 - r_3)} + O\left(\frac{1}{\sqrt{t}}\right). \tag{5.83}$$

Likewise, when $c_F < x/t < c_0$ the approximate solution is $O(t^{-1/2})$, and when $x/t > c_0$, the asymptotic solution is exponentially small in comparison with $t^{-1/2}$.

The asymptotic solution makes sense physically. After a large amount of time, a stationary observer located at $x < c_F t$ should expect to witness a wave field dominated by the forced wave. In addition to the forced wave, the observer would measure transient signals as a result of the impulsive forcing. If the observer were located in the interval $c_F t < x < c_0 t$, beyond the leading edge of the forced wave, only transients would be observable. Similarly, at a location $x > c_0 t$, no measurable signals could have reached the observer.

In contrast with the exact solution described in Section 5.2.3, the approximate solution (5.83) is simple to understand and useful. The amplitude, phase, and frequency of the forced waves are immediately obvious, and the decay rate of transients is apparent. In the next section the leading-order solution when $x/t < c_F$ is verified using a numerical comparison.

5.2.5 Verifying the Asymptotic Solution

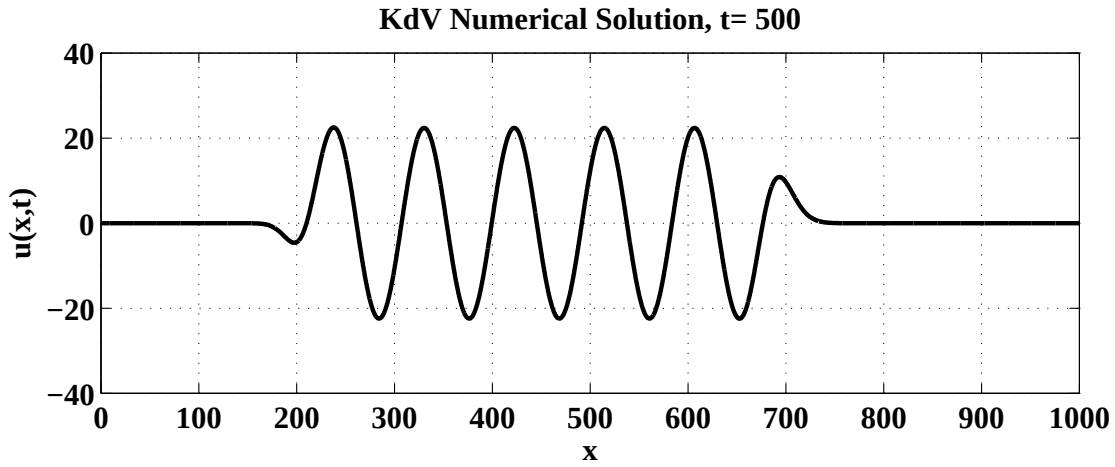

Figure 5.4: The numerical solution to the KdV equation. Even after just five forcing periods a regular wave train is visible in the main body of the wave packet. The forcing center lies at $x = 200$.

In this section the validity of the leading-order component of the asymptotic solution is confirmed by direct comparison against a numerical solution. The numerical solution used for comparison is computed by applying the inverse FFT to equation (5.66). This is used for comparison instead of the exact solution simply because it is easier to construct. All quantities described below and used in the simulation are dimensionless.

For the comparison shown here, the KdV parameters $c_0 = 1$ and $\nu = 1/2$. A unit forcing amplitude is used, and the forcing shape $f(x)$ and its Fourier transform $F(k)$ are

given by

$$f(x) = \exp(-a(x - x_0)^2), \qquad F(k) = \sqrt{\frac{\pi}{a}} \exp(-ikx_0) \exp\left(-\frac{k^2}{4a}\right). \tag{5.84}$$

with $a = 1/400$ and $x_0 = L/5$. The forcing function satisfies $|f(x| < 10^{-6}$ for $x > 274.6$ and $x < 125.6$. The forcing frequency is taken to be $\omega = \omega_c/8 \approx 0.068$, corresponding to a period of $T \approx 92.3$. The wavenumber of the rightward-propagating forced wave is then $r_2 \approx -0.0682$, corresponding to a wavelength of $\lambda \approx 92.1$ and a group velocity of $c_F \approx 0.99$.

The numerical solution is plotted in Figure 5.4 at $t = 500$. Note the regular shape of the waves in the main body of the wave train. At $t = 500$, about 5.4 forcing periods have elapsed. Even with so few waves the regular shape of the numerical solution suggests the asymptotic approximation could provide an accurate description.

The discussion in Section 5.1.3, combined with the above description of $f(x)$, suggests that at $t = 500$ the leading-order asymptotic approximation

$$u_a(x,t) \sim \mathrm{Re}\left\{-A\frac{F(r_2)}{\nu}\frac{\exp\left(i(r_2x + \omega t)\right)}{(r_2 - r_1)(r_2 - r_3)}\right\} + O(t^{-1/2}) \tag{5.85}$$

should be accurate in the interval $275 < x < 625$. This is apparent in Figure 5.5. In the top subplot the asymptotic and numerical solution appear to agree very well in the expected interval. This is further confirmed in the bottom subplot, where the absolute difference is plotted and it is clear that the two solutions agree to machine precision in the main body of the wave train. In this instance the asymptotic solution is an excellent representation of the exact solution in the interval where it is valid. The accuracy of the solution is many orders of magnitude better than the predicted $O(t^{-1/2})$.

5.3 The Forced Linear BBM Equation

The KdV equation models the dispersive behaviour of long waves, but it exhibits undesirable behaviour for shorter waves. In particular, as the wavelength decreases the phase speed and group velocity becomes unbounded. This property makes simulations involving the KdV equation difficult, and led to the development of alternative dispersive models. One such model, known as the Benjamin-Bona-Mahony (BBM) equation [7], is derived from the KdV equation by considering the leading order approximation

$$u_x = -\frac{1}{c_0}u_t. \tag{5.86}$$

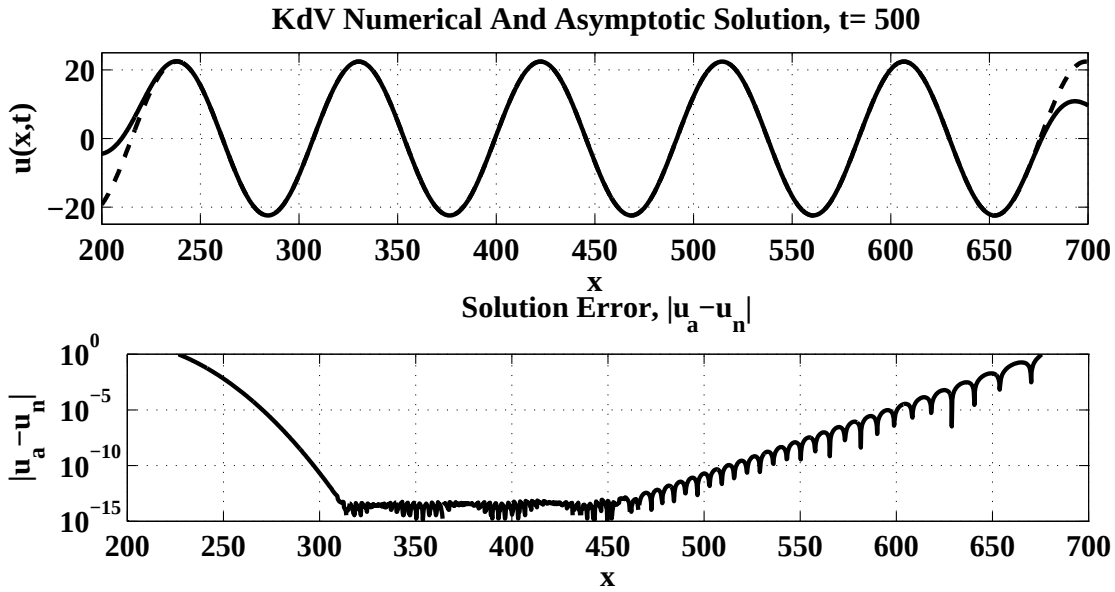

Figure 5.5: In the top subplot, the numerical solution (solid line) and asymptotic solution (dashed line) for the KdV equation are plotted. The curves are only visibly different near the forcing region at $x = 200$, and near the leading edge of the wave at $x = 700$. In the bottom subplot, the absolute difference between the numerical and asymptotic solutions, denoted by $|u_a - u_n|$ is plotted in log scale. The difference is on the order of machine precision in the center of the wave train.

Using this approximation in the dispersive term of the forced KdV equation leads to the forced linear BBM equation:

$$\begin{gathered} u_t + c_0 u_x - \mu u_{xxt} = A\exp(i\omega t)\delta(x), \\ -\infty < x < \infty,\ t \geq 0, \end{gathered} \tag{5.87}$$

with initial condition

$$u(x,0) = u_0(x), \tag{5.88}$$

and far-field conditions

$$\begin{gathered} u(x,t) \to 0 \text{ as } x \to \pm\infty, \\ u_x(x,t) \to 0 \text{ as } x \to \pm\infty. \end{gathered} \tag{5.89}$$

where $\mu = \nu/c_0 > 0$. As shown below, this modified equation has favourable properties in the short-wave limit. However, the introduction of the term u_{xxt} does complicate the Fourier analysis.

Unlike the analysis for the KdV problem, only a point source forcing function is studied. The implications for more general forcing terms are considered later. The general solution process followed here is very similar to that taken for the impulsively-forced KdV problem. After discussing the group velocity and dispersion relation, the solution is found in Fourier space. The difficulties involved in inverting the spectral solution are described, and an asymptotic solution is then calculated and verified numerically.

5.3.1 The Dispersion Relation and Group Velocity

The dispersion relation for the BBM equation is found by substituting $u = \exp(i(kx - \sigma t))$ into the homogeneous problem. The result is

$$\sigma(k) = \frac{c_0 k}{1 + \mu k^2}. \tag{5.90}$$

The group velocity for the BBM equation, $c_g = d\sigma/dk$ is given by

$$c_g = c_0 \frac{1 - \mu k^2}{(1 + \mu k^2)^2}. \tag{5.91}$$

The group velocity is zero at wavenumbers $k = \pm 1/\sqrt{\mu}$. For $|k| < 1/\sqrt{\mu}$, the group velocity is positive, and for $|k| > 1/\sqrt{\mu}$ the group velocity is negative. The group velocity achieves extreme values when $dc_g/dk = 0$. Since

$$\frac{d}{dk} c_g(k) = 2c_0 \mu k \frac{\mu k^2 - 3}{(1 + \mu k^2)^3}, \tag{5.92}$$

the maximum group velocity occurs at $k = 0$, with $c_g(0) = c_0$. The minimum group velocity occurs at wavenumbers $k = \pm\sqrt{3/\mu}$, with $c_g(\pm\sqrt{3/\mu}) = -c_0/8$. Like the group velocity, the phase speed is bounded above by c_0. This is in contrast to the KdV problem where the group velocity and phase speed are unbounded in the limit $k \to \infty$.

In the top subplot of Figure 5.6 the BBM dispersion relation is plotted. The group velocity $c_g(k)$ is plotted against wavenumber in the bottom subplot. Clearly visible are regions where the group velocity is positive and negative. For the plot $c_0 = 1$, and $\mu = 1/2$ are used.

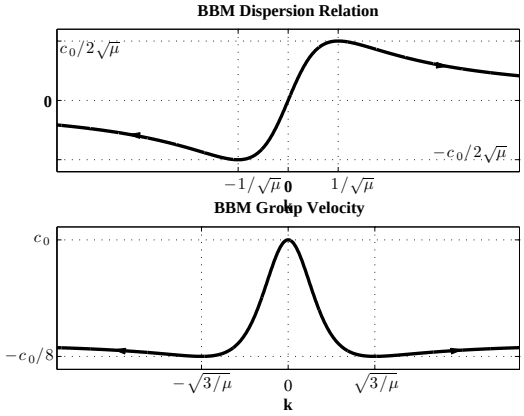

Figure 5.6: The dispersion relation (top subplot) and group velocity (bottom subplot) plotted against wavenumber k for the BBM equation.

5.3.2 The Spectral Solution

It is relatively simple to find a solution for the BBM problem in Fourier space. Defining $U(k,t) = \mathcal{F}\{u(x,t)\}$, the Fourier transform of (5.87) reveals the ordinary differential equation

$$U_t(k,t) + \sigma(k)U(k,t) = A\frac{e^{i\omega t}}{1+\mu k^2}, \tag{5.93}$$

with the initial condition $U(k,0) = U_0(k) = \mathcal{F}\{u_0(x)\}$. This first-order equation can be solved using the integrating factor $\exp(i\sigma(k)t)$. The result is

$$U(k,t) = U_0(k)\exp(-i\sigma(k)t) + A\frac{1}{1+\mu k^2}\left(\frac{\exp(i\omega t)}{i(\sigma(k)+\omega)} - \frac{\exp(-i\sigma(k)t)}{i(\sigma(k)+\omega)}\right). \tag{5.94}$$

This is the solution to (5.87) in Fourier space. This spectral solution is important, especially for use with numerical approximations, but it does not clearly reveal the behaviour of the

forced BBM waves. To determine the physical characteristics of the generated waves a transformation into physical coordinates is needed.

5.3.3 The Physical Solution

Determining the solution to (5.87) in physical space can, in theory, be achieved by applying the inverse Fourier transform to (5.94). While this is a suitable approach when numerical inverse Fourier transforms are used, an analytical solution may be impossible to find.

Finding the evolution of an initial profile under the BBM equation is harder than for the KdV equation. This is because $\exp(-i\sigma(k)t)$ does not appear to have a simple inverse in terms of special functions. Since the evolution of forced waves is of primary interest, the assumption $u_0(x) = 0$ is made for the remainder of the analysis. The asymptotic techniques used to study the forced response could be applied to determine the evolution of the initial condition, but that problem is not pursued in this chapter.

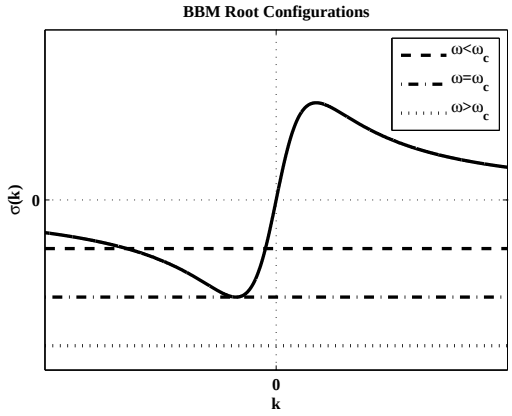

Figure 5.7: Possible root configurations of $\sigma(k) + \omega$ are determined by the intersections of $\sigma(k)$, the solid line, with the horizontal lines. When $\omega < \omega_c$ two negative roots exist, when $\omega = \omega_c$ one real negative root exists, and when $\omega > \omega_c$ no real roots are present.

Finding the integration contour needed for the inverse Fourier transform requires an analysis of the real poles of the integrand. Returning to equation (5.94), consider the polynomial denominator $(1 + \mu k^2)(\sigma(k) + \omega)$, which has the same real roots as $\sigma(k) + \omega$. Based on the values of ω, c_0, and μ the poles of the integrand, lying at the roots of $(1 + \mu k^2)(\sigma(k) + \omega) = 0$, differ qualitatively. These roots are located at

$$k = -\frac{c_0}{2\mu\omega} \pm \frac{c_0}{2\mu\omega}\sqrt{1 - \frac{4\omega^2\mu}{c_0^2}}. \tag{5.95}$$

Considering the discriminant, the critical frequency

$$\omega_c = \frac{c_0}{2\sqrt{\mu}} \tag{5.96}$$

is apparent. This suggests that there are three important cases for the roots of $\sigma(k)+\omega = 0$, they are:

- Case 1: $|\omega| < \omega_c$. Two distinct real roots $k = r_1$ and $k = r_2$ exist with $r_2 < -1/\sqrt{\mu} < r_1 < 0$. The group velocities at these wavenumbers satisfy $c_g(r_1) > 0$, and $c_g(r_2) < 0$.
- Case 2: $|\omega| = \omega_c$. A single real root exists at $k = r_1$. The group velocity at this wavenumber is $c_g(r_1) = 0$.
- Case 3: $|\omega| > \omega_c$. Two complex roots exist at $k = r_1$ and $k = r_1^*$. The corresponding poles do not lie on the real k-axis.

In Figure 5.7 the three possible root configurations for $\sigma(k) + \omega = 0$ are illustrated. The group velocities of the corresponding poles are evident from the slopes of the curves. The BBM root configurations are different from those of the KdV equation, where at least one real root is always present.

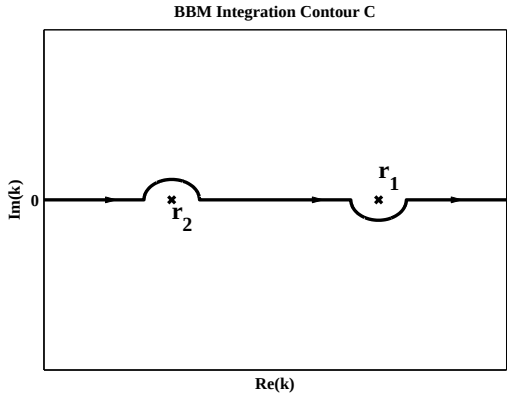

Figure 5.8: The integration contour C for the BBM problem. The contour is directed from left to right.

Based on the discussion in Section 5.1.2 and the description of the group velocities at the poles, the integration contour C needed for the inverse Fourier transform can be determined. When $|\omega| < \omega_c$, the contour C must traverse the real axis with a deformation above the pole at r_2 and below the pole at r_1. This contour is illustrated in Figure 5.8.

When $|\omega| = \omega_c$, the pole at r_1 has zero group velocity so it is not possible to determine how to deform the contour around it. However, since these forced waves cannot escape the forcing region the integration contour can be made to pass through the pole provided the residue contribution is ignored. Finally, when $|\omega| > \omega_c$, the two poles lie off the real axis so no contour deformations are required. For the remainder of this discussion, the most physically relevant case where $|\omega| < \omega_c$ is assumed, remarks on the other two cases are given later.

With zero initial conditions and the above definition of C, the physical space solution can be expressed as

$$u(x,t) = \frac{A}{2\pi i \mu \omega} \left(\int_C \frac{e^{i(kx+\omega t)}}{(k-r_1)(k-r_2)}\, dk - \int_C \frac{e^{i(kx-\sigma(k)t)}}{(k-r_1)(k-r_2)}\, dk \right). \tag{5.97}$$

The first integral in (5.97) can be computed exactly. When $x \geq 0$, C can be closed with a semicircular arc in the upper half-plane. When $x < 0$, C can be closed with a semicircular arc in the lower half-plane. Jordan's lemma dictates that the contribution from the semicircular arcs is zero in both cases as the radius tends to infinity. Since the integrand is otherwise analytic, there will only be residue contributions from the poles at r_1 when $x \geq 0$ and r_2 when $x < 0$. Thus

$$\int_C \frac{e^{i(kx+\omega t)}}{(k-r_1)(k-r_2)}\, dk = \begin{cases} 2\pi i \frac{\exp(i(r_1 x+\omega t))}{r_1-r_2} \text{ when } x \geq 0 \\ 2\pi i \frac{\exp(i(r_2 x+\omega t))}{r_1-r_2} \text{ when } x < 0. \end{cases} \tag{5.98}$$

In order to evaluate $\int_C \exp(i(kx-\sigma(k)t))/((k-k_+)(k-k_-))\, dk$ observe that for fixed t, $c_0 tk/(1+\mu k^2)) \to 0$ as $|k| \to \infty$. Therefore, whether the contour C should be closed in the upper or lower half-plane depends entirely on the sign of x. When $x \geq 0$, C can be closed with a semicircular arc in the upper half-plane and when $x < 0$ it can be closed with a semicircular arc in the lower half-plane. Jordan's lemma ensures that the integrals along the semicircular arcs are zero. With the contour closed in the upper half-plane, residue contributions from the essential singularity at $k = i/\sqrt{\mu}$ and the simple pole at r_1 must be included. When the contour is closed in the lower half-plane, the essential singularity at $-i/\sqrt{\mu}$ and pole at r_2 contribute. Therefore when $x \geq 0$:

$$\int_C \frac{e^{i(kx-\sigma(k)t)}}{(k-r_1)(k-r_2)}\, dk = 2\pi i \frac{\exp\left(i(r_1 x+\omega t)\right)}{r_1-r_2} + 2\pi i \mathrm{Res}(i/\sqrt{\mu}), \tag{5.99}$$

and when $x < 0$:

$$\int_C \frac{e^{i(kx-\sigma(k)t)}}{(k-r_1)(k-r_2)}\, dk = -2\pi i \frac{\exp\left(i(r_2 x+\omega t)\right)}{r_2-r_1} - 2\pi i \mathrm{Res}(-i/\sqrt{\mu}), \tag{5.100}$$

where $\text{Res}(\pm i/\sqrt{\mu})$ is the residue of the integrand evaluated at $k = \pm i/\sqrt{\mu}$. Substituting these results back into (5.97) and using the definition of the residue reveals that, when $x \geq 0$

$$u(x,t) = -\frac{A}{2\pi i \mu\omega} \oint_{C_+} \frac{\exp(i(kx - \sigma(k)t))}{(k - r_1)(k - r_2)}\, dk, \tag{5.101}$$

where C_+ is the small circular contour, oriented counter-clockwise, enclosing $i/\sqrt{\mu}$ but not r_1 or r_2. Figure 5.9 depicts the circular contour C_+. Similarly, when $x < 0$

$$u(x,t) = \frac{A}{2\pi i \mu\omega} \oint_{C_-} \frac{\exp(i(kx - \sigma(k)t))}{(k - r_1)(k - r_2)}\, dk, \tag{5.102}$$

where C_- is the small circular contour, oriented counter-clockwise, centered around $-i/\sqrt{\mu}$, but not enclosing r_1 or r_2.

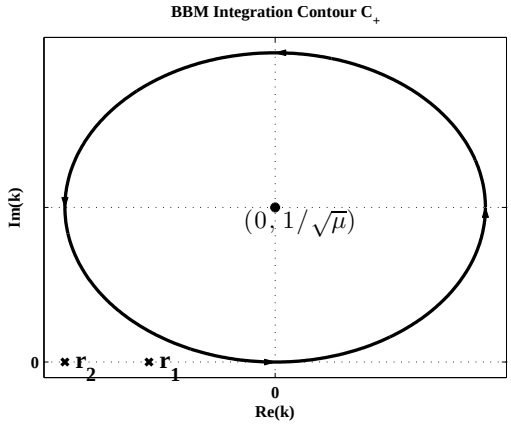

Figure 5.9: The integration contour C_+ for the BBM problem. The contour is directed in counter-clockwise fashion.

At this point, exactly solving for $u(x,t)$ requires direct evaluation of the residues of the integrand at the essential singularities $k = \pm i/\sqrt{\mu}$. This is no easy task, and motivates the decision to apply asymptotic techniques and only consider the limit $t \to \infty$.

5.3.4 Asymptotic Analysis

Equations (5.101) and (5.102) are exact expressions for $u(x,t)$, valid for any positive t in their respective range of x values. Exactly how these solutions behave is unclear because of the difficult problem of evaluating the residues at the essential singularities of the integrands. Headway can be made by applying the method of steepest descents to approximate

the residue at the essential singularities, and ultimately $u(x,t)$ in the large t limit. While the analysis is similar for both cases, only $x \geq 0$ is discussed here. It is further assumed that $|\omega| < \omega_c$, since this range of forcing frequencies leads to traveling waves.

The analysis for the BBM problem is substantially harder than that for the KdV problem, owing to the more complicated integrand. The full details are presented in Appendix D.2 for the interested reader. The steepest descents analysis yields different estimates for the solution depending on the ratio x/t as $t \to \infty$. Letting $c_F = \sigma'(r_1)$ denote the group velocity of the forced wave, the appendix shows that if $0 < x/t < c_F$ then

$$u(x,t) \sim \frac{A}{\mu\omega} \frac{\exp(i(r_1 x + \omega t))}{r_1 - r_2} + O\left(\frac{1}{\sqrt{t}}\right) \tag{5.103}$$

as $t \to \infty$. Similarly, when $c_F < x/t < c_0$, the leading order solution decays like $t^{-1/2}$, and for $x/t > c_0$ the asymptotic solution is exponentially small in comparison with $t^{-1/2}$.

The asymptotic solution can be justified with physical reasoning. At a large value of t, a stationary observer located at a position $x < c_F t$ should expect to see a wave field dominated by the forced wave. Similarly, an observer situated in the interval $c_F t < x < c_0 t$ would lie beyond the leading edge of the forced wave, and could only expect to observe transients. Finally, a stationary observer located at $x > c_0 t$ lies beyond the maximum distance reached by waves in the system, and should not observe any disturbances.

The asymptotic analysis presented in the appendix also extends to the case $|\omega| \geq \omega_c$ with ease. When $|\omega| = \omega_c$, the group velocity of the forced wave is zero, so at any distance from the forcing region only transient waves are observable. When $|\omega| > \omega_c$ the forced waves are evanescent, as they have a complex wavenumber resulting in exponential decay in space. For a stationary observers located sufficiently far from the forcing region, only decaying transients are observable.

5.3.5 Verifying the Asymptotic Solution

In this section, the validity of the asymptotic solution is confirmed through comparisons with numerical simulations. Forcing with a δ-function poses numerical challenges that are not addressed here. Instead, guided by the discussion in Section 5.1.3, a continuous forcing function is used. The difficulties of working with an infinite domain are circumvented by using a periodic domain and stopping simulations before waves reach the boundary. To simplify matters, all variables described here are dimensionless.

Consider the forced BBM equation with $\mu = 1/3$, $\omega = 1/3$, $c_0 = 1$ (note $|\omega| < \omega_c$). The group velocity of the rightward-propagating forced wave is $c_F \approx 0.89$, with corresponding

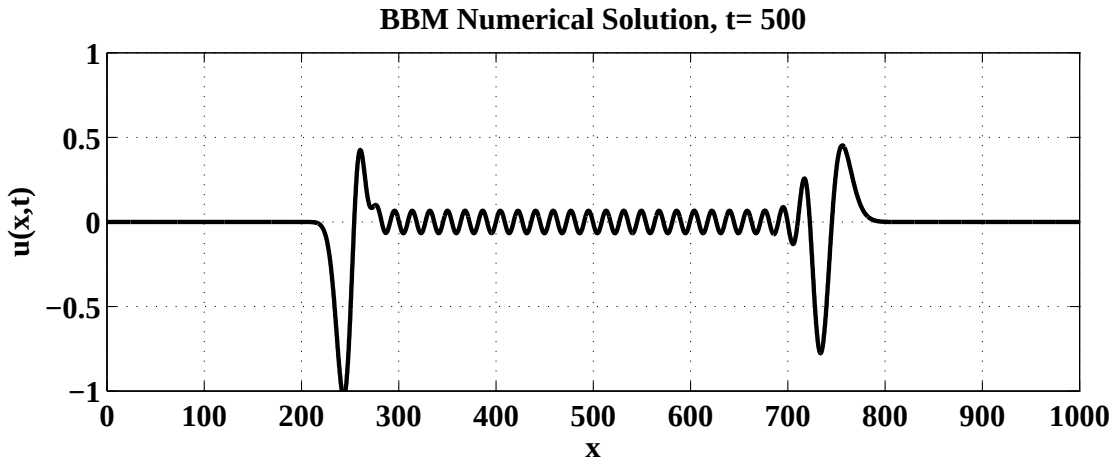

Figure 5.10: The numerical solution to the BBM equation. Notice how the solution involves a very regular wave train, except near the forcing region (centered at $x = 250$), and the leading edge.

wavenumber $r_1 \approx -0.347$. The computational domain is taken to be periodic with length $L = 1000$. The horizontal forcing shape

$$f(x) = \exp(-a(x - x_0)^2) \tag{5.104}$$

with $a = 1/200$, $x_0 = L/4$ is used. For these parameters, $|f(x)| < 10^{-6}$ for $x < 197$ or $x > 303$. In Fourier space, the forcing function takes the form

$$F(k) = \sqrt{\frac{\pi}{a}} \exp(-ikx_0) \exp(-\frac{k^2}{4a}). \tag{5.105}$$

The unit-amplitude temporal forcing dependence $\cos(\omega t)$ is used, so for comparison only the real part of the asymptotic solution found above is taken. According to the discussion in Section 5.1.3 and the preceding analysis, the leading-order solution to the problem is

$$u(x,t) \sim \mathrm{Re}\left\{ A \frac{F(r_1)}{\mu\omega(r_1 - r_2)} \exp(i(r_1 x + \omega t)) \right\} + O(t^{-1/2}), \tag{5.106}$$

and it can be expected to be valid in the interval $300 < x < c_F t + 200$ as $t \to \infty$.

The numerical method used to solve the BBM equation is based on the FFT and is similar to that used in the linear Matlab solver described in Section 3.2.1. In the plots given here, data is presented at $t = 500$, corresponding to about 26.5 forcing periods. In Figure 5.10 the numerical solution to the forced BBM problem is plotted. Clearly evident is a regular wave train sandwiched between a transient leading edge and the forcing region.

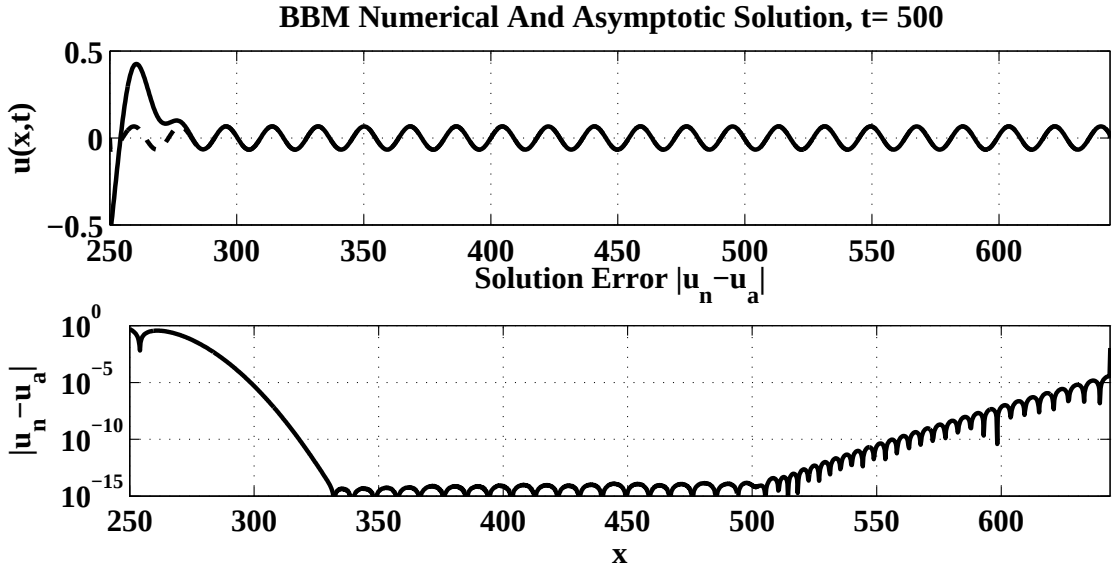

Figure 5.11: In the top subplot, the numerical solution (solid line) and asymptotic solution (dashed line) are plotted. The curves are indistinguishable near the edge of the forcing region. In the bottom subplot, the absolute difference between the numerical and asymptotic solutions, denoted by $|u_n - u_a|$ is plotted in log scale.

In Figure 5.11 the difference between the numerical and leading order asymptotic solution are plotted at $t = 500$. Note the logarithmic scale of the vertical axis. The leading order asymptotic solution matches the numerical solution to machine precision away from the forcing region and leading edge of the wave train. Even at the edge of the forcing region, near $x = 300$, the solutions agree to roughly 10^{-5}. This is somewhat remarkable as the error in the asymptotic solution is $O(t^{-1/2})$. The two solutions agree to a much greater degree of accuracy than predicted by the analysis, even at the relatively small time value shown.

5.4 The Forced Linear IGW Equation

In Chapter 2, an evolution equation for the streamfunction for internal gravity waves (IGW) was derived. The basic assumptions of the Boussinesq approximation and rigid lids were made. In this section the additional restriction of a constant buoyancy frequency is also assumed. The impulsively-forced, oscillatory source problem is then:

$$\begin{gathered}\nabla^2\psi_{tt} + N^2\psi_{xx} = A\exp(i\omega t)\delta(x)h(z), \\ -\infty < x < \infty,\ 0 \le z \le 1,\ t \ge 0,\end{gathered} \tag{5.107}$$

subject to initial conditions

$$\begin{gathered}\psi(x,z,0) = 0, \\ \psi_t(x,z,0) = 0,\end{gathered} \tag{5.108}$$

and far-field conditions

$$\begin{gathered}\psi(x,0,t) = 0,\ \psi(x,1,t) = 0, \\ \psi(x,z,t) \to 0 \text{ as } x \to \pm\infty.\end{gathered} \tag{5.109}$$

The Laplacian operator is defined by $\nabla^2 = \partial^2/\partial x^2 + \partial^2/\partial z^2$.

The related source problem for an unbounded fluid with a spherically symmetric source has been studied by Lighthill [45] and Voisin [71]. In addition, Duffy [22] presents an exact Green's function solution for the problem with a point source in time and space. A comparison with the exact solution presented by Duffy is given in Section 5.4.6. The approach used here is quite different, however, and follows the same strategy that was applied to the KdV and BBM equations.

5.4.1 The Dispersion Relation and Group Velocity

The dispersion relation for the IGW equation is found by substituting $\psi(x,z,t) = \exp(i(kx - \sigma t))g(z)$ into the homogeneous version of (5.107). The result is the eigenvalue problem

$$g''(z) + k^2\left(\frac{N^2}{\sigma^2} - 1\right)g(z) = 0, \tag{5.110}$$

with boundary conditions $g(0) = 0 = g(1)$. This is a simplified form of the problem discussed at great length in Section 2.3.

Since $N^2(z)$ is constant, the eigenvalue problem is exactly solvable, and the n^{th} eigenfunction is given by $g_n(z) = \sin(n\pi z)$ and

$$\sigma_n^2(k) = \frac{k^2 N^2}{k^2 + n^2\pi^2}. \tag{5.111}$$

There are two branches of the dispersion relation for a mode-n wave, corresponding to leftward and rightward-propagating waves. This introduces a complication not seen in the analysis of the KdV and BBM equations. The dispersion relation is plotted in the top subplot of Figure 5.12. The group velocity is defined by

$$\frac{d\sigma_n(k)}{dk} = \pm\frac{n^2\pi^2 N}{(k^2 + n^2\pi^2)^{3/2}}, \tag{5.112}$$

where the sign determined by the branch of σ_n. Long waves ($k \to 0$) have the fastest group velocity, while the short wave limit gives the slowest waves. These ideas are evident in the bottom subplot of Figure 5.12. In the remainder of this analysis $\sigma_n(k)$ is taken to be the positive root of (5.111).

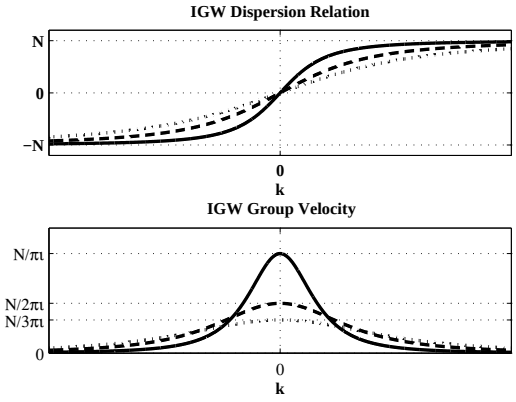

Figure 5.12: The dispersion relation (top subplot) and group velocity (bottom subplot) for the first three vertical modes of the IGW equation. Modes one, two, and three are drawn with the solid, dashed, and dotted lines, respectively. Only one branch of the dispersion relation is plotted.

5.4.2 The Spectral Solution

The natural approach to solving the problem with Fourier transforms is to first decompose $\psi(x,z,t)$ into vertical modes. That is, let

$$\psi(x,z,t) = \sum_{n=1}^{\infty} \psi_n(x,t)\sin(n\pi z). \tag{5.113}$$

The vertically-varying term in the right-hand side of (5.107) can be decomposed as

$$h(z) = \sum_{n=1}^{\infty} h_n \sin(n\pi z), \quad \text{where} \quad h_n = \int_0^1 h(z)\sin(n\pi z)\ dz. \tag{5.114}$$

Substituting the series (5.113) into (5.107), projecting onto the n^{th} vertical mode, then taking the Fourier transform reveals

$$\frac{\partial^2}{\partial t^2}\Psi_n(k,t) + \sigma_n^2(k)\Psi_n(k,t) = -\frac{\sigma_n^2(k)}{k^2}Ae^{i\omega t}h_n, \tag{5.115}$$

where $\Psi_n(k,t) = \mathcal{F}\{\psi_n(x,t)\}$. This is the evolution equation for the n^{th} vertical mode of the streamfunction in Fourier space. The initial conditions specified in (5.107) imply $\Psi_n(k,0) = \partial_t\Psi_n(k,0) = 0$, so solving the ordinary differential equation is straightforward. The result is:

$$\begin{array}{rl} \Psi_n(k,t) = & \frac{A\sigma_n h_n}{2k^2(\sigma_n-\omega)}\exp(i\sigma_n t) + \frac{A\sigma_n h_n}{2k^2(\sigma_n+\omega)}\exp(-i\sigma_n t) \\ & -\frac{A\sigma_n^2 h_n}{k^2(\sigma_n^2-\omega^2)}\exp(i\omega t). \end{array} \tag{5.116}$$

Equation (5.116) is the exact solution to the IGW problem (5.107) in Fourier space. Comparing against the Fourier space solutions for the BBM and KdV equations, the presence of the extra term is clearly a result of the higher-order derivatives and initial conditions.

5.4.3 The Physical Solution

The solution $\psi(x,t)$ is found by summing the different vertical mode contributions. Each of these contributions is found by inverting the corresponding Fourier solution (5.116). The physical solution of the mode-n streamfunction is

$$\begin{array}{rcl} \psi_n(x,t) & = & \frac{1}{2\pi}\int_{C_1}\frac{A\sigma_n h_n}{2k^2(\sigma_n-\omega)}\exp\big(i(kx+\sigma_n t)\big)\ dk \\ & & +\frac{1}{2\pi}\int_{C_2}\frac{A\sigma_n h_n}{2k^2(\sigma_n+\omega)}\exp\big(i(kx-\sigma_n t)\big)\ dk \\ & & -\frac{1}{2\pi}\int_{C_3}\frac{A\sigma_n^2 h_n}{k^2(\sigma_n^2-\omega^2)}\exp\big(i(kx+\omega t)\big)\ dk \\ & = & I_1 + I_2 + I_3, \end{array} \tag{5.117}$$

where the contours C_1, C_2, and C_3 must be determined from an analysis of the poles of the integrands using the discussion in Section 5.1.2.

The integrands of I_1 and I_2 posses branch cuts and essential singularities owing to the presence of the terms $\exp(\pm i\sigma_n(k)t)$. The essential singularities lie at $k = \pm in\pi$, and the branch cuts are chosen to lie along the imaginary axis directed away from the origin. While these features play a critical role in the end result, they do not affect the form of the inverse Fourier transform contours.

Considering equation (5.117), the integrands also appear to have poles wherever $\sigma_n(k) \pm \omega = 0$. In addition, a removable second-order pole at $k = 0$ appears in each integrand. For I_3 it is easy to see that the pole is removable because $\sigma_n(0) = 0$ and $\sigma_n'(0)$ is bounded. To show that the pole is removable for I_1 and I_2, return to expression (5.116) and add the first two terms using the common denominator $\sigma_n^2(k) - \omega^2$ to find

$$\begin{aligned}\Psi_n(k,t) = \; & \tfrac{Ah_n}{2(\sigma_n^2-\omega^2)}\tfrac{\sigma_n^2}{k^2}(\exp(i\sigma_n t) + \exp(-i\sigma_n t)) \\ & + \tfrac{Ah_n}{2(\sigma_n^2-\omega^2)}\tfrac{\omega\sigma_n}{k^2}(\exp(i\sigma_n t) - \exp(-i\sigma_n t)) \\ & - \tfrac{A\sigma_n^2 h_n}{k^2(\sigma_n^2-\omega^2)}\exp(i\omega t).\end{aligned} \tag{5.118}$$

The term on the first line of (5.118) involves the factor $\sigma_n^2(k)/k^2$, which has a removable singularity at $k = 0$. The second line of (5.118) has the factor $\sigma_n(k) \cdot (\exp(i\sigma_n t) - \exp(-i\sigma_n t))/k^2$. Again, since $\sigma_n(0) = 0$, the singularity is removable. This discussion shows that the inversion contours need not be deformed about $k = 0$, and no residues from that point contribute in the computation of $\psi_n(x,t)$.

In (5.117), the poles stemming from the roots of $\sigma_n(k) \pm \omega = 0$ require special consideration. Depending on the forcing frequency, these poles may be real or complex. Since $-N < \sigma_n(k) < N$, the natural critical forcing frequency is

$$\omega_c = N. \tag{5.119}$$

Unlike the previous examples, no finite value of k will satisfy the equation $\sigma_n(k) = \omega_c$, therefore only two cases are necessary.

- Case 1: $|\omega| < \omega_c$. A single root for the equations $\sigma_n(k) + \omega = 0$ and $\sigma_n(k) - \omega = 0$ exists. With
$$r = \frac{n\pi\omega}{\sqrt{N^2 - \omega^2}}. \tag{5.120}$$
it follows that $\sigma_n(-r) + \omega = 0$ and $\sigma_n(r) - \omega = 0$.

- Case 2: $|\omega| \geq \omega_c$. No real roots exist for the equations $\sigma_n(k) \pm \omega = 0$. Two purely imaginary roots do exist, but they can only give rise to spatially decaying (evanescent) waves.

Since the primary focus of this study is understanding the traveling waves produced by the forcing, only Case 1 is considered. The group velocity $\sigma_n'(k)$ is strictly positive, therefore the integration contours used must be deformed below the pole at $k = -r$. To understand how to deform the contour about the root of $\sigma_n(k) - \omega = 0$, a modified version of the approaches outlined in Section 5.1.2 must be used. It is simple to show with Lighthill's approach that since $\sigma_n'(r) > 0$, the integration contours must be deformed above the pole at $k = r$.

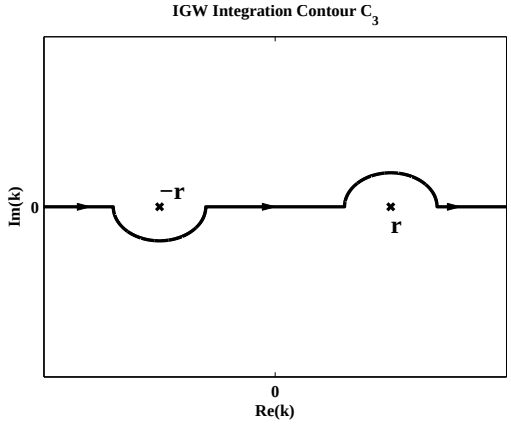

Figure 5.13: The integration contour C_3 in the complex $k-$plane.The poles at $k = \pm r$ are marked by 'x' symbols. The contour traverses the entire real axis.

The results of this discussion lead to the inversion contour C_3 depicted in Figure 5.13. This contour traverses the real axis with deformations above $k = r$ and below $k = -r$. The integration contours C_1 and C_2 follow immediately. Since I_1 has no pole at $k = -r$, the contour is only deformed above $k = r$. Likewise, the contour C_2 traverses the real line with a deformation below $k = -r$.

While expression (5.116) is suitable for use in the numerical inversion of the Fourier transform, the actual solution (5.117) involves terms that are difficult to evaluate analytically. Certainly I_3 can be computed, and for $x \geq 0$

$$I_3 = \frac{iAh_n\omega}{2r^2\sigma_n'(-r)} \exp(-irx + i\omega t). \tag{5.121}$$

The presence of essential singularities and branch cuts in I_1 and I_2 make their inversion difficult. Some simplifications can be made by expressing I_1 and I_2 in an alternative form. Using Jordan's lemma, integration along quarter-circular arcs at large radius yield no net contributions. It follows that I_1 and I_2 can be expressed in terms of a simpler branch cut integral. Let C_0 denote the contour that traverses the imaginary axis in the first quadrant

from $+i\infty$ to $in\pi$, encircles the branch point at $in\pi$ and proceeds up the imaginary axis on the other side of the branch cut to $+i\infty$. The contour C_0 is illustrated in Figure 5.14, and it can be used to derive the expressions:

$$I_1 = -\frac{Ah_n}{4\pi} \int_{C_0} \frac{\sigma_n(k) \exp(i(kx + \sigma_n t))}{k^2(\sigma_n(k) - \omega)} \, dk, \tag{5.122}$$

and

$$\begin{aligned} I_2 = \quad & -\tfrac{iAh_n\omega}{2r^2\sigma_n'(-r)} \exp(-irx + i\omega t)) \\ & -\tfrac{Ah_n}{4\pi} \textstyle\int_{C_0} \tfrac{\sigma_n(k) \exp(i(kx - \sigma_n t))}{k^2(\sigma_n(k)+\omega)} \, dk. \end{aligned} \tag{5.123}$$

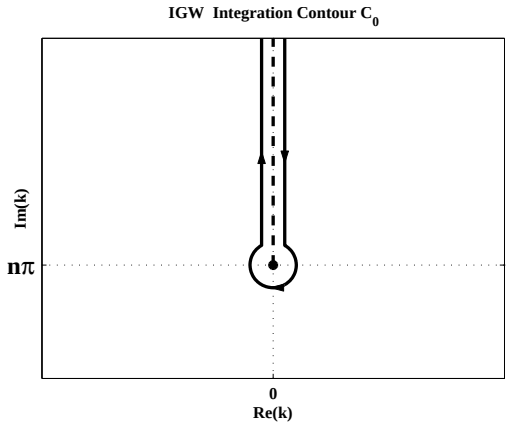

Figure 5.14: The integration contour C_0 in the complex $k-$plane. The branch cut along the imaginary axis is marked by a dashed line emanating from $in\pi$ and continues to $+i\infty$. The integration contour is marked by the solid line, and traversed in the direction marked by the arrowheads.

Using these expressions for I_1 and I_2, and the definition of $\psi_n(x,t)$ from equation (5.117), it is possible to write

$$\begin{aligned} \psi_n(x,t) &= -\tfrac{Ah_n}{4\pi} \textstyle\int_{C_0} \tfrac{\sigma_n(k) \exp(i(kx+\sigma_n t))}{k^2(\sigma_n(k)-\omega)} \, dk - \tfrac{Ah_n}{4\pi} \textstyle\int_{C_0} \tfrac{\sigma_n(k) \exp(i(kx-\sigma_n t))}{k^2(\sigma_n(k)+\omega)} \, dk, \\ &= \hat{I}_1 + \hat{I}_2. \end{aligned} \tag{5.124}$$

This is an exact expression, but it offers little physical insight into the nature of the IGW solution. It is not clear what the frequency, phase, or amplitude of waves emanating from the forcing region might be. However, the form of the solution in (5.124) is a sound starting point for asymptotic analysis, as discussed in the next section.

5.4.4 Asymptotic Analysis

The method of steepest descents can be applied to approximate the solution to $\psi_n(x,t)$ for $x \geq 0$ in the limit as $t \to \infty$. The method must be applied to both $\hat{I}_1$ and $\hat{I}_2$ separately. The details are rather involved because of the branch cuts that arise from the dispersion relation, and the interested reader is referred to Appendix D.3 for the full calculations. Here only the important points are discussed.

The analysis in the appendix shows that $\hat{I}_1$ is sub-dominant to $\hat{I}_2$. As $t \to \infty$, the estimation of the dominant term $\hat{I}_2$ requires consideration of several cases depending on the ratio x/t. The case of most physical interest occurs when $x/t < c_F$, where $c_F = \sigma_n'(r)$ is the group velocity of the forced wave. In that situation, the asymptotic solution takes the form:

$$\psi_n(x,t) \sim -A\frac{h_n\omega}{2r^2\sigma_n'(-r)}\exp(-i(rx-\omega t)+i\pi/2)+O(t^{-1/2}). \tag{5.125}$$

Letting $c_L = N/(n\pi)$ denote the maximum group velocity for a mode-n wave (achieved in the long-wave limit), it is shown in the appendix that if $c_F < x/t < c_L$, the dominant contribution to the streamfunction decays like $t^{-1/2}$. This decaying term is not surprising, the impulsively forced system should generate transients that must diminish in time. Finally, when $x/t > c_L$ the analysis shows that the approximate streamfunction solution must be small beyond all orders in comparison with $t^{-1/2}$. This is also physically plausible, as waves could not reach an observer at that distance in t units of time.

The above approximation describes the behaviour of the mode-n streamfunction. The full streamfunction is found by summing the asymptotic contributions. That is,

$$\psi(x,t) \sim \sum_{n=1}^{\infty}\psi_n(x,t). \tag{5.126}$$

Typically the forcing function of interest only produces one, or at most a few, vertical modes. In the verification of the solution demonstrated below, only the mode-1 contribution is considered.

5.4.5 Verifying the Asymptotic Solution

A closed-form solution to the forced IGW equation is not known so verification of the asymptotic solution requires comparison with a numerical solution. The numerical solution presented here is found by direct application of Matlab's inverse FFT to the spectral solution (5.116), with special treatment for $k = 0$. The numerical solution is found for a periodic domain, and can only be compared against the asymptotic solution provided waves are not near the boundary and the forcing region decays sufficiently quickly to zero.

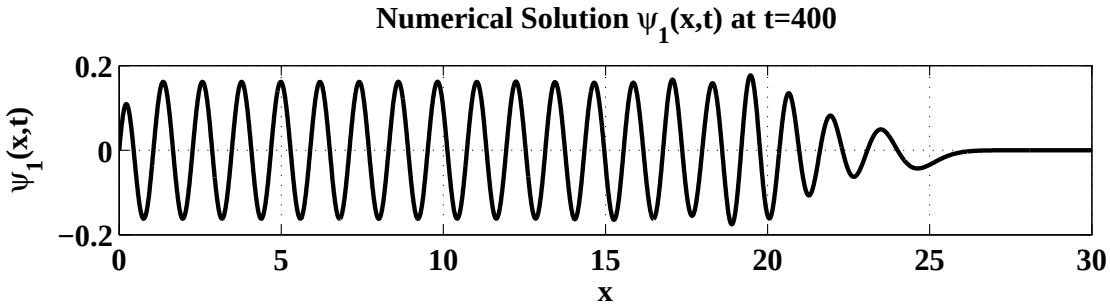

Figure 5.15: Numerical solution to the IGW equations for $\psi_1(x,t)$. Only a subset of the right half of the domain is shown. Note the uniform wave train in the interior of the wave packet.

The dimensionless computational domain is taken to be $-40 \leq x \leq 40$. The domain depth is set to $H = 0.2$ so that the dispersion relation is of the form $\sigma_n^2 = k^2N^2/(k^2 + n^2\pi^2/H^2)$. The buoyancy frequency is set to $N^2 = 1$, and the projection term $h_n = 1$ is fixed. The forcing function

$$f(x) = -2a(x - x_0)\exp(-a(x - x_0)^2) \tag{5.127}$$

is used with $a = 12.5$ and $x_0 = 0$. With these choices, $|f(x)| \leq 10^{-6}$ whenever $|x| \geq 1.2$. Since this forcing function is just the derivative of the Gaussian, its Fourier transform is simply

$$F(k) = ik\sqrt{\frac{\pi}{a}}\exp(-ikx_0)\exp\left(-\frac{k^2}{4a}\right). \tag{5.128}$$

The unit-amplitude temporal forcing component $\cos(\omega t + \pi/4)$ is used with dimensionless frequency $\omega = 2\pi/20$. This is achieved by setting $A = \exp(i\pi/4)$ and taking the real part of the final solution for both the numerical and asymptotic computations. The wavenumber of the forced wave is $-r \approx -5.2$ and its group velocity is $c_F \approx 0.054$. The numerical solution $\psi_1(x,t)$ for $x \geq 0$ at $t = 400$, corresponding to 20 forcing periods, is plotted in Figure 5.15. A regular wave train is visible in the interior of the wave packet, with transient regions at the far left and leading right edge of the signal. The forced wave is predicted to travel a distance of 21.8 units.

With these parameters, and using the discussion in Section 5.1.3, the leading-order asymptotic solution is given by:

$$\psi_1^a \sim \mathrm{Re}\left\{F(-r)\frac{\omega}{2r^2c_F}\exp(i\pi/4)\exp(-i(rx - \omega t) + i\pi/2)\right\} + O(t^{-1/2}). \tag{5.129}$$

Since the forcing amplitude is negligible outside $|x| < 1.2$, the discussion in Section 5.1.3 suggests that the asymptotic solution should be a good approximation in the interval

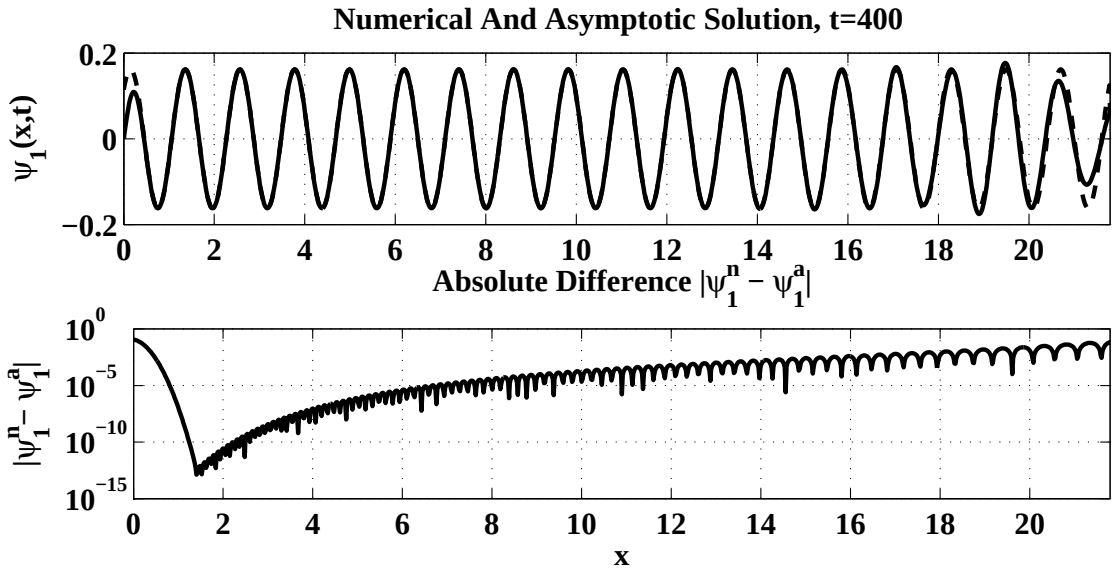

Figure 5.16: In the top subplot the numerical solution ψ_1^n (solid line) and asymptotic solution ψ_1^a (dashed line) are displayed. Visible differences between the solutions only occur at the far left and right edges of the plot. The absolute difference between the two solutions is plotted in the bottom subplot. The two solutions are very similar away from the forcing region and leading-edge region of the wave train.

$1.2 \leq x \leq 20.6$. A direct comparison between the asymptotic solution, denoted by ψ_1^a and the numerical solution ψ_1^n is shown in Figure 5.16. In the top subplot, the two waves are plotted together. Differences between the two curves are only noticeable in the forcing region (near $x = 0$) and towards the right edge of the plot. In the bottom subplot, the absolute difference between the two approximate solutions is plotted with log-scale on the vertical axis. The error is small in comparison with the signal amplitudes.

This simple experiment suggests that the predicted amplitude, phase, and frequency of the waves described by the leading-order asymptotic solution provide an accurate description of the forced waves being approximated. The comparison is being made against a numerical solution that is not an exact solution to the IGW equation, so the relatively minor difference between it and the asymptotic solution is not a major concern. The accuracy witnessed in the approximation for the KdV and BBM equation is not reproduced here, but the asymptotic and numerical solutions are still in strong agreement.

5.4.6 Comparison with an Exact Solution

An exact representation for the Green's function for the IGW equation is known. This is reported by Duffy [22, pages 165-167] and the references therein. The Green's function in question satisfies the equation:

$$\partial_{tt}\nabla^2 g + N^2 g_{xx} = \delta(x-\xi)\delta(z-\zeta)\delta(t-\tau), \tag{5.130}$$

where $g = g(x,z,t|\xi,\zeta,\tau)$ and $-\infty < x,\xi < \infty$, $0 < z,\zeta < L$ and $t,\tau > 0$. The Green's function satisfies the condition $g(x,0,t|\xi,\zeta,\tau) = g(x,L,t|\xi,\zeta,\tau) = 0$ and initial conditions $g(x,z,0|\xi,\zeta,\tau) = g_t(x,z,0|\xi,\zeta,\tau) = 0$. The solution, after correcting a small error, takes the form

$$g(x,z,t|\xi,\zeta,\tau) = \frac{\mathcal{H}(t-\tau)}{4N\pi^2}\int_0^{\pi/2} \begin{array}{l} \frac{\sin[N(t-\tau)\sin(\varphi)]}{\sin(\varphi)} \\ \times \log\left[\left|\frac{\cos(\eta)-\cos(\pi(z-\zeta)/L)}{\cos(\eta)-\cos(\pi(z+\zeta)/L)}\right|\right]\ d\varphi, \end{array} \tag{5.131}$$

where $\eta = |x-\xi|\pi\tan(\varphi)/L$. While arriving at this solution is certainly an admirable feat of algebra, the usefulness of the overall result is questionable. To make matters more complicated, studying the response of the system to an oscillatory source requires an additional convolution integral.

Expression (5.131) is difficult to interpret in the limit of large x or t values, especially for an oscillatory source. It is unclear how an asymptotic expansion of the exact form would be undertaken. Compare this with the simple approximate solution given by (5.125). The solution found by steepest descents is much more insightful as to how waves are generated and propagate; it gives the amplitude, frequency, and phase of the dominant wave train and specifies how transients decay. The verification of the approximate solution in Section 5.4.5 strengthens the argument that the leading-order approximate solution is adequate.

5.5 Discussion

In this chapter a sequence of forced wave equations has been studied with asymptotic techniques. In this section some of the difficulties involved in extending steepest descents analysis to variable coefficient problems are discussed. In addition, causality principles are considered for the equations under study.

5.5.1 Difficulties Extending the IGW Analysis

In this section the possibility of applying steepest descents analysis to the linear IGW equations for nonconstant $N^2(z)$ is considered. It is shown that significant roadblocks are

present and an entirely new approach may be required. The forced problem under study is now

$$\begin{array}{c} \nabla^2\psi_{tt} + N^2(z)\psi_{xx} = A\exp(i\omega t)\delta(x)h(z) \\ -\infty < x < \infty,\ 0 \le z \le 1,\ t \ge 0, \end{array} \tag{5.132}$$

with the same boundary conditions as (5.107). It is assumed that $N^2(z)$ is strictly positive and continuous. The dispersion relation and eigenfunctions for this problem have been discussed at length in Chapter 2. For general $N^2(z)$ the dispersion relation does not have an analytical form, nor do the eigenfunctions.

The Spectral Solution

In Fourier space, the streamfunction can be decomposed in a similar manner to that used when $N^2(z)$ is constant:

$$\psi(k,z,t) = \sum_{n=1}^{\infty} \Psi_n(k,t) g_n(z,k). \tag{5.133}$$

Here $g_n(z,k)$ is the mode-n eigenfunction satisfying

$$g_n'' + k^2\left(\frac{N^2(z)}{\sigma_n^2(k)} - 1\right) g_n = 0,\ g_n(0) = 1,\ g_n(1) = 0. \tag{5.134}$$

It is not difficult to show that the functions $\Psi_n(k,t)$ satisfy

$$\frac{\partial^2}{\partial t^2}\Psi_n(k,t) + \sigma_n(k)^2\Psi_n(k,t) = -\frac{\sigma_n^2}{k^2} A e^{i\omega t} h_n(k), \tag{5.135}$$

where

$$h_n(k) = \int_0^1 h(z) g_n(z,k)\ dz. \tag{5.136}$$

The solution in Fourier space is then

$$\begin{array}{rl} \Psi_n(k,t) = & \frac{A\sigma_n h_n(k)}{2k^2(\sigma_n - \omega)}\exp(i\sigma_n t) + \frac{A\sigma_n h_n(k)}{2k^2(\sigma_n + \omega)}\exp(-i\sigma_n t) \\ & -\frac{A\sigma_n^2 h_n(k)}{k^2(\sigma_n^2 - \omega^2)}\exp(i\omega t). \end{array} \tag{5.137}$$

This is identical to the result for constant $N^2(z)$, except that the precise forms of $h_n(k)$ and $\sigma_n(k)$ are unknown.

The Physical Solution

The solution in physical space is found through the definition of the inverse Fourier transform. That is,

$$\psi(x,z,t) = \frac{1}{2\pi}\sum_n \left(\int_C \Psi_n(k,t) g_n(z,k) \exp(ikx)\ dk \right), \tag{5.138}$$

where C must be determined. Notice how the eigenfunctions $g_n(z,k)$ must be kept inside the integral, in contrast to the case when $N^2(z)$ is constant.

The integration contour C must traverse the real line with indentations about the poles of $\Psi_n(k,t)$. Like the case of constant $N^2(z)$, the pole at $k=0$ is removable. From the arguments of Chapter 2, it is clear that when $|\omega| < \max N(z)$ the equations $\sigma_n(k) \pm \omega = 0$ will have a single real root for any vertical mode number n.

With $N^2(z)$ nonconstant the extension of $\sigma_n(k)$ and $h_n(k)$ to the greater complex plane becomes problematic. In fact, the very notion of a vertical mode number becomes ambiguous when k takes on complex values. In addition, because their analytical form is unknown, it is difficult to know where the poles or branch points of $\sigma_n(k)$ and $h_n(k)$ lie in the complex plane. It is true, however, that these functions are continuous and differentiable on the real k line.

The application of the method of steepest descents to the problem is hindered by the above issues. To further complicate matters, without an analytical form for $\sigma_n(k)$ the nature of a steepest descents path cannot be discerned and therefore asymptotic contributions cannot be determined. Lighthill [45, Chapter 4] has suggested that a possible solution to this problem may be found through a hybrid method involving ray-tracing. As an alternative, the leading order solution for the constant $N^2(z)$ case could serve as a guess for the asymptotic behavior but this would have to be verified experimentally.

5.5.2 Causality

Causality principles for each of the equations studied in this chapter can be inferred from the asymptotic analysis presented. The basic question is, how long will it take for a distant observer to witness the forced waves passing by? To understand the causality principle for a given equation, consider two observers; one traveling faster than the maximum group velocity and one traveling slower. For the KdV, BBM, and IGW equations the observer traveling faster than the maximum (rightward) group velocity will witness a signal that is small beyond all orders compared to that witnessed by the other observer. Similarly, only decaying transients can exist ahead of the front of the forced wave train for each of these equations.

These ideas confirm the expected result that information must travel at the group velocity of the underlying wave. This concept, however, is not immediately obvious from the underlying equations. Take the BBM equation, for instance. Since causality results are often understood through a Laplace transform the technique is used here (see Duffy [23] for an introduction to the Laplace transform). Taking the Fourier transform in x and the Laplace transform in t for the BBM equation defines a new function $U(k,s)$ such that

$$U(k,s) = \frac{A}{\mu s(s-i\omega)(k^2 + \frac{ic_0}{\mu s} + \frac{1}{\mu})}. \tag{5.139}$$

The inverse Fourier transform, taken for $x \geq 0$, gives

$$U(x,s) = \frac{A}{(s-i\omega)} \frac{\exp\left(\left(\frac{c_0}{2\mu s} - \frac{1}{2}\sqrt{\frac{c_0^2}{\mu^2 s^2} + \frac{4}{\mu}}\right)x\right)}{\sqrt{c_0^2 + 4\mu s^2}} \tag{5.140}$$

The final solution in physical space is found by inverting this function using the Bromwich integral:

$$u(x,t) = A\int_{\gamma-i\infty}^{\gamma+i\infty} \left[\frac{\exp\left(st + \left(\frac{c_0}{2\mu s} - \frac{1}{2}\sqrt{\frac{c_0^2}{\mu^2 s^2} + \frac{4}{\mu}}\right)x\right)}{(s-i\omega)\sqrt{c_0^2 + 4\mu s^2}}\right] ds. \tag{5.141}$$

All of the singularities lie on the imaginary axis so γ can be any positive real number. Note there is an essential singularity at $s = 0$. Using Jordan's lemma, this integral must always be closed in the left half-plane. Therefore even when $x > c_0 t$ and the solution is expected to be zero, the difficult residues must be evaluated. The solution can only be zero because the contributions from the essential singularity must exactly cancel the contributions from the other poles. This is not an obvious idea and shows how causality for the BBM equation is not a simple matter.

Chapter 6

Conclusions

In this dissertation problems involving internal gravity waves have been investigated. In particular, the problems of near-resonant triad interaction theory, simulations of resonant interactions, and forcing theory of dispersive wave equations have been the central focus. The major results are now summarized, and possible future projects are suggested. The contributions and future projects are organized by the three problems under investigation in this thesis.

6.1 Theory of Near-Resonant Triad Interactions

6.1.1 Contributions

1. The derivation of the near-resonant interaction equations for spatially-varying wave trains with nonuniform stratifications and rotational effects is novel. The analysis presented in Chapter 2 and Appendix B provides a general framework for predicting and explaining near-resonant interactions in a general class of fluids. The results are an extension of the work done by Davis and Acrivos [17], Lamb [41], and Hu [34].

2. In Section 2.3 a number of properties of the eigenvalue problem for horizontally-propagating internal waves were found. Several of these properties were derived by Yih [76], but the proofs presented in Section 2.3 are original. Although the result is physically intuitive, the mathematical proof of Theorem 4 is new. The derivation of the upper bounds for phase speeds in Boussinesq fluids with rigid lids (Theorem 5 and Theorem 6) are also new results.

The derivation of the near-resonant interaction equations is important because it extends the applicability of resonant triad theory to a broad class of interesting flows. Future

researchers can use the calculations to predict triad interactions and design numerical and laboratory experiments. The properties of the dispersion relation, group velocity, and phase speed, as derived in Section 2.3, are important because they provide a mathematical foundation for discussions of internal waves in continuously stratified fluids.

6.1.2 Future Projects

1. The simulations in Chapter 4 demonstrated that the applicability of the weakly-nonlinear analysis is limited because, even at very small amplitudes, waves take on a nonlinear shape. Perhaps a resonant interaction theory could be constructed for cnoidal waves. The analysis would undoubtedly be complicated, but progress may be possible using techniques developed by Osborne [56] to study a superposition of nonlinear waves. The development of such a theory would be very useful for comparisons with numerical experiments where wave amplitudes are of moderate size.

6.2 Near-Resonant Triad Simulations

6.2.1 Contributions

1. The modal decomposition of the pseudo-energy in Section 3.3, along with the explanation of the shape of the resulting spectrum in Section 3.4 is original. The analysis illustrates the need for care in the interpretation of pseudo-energy spectra. The results could serve as a useful guide for investigators studying energy transfers in internal wave simulations.

2. The simulations of internal wave phenomena and resonant wave interactions in Chapter 4 are original. An important feature of these experiments was the use of variable buoyancy frequencies. Resonant interactions were observed in lab-scale experiments, but at the ocean-scale the dominance of nonlinear steepening effects prevented the interactions from developing. Rotational effects were not included in the simulations.

Future investigations of wave interactions and numerical simulations of internal waves may find these contributions to be valuable. The data decomposition method could provide a convenient approach for studying internal wave dynamics. The results of the numerical simulations are particularly interesting and emphasize the importance of nonlinear effects, even at small wave amplitudes. This may stimulate a more advanced study of wave interactions among nonlinear waves. In addition, to better understand the role of resonant interactions in the ocean the inclusion of rotational effects is necessary.

6.2.2 Future Projects

1. The simulations in Chapter 4 reveal that even small-amplitude internal waves possess a complicated shape. The modal decomposition onto sinusoidal basis functions for energy calculations is not always appropriate as a result. A more general nonlinear Fourier decomposition, possibly based on work done by Osborne [56], would provide a better understanding of energy transfer in triad interactions.

2. The nonlinear steepening observed in the ocean-scale experiments affected the resonant interaction process. In the oceans, the effects of rotation can reduce internal wave steepening (see Helfrich and Grimshaw [31], or Farmer et al. [25]). The length and velocity scales involved in the ocean-scale simulations were such that the corresponding physical flows would have small Rossby numbers. Revisiting the experiments of Chapter 4 with rotational effects included through the f-plane model would provide valuable insight into the importance of resonant interactions in the oceans.

3. Tide-topography interactions are a strong source of internal waves in the oceans (see Garrett and Kunze [27], or Helfrich and Melville [32]). A natural extension of the simulations shown in Chapter 4 would be to look for near-resonant triads in flow past topography. This would also extend the work done by Lamb [41] and Hu [34], who considered the problem for uniform stratifications.

6.3 Dispersive Wave Forcing Theory

6.3.1 Contributions

1. In Section 3.5 a systematic analysis of the forcing problem for the IGW equations with nonuniform stratification on a periodic domain is given. The analysis presented there provides a clear explanation for how the vertical momentum equation can be forced to generate desired internal waves. The theory was tested extensively in Chapter 4 for the nonlinear problem, and found to be successful.

2. In Section 5.2 and Appendix D.1, the steepest descents analysis of the impulsively-forced, linear KdV equation is novel. The comparison with a numerical solution shows that, for the parameters being demonstrated, the asymptotic solution agrees very well with the numerical result.

3. In Section 5.3 and Appendix D.2, the steepest descents analysis of the impulsively-forced linear BBM equation is novel. Numerical experiments confirm that the asymptotic solution gives an excellent approximate solution to the problem even at moderate values of time.

4. In Section 5.4 and Appendix D.3, the steepest descents analysis of the impulsively-forced linear IGW equation with uniform stratification in a vertically bounded domain is novel. Lighthill [45] and Voisin [71] have studied the problem on an unbounded domain, and Duffy [22] presents an exact solution for a related Green's function. However, the exact solution presented by Duffy has limited practical value. The approximate solution found in Section 5.4 is easy to interpret and agrees well with numerical experiments.

The systematic approach to forcing on a periodic domain, as described in Section 3.5, may serve as a useful starting point for researchers attempting to generate internal waves numerically. The forcing approach could be beneficial to researchers studying a range of internal wave phenomena, not just resonant interactions. The asymptotic analysis used in Chapter 5 provides a framework for studying the forced response of a broad class of PDEs. The analysis presented there may prove useful to investigators studying wave generation or heat conduction from many different disciplines.

6.3.2 Future Projects

1. The framework used to find approximate solutions for the linearized KdV, BBM, and IGW equations could be adapted to any number of other equations with constant coefficients. For instance, an immediate, albeit minor, extension could be made by repeating the IGW analysis with a non-zero Coriolis parameter.

2. The major question of how to apply asymptotic analysis techniques to the IGW equation with nonuniform stratification remains open. The underlying variable-coefficient eigenvalue problem has subtle properties in the complex k-plane that hinder the analysis. Lighthill [45] has suggested that a possible solution may be found through a hybrid method involving ray-tracing, and that may be the best starting point for this problem.

Appendix A

Waves in a Two-Layer Fluid

In this appendix some basics of waves in two-layer fluids are presented. The results given here are standard exercises in the study of waves.

Consider a two-layer incompressible, inviscid fluid. Suppose the interface lies at $z = 0$, and solid impermeable boundaries lie at $z = H_1$ and $z = -H_2$. Suppose the density of the upper fluid is ρ_1, and ρ_2 is the density for the lower fluid, with $\rho_1 < \rho_2$.

Suppose a wave on the surface is of the form $\eta = A\exp(i(kx - \sigma t))$, with the real part being taken. The unknown frequency σ is defined by the unknown dispersion relation.

Assuming the flow is irrotational, a velocity potential can be defined in each layer. Using indices matching those for density, the fluid satisfies the following set of equations and boundary conditions:

$$\nabla^2\phi_1 = 0,\ \nabla^2\phi_2 = 0 \tag{A.1a}$$

$$\frac{\partial\phi_1}{\partial z} = \frac{\partial\phi_2}{\partial z} = \frac{\partial\eta}{\partial t} \text{ at } z = 0 \tag{A.1b}$$

$$\rho_1\frac{\partial\phi_1}{\partial t} + \rho_1 g\eta = \rho_2\frac{\partial\phi_2}{\partial t} + \rho_2 g\eta \text{ at } z = 0 \tag{A.1c}$$

$$\left.\frac{\partial\phi_1}{\partial z}\right|_{z=H_1} = \left.\frac{\partial\phi_2}{\partial z}\right|_{z=-H_2} = 0. \tag{A.1d}$$

Equations (A.1a) come from incompressibility. Equation (A.1b) is the kinematic boundary condition at the fluid interface. Equation (A.1c) is the dynamic boundary condition at the fluid interface. The boundary conditions (A.1d) ensure fluid cannot flow through the rigid boundaries at $z = H_1, -H_2$.

The solutions for the potentials take the form

$$\begin{aligned}\phi_1 &= B\cosh(k(z - H_1))\exp(i(kx - \sigma t))\\ \phi_2 &= C\cosh(k(z + H_2))\exp(i(kx - \sigma t)).\end{aligned} \tag{A.2}$$

The relations between η, ϕ_1 and ϕ_2 define a set of three equations of the form

$$\begin{pmatrix} -i\sigma & k\sinh(kH_1) & 0 \\ -i\sigma & 0 & -k\sinh(kH_2) \\ (\rho_1-\rho_2)g & -i\sigma\rho_1\cosh(kH_1) & i\sigma\rho_2\cosh(kH_2) \end{pmatrix} \begin{pmatrix} A \\ B \\ C \end{pmatrix} = \begin{pmatrix} 0 \\ 0 \\ 0 \end{pmatrix}. \tag{A.3}$$

Denoting the first matrix by M, the dispersion relation is found by solving $\det(M) = 0$. The result is

$$\sigma^2(k) = (\rho_2 - \rho_1)gk\frac{\tanh(kH_1)\tanh(kH_2)}{\rho_1\tanh(kH_2) + \rho_2\tanh(kH_1)}. \tag{A.4}$$

The phase speed $c = \sigma/k$ is then

$$c(k) = \sqrt{(\rho_2 - \rho_1)g}\sqrt{\frac{\tanh(kH_1)\tanh(kH_2)}{k(\rho_1\tanh(kH_2) + \rho_2\tanh(kH_1))}}. \tag{A.5}$$

In the long wave limit $k \to 0$ and the phase speed has the limit

$$c_{LW} = \sqrt{(\rho_2 - \rho_1)g\frac{H_1H_2}{\rho_1H_2 + \rho_2H_1}}. \tag{A.6}$$

The Boussinesq approximation makes for minor simplifications. In the denominator ρ_1 and ρ_2 are replaced by their mean ρ_0, and $\Delta\rho = \rho_2 - \rho_1$ is defined.

An important special case arises when the two fluids have equal depths of $H/2$ (so that the entire fluid is contained within the depth H). In that event,

$$c_{LW} = \sqrt{\frac{\Delta\rho}{4\rho_0}gH}. \tag{A.7}$$

Throughout this thesis two-layer fluids are approximated using continuous stratifications, in particular a tanh profile is used. For analytical purposes, the long wave phase speed is used for non-dimensionalization. How appropriate is this when the pycnocline is not centered in the domain? To determine this, consider the function

$$f(z) = \sqrt{\frac{z(H-z)}{H}}, \tag{A.8}$$

which describes the behavior of c_{LW}. Clearly $f(H/2) = \sqrt{H}/2$, and $f(H/4) = \sqrt{3H}/4 \approx 0.43H$. Indeed, $f(z)$ does not decay very quickly, as evident in Figure A.1. It is also apparent from the figure that even at $z = 0.9$, $f(z) > H/4$. This plot suggests that as long as the pycnocline is not located extremely close to the fluid boundaries, the centered long wave phase speed is an appropriate value for non-dimensionalization.

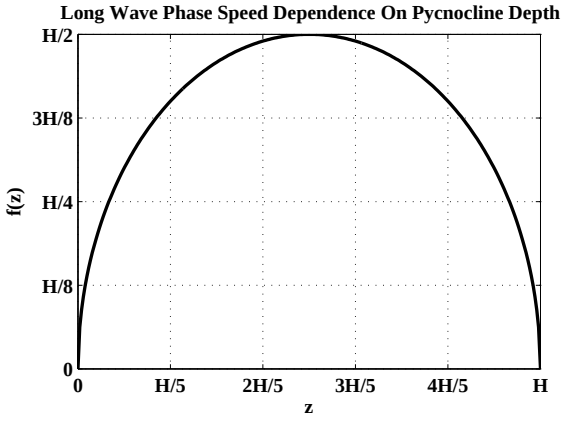

Figure A.1: Demonstrating the decay of $f(z)$ with z. Note how slowly it decays, it is only in the immediate neighborhood of $z = 0, H$ that $f(z)$ differs significantly from $f(H/2)$.

Appendix B

Detailed Triad Calculations

In this appendix the triad interaction equations are derived in detail. This involves expanding the right hand side of equation (2.15) and eliminating secular forcing terms. Exact formulas for the velocity and interaction coefficients are found.

B.1 The Linear Terms

There are three linear terms on the right hand side of (2.15). Based on the structure of $\psi^{(0)}$, these are easily found.

First,

$$\frac{\partial^2}{\partial t^2}\frac{\partial^2}{\partial x \partial X}\psi^{(0)} = -\sum_{p=1}^{3}\left(ik_p\omega_p^2 a_{pX}e^{i\theta_p+i\frac{\pi}{2}} - ik_p\omega_p^2 a_{pX}^* e^{-i\theta_p-i\frac{\pi}{2}}\right) g_p(z). \tag{B.1}$$

The repeated occurrences of $\nabla^2\psi$ leads to terms proportional to $g_p''(z) - k_p^2 g_p(z)$ which are rewritten as

$$\begin{aligned} g_p''(z) - k_p^2 g_p(z) &= k_p^2\left(\tfrac{f^2-N^2(z)}{\omega_p^2-f^2}\right) g_p(z) \\ &= \alpha_p(z) g_p(z). \end{aligned} \tag{B.2}$$

Note $\alpha_p(z)$ is real and $g_p''(z) = (\alpha_p(z) + k_p^2)g_p(z)$.

The second linear term can then be written

$$\nabla^2\frac{\partial^2}{\partial t \partial T}\psi^{(0)} = \sum_{p=1}^{3}\left(-i\omega_p a_{pT}e^{i\theta_p+i\frac{\pi}{2}} + i\omega_p a_{pT}^* e^{-i\theta_p-i\frac{\pi}{2}}\right)\alpha_p(z) g_p(z). \tag{B.3}$$

Finally, the third linear term is

$$N^2(z)\frac{\partial^2}{\partial x \partial X}\psi^{(0)} = \sum_{p=1}^{3}\left(ik_p a_{pX} e^{i\theta_p + i\frac{\pi}{2}} - ik_p a^*_{pX} e^{-i\theta_p - i\frac{\pi}{2}}\right) N^2(z) g_p(z). \tag{B.4}$$

The coefficient of $e^{i\theta_p}$ from the linear terms on the right hand side of equation (2.15) is then

$$i2\omega_p \alpha_p(z) g_p(z) e^{i\frac{\pi}{2}} \frac{\partial a_p}{\partial T} + i2k_p(\omega_p^2 - N^2(z)) g_p(z) e^{i\frac{\pi}{2}} \frac{\partial a_p}{\partial X}, \tag{B.5}$$

The rationale for the use of the factor $\exp(i\pi/2)$ in the definition of $\psi^{(0)}$ is also apparent, it cancels the complex factor i in each term.

B.2 The Nonlinear Terms

Assume the triad being studied satisfies the following near-resonance conditions

$$\begin{aligned} k_1 + k_2 + k_3 &= \epsilon\hat{k} \\ \omega_1 + \omega_2 + \omega_3 &= \epsilon\hat{\omega}. \end{aligned} \tag{B.6}$$

This implies

$$\theta_1 + \theta_2 + \theta_3 = \Delta = \hat{k}X - \hat{\omega}T. \tag{B.7}$$

The nonlinear terms involved in the right hand side of equation (2.15) are rather complicated. Since the arguments of the Jacobian operator are each sums of three elements, a total of nine terms are produced. Based on the structure of $(\psi^{(0)}, b^{(0)}, v^{(0)})$, however, not all of these terms are of interest. In this analysis, all of the terms that do not lead to secular forcing are ignored. The rationale for this is that if a term on the right-hand-side of (2.15) is not resonant, it only modifies the solutions $\psi^{(1)}, v^{(1)}, b^{(1)}$ in a small way. Terms that are resonant generate temporal growth and eventually destroys the ordering of the asymptotic expansion.

Considering the near-resonance conditions, only terms involving sums of exponents are retained. The notation $f|_{\propto e^{i\theta_p}}$ and the symbol "$\simeq$" to indicate the terms in f proportional to $e^{i\theta_p}$.

In this section function arguments are dropped and the prime symbol is used to denote differentiation with respect to z. Notation is further simplified with the definition of the set $S_p = \{(q,r),(r,q))\}$, where p,q,r are distinct and $p,q,r \in \{1,2,3\}$. For example $S_1 = \{(2,3),(3,2)\}$.

Write

$$\begin{aligned} J(\psi^{(0)},\nabla^2\psi^{(0)}) &= i\sum_{m=1}^{3}\sum_{n=1}^{3}\Big[\Big(k_m g_m(z)\tfrac{d}{dz}(\alpha_n(z)g_n(z)) \\ &\qquad - k_n\tfrac{dg_m(z)}{dz}\alpha_n(z)g_n(z)\Big)a_m a_n e^{i\theta_m+i\theta_n+i\pi} \\ &\qquad +C.C.\Big] \end{aligned} \tag{B.8}$$

where "C.C." is used to denote the complex conjugate terms.

Letting

$$c_{mn}(z) = k_m g_m(z)\frac{d}{dz}(\alpha_n(z)g_n(z)) - k_n\frac{dg_m(z)}{dz}\alpha_n(z)g_n(z), \tag{B.9}$$

which is real, it follows that

$$\begin{aligned} -\tfrac{\partial}{\partial t}J(\psi^{(0)},\nabla^2\psi^{(0)}) &= \sum_{m=1}^{3}\sum_{n=1}^{3}\Big[(\omega_m+\omega_n)\left(c_{mn}(z)\right)a_m a_n e^{i\theta_m+i\theta_n} \\ &\qquad +C.C.\Big]. \end{aligned} \tag{B.10}$$

Defining

$$F_{pqr} = -(\omega_p - \epsilon\hat{\omega})(c_{qr}(z)+c_{rq}(z)) \tag{B.11}$$

the resonance conditions are used to find

$$-\frac{\partial}{\partial t}J(\psi^{(0)},\nabla^2\psi^{(0)})\Big|_{\propto e^{i\theta_p}} \simeq F_{pqr}a_q^* a_r^* e^{i\theta_p}e^{-i\Delta}.$$

where $(q,r)\in S_p$.

Next consider

$$\begin{aligned} J(\psi^{(0)},b^{(0)}) &= -i\sum_{m=1}^{3}\sum_{n=1}^{3}\Big[\Big(\tfrac{k_m k_n}{\omega_n}g_m(z)\tfrac{d}{dz}(N^2(z)g_n(z)) \\ &\qquad -\tfrac{k_n^2}{\omega_n}\tfrac{dg_m(z)}{dz}N^2(z)g_n(z)\Big)a_m a_n e^{i\theta_m+i\theta_n+i\pi} \\ &\qquad +C.C.\Big]. \end{aligned} \tag{B.12}$$

Defining the real quantity

$$d_{mn}(z) = \frac{k_m k_n}{\omega_n}g_m(z)\frac{d}{dz}(N^2(z)g_n(z)) - \frac{k_n^2}{\omega_n}\frac{dg_m(z)}{dz}N^2(z)g_n(z) \tag{B.13}$$

so that

$$\begin{aligned} \tfrac{\partial}{\partial x}J(\psi^{(0)},b^{(0)}) &= -\sum_{m=1}^{3}\sum_{n=1}^{3}(k_m+k_n)\left[d_{mn}(z)a_m a_n e^{i\theta_m+i\theta_n}\right. \\ &\qquad \left.+C.C.\right], \end{aligned} \tag{B.14}$$

and letting

$$G_{pqr} = (k_p - \epsilon\hat{k})(d_{qr}(z) + d_{rq}(z)), \tag{B.15}$$

leads to

$$\frac{\partial}{\partial x} J(\psi^{(0)}, b^{(0)})\bigg|_{\propto e^{i\theta_p}} \simeq G_{pqr} a_q^* a_r^* e^{i\theta_p} e^{-i\Delta}.$$

The final term required is $f\partial_z J(\psi^{(0)}, v^{(0)})$. This is found by considering

$$\begin{aligned} J(\psi^{(0)}, v^{(0)}) &= -f \sum_{m=1}^{3}\sum_{n=1}^{3} \Big[\Big(\tfrac{k_m}{\omega_n} g_m(z) \tfrac{d^2 g_n(z)}{dz^2} \\ &\quad - \tfrac{k_n}{\omega_n} \tfrac{dg_m(z)}{dz} \tfrac{dg_n(z)}{dz} \Big) a_m a_n e^{i\theta_m + i\theta_n + i\pi} \\ &\quad + C.C. \Big]. \end{aligned} \tag{B.16}$$

Define the real quantity

$$e_{mn}(z) = \frac{k_m}{\omega_n} g_m(z) \frac{d^2 g_n(z)}{dz^2} - \frac{k_n}{\omega_n} \frac{dg_m(z)}{dz} \frac{dg_n(z)}{dz}, \tag{B.17}$$

so that

$$f\tfrac{\partial}{\partial z} J(\psi^{(0)}, v^{(0)}) = f^2 \sum_{m=1}^{3}\sum_{n=1}^{3} \left[\tfrac{d}{dz} e_{mn}(z) a_m a_n e^{i\theta_m + i\theta_n} + C.C. \right]. \tag{B.18}$$

From this it is natural to write

$$f\frac{\partial}{\partial z} J(\psi^{(0)}, v^{(0)})\bigg|_{\propto e^{i\theta_p}} \simeq H_{pqr} a_q^* a_r^* e^{i\theta_p} e^{-i\Delta} \tag{B.19}$$

where

$$H_{pqr} = f^2 \frac{d}{dz}(e_{qr}(z) + e_{rq}(z)). \tag{B.20}$$

Note that

$$\begin{aligned} \tfrac{d}{dz} e_{qr}(z) &= \tfrac{k_q}{\omega_r} \left(\tfrac{dg_q(z)}{dz}(k_r^2 + \alpha_r(z)) g_r(z) + g_q(z) \tfrac{d}{dz}(\alpha_r(z) g_r(z)) \right) \\ &\quad - \tfrac{k_r}{\omega_r} \left((k_q^2 + \alpha_q(z)) g_q(z) \tfrac{d}{dz} g_r(z) + \tfrac{d}{dz} g_m(z)(k_r^2 + \alpha_r(z)) g_r(z) \right). \end{aligned} \tag{B.21}$$

The combination of linear and nonlinear terms in equation (2.15) can now be examined. Adding the linear and nonlinear terms discussed above shows that the coefficient of $e^{i\theta_p}$ on the right hand side of equation (2.15) is

$$-2\omega_p \alpha_p g_p \frac{\partial a_p}{\partial T} + -2k_p(\omega_p^2 - N^2) g_p \frac{\partial a_p}{\partial X} + (F_{pqr} + G_{pqr} + H_{pqr})\, a_q^* a_r^* e^{-i\Delta},$$

while the complex conjugate of this equation gives the coefficient of $e^{-i\theta_p}$.

B.3 Removing Resonant Forcing Terms

Consider the $O(\epsilon^2)$ problem that is satisfied by $\psi^{(1)}$, the solution is determined by equation (2.15). Consider the behaviour of a solution of the form $g(z)\exp(i\theta_p)$, where θ_p is defined in the $O(\epsilon)$ problem. How do the inhomogeneous terms affect the evolution of the solution? The structure of the equation leads to the standard eigenvalue problem for $g(z)$. Integrating both sides of the resulting equation by $g_p(z)$, the eigenfunction corresponding to eigenvalue ω_p for parameter k_p, the left hand side becomes zero. It follows that the integral of the produce of $g_p(z)$ with the coefficient of $e^{i\theta_p}$ on the right-hand side of (2.15) must also be zero. This means

$$\begin{aligned} &2\omega_p \left(\int_0^1 \alpha_p(z) g_p^2(z) dz\right) \tfrac{\partial a_p}{\partial T} \\ &+2k_p \left(\int_0^1 (\omega_p^2 - N^2(z)) g_p^2(z) dz\right) \tfrac{\partial a_p}{\partial X} \\ &+\left(\int_0^1 \left(F_{pqr} + G_{pqr} + H_{pqr}\right) g_p(z) dz\right) a_q^* a_r^* e^{-i\Delta} = 0. \end{aligned} \tag{B.22}$$

For the Sturm-Liouville problem (2.10), orthogonality of eigenfunctions $g_m(z)$ and $g_n(z)$ with frequencies ω_m, ω_n at the wavenumber k is defined by the condition

$$\int_{z_1}^{z_2} (N^2(z) - f^2) g_m(z) g_n(z) dz = \begin{cases} 1 & \text{if } m = n \\ 0 & \text{otherwise.} \end{cases}$$

With this normalization equation (B.22) becomes

$$\begin{aligned} &-2\omega_p \tfrac{k_p^2}{\omega_p^2 - f^2} \tfrac{\partial a_p}{\partial T} + 2k_p \textstyle\int_0^1 (\omega_p^2 - N^2(z)) g_p^2(z) dz \tfrac{\partial a_p}{\partial X} \\ &+\left(\int_0^1 \left(F_{pqr} + G_{pqr} + H_{pqr}\right) g_p(z) dz\right) a_q^* a_r^* e^{-i\Delta} = 0. \end{aligned}$$

This can be rewritten as

$$\frac{\partial a_p}{\partial T} + v_p \frac{\partial a_p}{\partial X} = \gamma_p a_q^* a_r^* e^{-i\Delta},$$

where

$$\begin{aligned} v_p &= -\left(\tfrac{\omega_p^2 - f^2}{k_p \omega_p}\right) \cdot \textstyle\int_0^1 (\omega_p^2 - N^2(z)) g_p^2(z) dz \\ &= \tfrac{(\omega_p^2 - f^2)}{\omega_p k_p} - \tfrac{(\omega_p^2 - f^2)^2}{\omega_p k_p} \textstyle\int_0^1 g_p^2(z)\ dz. \end{aligned} \tag{B.23}$$

From Theorem 2 in Section 2.3, it is clear that

$$v_p = \left.\frac{d\sigma_{n_p}}{dk}\right|_{k_p, \omega_p} \tag{B.24}$$

is the group velocity of a wave at wavenumber k_p and frequency ω_p (this implicitly defines the mode number).

The interaction coefficient γ_p is defined by

$$\gamma_p = \left(\frac{\omega_p^2 - f^2}{2k_p^2 \omega_p} \right) \int_0^1 \left(F_{pqr} + G_{pqr} + H_{pqr} \right) g_p(z) dz, \tag{B.25}$$

for $p = 1, 2, 3$. Recall that F_{pqr}, G_{pqr}, and H_{pqr} are all real-valued functions of z. In general the advection and interaction coefficients must be computed numerically, but when $N^2(z)$ is constant significant simplifications can be made, as discussed next.

B.4 Special Case: Linear Stratification

An important special case arises for fluids with linear density stratifications. The resulting buoyancy frequency is constant, and direct comparisons can be made with the formulas presented in Hu [34] and Lamb [41]. Since the advection coefficient has already been shown to equal the group velocity, which holds for $N^2(z)$ constant, only the interaction coefficients are considered here.

The formula

$$\gamma_{pqr} = \frac{\int_0^1 \left(F_{pqr} + G_{pqr} + H_{pqr} \right) g_p(z) dz}{2\omega_p \int_0^1 \alpha_p(z) g_p^2(z) \; dz} \tag{B.26}$$

is used as the starting point because it does not assume that the eigenfunctions are normalized. Integrals can be computed exactly because the eigenfunctions are explicitly known and simple. To compare results, wave amplitudes are set as

$$g_p(z) = A_p \sin(m_p z), \tag{B.27}$$

with $A_p = 1/(2m_p)$. The normalization conditions for the eigenfunctions must be reconsidered.

Assume the additional constraint

$$m_1 + m_2 + m_3 = 0, \tag{B.28}$$

where $m_p = j_p \pi$, j_p is an integer. The more general case does not have such a condition because the vertical wavenumbers depend on z. Under this constraint

$$\int_0^1 \sin(m_p z) \sin(m_q z) \cos(m_r z) \; dz = -1/4. \tag{B.29}$$

When $N^2(z)$ is constant, the coefficient α_p simplifies to

$$\alpha_p = -(k_p^2 + m_p^2) = -\kappa_p^2. \tag{B.30}$$

The first integral in γ_{pqr} becomes

$$\int_0^1 F_{pqr}(z)g_p(z)\ dz = -A_p\omega_p \int_0^1 (c_{qr}+c_{rq})\sin(m_p z)\ dz \tag{B.31}$$

with

$$\begin{aligned} c_{qr}(z) &= A_q A_r m_q m_r \left(-\tfrac{k_q}{m_q}\kappa_r^2 \sin(m_q z)\cos(m_r z)\right. \\ &\quad \left. +\tfrac{k_r}{m_r}\cos(m_q z)\sin(m_r z)\right) \end{aligned} \tag{B.32}$$

the integral is found to be

$$\int_0^1 F_{pqr}g_p\ dz = \omega_p \frac{A_p A_q A_r}{4} m_q m_r \left(\frac{k_q}{m_q}-\frac{k_r}{m_r}\right)\left(\kappa_q^2-\kappa_r^2\right). \tag{B.33}$$

Next observe that

$$\begin{aligned} d_{qr} &= N^2 A_q A_r \left(\tfrac{k_q k_r}{\omega_r} m_r \sin(m_q z)\cos(m_r z)\right. \\ &\quad \left. -\tfrac{k_r^2}{\omega_r} m_q \cos(m_q z)\sin(m_r z)\right). \end{aligned} \tag{B.34}$$

So $\int_0^1 G_{pqr}g_p\ dz$ can be written

$$-k_p N^2 \frac{A_p A_q A_r}{4}\left(\frac{k_q k_r}{\omega_r}m_r - \frac{k_r^2}{\omega_r}m_q + \frac{k_q k_r}{\omega_q}m_q - \frac{k_q^2}{\omega_q}m_r\right) \tag{B.35}$$

which simplifies to

$$\int_0^1 G_{pqr}g_p(z)\ dz = -k_p N^2 m_q m_r \frac{A_p A_q A_r}{4}\left(\frac{k_q}{m_q}-\frac{k_r}{m_r}\right)\left(\frac{k_r}{\omega_r}-\frac{k_q}{\omega_q}\right). \tag{B.36}$$

Next, consider $\int_0^1 H_{pqr}g_p\ dz$. Observe that

$$\begin{aligned} e_{qr} &= A_q A_r \left(-\tfrac{k_q}{\omega_r} m_r^2 \sin(m_q z)\sin(m_r z)\right. \\ &\quad \left. -\tfrac{k_r}{\omega_r} m_q m_r \cos(m_q z)\cos(m_r z)\right) \end{aligned} \tag{B.37}$$

from this it follows that

$$\begin{aligned} \tfrac{d}{dz}e_{qr}(z) &= A_q A_r \left(-\tfrac{k_q}{\omega_r} m_r^2 \left(m_q \cos(m_q z)\sin(m_r z) + m_r \sin(m_q z)\cos(m_r z)\right]\right. \\ &\quad \left. -\tfrac{k_r}{\omega_r} m_q m_r \left(-m_q \sin(m_q z)\cos(m_r z) - m_r \cos(m_q z)\sin(m_r z)\right)\right). \end{aligned} \tag{B.38}$$

Using this, the integral $\int_0^1 H_{pqr} g_p \, dz$ becomes

$$- f^2 \frac{A_p A_q A_r}{4} (m_q + m_r) \left(-\frac{k_q}{\omega_r} m_r^2 + \frac{k_r}{\omega_r} m_q m_r - \frac{k_r}{\omega_q} m_q^2 + \frac{k_q}{\omega_q} m_q m_r \right) \tag{B.39}$$

this can be factored to reveal

$$\int_0^1 H_{pqr} g_p \, dz = f^2 \frac{A_p A_q A_r}{4} m_p m_q m_r \left(\frac{k_q}{m_q} - \frac{k_r}{m_r} \right) \left(\frac{m_q}{\omega_q} - \frac{m_r}{\omega_r} \right). \tag{B.40}$$

The final integral required for a comparison with Hu and Lamb's result is

$$2\omega_p \int_0^1 \alpha_p(z) g_p^2(z) \, dz = -\omega_p \kappa_p^2. \tag{B.41}$$

Combining these results together yields

$$\begin{aligned} \gamma_{pqr} \quad = \quad & \tfrac{A_q A_r}{4 A_p \kappa_p^2 \omega_p} m_q m_r \left(\tfrac{k_q}{m_q} - \tfrac{k_r}{m_r} \right) [\omega_p (\kappa_q^2 - \kappa_r^2) \\ & - k_p N^2 \left(\tfrac{k_r}{\omega_r} - \tfrac{k_q}{\omega_q} \right) + m_p f^2 \left(\tfrac{m_q}{\omega_q} - \tfrac{m_r}{\omega_r} \right)]. \end{aligned} \tag{B.42}$$

This can be simplified further by using $\kappa_q^2 = (k_q^2 N^2 + m_q^2 f^2)/\omega_q^2$ and likewise for κ_r^2. Then

$$\begin{aligned} \gamma_{pqr} \quad = \quad & - \tfrac{A_q A_r}{4 A_p \kappa_p^2} m_q m_r \left(\tfrac{k_q}{m_q} - \tfrac{k_r}{m_r} \right) \times \\ & \left[N^2 \left(\tfrac{k_q^2}{\omega_q^2} - \tfrac{k_r^2}{\omega_r^w} + \tfrac{k_p}{\omega_p} \left(\tfrac{k_q}{\omega_q} - \tfrac{k_r}{\omega_r} \right) \right) \right. \\ & \left. + f^2 \left(\tfrac{m_q^2}{\omega_q^2} + \tfrac{m_r^2}{\omega_r^2} - \tfrac{m_p}{\omega_p} \left(\tfrac{m_q}{\omega_q} - \tfrac{m_r}{\omega_r} \right) \right) \right]. \end{aligned} \tag{B.43}$$

Now it is easy to factor what is left to find

$$\begin{aligned} \gamma_{pqr} \quad = \quad & - \tfrac{A_q A_r N^2}{4 A_p \kappa_p^2} m_q m_r \left(\tfrac{k_q}{m_q} - \tfrac{k_r}{m_r} \right) \times \\ & \left[\left(\tfrac{k_q}{\omega_q} - \tfrac{k_r}{\omega_r} \right) \left(\tfrac{k_1}{\omega_1} + \tfrac{k_2}{\omega_2} + \tfrac{k_3}{\omega_3} \right) \right. \\ & \left. + \tfrac{f^2}{N^2} \left(\tfrac{m_q}{\omega_q} - \tfrac{m_r}{\omega_r} \right) \left(\tfrac{m_1}{\omega_1} + \tfrac{m_2}{\omega_2} + \tfrac{m_3}{\omega_3} \right) \right]. \end{aligned} \tag{B.44}$$

Finally, with the choice for amplitudes, this reduces to

$$\begin{aligned} \gamma_{pqr} \quad = \quad & - \tfrac{m_p N^2}{8 \kappa_p^2} \left(\tfrac{k_q}{m_q} - \tfrac{k_r}{m_r} \right) \times \\ & \left[\left(\tfrac{k_q}{\omega_q} - \tfrac{k_r}{\omega_r} \right) \left(\tfrac{k_1}{\omega_1} + \tfrac{k_2}{\omega_2} + \tfrac{k_3}{\omega_3} \right) \right. \\ & \left. + \tfrac{f^2}{N^2} \left(\tfrac{m_q}{\omega_q} - \tfrac{m_r}{\omega_r} \right) \left(\tfrac{m_1}{\omega_1} + \tfrac{m_2}{\omega_2} + \tfrac{m_3}{\omega_3} \right) \right]. \end{aligned} \tag{B.45}$$

This agrees with the results of Hu [34] and Lamb [41], except for the minus sign in front and the use of a dimensionless parameter for the Coriolis term. The minus sign is readily accounted for upon comparing the definition of the streamfunction. In this document $(u, w) = (-\psi_z, \psi_x)$, while Hu and Lamb use $(u, w) = (\psi_z, -\psi_x)$. Each of the nonlinear Jacobian terms then has an extra minus sign present. The presence of the minus sign does not affect the dynamics since it is the products of the interaction coefficients that govern the system.

Appendix C

Stokes Drift for Internal Waves

Stokes drift calculations for monochromatic internal waves are presented here. This provides a quantitative explanation for some of the behaviour witnessed in the simulations of Chapter 4. Two arguments are considered here. First, the averaged Lagrangian velocity of a fluid particle in an internal wave is calculated. Then, the averaged isopycnal displacements within a wave are computed. It is shown that when wave amplitude is a, the isopycnals are modified at $O(a^2)$. The method used here is similar to an approach used by Thorpe [65], who considered similar problems for interfacial waves and waves in continuously stratified fluids. Bretherton [11] has also studied this problem.

Consider a monochromatic, horizontally-propagating wave in a stratified fluid. The vertical velocity takes the form:

$$w = a\cos(kx - \omega t)\phi_n(z) + O(a^2), \tag{C.1}$$

where ϕ_n is the dimensional mode-n eigenfunction at wavenumber k, with frequency $\omega = \sigma_n(k)$. Incompressibility demands that

$$u = -\frac{a}{k}\sin(kx - \omega t)\frac{d}{dz}\phi_n(z) + O(a^2). \tag{C.2}$$

The notation used in the following analysis is consistent with that developed in Chapter 2.

C.1 The Average Lagrangian Velocity

Consider the horizontal and vertical velocity components given above. It is clear that, after time-averaging over one period, the average horizontal and vertical Eulerian velocity are

zero. The time-averaged Lagrangian horizontal velocity is not zero, however. To see this, let $u_L(x_0, z_0, t)$ be the Lagrangian velocity of a fluid particle initially at (x_0, z_0). Then, following the method used by Kundu and Cohen [37, Chapter 7] for surface waves, the velocity satisfies:

$$u_L(x_0, z_0, t) \approx u(x_0, z_0, t) + (x - x_0)\frac{\partial u}{\partial x}\bigg|_{x_0,z_0,t} + (z - z_0)\frac{\partial u}{\partial z}\bigg|_{x_0,z_0,t} \ldots, \tag{C.3}$$

where the velocities on the right-hand side are Eulerian. For small waves $x - x_0 = \int^t u\, dt = -(a/k\omega)\phi_n'(z_0)\cos(kx_0 - \omega t)$, and similarly $z - z_0 = -(a/\omega)\phi_n(z_0)\sin(kx_0 - \omega t)$. Then, taking the time-average over one period of both sides of (C.3) reveals:

$$\langle u_L(x_0, z_0, t)\rangle = \frac{a^2}{2\omega k}(\phi_n'^2(z_0) + \phi_n(z_0)\phi_n''(z_0)). \tag{C.4}$$

The term in brackets on the right-hand side can be simplified to show that

$$\langle u_L(x_0, z_0, t)\rangle = \frac{a^2}{4\omega k}\frac{d^2}{dz^2}\phi_n^2\bigg|_{z_0}. \tag{C.5}$$

This demonstrates the leading-order velocity experienced by a particle initially at (x_0, z_0). The velocity is only zero at inflection points of ϕ_n^2. More information about the underlying stratification and eigenfunction ϕ_n is needed to make precise predictions about regions where the drift velocity will be positive or negative, but these can be computed numerically.

C.2 The Average Isopycnal Displacements

In the presence of the wave, the background density field is found from $\rho_t + u\rho_x + w\rho_z = 0$. Expanding $\rho = \rho_0 + \bar{\rho}(z) + a\rho_1(x, z, t) + a^2\rho_2(x, z, t) + O(a^3)$, simple calculation reveals that

$$\rho_1 = -\frac{\rho_0}{\omega g}\sin(kx - \omega t)\phi_n(z)N^2(z) \tag{C.6}$$

where $N^2(z) = -(g/\rho_0)d\bar{\rho}/dz$. The next term is

$$\rho_2 = \frac{1}{\omega k}\cos(kx - \omega t)\frac{d}{dz}\phi_n + \frac{\rho_0}{2\omega^2 g}\cos(2(kx - \omega t))\phi_n\frac{d}{dz}\left(N^2(z)\phi_n\right). \tag{C.7}$$

Next, expand $z = z_0 + az_1 + a^2z_2 + O(a^3)$, the goal is to find the average value of a particular isopycnal height. Substituting this in and collecting like powers of a shows that

$$\begin{aligned} \rho \;=\; & \rho_0 + \bar{\rho}(z_0) \\ & + a\left(z_1\tfrac{d\bar{\rho}}{dz}(z_0) + \rho_1(x, z_0, t)\right) \\ & + a^2\left(z_2\tfrac{d\bar{\rho}}{dz}(z_0) + \tfrac{z_1^2}{2}\tfrac{d^2\bar{\rho}}{dz^2}(z_0) + z_1\tfrac{\partial\rho_1}{\partial z}(x, z_0, t) + \rho_2(x, z_0, t)\right). \end{aligned} \tag{C.8}$$

This can be solved for the components of z. The result is

$$z_0 = \bar{\rho}^{-1}(\rho - \rho_0), \tag{C.9}$$

so

$$z_1 = -\frac{\rho_1(x, z_0, t)}{\frac{d\bar{\rho}}{dz}(z_0)} = \frac{g}{\rho_0}\frac{\rho_1(x, z_0, t)}{N^2(z_0)}, \tag{C.10}$$

and

$$z_2 = \frac{\frac{z_1^2}{2}\frac{d^2\bar{\rho}}{dz^2}(z_0) + z_1\frac{\partial\rho_1}{\partial z}(x, z_0, t) + \rho_2(x, z_0, t)}{\frac{\rho_0}{g}N^2(z_0)}. \tag{C.11}$$

Next, time-averages over one period are taken. Since $\langle\rho_1(x, z_0, t)\rangle = \langle\rho_2(x, z, t)\rangle = 0$, it follows that $\langle z_1\rangle = 0$ and $\langle z_1^2\rangle = \phi_n^2/(2\omega^2)$, so

$$\begin{aligned} \langle z_2\rangle &= \frac{-\frac{\rho_0}{g}\frac{\phi_n^2}{4\omega^2}\frac{dN^2}{dz} + \frac{\rho_0}{g}\frac{1}{2\omega^2}\phi_n\frac{d}{dz}\left(\phi_n N^2\right)}{\frac{\rho_0}{g}N^2(z_0)} \\ &= \frac{1}{4\omega^2}\frac{\frac{d(\phi_n^2 N^2)}{dz}\Big|_{z_0}}{N^2(z_0)} \end{aligned} \tag{C.12}$$

so

$$\langle z\rangle = z_0 + a^2\frac{1}{4\omega^2}\frac{\frac{d(\phi_n^2 N^2)}{dz}\big|_{z_0}}{N^2(z_0)}. \tag{C.13}$$

This averaged isopycnal displacement can be used to reverse-engineer the corresponding background density stratification. Taking the averaged z value to be the height of an isopycnal in a quiescent fluid, perturbation theory is used to find the corresponding stratification. This is done by expanding $\rho = \rho^{(0)} + a\rho^{(1)} + a^2\rho^{(2)} + O(a^3)$, with each term being a function of z. To avoid confusion, let $q(z) = \bar{\rho}^{-1}(z)$, so that $z_0 = q(\rho - \rho_0)$. This can be expanded to show

$$z_0 = q(\rho^{(0)} - \rho_0) + (a\rho^{(1)} + a^2\rho^{(2)})q'(\rho^{(0)} - \rho_0) + O(a^3). \tag{C.14}$$

This reveals that $\rho^{(0)} = \rho_0 + \bar{\rho}(z)$, which should be expected as waves with amplitude $O(a)$ should not alter the $O(1)$ nature of the background stratification. This also shows that to leading-order $z_0 = q(\bar{\rho}(z)) = z$. Considering the $O(a)$ term in the expansion reveals $\rho^{(1)} = 0$. Also, since $q'(\rho^{(0)} - \rho_0) = 1/(d\bar{\rho}/dz)$,

$$\rho^{(2)} = \frac{\rho_0}{g}\frac{1}{4\omega^2}\frac{d(\phi_n^2 N^2)}{dz} \tag{C.15}$$

readily follows. The final result is

$$\rho = \rho_0 + \bar{\rho}(z) + a^2\frac{\rho_0}{g}\frac{1}{4\omega^2}\frac{d(\phi_n^2 N^2)}{dz} + O(a^3). \tag{C.16}$$

This shows how the stratification is altered, on average, in the presence of a monochromatic wave. Considering a wave train impinging on a quiescent fluid, it is then clear that there must on average be a slope in the isopycnals between the two regions of fluid. This will induce a mean flow, or if the wavy regions is of finite extent, will appear as a long wave disturbance.

Appendix D

Steepest Descents Analysis

In this appendix some of the laborious calculations involved in the steepest descents analysis of Chapter 5 are presented. This appendix is divided into sections for each of the KdV, BBM, and IGW problems.

D.1 KdV Calculations

The main purpose of this analysis is to better understand the impulsively-forced response to the linear KdV equation. To that end, the initial condition

$$u_0(x) = 0 \tag{D.1}$$

is taken. To further simplify the analysis, only the point source $f(x) = \delta(x)$ is considered. Under these restrictions, the KdV solution in Fourier space becomes

$$U(k,t) = A\left(\frac{e^{i\omega t} - e^{-i\sigma(k)t}}{i(\sigma(k)+\omega)}\right), \tag{D.2}$$

which leads to the physical solution

$$u(x,t) = A\big(\mathcal{F}^{-1}\{G_1(k)\} + \mathcal{F}^{-1}\{G_2(k)\}\big). \tag{D.3}$$

The inverse Fourier transform of $G_1(k)$ requires no special treatment, it simply consists of leftward and rightward-propagating wave trains, (see equation (5.78)). This component of the forced response is well understood for all values of x and t.

Due to the complicated nature of the dispersion relation, it is the inverse Fourier transform of $G_2(k)$ that benefits most from the application of approximation techniques. The exact integral form of $g_2(x,t) = \mathcal{F}^{-1}\{G_2(k)\}$ is

$$g_2(x,t) = -\frac{1}{2\pi}\int_C \frac{\exp(i(kx - \sigma(k)t))}{i(\sigma(k)+\omega)}\, dk, \tag{D.4}$$

where the contour C is shown in Figure 5.3. Letting $v = x/t$ be a fixed quantity, the integral can be rewritten as

$$g_2(x,t) = -\frac{1}{2\pi i}\int_C \frac{\exp(\phi(k)t)}{\sigma(k)+\omega}\, dk, \tag{D.5}$$

where

$$\phi(k) = i((v-c_0)k + \nu k^3). \tag{D.6}$$

It is equation (D.5) that is amenable to treatment by the method of steepest descents. The process followed below is outlined at the end of Section 5.1.4.

D.1.1 Description of the Critical Points

The set of critical points of the integrand $G_2(k)$ consists of the poles at $k = r_1, r_2, r_3$ and saddle points of ϕ. Provided $|\omega| < \omega_c$, the poles are first order and lie on the real axis. When $|\omega| = \omega_c$, the second order pole at $k = r_2$ corresponds to waves of zero group velocity and thus the residue from that pole does not contribute to the asymptotic analysis.

Saddle points of ϕ occur where $\phi'(k) = 0$. For every v, two saddle points exist. These are labeled $s_\pm$ and are given by

$$s_\pm = \pm\sqrt{\frac{c_0 - v}{3\nu}}. \tag{D.7}$$

For $v \neq c_0$ these saddle points are distinct and first order. When $v < c_0$ the saddle points lie on the real axis, when $v > c_0$ they lie on the imaginary axis.

The directions of steepest descent emanating from the saddle points can be determined from $\phi''(s_\pm)$. Clearly

$$\phi''(s_\pm) = i6\nu s_\pm. \tag{D.8}$$

Using equation (5.43), the angles of steepest descent are easily found. These are presented in Table D.1. The qualitative change in the steepest descent paths as v passes through c_0 is abrupt. When $v = c_0$, the saddle point lies at the origin and is of second order, but this special case is not considered here.

Finally, note that for $0 < v < c_0$, the saddle point s_+ must lie strictly to the left of the pole r_1 and the saddle point s_- must lie strictly to the right of the pole r_3. Because the initial contour C lies above r_1, r_3, the deformed contour will never include contributions from those poles when $v > 0$.

Range	$\theta(s_+)$	$\theta(s_-)$
$0 < v < c_0$	$\frac{\pi}{4}, \frac{5\pi}{4}$	$\frac{3\pi}{4}, \frac{7\pi}{4}$
$v > c_0$	$0, \pi$	$\frac{\pi}{2}, \frac{3\pi}{2}$

Table D.1: Steepest descent directions for the KdV problem. The angles of steepest descent from the saddle point $s_\pm$ is denoted by $\theta(s_\pm)$.

D.1.2 The Paths of Steepest Descent

For the KdV problem the dispersion relation is simple enough that an exact description of the steepest descent paths is possible. This is accomplished by splitting k and ϕ into their real and imaginary components. With $k = \eta + i\xi$, and $\phi(\eta, \xi) = \phi_R(\eta, \xi) + i\phi_I(\eta, \xi)$, it follows that

$$\begin{aligned} \phi_R(\eta, \xi) &= (c_0 - v)\xi - 3\nu\eta^2\xi + \nu\xi^3 \\ \phi_I(\eta, \xi) &= (v - c_0)\eta + \nu\eta^3 - 3\nu\eta^2\xi. \end{aligned} \tag{D.9}$$

Along paths of steepest descent through $s_\pm$, $\phi_I(\eta, \xi)$ must remain constant, so $\xi(\eta)$ can be found explicitly. It turns out that

$$\xi_\pm^2(\eta) = \frac{v - c_0}{3\nu} + \frac{1}{3}\eta^2 - \frac{\phi_I(s_\pm)}{3\nu\eta}. \tag{D.10}$$

where the subscript on ξ determines which saddle point the path crosses through. Note that when $0 < v < c_0$

$$\phi(s_\pm) = \mp i\frac{2}{3}\sqrt{\frac{c_0 - v}{3\nu}}(c_0 - v) \tag{D.11}$$

so $\phi_I(s_+) = -\phi_I(s_-) < 0$. Also, observe that if $v > c_0$ then $\phi(s_\pm)$ is real. This suggests the steepest descent paths are qualitatively different when $0 < v < c_0$ and $v > c_0$, so these cases are discussed separately.

When $0 < v < c_0$, the steepest descent path emanating from s_+ at the angle $\theta = \pi/4$ proceeds along a trajectory that approaches the line $\xi = \eta$ from below as $\eta \to \infty$. Leaving s_+ along the path at angle $\theta = 5\pi/4$, $\xi \to -\infty$ as $\eta \to 0^+$. Likewise, from the saddle point s_-, the path of steepest descent leaving at $\theta = 3\pi/4$ asymptotically approaches the line $\xi = -\eta$ from below as $\eta \to -\infty$. Leaving s_- at the angle $7\pi/4$ the steepest descent path has $\xi \to -\infty$ as $\eta \to 0^-$. Since $\phi_I(s_+) = -\phi_I(s_-) \neq 0$, the two paths of steepest descent do not meet in the finite complex plane, though they become arbitrarily close along the negative imaginary axis.

When $v > c_0$, the steepest descent paths are described by the parametric equation

$$\xi_\pm^2(\eta) = \frac{v - c_0}{3\nu} + \frac{1}{3}\eta^2. \tag{D.12}$$

The path of steepest descent leaving s_+ is just the upper branch of the hyperbola $\xi_+(\eta) = \sqrt{(v-c_0)/(3\nu) + \eta^2/3}$. From s_- the path of steepest descent lies along the imaginary axis, proceeding upward to s_+ and downward to $-i\infty$.

D.1.3 The Integration Contours

The above discussion of the saddle points and steepest descents contours provides enough information to select appropriate contours for approximating $g_2(x,t)$. For he discussion presented here, $|\omega| < \omega_c$, (Case 1),is assumed. Extensions are discussed later.

To facilitate this discussion, let

$$c_F = c_0 - 3\nu r_2^2. \tag{D.13}$$

By definition, this is the group velocity of the forced wave at wavenumber r_1.

For $0 < v < c_F$, the deformed contour $\hat{C}$ is depicted in Figure D.1. The new path of integration is formed by stretching C onto the two steepest descent paths through the saddle points s_+ and s_-. Because the saddle point s_- lies to the left of r_2 in this regime and the initial contour C is deformed below the pole at $k = r_2$, the deformation process does not introduce a residue contribution from any of the poles.

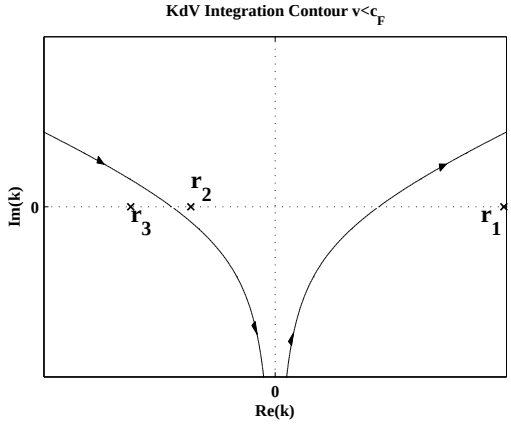

Figure D.1: Steepest descents contour when $0 < v < c_F$ in the complex k-plane. Poles are marked by 'x' symbols. The two saddle points lie at the intersections of the contour with the real k-axis. No residue contributions are introduced in the deformation process. The two halves of the curve follow the negative imaginary axis and meet at $-i\infty$.

For $c_F < v < c_0$, the deformed integration contour is shown in Figure D.2. This contour consists of the steepest descent paths through s_+ and s_-, with an additional contribution

from the encirclement of the pole at $k = r_2$. This additional contribution occurs because for v in this range the saddle point s_- lies to the right of r_2. Integration is performed in both directions along the segment connecting the saddle point and the circle around r_2, so no weight is contributed from that segment.

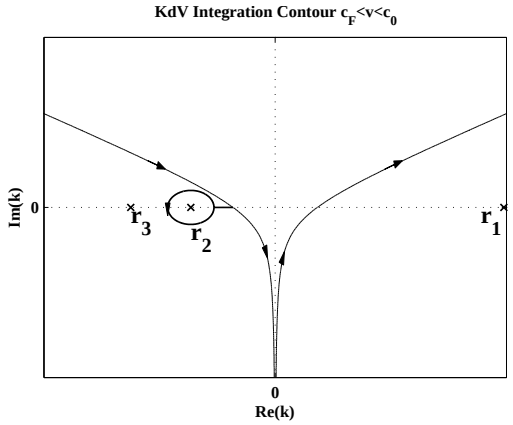

Figure D.2: Steepest descents integration contour when $c_F < v < c_0$ in the complex k-plane. Poles are marked by 'x' symbols. The two saddle points lie at the intersection of the contours with the real k-axis. The direction of integration is marked by the arrowheads. Deforming the contour requires encirclement of the pole at $k = r_2$. Since integration along the segment connecting the steepest descents path and the circle enclosing the pole is performed in both directions it contributes no weight.

When $v > c_0$, the steepest descents contour used to evaluate $g_2(x,t)$ is shown in Figure D.3. The depicted contour is the hyperbolic arc passing through s_+ on the positive imaginary axis. The deformation process involves an encirclement of the pole at $k = r_2$. The short segment joining the steepest descent path to the small circle integrated in both directions so it contributes no weight.

D.1.4 The Asymptotic Solution

With the deformed integration contours presented above, it is a relatively simple matter to determine the asymptotic saddle point contributions using equation (5.57). Because the steepest descent paths enter and leave each saddle point along two different directions care must be taken to account for both contributions.

When $v < c_F$, the asymptotic behaviour is dominated by the two saddle point contri-

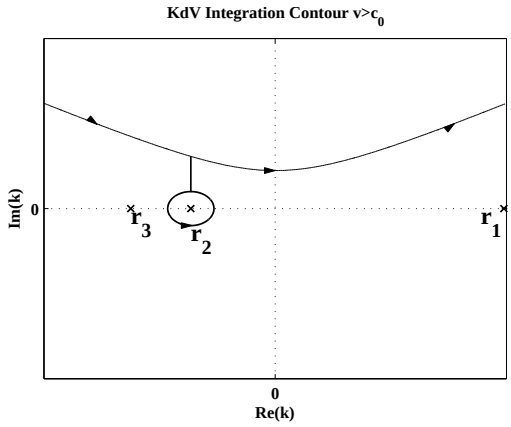

Figure D.3: Steepest descents contour when $v > c_0$ in the complex k-plane. Poles are indicated by the 'x' symbols. The saddle point lies on the positive imaginary axis. Deforming C onto the steepest descents path introduces the residue contribution from the pole at r_2. Integration is performed along the contour in the direction of the arrowheads.

butions, thus

$$\begin{aligned} g_2(x,t) \quad \sim \quad & -\tfrac{1}{2\pi i}\sqrt{\tfrac{\pi}{3\nu s_+ t}}\,\tfrac{\exp\left(i\left(\frac{\pi}{4}+\left(c_0 s_+ - \nu s_+^3\right)t\right)\right)}{c_0 s_+ - \nu s_+^3 + \omega} \\ & +\tfrac{1}{2\pi i}\sqrt{\tfrac{\pi}{-3\nu s_- t}}\,\tfrac{\exp\left(i\left(\frac{3\pi}{4}+\left(c_0 s_- - \nu s_-^3\right)t\right)\right)}{c_0 s_- - \nu s_-^3 + \omega} \\ & +O\left(\tfrac{1}{t}\right). \end{aligned} \tag{D.14}$$

The identities $e^{i\pi/4} - e^{i5\pi/4} = 2e^{i\pi/4}$ and $e^{i3\pi/4} - e^{i7\pi/4} = 2e^{i3\pi/4}$ have been used. When $c_F < v < c_0$, the saddle point contributions remain unchanged in form. The dominant contribution to $g_2(x,t)$ comes from the residue of the pole at $k = r_2$. Then

$$\begin{aligned} g_2(x,t) \quad \sim \quad & \tfrac{1}{\nu}\tfrac{\exp\left(i(r_2 x+\omega t)\right)}{(r_2-r_1)(r_2-r_3)} \\ & -\tfrac{1}{2\pi i}\sqrt{\tfrac{\pi}{3\nu s_+ t}}\,\tfrac{\exp\left(i\left(\frac{\pi}{4}+\left(c_0 s_+ - \nu s_+^3\right)t\right)\right)}{c_0 s_+ - \nu s_+^3 + \omega} \\ & +\tfrac{1}{2\pi i}\sqrt{\tfrac{\pi}{-3\nu s_- t}}\,\tfrac{\exp\left(i\left(\frac{3\pi}{4}+\left(c_0 s_- - \nu s_-^3\right)t\right)\right)}{c_0 s_- - \nu s_-^3 + \omega} \\ & +O\left(\tfrac{1}{t}\right). \end{aligned} \tag{D.15}$$

Finally, when $v > c_0$, the asymptotic behaviour of $g_2(x,t)$ is determined by the residue contribution at r_2 plus the lone saddle point contribution at s_+. The result is

$$\begin{aligned} g_2(x,t) \quad \sim \quad & \tfrac{1}{\nu}\tfrac{\exp\left(i(r_2 x+\omega t)\right)}{(r_2-r_1)(r_2-r_3)} \\ & -\tfrac{1}{2\pi i}\sqrt{\tfrac{\pi}{3\nu |s_+| t}}\,\tfrac{\exp\left(-\left(c_0|s_+| + \nu|s_+|^3\right)t\right)}{c_0 s_+ - \nu s_+^3 + \omega} \\ & +O\left(\tfrac{1}{t}\right). \end{aligned} \tag{D.16}$$

Since $u(x,t) = A(g_1(x,t) + g_2(x,t))$, these formulas can be substituted in to reveal the asymptotic behaviour of u in the large t limit. In particular,

$$\begin{aligned} u(x,t) \quad \sim \quad & -\tfrac{A}{\nu}\tfrac{\exp\left(i(r_2 x+\omega t)\right)}{(r_2-r_1)(r_2-r_3)} \\ & -\tfrac{A}{2\pi i}\sqrt{\tfrac{\pi}{3\nu s_+ t}}\tfrac{\exp\left(i\left(\frac{\pi}{4}+\left(c_0 s_+ - \nu s_+^3\right)t\right)\right)}{c_0 s_+ - \nu s_+^3 + \omega} \\ & +\tfrac{A}{2\pi i}\sqrt{\tfrac{\pi}{-3\nu s_- t}}\tfrac{\exp\left(i\left(\frac{3\pi}{4}+\left(c_0 s_- - \nu s_-^3\right)t\right)\right)}{c_0 s_- - \nu s_-^3 + \omega} \\ & +O\left(\tfrac{1}{t}\right) \end{aligned} \tag{D.17}$$

when $x < c_F t$, and

$$\begin{aligned} u(x,t) \quad \sim \quad & -\tfrac{A}{2\pi i}\sqrt{\tfrac{\pi}{3\nu s_+ t}}\tfrac{\exp\left(i\left(\frac{\pi}{4}+\left(c_0 s_+ - \nu s_+^3\right)t\right)\right)}{c_0 s_+ - \nu s_+^3 + \omega} \\ & +\tfrac{A}{2\pi i}\sqrt{\tfrac{\pi}{-3\nu s_- t}}\tfrac{\exp\left(i\left(\frac{3\pi}{4}+\left(c_0 s_- - \nu s_-^3\right)t\right)\right)}{c_0 s_- - \nu s_-^3 + \omega} \\ & +O\left(\tfrac{1}{t}\right) \end{aligned} \tag{D.18}$$

when $c_F t < x < c_0 t$, and

$$\begin{aligned} u(x,t) \quad \sim \quad & -\tfrac{A}{2\pi i}\sqrt{\tfrac{\pi}{3\nu |s_+| t}}\tfrac{\exp\left(-\left(c_0 |s_+| + \nu |s_+|^3\right)t\right)}{c_0 s_+ - \nu s_+^3 + \omega} \\ & +O\left(\tfrac{1}{t}\right) \end{aligned} \tag{D.19}$$

when $x > c_0 t$. In each of these asymptotic formulas, s_+ and s_- are dependent on v and defined in equation (D.7).

The asymptotic solution can be used to describe the wave behaviour when the forcing frequency $|\omega| \geq \omega_c$. When $|\omega| = \omega_c$, the forced waves are trapped in the forcing region as they have zero group velocity. Only the transient component, decaying like $t^{-1/2}$ would be seen by an observer at some distance away from the forcing region. At higher forcing frequencies $|\omega| > \omega_c$, and the pole corresponding to rightward-propagating waves lies off the real axis. The forced waves are then evanescent, and decay exponentially away from the forcing region. The KdV equation is intended as a model of long, low-frequency waves, so the higher frequency limits are of less physical significance.

D.2 BBM Calculations

Here a detailed steepest descents analysis of the BBM problem is given. Only rightward-propagating waves are considered in the large time limit. To facilitate the analysis, $u(x,t)$ is written in a more suitable form. Let $x/t = v$ be a fixed positive quantity, and rewrite (5.101) as

$$u(x,t) = -\frac{A}{2\pi i \mu \omega} \oint_{C_+} g(k) \exp(\phi(k) t)\ dk, \tag{D.20}$$

where

$$g(k) = \frac{1}{(k - r_1)(k - r_2)}, \tag{D.21}$$

and

$$\phi(k) = ikv - ic_0 \frac{k}{1 + \mu k^2}. \tag{D.22}$$

The contour C_+ is the small circular contour enclosing the essential singularity at $k = i/\sqrt{\mu}$, as defined at the end of Section 5.3.3. In what follows, the steps outlined in Section 5.1.4 are executed to determine how $u(x,t)$ behaves as $t \to \infty$.

D.2.1 Description of the Critical Points

The set of critical points of the integrand in (D.20) consists of the saddle points of ϕ, the simple poles of $g(k)$ and the essential singularities located at $k = \pm i/\sqrt{\mu}$. Since the integration contour C_+ is circular, there are no endpoints to consider. Away from the poles and essential singularities the integrand is analytic.

The saddle points of $\phi(k)$ satisfy $\phi'(k) = 0$. That is, they lie at the roots of the equation $c_g(k) = v$. This leads to a fourth-order polynomial in k with roots satisfying

$$k^2 = \frac{-(2v + c_0) \pm \sqrt{c_0^2 + 8c_0 v}}{2\mu v}. \tag{D.23}$$

Evidently there can be at most four distinct saddle points. These are labeled s_1, s_2, s_3, s_4, with

$$\begin{aligned} s_1 &= \sqrt{\tfrac{-(2v+c_0)+\sqrt{c_0^2+8c_0v}}{2\mu v}}, \quad s_2 = -s_1 \\ s_3 &= \sqrt{\tfrac{-(2v+c_0)-\sqrt{c_0^2+8c_0v}}{2\mu v}}, \quad s_4 = -s_3. \end{aligned} \tag{D.24}$$

Computing the directions of steepest descent for the saddle point s_n requires knowledge of where s_n lies in the complex plane and the evaluation of $\phi''(s_n)$. Differentiating shows that

$$\phi''(k) = i2c_0\mu k \frac{3 - \mu k^2}{(1 + \mu k^2)^3}, \tag{D.25}$$

which is an odd function of k.

When $v > 0$, s_1 and s_2 are real provided $(2v + c_0) \leq \sqrt{c_0^2 + 8c_0 v}$, which holds when $v \leq c_0$. With minor algebra, it can be shown that $\mathrm{Arg}\,(\phi''(s_1)) = \pi/2$. Using equation (5.43), the angles of descent from s_1 are $\theta = \pi/4, 5\pi/4$. Since $\phi''(k)$ is odd, the angles of descent from s_2 are $\theta = 3\pi/4, 7\pi/4$ when $0 < v < c_0$. As $v \to c_0^-$, the saddle points s_1 and

Range	$\theta(s_1)$	$\theta(s_2)$	$\theta(s_3)$	$\theta(s_4)$
$0 < v < c_0$	$\frac{\pi}{4}, \frac{5\pi}{4}$	$\frac{3\pi}{4}, \frac{7\pi}{4}$	$\frac{\pi}{2}, \frac{3\pi}{2}$	$0, \pi$
$v > c_0$	$0, \pi$	$\frac{\pi}{2}, \frac{3\pi}{2}$	$\frac{\pi}{2}, \frac{3\pi}{2}$	$0, \pi$

Table D.2: Summary of the steepest descent directions from the saddle points for the BBM problem.

s_2 tend to the origin, s_2 approaches from the negative real axis, and s_1 approaches from the positive real axis.

When $v > c_0$, s_1 and s_2 lie on the positive and negative imaginary axis, respectively. A little algebra reveals that $\phi''(s_1)$ is a positive real number, so the angles of descent from s_1 are given by $\theta = \pi/2, 3\pi/2$. The angles of descent from s_2 are then easily found to be $\theta = 0, \pi$. As $v > c_0$ increases s_1 crawls up the imaginary axis but never reaches the essential singularity. This is because when $v > c_0$, $s_1 = (i/\sqrt{\mu})\sqrt{1 + (c_0 - \sqrt{c_0^2 + 8c_0 v}/(2v)}$, so $Im(s_1) < 1/\sqrt{\mu}$.

For $v > 0$, s_3 lies on the positive imaginary axis above $i/\sqrt{\mu}$. As $v \to 0^+$ s_3 tends to $+i\infty$. As $v \to \infty$ s_3 approaches the essential singularity at $i/\sqrt{\mu}$ from above. With $v > 0$, $\phi''(s_3)$ is a positive real number, so the angles of steepest descent from s_3 are $\theta = \pi/2, 3\pi/2$. It immediately follows that for $v > 0$ the angles of steepest descent from s_4 are $\theta = 0, \pi$. The angles of steepest descent from the saddle points for the two important ranges of v values are summarized in Table D.2.

Finally, note that if $v > c_F$, where $c_F = c_g(r_1)$ is the group velocity of the rightward-propagating wave at the forcing frequency, then s_2 lies to the right of r_1 on the negative real axis. It is easy to show that $\lim_{v \to 0^+} s_2 = -1/\sqrt{\mu}$ from the right, so there will always be v values for which s_2 lies to the left of r_1.

D.2.2 Steepest Descent Paths and Integration Contours

Parametric equations describing the paths of steepest descent can be found by splitting $k = \eta + i\xi$ and $\phi(k) = \phi_R(\eta, \xi) + i\phi_I(\eta, \xi)$, where

$$\phi_R(\eta, \xi) = -v\xi + c_0 \xi \frac{1 - \mu(\eta^2 + \xi^2)}{1 + 2\mu(\eta^2 - \xi^2) + \mu^2(\eta^2 + \xi^2)^2} \tag{D.26}$$

and

$$\phi_I(\eta, \xi) = v\eta - c_0 \eta \frac{1 + \mu(\eta^2 + \xi^2)}{1 + 2\mu(\eta^2 - \xi^2) + \mu^2(\eta^2 + \xi^2)^2}. \tag{D.27}$$

For convenience, the notation $\phi(k) = \phi_R(k) + i\phi_I(k)$ is also used. The analysis is now split into two major cases, $v < c_0$ and $v > c_0$.

Case $v < c_0$

When $0 < v < c_0$, the paths of steepest descent through s_1 and s_2 are of most interest. Clearly $\phi_R(s_1) = \phi_R(s_2) = 0$. Along the steepest descent paths from s_1, $\phi_I(\eta, \xi) = \phi_I(s_1) \neq 0$ remains constant. Similarly, along the steepest descent path from s_2, $\phi_I(\eta, \xi) = \phi_I(s_2) = -\phi_I(s_1)$ remains constant. The two paths are symmetric about the ξ axis, but they cannot intersect in the finite complex plane except, perhaps, at an essential singularity.

It is possible to solve for $\xi(\eta)$ along paths where $\phi_I(\eta, \xi)$ is constant. Along such a path passing through s_1, at a given η there are at most four possible ξ values given by

$$\xi_{\pm\pm}(\eta) = \pm\sqrt{\frac{-2\mu\eta^2 + 2 + p \pm \sqrt{p^2 + 8p - 16\mu\eta^2}}{2\mu}}, \tag{D.28}$$

where

$$p = \frac{c_0\eta}{v\eta - \phi_I(s_1)}. \tag{D.29}$$

The four possible configurations of plus or minus signs (read from left to right) define the four possible curves where $\phi_I(\eta, \xi)$ remains constant.

Note that as $\eta \to 0^+$, $\xi_{\pm+} \to \pm 1/\sqrt{\mu}$ from above. Differentiating shows that $\xi_{\pm+}(\eta)$ approaches $\pm 1/\sqrt{\mu}$ with a vertical asymptote as $\eta \to 0^+$. In a similar manner, it is easy to see that the steepest descent paths through s_2 also approach the essential singularities with vertical asymptotes. Therefore the steepest descent paths through s_1 and s_2 do intersect at the essential singularities at $\pm i/\sqrt{\mu}$. This is problematic because it means C_+ cannot be deformed directly onto these paths. Instead, a modified steepest descents contour is required.

To avoid integration through an essential singularity, C_+ can be deformed onto a path that follows the steepest descent paths for a time, and is then deflected onto a contour along which $\phi_R(k)$ remains negative and constant. This is possible because $\phi_R(s_1) = \phi_R(s_2) = 0$ and $\phi_R(k)$ is strictly decreasing along the paths of descent from s_1 and s_2. The simplest choice is to deflect the steepest descent paths from s_1 and s_2 onto the contour of constant ϕ_R passing through s_3. Consider that, along a contour passing through s_3 and satisfying $\phi_R(\eta, \xi) = \phi_R(s_3)$, it is possible to solve for $\eta(\xi)$ explicitly. The result is

$$\eta_{\pm\pm}(\xi) = \pm\sqrt{\frac{-2\mu\xi^2 - 2 - q \pm \sqrt{q^2 + 8q + 16\mu\xi^2}}{2\mu}} \tag{D.30}$$

where

$$q = \frac{c_0\xi}{v\xi + \phi_R(s_3)}, \tag{D.31}$$

and the different combinations of plus or minus signs (read from left to right) define the four possible values of η at a given ξ. Note that $\phi_R(s_3) < 0$. Even as $v \to 0^+$, $s_3 \to i\infty$ and $\phi_R(s_3) \to 0^-$ like $-\sqrt{c_0 v/\mu}$.

The deformed contour of integration can now be described accurately. In the first quadrant, C_+ is deformed onto the path of steepest descent originating at s_1 and leaving at the angle $\theta = \pi/4$. This curve is defined by $\xi_{+-}(\eta)$ until a vertical asymptote is reached, at which point $p^2 + 8p - 16\mu\eta^2$ changes sign. The curve continues along $\xi_{++}(\eta)$, until reaching (η_1, ξ_1), where $\phi_R(\eta_1, \xi_1) = \phi_R(s_3) < 0$. From this point the contour C_+ is deformed onto the path of constant ϕ_R passing through s_3, governed by $\eta_{++}(\xi)$. The deformed contour proceeds from (η_1, ξ_1) all the way up to s_3, where $\eta_{++}(\xi)$ crosses the ξ axis.

In the fourth quadrant, C_+ is deformed onto the path of steepest descent leaving s_1 at the angle $5\pi/4$. This path is followed until (η_2, ξ_2), where $\phi_R(\eta_2, \xi_2) = \phi_R(s_3)$. From this intersection point C_+ is deformed onto $\eta_{+-}(\xi)$, which crosses the ξ axis at a point above $(0, -1/\sqrt{\mu})$.

The deformed contour of integration in the second and third quadrants is simply the reflection of the contour fin the right half-plane across the ξ axis. This is possible because $\phi_I(s_2) = -\phi_I(s_1)$. The only problem arises when $v < c_F$, so that s_2 lies to the left of k_+. In that situation the process of deforming the contour into the left half-plane requires encirclement of the simple pole at r_1. The pole is enclosed with a small clockwise oriented circle, connected to s_2 with a straight line segment.

In Figure D.4 the deformed contour of integration when $v < c_F$ is illustrated. In Figure D.5 the contour of integration for $v > c_F$ is shown. Qualitatively the two plots are very similar, except for the encirclement of the pole at $k = r_1$ when $v < c_F$. To ease the analysis the contour segments are labelled in the plots. The segment of the contour connecting (η_2, ξ_2) to (η_1, ξ_1) is labelled C_1. The bridging contour connecting (η_1, ξ_1) to $(-\eta_1, \xi_1)$ across s_3 is labelled C_2. The contour C_3 joins $(-\eta_1, \xi_1)$ to $(-\eta_2, \xi_2)$. The bridging contour C_4 connects $(-\eta_2, \xi_2)$ to (η_2, ξ_2). In Figure D.4 the circle enclosing r_1 is denoted by C_5. No label is assigned to the straight line connecting C_3 and C_5 as the integral is conducted in both directions and therefore does not contribute.

Case $v > c_0$.

In this situation, since s_1 lies on the positive imaginary axis below $i/\sqrt{\mu}$, C_+ is simply deformed onto the steepest descent path through s_1 and s_3. This path remains entirely in the upper half-plane. Along this contour $\phi_I(\eta, \xi) = 0$ so it is possible to find a relatively simple description for the closed loop. The path is described by the equation

$$\mu^2 v(\eta^2 + \xi^2)^2 + \mu(2v - c_0)\eta^2 - \mu(2v + c_0)\xi^2 + v - c_0 = 0, \tag{D.32}$$

which is just a quadratic in η^2 and ξ^2. The path passes through s_1 and s_3 at angles $0, \pi$. Figure D.6 depicts the contour of integration when $v > c_0$. Like C_+, the deformed path is traversed in counter-clockwise fashion.

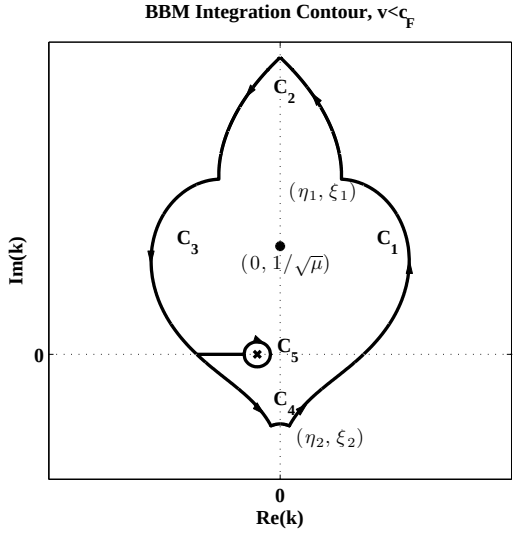

Figure D.4: Steepest descents contour of integration for $v < c_F$. The pole at r_1, enclosed with a circle by the deformation process, is marked by an 'x'. The saddle points s_1 and s_2 lie at the intersections of C_1 and C_3 with the real axis, respectively.

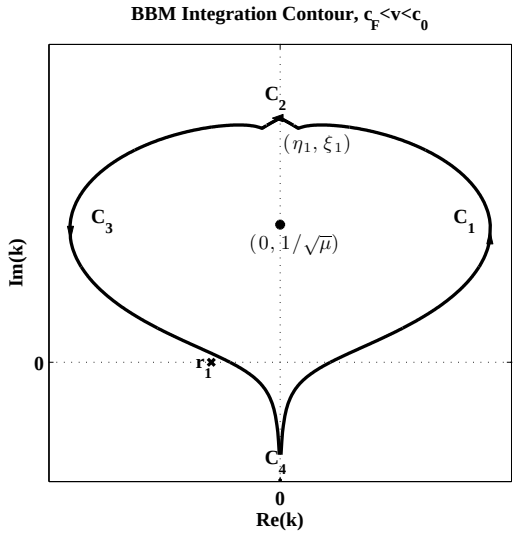

Figure D.5: Steepest descents integration contour for the BBM problem when $c_F < v < c_0$. The pole at r_1, marked by the 'x', is not enclosed by the deformation process. The contour C_4 is so short it is difficult to visualize on this scale.

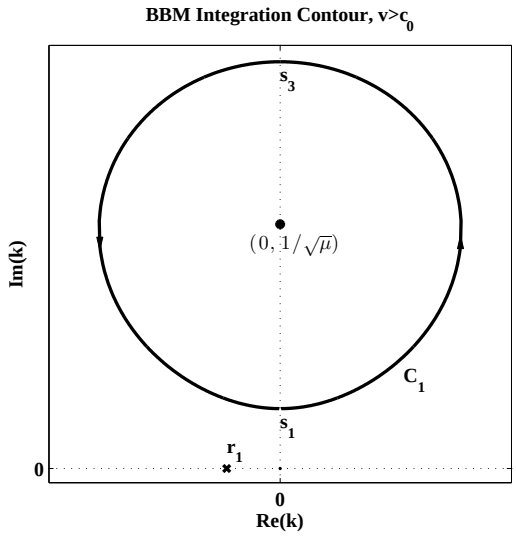

Figure D.6: BBM steepest descents integration contour when $v > c_0$. The saddle points s_1 and s_3 lie at the intersection of C_1 with the imaginary axis.

D.2.3 The Asymptotic Solution

With the above descriptions of the integration contours, $u(x,t)$ can be approximated by summing the relevant residue and saddle point contributions. Different contributions arise depending on the range v lies in.

Case $v < c_0$.

When $v < c_F$, Figure D.4 can be used to show $\int_{C_+} = \int_{C_1} + \int_{C_2} + \int_{C_3} + \int_{C_4} + \int_{C_5}$, where integrands have been dropped for shorthand. Since the integral is conducted in both directions along the line segment joining C_3 and C_5, there is no additional contribution. When $v > c_F$, Figure D.5 shows that $\int_{C_+} = \int_{C_1} + \int_{C_2} + \int_{C_3} + \int_{C_4}$.

The decomposition of $\int_{C_+}$ is useful because each of the integrals involved can be evaluated approximately. Consider the saddle point contributions from the integrals along C_1 and C_3. Making use of the basic identities $e^{i\pi/4} - e^{i5\pi/4} = 2e^{i\pi/4}$ and $e^{i7\pi/4} - e^{i3\pi/4} = 2e^{i7\pi/4}$, Laplace's method reveals

$$\int_{C_1} \sim \frac{2e^{i\pi/4}}{(s_1 - r_1)(s_1 - r_2)} e^{\phi(s_1)t} \sqrt{\frac{\pi}{2t|\phi''(s_1)|}} \tag{D.33}$$

and

$$\int_{C_3} \sim \frac{2e^{i7\pi/4}}{(s_2 - r_1)(s_2 - r_2)} e^{\phi(s_2)t} \sqrt{\frac{\pi}{2t|\phi''(s_2)|}}. \tag{D.34}$$

Next, consider the bridging contours C_2 and C_4. These contribute asymptotically negligible terms. This is evident because along these curves, $\phi_R(k) = \phi_R(s_3) < 0$ can be factored out of the integral, and the remaining integrand is bounded.

The final contribution to consider, only needed when $v < c_F$, is from C_5. Since r_1 is a simple pole, this is easily found to be

$$\int_{C_5} = -2\pi i \frac{\exp(i(r_1 x + \omega t))}{r_1 - r_2}, \tag{D.35}$$

the minus sign arises because C_5 is oriented clockwise.

Combining these results and substituting them into (5.101) reveals that as $t \to \infty$, with $x < c_F t$, the solution behaves like:

$$\begin{aligned} u(x,t) \sim \quad & \tfrac{A}{\mu\omega} \tfrac{\exp(i(r_1 x+\omega t))}{r_1 - r_2} - \tfrac{A}{2\pi i \mu\omega} \tfrac{e^{i\pi/4}}{(s_1-r_1)(s_1-r_2)} e^{\phi(s_1)t} \sqrt{\tfrac{2\pi}{t|\phi''(s_1)|}} \\ & - \tfrac{A}{2\pi i \mu\omega} \tfrac{e^{i7\pi/4}}{(s_2-r_1)(s_2-r_2)} e^{\phi(s_2)t} \sqrt{\tfrac{2\pi}{t|\phi''(s_2)|}}. \end{aligned} \tag{D.36}$$

It should be recognized that s_1 and s_2 are functions of $v = x/t$ when using this formula. Similarly, when $c_F < v < c_0$

$$\begin{aligned} u(x,t) \sim \quad & - \tfrac{A}{2\pi i \mu\omega} \tfrac{e^{i\pi/4}}{(s_1-r_1)(s_1-r_2)} e^{\phi(s_1)t} \sqrt{\tfrac{2\pi}{t|\phi''(s_1)|}} \\ & - \tfrac{A}{2\pi i \mu\omega} \tfrac{e^{i7\pi/4}}{(s_2-r_1)(s_2-r_2)} e^{\phi(s_2)t} \sqrt{\tfrac{2\pi}{t|\phi''(s_2)|}}. \end{aligned} \tag{D.37}$$

Comparing these expressions, it is apparent that the solution transitions from being $O(A)$ to $O(t^{-1/2})$ as v exceeds c_F. A uniform approximation could be obtained using more advanced methods described by Bleistein and Handelsman [8, Chapter 9].

Case $v > c_0$.

The path of integration, illustrated in Figure D.6, is just a simple closed loop passing through s_1 and s_3. Neither of the poles r_1, r_2 are introduced in the deformation of C_+ onto the loop. Since $\phi_R(s_3) < \phi_R(s_1) < 0$ the dominant saddle point on the loop is s_1. The asymptotic contributions from s_1 are then readily found and yield

$$u(x,t) \sim -\frac{A}{\pi i \mu\omega} \frac{e^{\phi(s_1)t}}{(s_3 - r_1)(s_3 - r_2)} \sqrt{\frac{\pi}{2t|\phi''(s_3)|}}. \tag{D.38}$$

Since $\phi(s_1) = \phi_R(s_1) < 0$, this solution is small beyond all orders in comparison with the solution for $v < c_0$ as $t \to \infty$. This is not surprising since the fastest possible group velocity supported by the system is $v = c_0$.

D.3 IGW Calculations

Here the method of steepest descents is applied to approximate the integrals $\hat{I}_1$ and $\hat{I}_2$ from equation (5.124), and ultimately the streamfunction solution to the IGW equation. The method must be applied to each integral separately, and both integrands must be written in a suitable form. Rewrite

$$\hat{I}_1 = -\frac{Ah_n}{4\pi}\int_{C_0} f_1(k)\exp(\phi_1(k)t)\ dk \tag{D.39}$$

where $\phi_1(k) = i(kv + \sigma_n(k))$, $f_1(k) = \sigma_n(k)/\big(k^2(\sigma_n(k) - \omega)\big)$, and

$$\hat{I}_2 = -\frac{Ah_n}{4\pi}\int_{C_0} f_2(k)\exp(\phi_2(k)t)\ dk, \tag{D.40}$$

where $\phi_2(k) = i(kv - \sigma_n(k))$ and $f_2(k) = \sigma_n(k)/\big(k^2(\sigma_n(k) + \omega)\big)$, and C_0 is the contour depicted in Figure 5.14. The parameter $v = x/t$ is considered to be a positive fixed quantity for both integrals. The full solution is found by considering the full range of v values. The analysis procedure employed below closely follows the steps outlined in Section 5.1.4.

D.3.1 Description of the Critical Points for $\hat{I}_1$

In order to establish the asymptotic contribution to $\psi_n(x,t)$ from $\hat{I}_2$, a critical point analysis is needed. From that analysis the integration contour must then be determined. The splitting $\phi_1(k) = \phi_{1R}(k) + i\phi_{1I}(k)$ is used.

The set of critical points for the integral $\hat{I}_1$ consists of the saddle points of ϕ_1, the essential singularity and branch cut in $\exp(\phi_1(k)t)$, and the simple poles of $f_1(k)$. Only the saddle points are needed for the deformation of C_0, so they are the focus of this discussion.

Saddle points are found by solving $\phi_1'(k) = 0$. Since

$$\phi_1'(k) = i\left(v + \frac{n^2\pi^2 N}{(k^2 + n^2\pi^2)^{3/2}}\right), \tag{D.41}$$

there are four saddle points; one in each quadrant of the complex k-plane. The saddle points in the first and second quadrants are of primary interest. These lie at

$$\begin{aligned} s_{1+} &= \sqrt{\left(\tfrac{n^2\pi^2 N}{v}\right)^{2/3}\exp(i2\pi/3) - n^2\pi^2} \\ s_{1-} &= -\sqrt{\left(\tfrac{n^2\pi^2 N}{v}\right)^{2/3}\exp(-i2\pi/3) - n^2\pi^2}. \end{aligned} \tag{D.42}$$

Clearly $s_{1-} = -s_{1+}^*$, and the other two saddle points are given by $-s_{1+}, s_{1+}^*$,.

To determine directions of steepest descent through the saddle points $\phi_1''(s_{1\pm})$ is required. With

$$\phi_1''(k) = -\frac{i3n^2\pi^2 Nk}{(k^2+n^2\pi^2)^{5/2}}, \tag{D.43}$$

and the fact that $(s_{1\pm}^2 + n^2\pi^2)^{3/2} = -n^2\pi^2 N/v$, it follows that

$$\begin{array}{rcl} \phi_1''(s_{1+}) = & \frac{3v^{5/3}}{N^{2/3}n^{4/3}\pi^{4/3}} s_{1+} e^{i\pi/2}, \\ \phi_1''(s_{1-}) = & \frac{3v^{5/3}}{N^{2/3}n^{4/3}\pi^{4/3}} s_{1-} e^{i\pi/2}. \end{array} \tag{D.44}$$

Since s_{1+} lies in the first quadrant, $\pi/2 < \mathrm{Arg}(\phi_1''(s_{1+})) < \pi$, and since s_{1-} lies in the second quadrant, $\pi < \mathrm{Arg}(\phi_1''(s_{1-})) < 3\pi/2$. The angles of steepest descent are given by

$$\begin{array}{l} \theta_1(s_{1\pm}) = -\frac{\mathrm{Arg}(s_{1\pm})+\pi/2}{2} + \frac{\pi}{2} \\ \theta_2(s_{1\pm}) = -\frac{\mathrm{Arg}(s_{1\pm})+\pi/2}{2} + \frac{3\pi}{2}, \end{array} \tag{D.45}$$

both of which depend on v. Now consider $\phi_1(s_{1\pm})$. With

$$\begin{array}{rcl} \phi_1(s_{1+}) & = & is_{1+}v + i\frac{N^{2/3}v^{1/3}}{n^{2/3}\pi^{2/3}} s_{1+} \exp(-i\pi/3) \\ & = & s_{1+}v\exp(i\pi/2) + \frac{N^{2/3}v^{1/3}}{n^{2/3}\pi^{2/3}} s_{1+}\exp(i\pi/6) \end{array} \tag{D.46}$$

and the relation $s_{1-} = -s_{1+}^*$,

$$\begin{array}{rcl} \phi_1(s_{1-}) & = & -is_{1+}^*v - i\frac{N^{2/3}v^{1/3}}{n^{2/3}\pi^{2/3}} s_{1+}^* \exp(i\pi/3) \\ & = & s_{1+}^*v\exp(-i\pi/2) + \frac{N^{2/3}v^{1/3}}{n^{2/3}\pi^{2/3}} s_{1+}^*\exp(-i\pi/6). \end{array} \tag{D.47}$$

Clearly $\phi_1(s_{1-}) = (\phi_1(s_{1+}))^*$, so $\phi_{1I}(s_{1+}) = -\phi_{1I}(s_{1-})$. It follows that the paths of steepest descent through the two saddle points cannot intersect. In addition, $\phi_{1R}(s_{1+}) = \phi_{1R}(s_{1-}) < 0$ can be proven for positive v. To see this write $s_{1+} = re^{i\vartheta}$ where $0 < \vartheta < \pi/2$. A better lower bound on ϑ is needed, and after careful consideration the formula

$$\vartheta = \frac{\pi}{2} - \frac{1}{2}\mathrm{Atan}\left(\frac{\sqrt{3}(n^2\pi^2N)^{2/3}}{(n^2\pi^2N)^{2/3} + 2v^{2/3}n^2\pi^2}\right) \tag{D.48}$$

is apparent. Since ϑ is an increasing function of v its minimum occurs as $v \to 0^+$. This yields the tighter lower bound $\vartheta > \pi/3$. Returning to $\phi_{1R}(s_{1+})$,

$$\phi_{1R}(s_{1+}) = -vr\sin(\vartheta+\pi/2) + \left(\frac{N^2v}{n^2\pi^2}\right)^{1/3} r\cos(\vartheta+\pi/6). \tag{D.49}$$

Since s_1 lies in the first quadrant of the complex plane, $\sin(\vartheta+\pi/2)$ is positive. In addition, since $\pi/3 < \vartheta < \pi/2$, $\cos(\vartheta+\pi/6)$ must be negative. Therefore $\phi_{1R}(s_{1+})$ is negative.

D.3.2 The Integration Contour for $\hat{I}_1$

For $\hat{I}_1$, the contour C_0 is deformed onto the paths of steepest descent through $s_{1\pm}$. A departure from the steepest descent paths is required to prevent deforming C_0 through the essential singularity at $in\pi$. Since these paths are symmetric about the imaginary axis in the complex k-plane, only the behaviour in the right half-plane is discussed.

Proceeding upward from s_{1+} along the steepest descent path with initial angle $\theta = -\text{Arg}(s_{1+})/2 + \pi/4$, a vertical asymptote is approached. This occurs because $|\sigma_n(k)| \to N$ as $|k| \to \infty$. The vertical asymptote lies along $Re(k) = (\phi_{1I}(s_{1+}) - N)/v$.

Proceeding from s_{1+} along the steepest descent path with initial angle $\theta = -\text{Arg}(s_{1+})/2 + 5\pi/4$, the contour approaches the essential singularity at $k = in\pi$. This is the only direct connection to the steepest descent path through s_{1-}. To avoid integrating through an essential singularity the integration contour must be adjusted. Note that along this descent path from s_{1+}, $\phi_{1R}(k)$ is a strictly negative, decreasing value. Orthogonal to the descent path lie contours of constant $\phi_{1R}(k) < \phi_{1R}(s_{1+})$ that pass through the imaginary axis below $in\pi$. At any finite distance from s_{1+} such a path can be followed to cross the imaginary axis and proceed into the left half-plane until the steepest descent path from s_{1-} is intersected.

Along this bridging contour, $\phi_1(k)$ has a constant, strictly negative real part, which is less than $\phi_{1R}(s_{1+})$. The constant $\phi_{1R}(k)$ can be factored out of the integrand. Evidently, the contribution to $\hat{I}_1$ must be small beyond all orders in comparison with the saddle point contributions from $s_{1\pm}$ because the nonconstant part of the integrand remains bounded along the bridge.

Finally, considering the locations of the poles of $f_1(k)$ and the branch cuts and singularities of $\phi_1(k)$, it is clear that the deformation process does not introduce any additional residue contributions.

The path of integration described above is illustrated in Figure D.7.

D.3.3 Asymptotic Contributions to $\hat{I}_1$

From the discussion above, the asymptotic behaviour of $\hat{I}_1$ is determined wholly from the saddle point contributions at $s_{1\pm}$. Therefore

$$\begin{aligned}\hat{I}_1 \sim\ & \tfrac{Ah_n}{4\pi} e^{\phi_1(s_{1+})t} \left[\tfrac{\sigma_n(s_{1+})}{s_{1+}^2(\sigma_n(s_{1+})-\omega)} \sqrt{\tfrac{\pi}{2t|\phi_1''(s_{1+})|}} (e^{i\theta_1(s_{1+})} - e^{i\theta_2(s_{1+})}) \right] \\ & + \tfrac{Ah_n}{4\pi} e^{\phi_1(s_{1-})t} \left[\tfrac{\sigma_n(s_{1-})}{s_{1-}^2(\sigma_n(s_{1-})-\omega)} \sqrt{\tfrac{\pi}{2t|\phi_1''(s_{1-})|}} (e^{i\theta_1(s_{1-})} - e^{i\theta_2(s_{1-})}) \right] \\ & + O\left(\tfrac{\exp(\phi_{1R}(s_{1+})t)}{t} \right).\end{aligned} \tag{D.50}$$

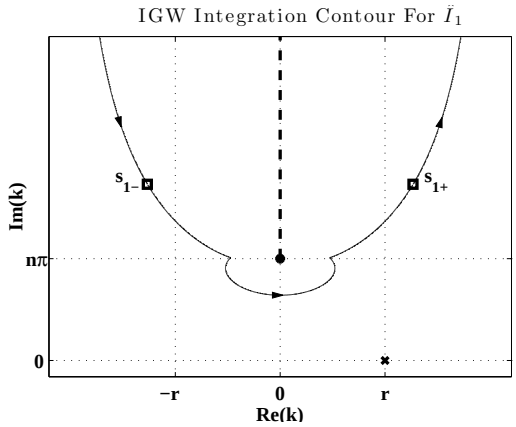

Figure D.7: Steepest descents contour for $\hat{I}_1$. The algebraic singularity at $(r, 0)$ is marked by a 'x'. The branch cut lies along the dashed line and the essential singularity at $(o, n\pi)$ is marked by a '*'. The saddle points $s_{1\pm}$ are marked by the square symbols.

Note the leading factors of $\exp(\phi_1(s_{1\pm})t)$, and recall $\phi_{1R}(s_{1\pm})$ is strictly negative for $v > 0$. As demonstrated in the next section, the integral contribution to $\psi_n(x, t)$ from $\hat{I}_1$ turns out to be asymptotically negligible compared to that of $\hat{I}_2$.

D.3.4 Description of the Critical Points of $\hat{I}_2$

The asymptotic analysis of $\hat{I}_2$ closely follows that of $\hat{I}_1$, though in some ways it is simpler. The analysis is based on the saddle points of

$$\phi_2(k) = ikv - i\frac{kN}{\sqrt{k^2 + n^2\pi^2}}. \tag{D.51}$$

As usual, the analysis requires ϕ_2', ϕ_2''; these are given by

$$\phi_2'(k) = iv - \frac{in^2\pi^2 N}{(k^2 + n^2\pi^2)^{3/2}} \tag{D.52}$$

and

$$\phi_2''(k) = \frac{i3n^2\pi^2 Nk}{(k^2 + n^2\pi^2)^{5/2}}. \tag{D.53}$$

The critical points include the algebraic singularity of $f_2(k)$ at $k = -r$, the essential singularities at $\pm in\pi$, and the branch cuts along the imaginary axis. There are also two

real saddle points found by solving the equation $\phi_2'(k) = 0$ provided $v < N/(n\pi)$. The critical speed $c_L = N/(n\pi)$ is the group velocity in the long wave limit $k \to 0$, and is an upper bound for the group velocity of a wave governed by the linear IGW equations. The two saddle points are of order one and are given by

$$s_{2\pm} = \pm\sqrt{\left(\frac{n^2\pi^2 N}{v}\right)^{2/3} - n^2\pi^2}. \tag{D.54}$$

As v approaches the maximum possible group velocity c_L, the first-order saddle points coalesce to a saddle point of order two at the origin of the complex k-plane, then proceed along the upper and lower imaginary axis as v continues to increase. This is much like the situation in the analysis of the BBM equation, and suggests splitting the problem into two cases.

The directions of steepest descent from the saddle points are found by evaluating $\phi_2''(s_{2\pm})$ and using the discussion in Section 5.1.4. The angles differ depending on the range where v lies, and are summarized in Table D.3.

Range	$\theta(s_{2+})$	$\theta(s_{2-})$
$0 < v < c_L$	$\frac{\pi}{4}, \frac{5\pi}{4}$	$\frac{3\pi}{4}, \frac{7\pi}{4}$
$v > c_L$	$0, \pi$	$\frac{\pi}{2}, \frac{3\pi}{2}$

Table D.3: Steepest descent directions from the saddle points of $\hat{I}_2$.

D.3.5 The Integration Contours for $\hat{I}_2$

To compute asymptotic contributions, the integration contour C_0 must be deformed onto steepest descent paths passing through the saddle points. The paths used are qualitatively different depending on v.

With the splitting $\phi_2(k) = \phi_{2R}(k) + i\phi_{2I}(k)$, it is clear that $\phi_{2I}(s_{2-}) = -\phi_{2I}(s_{2+})$, while $\phi_{2R}(s_{2-}) = \phi_{2R}(s_{2+}) = 0$. As was the case for ϕ_1 the contours of steepest descent through $s_{2\pm}$ cannot intersect, except at the essential singularities. Observe, however, that along the steepest descents paths in the lower half-plane $\phi_{2R}(k)$ decreases continuously from 0 to $-\infty$. In particular, each point along the steepest descents curve lies on a different curve of constant ϕ_{2R} that crosses the imaginary k-axis above $-in\pi$. Any of these contours is a suitable curve to bridge the steepest descents paths in the two half-planes. The contribution of integrating along such a curve is small beyond all orders in comparison with the contributions from the steepest descents paths.

The asymptotic integration contour used is found by deforming C_0 onto the paths of steepest descent through s_{2+} and s_{2-}, with a bridging contour joining the steepest descent

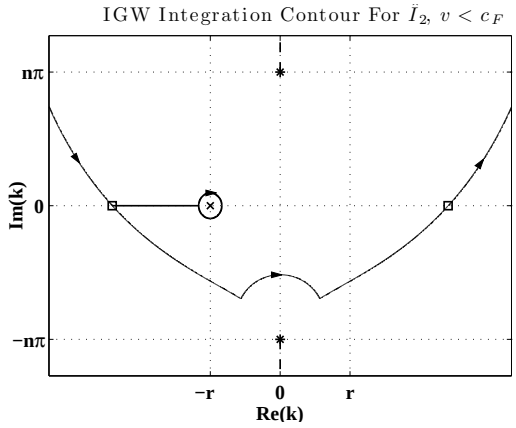

Figure D.8: Steepest descents contour used for $\hat{I}_2$ when $v < c_F$. The simple pole at $-r$ is enclosed by a clockwise-oriented circle and marked by a 'x' symbol The branch cuts are indicated by dashed lines and the essential singularities are illustrated with '*' symbols. Saddle points are marked with square symbols.

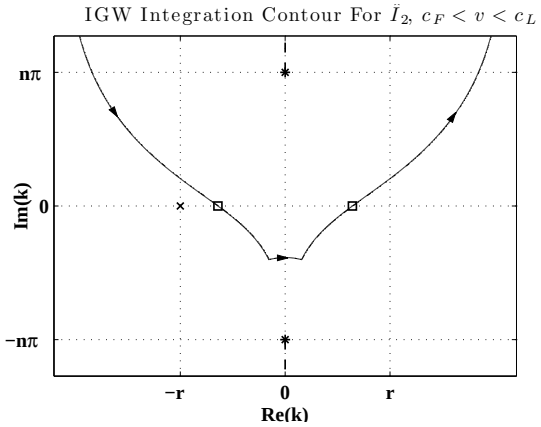

Figure D.9: Steepest descents contour used for $\hat{I}_2$ when $c_F < v < c_L$. The simple pole at $-r$ is marked by a 'x' symbol The branch cuts are indicated by dashed lines and the essential singularities are illustrated with '*' symbols. Square symbols mark the locations of the saddle points on the real line.

paths above $-in\pi$. In the upper half-plane, the steepest descent paths through $s_{2\pm}$ proceeds upwards and tends to a vertical asymptote at $Re(k) = (\phi_{2I}(s_{2\pm}) + N)/v$. When $v < c_F$, the deformation process also enclose the simple pole at $k = -r$. This is because s_{2-} lies to the left of $-r$ on the real axis. The pole is enclosed with a circle connected by a straight line to the steepest descent path through s_{2-}.

The deformed path of integration when $v < c_F$ is illustrated in Figure D.8. Note the encirclement of the pole at $k = -r$. The integration contour for $c_F < v < c_L$ is shown in Figure D.9, noticeably the saddle point s_{2-} lies to the right of $-r$ so the pole is not enclosed.

When $v > c_L$, the contour C_0 is deformed directly onto the steepest descent path through s_{2+} with no modifications. The path lies strictly in the upper half-plane and does not enclose the pole at $k = -r$. Figure D.10 illustrates the integration path.

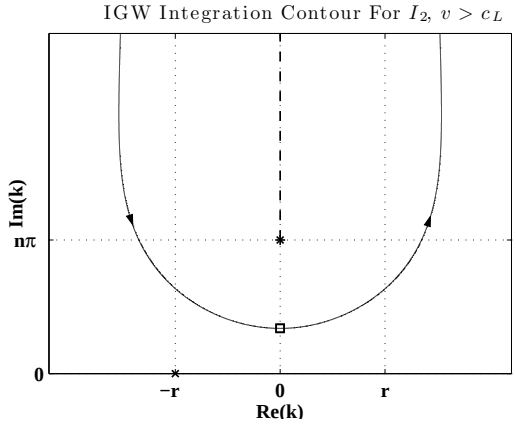

Figure D.10: Steepest descents contour used for $\hat{I}_2$ when $v > c_L$. The simple pole at $-r$ is marked by a 'x' symbol The branch cuts are indicated by dashed lines and the essential singularities are illustrated with '*' symbols. The square on the imaginary axis indicates the location of the saddle point s_{1+}.

D.3.6 Asymptotic Contributions to $\hat{I}_2$

With the discussion and diagrams above, the asymptotic contributions to $\hat{I}_2$ are readily found. When $0 < v < c_F$ the dominant contribution is from the simple pole encircled in

the deformation process, so:

$$\begin{aligned}\hat{I}_2 \sim \quad & A\tfrac{h_n\omega}{2r^2\sigma_n'(-r)}\exp(-i(rx-\omega t)+i\pi/2) \\ & +\tfrac{Ah_n}{2\pi}e^{\phi_2(s_{2+})t+i\pi/4}\left(\tfrac{\sigma_n(s_{2+}))}{s_{2+}^2(\sigma_n(s_{2+})+\omega)}\sqrt{\tfrac{\pi}{2t|\phi_2''(s_{2+})|}}\right) \\ & -\tfrac{Ah_n}{2\pi}e^{\phi_2(s_{2-})t+i3\pi/4}\left(\tfrac{\sigma_n(s_{2-}))}{s_{2-}^2(\sigma_n(s_{2-})+\omega)}\sqrt{\tfrac{\pi}{2t|\phi_2''(s_{2-})|}}\right) \\ & +O\left(\tfrac{1}{t}\right).\end{aligned} \tag{D.55}$$

The result is similar when $c_F < v < c_L$, except there is no residue contribution from the simple pole in the deformation process. Therefore the solution decays like $t^{-1/2}$. In particular:

$$\begin{aligned}\hat{I}_2 \sim \quad & \tfrac{Ah_n}{2\pi}e^{\phi_2(s_{2+})t+i\pi/4}\left(\tfrac{\sigma_n(s_{2+}))}{s_{2+}^2(\sigma_n(s_{2+})+\omega)}\sqrt{\tfrac{\pi}{2t|\phi_2''(s_{2+})|}}\right) \\ & -\tfrac{Ah_n}{2\pi}e^{\phi_2(s_{2-})t+i3\pi/4}\left(\tfrac{\sigma_n(s_{2-}))}{s_{2-}^2(\sigma_n(s_{2-})+\omega)}\sqrt{\tfrac{\pi}{2t|\phi_2''(s_{2-})|}}\right) \\ & +O\left(\tfrac{1}{t}\right).\end{aligned} \tag{D.56}$$

This is reasonable; an observer moving at speed $v > c_F$ should not witness the slower forced waves at sufficiently large times. Finally, when $v > c_L$ the integral contributions come entirely from the saddle point s_{2+}. The result is

$$\begin{aligned}\hat{I}_2 \sim \quad & \tfrac{Ah_n}{2\pi}e^{\phi_2(s_{2+})t}\left(\tfrac{\sigma_n(s_{2+}))}{s_{2+}^2(\sigma_n(s_{2+})+\omega)}\sqrt{\tfrac{\pi}{2t|\phi_2''(s_{2+})|}}\right) \\ & +O\left(\tfrac{\exp(\phi_{2R}(s_{2+})t)}{t}\right).\end{aligned} \tag{D.57}$$

Note that when $v > c_L$, $\phi_{2R}(s_{2+}) < 0$, so this solution is small beyond all orders compared with that for $v < c_L$. Once again, this is reasonable because an observer traveling at $v > c_L$ is moving faster than the fastest possible waves in the system. After a sufficient amount of time has elapsed no signal would be observable.

D.3.7 Solution Summary

The full asymptotic solution for the streamfunction is found by summing over all of the mode contributions. That is,

$$\psi(x,z,t) \sim \sum_{j=1}^{\infty}\psi_n(x,t)\sin(n\pi z). \tag{D.58}$$

The contribution from each mode is found by summing the asymptotic contributions from $\hat{I}_1$ and $\hat{I}_2$. Precise formulas for these contributions have been derived, here the leading-order behaviour is summarized.

Direct comparison shows that for $v < c_L$, $\hat{I}_1$ is subdominant to $\hat{I}_2$. Therefore when $v < c_F$, $\psi_n(x,t)$ behaves like:

$$\psi_n(x,t) \sim -A\frac{h_n\omega}{2r^2\sigma_n'(-r)}\exp(-i(rx-\omega t)+i\pi/2)+O(t^{-1/2}). \tag{D.59}$$

When $c_F < v < c_L$ the dominant contribution to the streamfunction is $O(t^{-1/2})$, and when $v > c_L$ the streamfunction must be small beyond all orders in comparison with $t^{-1/2}$. The most important feature of the solution is its regular sinusoidal nature when $v < c_F$. This enables the prediction of wave amplitudes, phases, and frequencies for a given forcing function, and can guide experimental design.

Bibliography

[1] M. J. Ablowitz and A. S. Fokkas. *Complex Variables: Introduction and Applications, Second Edition*. Cambridge University Press, Wellesley, MA, 2003. 129, 130, 131

[2] M. J. Ablowitz and H. Segur. *Solitons and the inverse scattering transform*. SIAM, Philadelphia, PA, 1981. 22

[3] T. R. Akylas, R. H. J. Grimshaw, S. R. Clarke, and A. Tabaei. Reflecting tidal wave beams and local generation of solitary waves in the ocean thermocline. *J. Fluid Mech.*, 593:297–313, 2007. 10

[4] W. Alpers. Theory of radar imaging of internal waves. *Nature*, 314:245–247, 1985. 3

[5] J. M. Becker and R. H. J. Grimshaw. Explosive resonant triads in a continuously stratified shear flow. *J. Fluid Mech.*, 257:219–228, 1993. 21

[6] C. M. Bender and S. A. Orszag. *Advanced Mathematical Methods For Scientists And Engineers: Asymptotic Methods and Perturbation Theory*. Springer-Verlag, New York, 1999. 45, 129

[7] T. B. Benjamin, J. L. Bona, and J. J. Mahony. Model equations for long waves in nonlinear dispersive systems. *Phil. Trans. Roy. Soc. A*, 227:47–78, 1972. 146

[8] N. Bleistein and R. A. Handelsman. *Asymptotic Expansions Of Integrals*. Dover, New York, 1986. 129, 136, 203

[9] P. Bouruet-Aubertot, J. Sommeria, and C. Staquet. Breaking of standing internal gravity waves through two-dimensional instabilities. *J. Fluid Mech.*, 285:265–301, 1995. 9, 10

[10] W. E. Boyce and R. C. DiPrima. *Elementary Differential Equations And Boundary Value Problems, Sixth Edition*. John Wiley and Sons, Inc., Toronto, 1997. 26

[11] F. P. Bretherton. On the mean motion induced by internal gravity waves. *J. Fluid Mech.*, 36:785–8034, 1969. 113, 186

[12] O. Bühler. *Waves and Mean Flows*. Cambridge University Press, Cambridge, 2009. 53

[13] R. Courant and D. Hilbert. *Methods of Mathematical Physics, Volume I*. Interscience Publishers Inc., New York, 1966. 35

[14] A. D. D. Craik. *Wave interactions and fluid flows*. Cambridge University Press, Cambridge, 1988. 8, 18, 21, 22

[15] A. D. D. Craik and J. A. Adam. Evolution in space and time of resonant wave triads. I. The 'pump-wave approximation'. *Proc. Roy. Soc. Lon. A*, 363:243–255, 1978. 24

[16] A. D. D. Craik and J. A. Adam. Explosive resonant wave interactions in a three-layer fluid flow. *J. Fluid Mech.*, 92:15–33, 1979. 21

[17] R. E. Davis and A. Acrivos. The stability of oscillatory internal waves. *J. Fluid Mech.*, 30:723–736, 1967. 8, 9, 170

[18] A. Degasperis, M. Conforti, F. Baronio, and S. Wabnitz. Stable control of pulse speed in parametric three-wave solitons. *Phys. Rev. Let.*, 97, 093901, doi:10.1103/PhysRevLett.97.093901, 2006. 22

[19] J. W. Demmel. *Applied Numerical Linear Algebra*. SIAM, Philadelphia, 1997. 47

[20] P. G. Drazin and R. S. Johnson. *Solitons: An Introduction, Second Edition*. Cambridge University Press, Cambridge, 1989. 112, 136

[21] P. G. Drazin and W. H. Reid. *Hydrodynamic Stability*. Cambridge University Press, New York, 1981. 8

[22] D. G. Duffy. *Green's Functions With Applications*. Chapman and Hall, New York, 2001. 41, 128, 157, 166, 173

[23] D. G. Duffy. *Transform Methods For Partial Differential Equations, Second Edition*. Chapman and Hall, New York, 2004. 123, 129, 169

[24] P. Echeverri, M. R. Flynn, K. B. Winters, and T. Peacock. Low-mode internal tide generation by topography: An experimental and numerical investigation. *J. Fluid Mech.*, 363:91–108, 2009. 10

[25] D. Farmer, Q. Li, and J.-H. Park. Internal wave observations in the South China Sea: the role of rotation and non-linearity. *Atm.-Ocean*, 47:267–280, 2009. 121, 172

[26] O. B. Fringer and R. L. Street. The dynamics of breaking progressive interfacial waves. *J. Fluid Mech.*, 494:319–353, 2003. 7, 66

[27] C. Garrett and E. Kunze. Internal tide generation in the deep ocean. *Annu. Rev. Fluid Mech.*, 39:57–87, 2007. 5, 10, 94, 172

[28] T. Gerkema and J. T. F. Zimmerman. An introduction to internal waves. *Lecture notes, Royal NIOZ, Texel*, 2008. 119

[29] A. E. Gill. *Atmosphere-Ocean Dynamics*. Academic Press, New York, 1982. 53

[30] R. Haberman. *Applied Partial Differential Equations with Fourier Series and Boundary Value Problems, 4th Edition*. Prentice Hall, Upper Saddle River, NJ, 2003. 64, 128, 139

[31] K. R. Helfrich and R. H. J. Grimshaw. Nonlinear disintegration of the internal tide. *J. Phys. Ocean.*, 38:686–701, 2008. 121, 172

[32] K. R. Helfrich and W. K. Melville. Long nonlinear internal waves. *Annu. Rev. Fluid Mech.*, 38:395–425, 2006. 4, 10, 172

[33] D. P. Hinson and G. L. Tyler. Internal gravity waves in Titan's atmosphere observed by Voyager radio occultation. *Icarus*, 54:337–352, 1983. 2

[34] Y. Hu. The Effects of the Earth's Rotation on Internal Wave Near-resonant Triads and Weakly Nonlinear Models. Master's thesis, University of Waterloo, 2007. 9, 14, 20, 170, 172, 182, 185

[35] R. Knobel. *An Introduction to the Mathematical Theory of Waves*. American Mathematical Society, Providence, Rhode Island, 2000. 25, 119

[36] C. R. Koudella and C. Staquet. Instability mechanisms of a two-dimensional progressive internal wave. *J. Fluid Mech.*, 548:165–196, 2006. 10

[37] P. K. Kundu and I. M. Cohen. *Fluid Mechanics, Third Edition*. Elsevier Academic Press, Boston, 2004. 4, 6, 15, 103, 113, 187

[38] K. G. Lamb. Nonlinear interaction among internal wave beams generated by tidal flow over supercritical topography. *Geophys. Res. Let.*, 31, L09313, doi:10.1029/2007GL030825, 2004. 52

[39] K. G. Lamb. Energy and pseudoenergy flux in the internal wave field generated by tidal flow over topography. *Cont. Shelf Res.*, 27:1208–1232, 2007. 53

[40] K. G. Lamb. Hydrodynamic stability. *University of Waterloo, AMATH 863 Lecture Notes*, 2007. 14

[41] K. G. Lamb. Tidally generated near-resonant internal wave triads at a shelf break. *Geophys. Res. Let.*, 34, L18607, doi:10.1029/2007GL030825, 2007. 9, 20, 120, 170, 172, 182, 185

[42] K. G. Lamb and L. Yan. The evolution of internal wave undular bores: comparisons of a fully nonlinear numerical model with weakly nonlinear theory. *J. Phys. Ocean.*, 26:2712–2734, 1996. 98, 116

[43] P. H. LeBlond and L. A. Mysak. *Waves In The Ocean*. Springer-Verlag, New York, 1980. 4, 27, 103

[44] J. J. Leichter, G. Shellenbarger, S. J. Genovese, and S. R. Wing. Breaking internal waves on a Florida (USA) coral reef: a plankton pump at work? *Mar. Eco. Proc.*, 16:83–97, 1998. 5

[45] J. Lighthill. *Waves In Fluids*. Cambridge University Press, Cambridge, 1978. 4, 11, 124, 126, 157, 168, 173

[46] J. Lighthill. Internal waves and related initial-value problems. *Dyn. Atm. and Oceans*, 23:3–17, 1996. 11

[47] P. N. Lombard and J. J. Riley. Instability and breakdown of internal gravity waves. I. Linear stability analysis. *Phys. Fluids*, 8:3271–3287, 1996. 7

[48] P. N. Lombard and J. J. Riley. On the breakdown into turbulence of propagating internal waves. *Dyn. Atm. and Oceans*, 23:345–355, 1996. 7

[49] S. Martin, W. Simmons, and C. Wunsch. The excitation of resonant triads by single internal waves. *J. Fluid Mech.*, 53:17–44, 1972. 9, 10, 74

[50] M. Mathur and T. Peacock. Internal wave beam propagation in non-uniform stratifications. *J. Fluid Mech.*, 639:133–152, 2009. 10

[51] C. H. McComas and P. Müller. Time scales of resonant interactions among oceanic internal waves. *J. Phys. Ocean.*, 11:139–147, 1981. 80

[52] G. L. Mellor. *Introduction To Physical Oceanography*. Springer-Verlag, New York, 1996. 94

[53] A. W. Naylor and G. R. Sell. *Linear Operator Theory in Engineering and Science*. Springer, New York, 1982. 26, 43

[54] NASA Earth Observatory. Ocean features from Seasat. `http://earthobservatory.nasa.gov/IOTD/view.php?id=3589`. xiv, 4

[55] NASA Earth Observatory. Wave clouds near Amsterdam Island. `http://earthobservatory.nasa.gov/IOTD/view.php?id=6151`. xiv, 2, 10

[56] A. R. Osborne. Numerical construction of nonlinear wave-train solutions of the periodic Korteweg-de Vries equation. *Phys. Rev. E*, 48(1):296–309, 1993. 120, 171, 172

[57] O. M. Phillips. On the dynamics of unsteady gravity waves of finite amplitude. Part 1. The elementary interactions. *J. Fluid Mech.*, 9:193–217, 1960. 8

[58] O. M. Phillips. Wave interactions - the evolution of an idea. *J. Fluid Mech.*, 106:215–227, 1981. 8

[59] K. L. Polzin, J. M. Toole, J. R. Ledwell, and R. W. Schmitt. Spatial variability of turbulent mxing in the abyssal ocean. *Science, New Series*, 276(5309):93–96, 1997. 5

[60] F. J. Poulin. Personal communication, 2010. 27

[61] D. Richards. *Advanced Mathematical Methods With Maple*. Cambridge University Press, Cambridge, 2002. 35

[62] S. Solomon. Stratospheric ozone depletion: A review of concepts and history. *Rev. Geophys.*, 37(3):275–316, 1999. 4

[63] C. Staquet and J. Sommeria. Internal gravity waves: From instabilities to turbulence. *Annu. Rev. Fluid Mech.*, 34:559–593, 2002. 8, 9

[64] C. Subich. *Simulation of the Navier-Stokes Equations in Three Dimensions with a Spectral Collocation Method*. PhD thesis, University of Waterloo, 2011. 5, 49, 51

[65] S. A. Thorpe. On the shape of progressive internal waves. *Phil. Trans. Roy. Soc. Lon. A*, 263(1145):563–614, 1968. 113, 186

[66] S. A. Thorpe. Statically unstable layers produced by overturning internal gravity waves. *J. Fluid Mech.*, 260:333–350, 1994. 8

[67] L. N. Trefethen. *Spectral Methods in Matlab*. SIAM, Philadelphia, 2000. 48

[68] C. D. Troy and J. R. Koseff. The instability and breaking of long internal waves. *J. Fluid Mech.*, 543:107–136, 2005. 8, 10, 74, 75

[69] C. D. Troy and J. R. Koseff. The viscous decay of progressive interfacial waves. *Phys. Fluids*, 18(2), 026602, doi:10.1063/1.2166849, 2006. 8, 10

[70] H. van Haren and L. Gostiaux. A deep-ocean Kelvin-Helmholtz billow train. *Geophys. Res. Let.*, 37, L03605, doi:10.1029/2009GL041890, 2010. 3

[71] B. Voisin. Internal wave generation in uniformly stratified fluids. Part 1. Green's function and point sources. *J. Fluid Mech.*, 231:439480, 1991. 11, 124, 157, 173

[72] J. A. Weideman and S. C. Reddy. A MATLAB differentiation matrix suite. *ACM Trans. Math. Soft.*, 26:465–519, 2000. 48

[73] K. B. Winters, J. A. Mackinnon, and B. Mills. A spectral model for process studies of rotating, density-stratified fluids. *J. Atmos. Ocean. Tech.*, 21(1):69–94, 2004. 5, 52

[74] M. G. Wurtele, R. D. Sharman, and A. Datta. Atmospheric lee waves. *Annu. Rev. Fluid Mech.*, 28:429–476, 1996. 10

[75] M. Yanowitch. Gravity waves in a heterogeneous incompressible fluid. *Comm. Pure. Apple. Math.*, 15:45–61, 1962. 27, 43, 45

[76] C. S. Yih. *Dynamics Of Nonhomogeneous Fluids*. MacMillan, New York, 1965. 27, 33, 45, 170

[77] C. S. Yih. Wave motion in stratified fluids. In S. Leibovich and A. R. Seebass, editors, *Nonlinear Waves*, pages 263–290. Cornell University Press, Ithica, 1974. 27, 32

[78] A. Zettl. *Sturm-Liouville Theory*. Mathematical Surveys And Monographs, v. 121, American Mathematical Society, 2005. 18, 26, 30, 37